Nanofabrication and its application in atomic force microscopy (AFM)

by

Ripon Dey

A thesis
presented to University of Waterloo
in fulfillment of the
thesis requirement for the degree of
Doctor of Philosophy
in
Electrical and Computer Engineering (Nanotechnology)

Waterloo, Ontario, Canada, 2015

Author's Declaration

I hereby declare that I am the sole author of this thesis. This is a true copy of the thesis, including any required final revisions, as accepted by my examiners.

I understand that my thesis may be made electronically available to the public.

Abstract

This thesis is focused on nanofabrication and its application in atomic force microscopy (AFM). The contribution of this thesis is thus the development, investigation and characterization of novel nanofabrication technique (Part I); and application of nanofabrication in manufacturing the high aspect ratio AFM tips (Part II).

In the first part of the thesis, firstly, unlike optical and mechanical lithography such as nanoimprint lithography, the throughput of EBL is very low, which demands for highly sensitive resists. We studied the dependency of e-beam exposure properties on molecular weight of the negative EBL resist polystyrene, and very high sensitivity of 1 $\mu C/cm^2$ was obtained for 900 kg/mol when exposed with electron beam of 2 keV. We also demonstrated that the exposure property of high PDI (polydispersity index) polystyrene resembles that of a monodisperse (PDI ≈ 1.06) polystyrene with similar number averaged molecular weight $\overline{Mn}$, which indicates that it is $\overline{Mn}$ rather than $\overline{Mw}$ (weight averaged molecular weight) that dominates the exposure properties of polystyrene resist.

Secondly, lift-off using negative resist is very challenging because the resist profile is typically positively tapered due to electron forward scattering, and upon exposure negative resist is cross-linked and thus insoluble in solvents. Here we demonstrated that low energy exposure could circumvent both issues simultaneously, and we achieved liftoff of Cr with polystyrene resist using a solvent xylene. Lastly, since low energy electrons are mostly stopped inside the resist layer, radiation damage to the sub-layer is greatly reduced.

Thirdly, an electron beam resist is usually coated by conventional coating methods such as spin-coating, but this cannot be reliably applied on irregular surfaces. We here reported a monolayer resist can be grafted on nonflat surface. As a proof of concept of patterning on irregular surfaces, we chose PMMA mono-layer "brush" and grafted it on irregular surfaces by thermal treatment which accelerates a chemical reaction between PMMA molecules and hydroxyl group on substrate. We achieved nanofabrication of 30 nm resolution on an AFM cantilever.

Fourthly, due to the lack of feedback, conventional electron beam lithography (EBL) is a “blind” open-loop process where the exposed pattern is examined only after *ex-situ* resist development, which is too late for any improvement. We reported that self-developing resist nitrocellulose, for which pattern shows up right after exposure without ex-situ development, can be used as in-situ feedback on the e-beam distortion and enlargement. Once the beam was optimized using nitrocellulose resist, under the same optimal beam condition, we exposed in the common resist PMMA. We achieved ~80 nm resolution across the entire large writing field of 1 mm^2, as compared to 210 nm without the beam optimization process. We also reported that self-developing resist can provide in-situ feedback for writing field alignment accuracy, which in turn can be used to optimize the alignment.

In the second part of the thesis, we demonstrated the batch fabrication of high aspect ratio (HAR) AFM tips. In order to obtain high quality and faithful images in AFM, very high aspect ratio tips are required in order to reach to the bottom of narrow and deep trenches/holes. But these HAR tips are extremely difficult to make and consequently very expensive. Currently all the commercially available HAR AFM tips are fabricated in a slow, costly (~5-20× that of regular AFM tips) and serial manner (one by one). We here developed a method to batch fabricate HAR AFM tips by forming a hard metal etching mask just on the apex of the pyramid tip followed by silicon dry etching to achieve the HAR pillar right below the metal island mask. Since it is a batch and lithography-free process, it has much higher throughput and much lower manufacturing cost per tip. This technique was first successfully applied on large-area pyramid arrays and then transferred to the commercial regular AFM tips, and has demonstrated the uniformity, reproducibility and yield of those HAR tips. The tip apex diameter and tip pillar height are controllable by tuning metal thickness and silicon dry etching time respectively. Finally, we demonstrated that the HAR tips fabricated using our technique gave a better imaging quality than the commercial regular tips.

Acknowledgement

This work was carried out using the nanofabrication facility at Quantum NanoFab, WATLab and Giga-to-Nanoelectronics (G2N) Laboratory in University of Waterloo. Quantum NanoFab infrastructure would not be possible without the significant contributions of the Canada Foundation for Innovation, the Ontario Ministry of Research & Innovation, Industry Canada and Mike & Ophelia Lazaridis. And, G2N laboratory is funded by Canada Foundation for Innovation, the Ontario Ministry of Research & Innovation and Industry Canada. Their support is also gratefully acknowledged. The work is partly supported by the NSERC-Industrial Postgraduate Scholarships and OCE TalentEdge internship fund. I am greatly acknowledged to NSERC and OCE authorities for giving me this opportunity.

First of all, I will be glad to express my heartiest gratitude to my beloved parents for their continuous encouragement throughout my studies; and to my lovely wife for her continuous support and enthusiasm during my study.

The person to whom I am greatly acknowledged is my supervisor Professor Bo Cui. I am very grateful for getting his kind guidance and invaluable suggestions throughout the entire work of my dissertation. I would also like to thank to my committee members of my PhD examination: Prof. Jun Yang, Prof. Raafat Mansour, Prof. Simarjeet Saini and Prof. Shirley Tang, who agreed to be my committee members and provided me many suggestions and remarks on my research.

I would like to sincerely thank to Prof. Tong Leung and Prof. Ting Tsui for their cordial assistance on using their laboratories, and to the lab managers in Cleanrooms, Richard Barber, and Vito Logiudice, for their friendly supports in laboratories. I would like to also thank Dr. Nathan Nelson-Fitzpatrick, Brian Goddard for their cooperation while doing my experiments at QNCfab lab.

I also thank to our nanofabrication group at Waterloo, especially to group mates Xiangcheng Sun, Celal Con, Babak Shokouhi, Arwa Abbas, Sondos Alqarni and Alanoud Alshammari. Also my thanks goes to lab mates Minoli Pathirane, Mark Ferguson, Eric for their cordial cooperation on my research.

Finally, I wish to express my thanks to Almighty for providing me the chance to fulfill my desire.

Dedication

"All the freedom-fighters of Bangladesh",

"My dear parents, my lovely wife, and my dear siblings".

Table of Contents

List of Figures

List of Tables

CHAPTER 1

Introduction

This chapter gives a brief introduction to nanofabrication.

1.1. What is nanotechnology?

Nanotechnology is the branch of technology that deals with the study at the nanoscale, which is about 1 to 100 nanometers (1 nanometer is 10^{-9} meters; one billionth of a meter). Nanotechnology includes the systemic study of synthesis, characterization, modification and fabrication in nanoscale. Nowadays, the application of nanotechnology expands greatly in many fields such as biomedical technology, nanoelectronics, automobile, and nanobiology etc. In application, nanoscale sized functional devices bring not only the reduction of raw materials and energies, but also lead to highly integrated multi-functionalities as well as reducing the cost of manufacturing per unit. Figure 1.1 compares a bunch of nanofibres with a human hair.

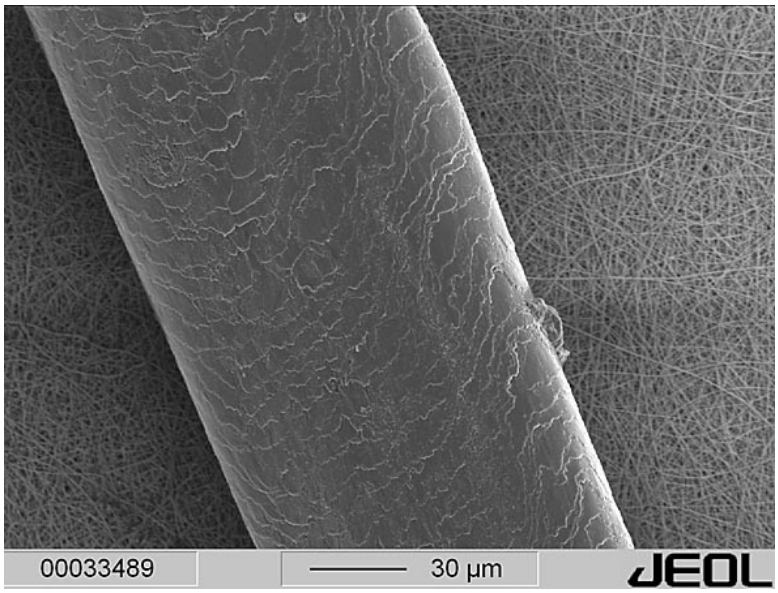

Figure 1.1. A human hair along with bunch of nanofibres [Picture courtesy to Ashraf Asran[1]].

1.2. Overview of nanofabrication

Nanofabrication is the technology which is capable of fabricating nanoscale structures with dimensions down to sub-100 nm. It plays very important role in all sectors of nanotechnology. There are three major parts in nanofabrication which involve lithography, thin film deposition techniques and etching techniques. Microfabrication is the basis for nanofabrication and photolithography is the core technology for microfabrication, whereas electron beam lithography plays major role in nanofabrication. There are two types of nanofabrication approaches: "top-down" and "bottom-up". The lateral size of the nanostructures is defined using lithography process, and the vertical dimension by thin film deposition and etching techniques. Nanolithography techniques include electron beam lithography (EBL), focused ion beam lithography, nanoimprint and scanning probe lithography. There are a variety of thin film deposition and etching techniques, which includes e-beam evaporation, sputtering deposition, chemical vapor deposition (CVD), and reactive ion etch (RIE), sputter etch, ion mill respectively. Figure 1.2 (a) shows an example of top-down approach where the resist is patterned firstly by lithography such as electron beam lithography, then the pattern is transferred by either metal deposition followed by liftoff (Figure 1.2 (a)(1)), or direct etching (Figure 1.2 (a)(2)). The

applications of top-down fabrication techniques are vast which include the random access memory, integrated circuits, storage device, microfluidics, solar cells etc.

Bottom-up approach is based on self-assembly of nanoscale blocks into ordered array of nanostructures and chemical synthesis of nanoparticles. It includes nanosphere lithography, self-assembly of block copolymers[2], atoms, molecules and supramolecular elements, and template-based methods that utilize nanoporous membranes. Figure 1.2 (b) shows a typical example of bottom-up approach where the substrate is coated by chemically synthesized nanospheres followed by pattern transfer.

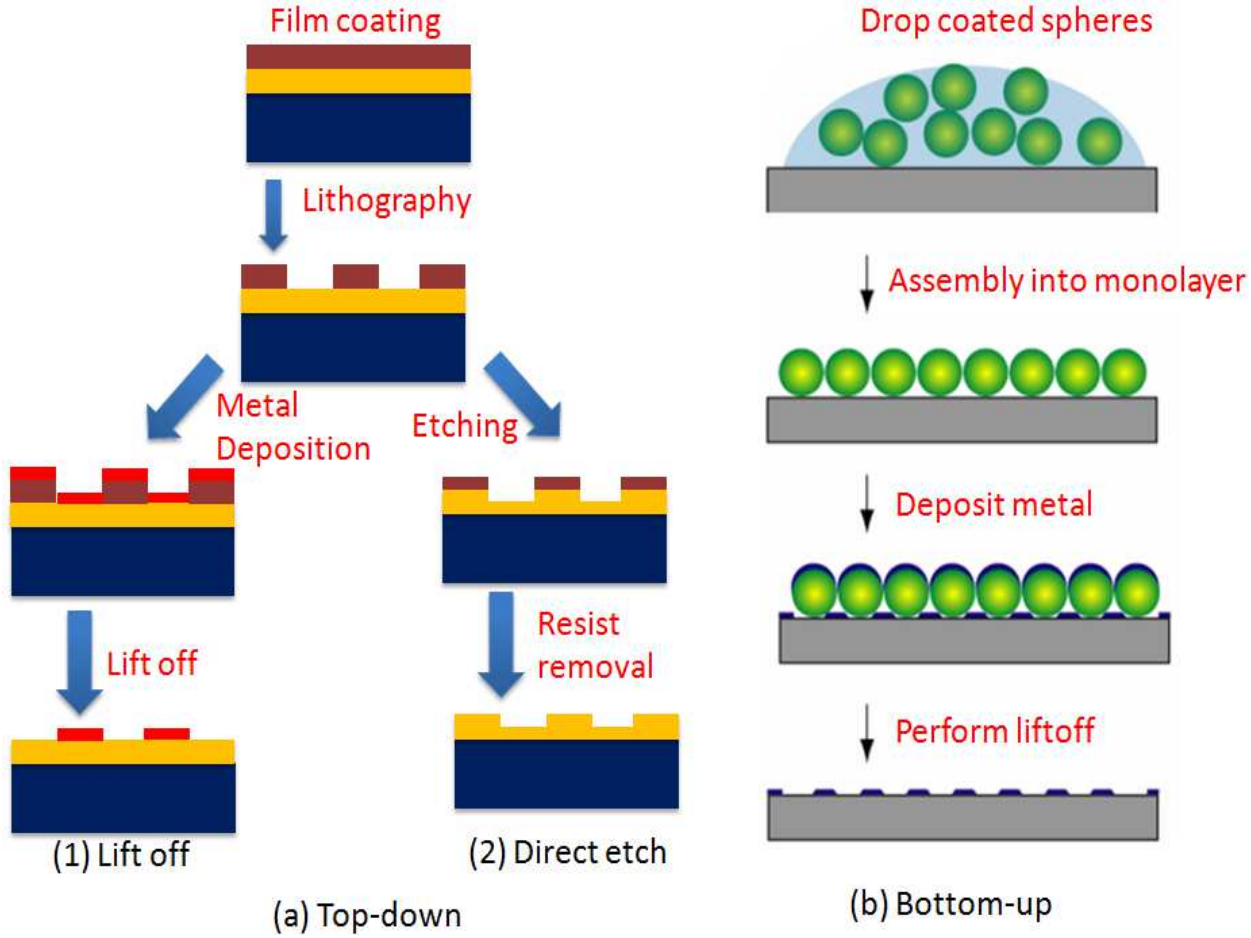

Figure 1.2. Schematic diagram of (a) top-down and (b) bottom-up approach. In the top-down approach, (1) the resist is patterned by lithography, and then the pattern is transferred by deposition followed by liftoff, or (2) the pattern is transferred by direct etch. In the bottom-up approaches, nanolithography is usually obtained by self-assembly followed by pattern transfer such as liftoff.

Lithography involves the transfer of the pattern information to a sensitive material either by mechanical force or by exposure of photon, ion or electron[3]. Lithography is widely used in many fields of nanoscience and nanotechnology (top-down fabrication technique) which includes the fabrication of integrated circuit to the fabrication of micro and nano-electromechanical systems (MEMS and NEMS). Lithography techniques can be classified into two types. The first type is capable of duplicating the pattern of the mask/mold which includes photolithography (or optical lithography), x-ray lithography (XRL), deep ultra-violet lithography (DUVL), extreme ultra-violet lithography (EUVL) and nanoimprint lithography (NIL). Broadly speaking, this type has high throughput as the mask/mold pattern is duplicated in one run. As a result, this is suitable for high volume production. The second type is capable of direct patterning that produces the pattern without employing any mask/mold which includes electron beam lithography (EBL), ion beam lithography (IBL) and scanning probe lithography (SPL)[4]. This type produces the pattern in a serial basis, thus it is time consuming with low throughput. Therefore it is suitable for R&D and mask/mold production.

For semiconductor manufacturing and other volume production, photolithography is the prime lithography technique which is popular for its low cost and high throughput. It can produce the pattern with high resolution. The resolution is limited by light diffraction, equipment and process control etc. To overcome these limitations, several resolution enhancement techniques (RET) have been developed such as off-axis illumination (OAI), phase shift masks (PSM), optical proximity correction (OPC), and double processing[5], which leads to the resolution down to sub-10 nm. Nanoimprint lithography is another popular nanolithography technique with low cost, high resolution and high throughput. It is a replication technology which replicates micro and nanostructures onto imprint resist (cured by heat or UV light) by pre-fabricated molds[6]. The achievable resolution is limited only by the mold resolution, not by light diffraction as in the case of optical lithography, or beam scattering as in the case of charged beam lithography.

Direct patterning lithography is a process to print patterns into a resist layer by an exposure of electrons or ions. Upon development, the resist pattern is transferred to the substrate/sub-layer by etching or deposition techniques. Electron beam lithography (originated from Scanning electron

microscope (SEM) by Baron Manfred von Ardenne in 1937[7]), the most fundamental technique for research and development, has been widely used to pattern very small features, which uses electrons to modify the polymer resist on a sample surface and develops the sample in a solvent to selectively etch resist in exposed area or unexposed area. The fundamental of electron beam lithography is detailed in Chapter 2. Focused ion beam was developed by Levi-Setti in 1975[8] and helium ion beam in 2005[9]. Focused ion beam (mainly includes Gallium, helium ion in helium ion beam microscope; proton in proton beam microscope) lithography exposes the resist without proximity effect but it contaminates the resist with the ion. Scanning probe lithography (originated from atomic force microscope (AFM) invented by Binnig in 1986[10]) is also widely used to pattern the nanostructure via oxidation, local heating or object manipulation. Such a tip-based nanofabrication (TBN) is an effective method compared to conventional fabrication processes due to its simplicity, high resolution, and low cost. Detail of tip-based nanofabrication is discussed in chapter 4.

Addition and subtraction of materials are important parts in nanofabrication to transfer/generate the pattern in nanoscale. Thin film deposition ('additive method') includes physical vapor deposition (PVD) (sputtering, e-beam or thermal evaporation), chemical vapor deposition (CVD) (metal-organic CVD, plasma-enhanced CVD, low pressure CVD), epitaxy (molecular beam epitaxy (MBE), liquid-phase epitaxy), electrochemical deposition, oxidation (growth of thermal oxide) and; spin-on and spray-on film coating (resist coating).

Etching ('subtractive method') techniques plays a major role in nanofabrication for material removal. It is consisted of three processes which includes mass transport of reactants (through a boundary layer) to the surface to be etched, reaction between reactants and the film to be etched at the surface, and mass transport of reaction products from the surface through the surface boundary layer. There are two types of etching: “dry” and “wet” etching. Wet etching uses liquid etchants with wafers immersed in etchant solution which is cheap and simple, but hard to control (may not reproducible), so it is not popular for nanoscale pattern transfer purpose. Dry etching uses gas phase etchants in a plasma, both chemical and physical (sputtering process). Dry plasma etch can be used for many dielectric materials and some metals. There are two categories in etching technique based on etched profile: isotropic etch and anisotropic etch. Generally

speaking, chemical process (wet etch, plasma etch) in etching leads to isotropic etch; whereas physical process (directional energetic bombardment) leads to anisotropic etch. In Chapter 5, the dry etching is required to prepare high aspect ratio tips.

1.3. Objectives of this thesis

As mentioned above, this thesis consists of two parts, thus with two main objectives. The objectives for Part I (electron beam lithography) are (a) to study the effect of 'molecular weight' and 'molecular weight distribution' on e-beam exposure properties of polystyrene; (b) to demonstrate the lift-off with solvent for negative resist using low energy electron beam exposure; (c) to design the process in order to graft PMMA monolayer brush on to irregular/non-flat surface for electron beam lithography; (d) to adjust the electron beam in large scale exposure of moderate resolution pattern with feedback using in-situ self-developed resist; and (e) to reduce the stitching error in electron beam lithography with in-situ feedback using self-developing resist for large area writing fields.

The objective for Part II is to develop the fabrication process for high aspect ratio AFM (atomic force microscope) tips. The key feature of the technology is that it is a low-cost batch fabrication process with high yield. The process starts from a wafer of AFM tips containing high density of low aspect ratio tips, and process them simultaneously to produce sharp and high aspect ratio tips. More specifically, our goals are to optimize and improve the fabrication process in order to make it a commercially viable technology for low cost and high volume production of high aspect ratio AFM tips. To sum up, the objectives are: (a) to optimize the process steps to achieve reproducible high aspect ratio AFM tips with desired tip dimensions; (b) to evaluate and improve the uniformity and yield of the process across an entire 4" wafer of pyramid tips; (c) to fabricate tips with controllable pillar diameters; (d) to fabricate tips with controlled shape, such as with a slight taper angle to make it more mechanically robust; (e) to transfer the technology to the commercial regular AFM tips (low aspect ratio) and demonstrate the uniformity, reproducibility and yield of processed tips; and (f) to fabricate tips with tilt compensation since during real AFM scanning, the tip cantilever is not parallel to the sample surface; instead it is tilted by ~10-13°. It

is thus desirable to fabricate an AFM tip with the pillar tilted at the similar angle, so that the tip is perpendicular to the sample surface when mounted onto AFM.

1.4. Structure of this thesis

In first part (Chapters 1-3), nanofabrication with electron beam lithography is introduced, optimized, adjusted and characterized. Chapter 1 gives a brief introduction to nanofabrication. Chapter 2 gives fundamentals of electron beam lithography. In addition, it elaborates my research on the nanofabrication techniques using electron beam lithography. Chapter 3 discusses about the electron beam adjustment in electron beam lithography. It demonstrates not only more accurate write field alignment, but also finer electron beam tuning within one large write field. The second part (Chapters 4-5) covers the application of novel nanofabrication techniques in manufacturing high aspect ratio AFM tips. Chapter 4 reviews recent AFM probe fabrication techniques. At the end, our technique to fabricate high aspect ratio AFM tips with low-cost will be introduced. Chapter 5 describes our method to batch fabricate the high aspect ratio AFM tips and its application on atomic force microscopy scanning. Chapter 6 is the general conclusion of this thesis.

1.5. References

[1] "Electrospun nanofibres in comparison with a human hair"- exposed by Ashraf Asran, http://www.international.uni-halle.de/university/campus_life/egyptian-papyri/

[2] M. J. Madou, "Fundamentals of Microfabrication: the science of miniaturization", CRC Press (2002).

[3] M. Geissler and Y. Xia, "Patterning: principles and some new developments", Advance Material **16(15),** 1249-1269 (2004).

[4] M. A. Mohammad, M. Mustafa, S. K. Dew, M. Stepanova, "The Interdependence of Exposure and Development Conditions when Optimizing Low-Energy EBL for Nano-Scale Resolution In: Nanofabrication Techniques and Principles", Springer M. Stepanova and S. Dew (Eds.) **350**, (2012).

[5] B. Cui, Retrieved from https://ece.uwaterloo.ca/~bcui/ECE_730.html.

[6] S. Y. Chou, P. R. Krauss and P. J. Renstrom, "Imprint Lithography with 25-Nanometer Resolution", Science **272 (5258),** 85–7 (1996).

[7] M. V. Ardenne, and D. Beischer, "Untersuchung von metalloxyd-rauchen mit dem universal-elektronenmikroskop", Zeitschrift Electrochemie (in German) **46,** 270–277 (1940).

[8] W. H. Escovitz, T. R. Fox and R. Levi-Setti, "Scanning Transmission Ion Microscope with a Field Ion Source", Proceedings of the National Academy of Sciences of the United States of America **72 (5),** 1826 (1975).

[9] NanoTechWire.com Press Release: "ALIS Corporation Announces Breakthrough in Helium Ion Technology for Next-Generation Atomic-Level Microscope", December 7th, 2005 (2005).

[10] G. K. Bennig, "Atomic force microscope and method for imaging surfaces with atomic resolution", US Patent. US4724318.

CHAPTER 2

Nanofabrication by electron beam lithography

This chapter describes fundamentals of electron beam lithography, and elaborates four research projects I carried out on e-beam lithography.

2.1. Introduction

Electron beam lithography (EBL)[1], focused ion beam (FIB) lithography[2] and nanoimprint lithography (NIL)[3] are the three most important techniques in nanofabrication. Among those three techniques, EBL is the most popular technique for research and development. Unlike nanoimprint, EBL can expose arbitrary nanostructure without the need of making a mold at the beginning. In compared with FIB, EBL is capable of exposing thick (much greater than 100 nm) resist without ion contamination to the resist.

Conventional lithography is a process to print patterns into a resist layer by an exposure of electrons, ions, or photons. Upon development, the resist pattern is transferred to the substrate by etching or deposition techniques. Electron beam lithography has been widely used to pattern very small features. Figure 2.1 shows a schematic of an electron beam lithography system. In general, an electron beam is deflected to a desired location and chemically modifies the resist. The beam would then be blanked (blocked), moved to a new location, and the blanking would be turned off again to expose the resist. This process can then be repeated until the desired pattern is fully exposed. The process is analogous to drawing a picture on a piece of paper with an extremely

sharp pencil and is therefore highly flexible. EBL is capable of achieving sub-10 nm resolution. However, exposures are done serially, which drastically reduces throughput and limits its application to scientific research and making masks for other lithography[4].

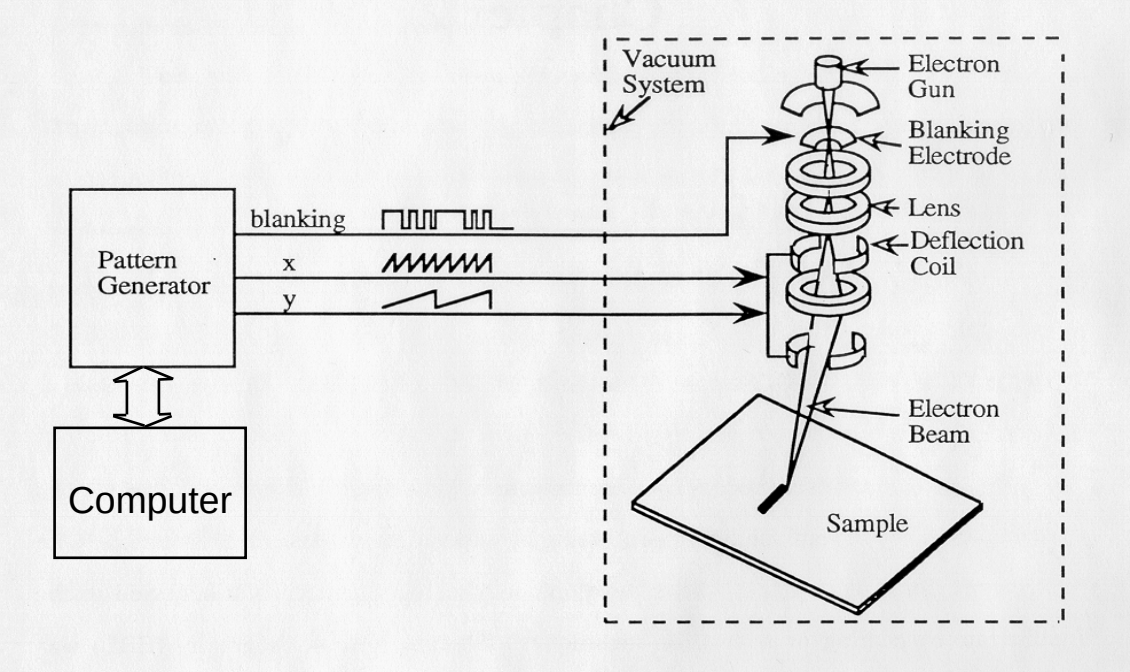

Figure 2.1. Schematic of an electron beam lithography system.

The following sections cover electron beam source, limitations on the minimum electron beam spot size, scattering of electrons during exposure and the proximity effect, and resists and developers.

2.1.1. Electron beam source

There are three common electron beam sources: thermionic, *thermal* field emission (Schottky) and cold field emission. The schematic of a typical electron gun is shown in figure 2.2 (a). Electrons can be emitted from a filament (emitter or cathode) by gaining additional energy from heat or electric field. For tungsten hairpin filament, the electrons emit from the head of the hairpin by thermionic emission, where the filament is heated to approximately 3000 K by a current source. For the field emission filament, electrons emits from a tip due to electric field. The electrode electro-statically focuses the emitted electrons to the crossover point (is an

effective real or virtual source for the downstream electron optical system.). The crossover point is then de-magnified by subsequent electron lenses to form the final electron probe at the surface of a sample. If the electron beam system did not have any aberrations, the final electron beam spot size d_0 would simply be $d_0 = D_0/M$ where D_0 is the crossover size and M is the demagnification. However, there are a number of common aberrations, such as spherical aberration, which limit the minimum electron beam spot size. Figure 2.2 (b) illustrates the band diagram of thermionic emission. At high temperature, some electrons have thermal kinetic energy high enough to overcome the energy barrier (work function). Figure 2.2 (c) illustrates the band diagram of field assisted thermionic emission guns for which the large field lowers the energy barrier by $\Delta\Phi$, thus greatly enhancing the emission current. Cold field emission works at even higher field for which tunneling becomes dominant at room temperature.

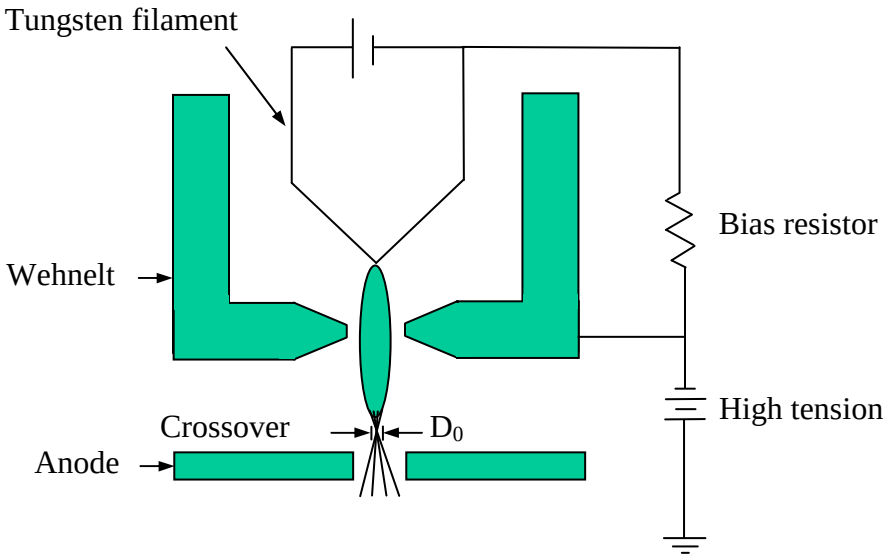

(a)

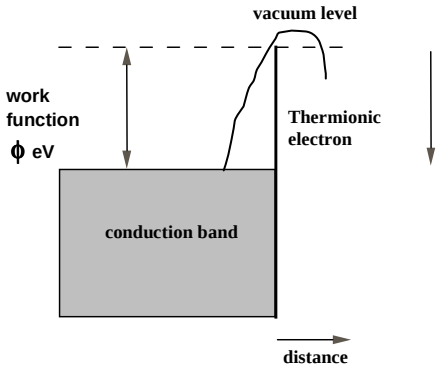

(b)

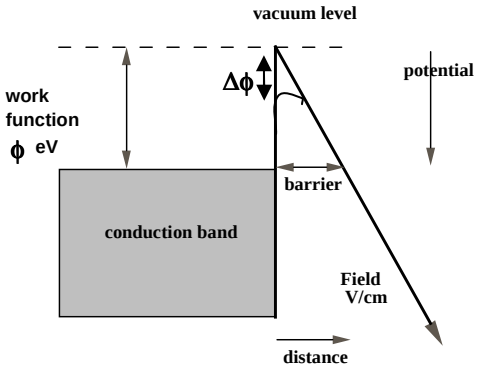

(c)

Figure 2.2. Schematic of (a) a typical electron gun with a tungsten filament, (b) band diagram of thermionic emission gun, and (c) band diagram of field assisted thermionic source (Schottky).

An important parameter of electron gun is their brightness which is the current emitted per unit area per solid angle. The brightness determines the maximum current density of the electron beam probe at the wafer surface. Tungsten thermionic filaments typically have a brightness of approximately 10^5 amp/cm^{2}ster. Cold tungsten field emission (tunneling current is temperature independent) tips have a much higher brightness, around 10^9 amp/cm^{2}ster, but their emission can vary rapidly with time thereby causing instability in the electron beam current. Thermal field emission tips, which are often used in commercial electron beam lithography system, have a relatively high brightness, 10^8 amp/cm^{2}ster, and have much more stable emission current than the cold field emission tips.

2.1.2. Limitations on electron beam spot size

The electrostatic and magnetic lenses in the scanning electron microscope (SEM) systems demagnify the crossover formed after the Wehnelt in the electron gun. The ideal final electron spot size is given by

$$do = \frac{d_v}{M},$$

Where d_v is virtual source diameter and M (>1) is demagnification by the lenses. However, there are several factors that degrade the spot size such as lens aberrations in the electron beam system and diffraction.

For electron traveling near the axial path of the system, the major lens aberrations are spherical aberration and chromatic aberration. Spherical aberration results from electrons passing through the outer regions of the lens being focused to a slightly different plane than the electrons passing near the center of the lens. The spot size contribution of spherical aberration d_s is given by

$$d_s = \frac{1}{2} C_s \alpha^3,$$

where C_s is the spherical aberration coefficient and α (≈sinα) is numerical aperture of the electron objective lens. For a well designed magnetic lens, the spherical aberration coefficient is roughly equal to the focal length *f* of the lens.

Chromatic aberration results from the energy spread, $\Delta E/E$, of the electrons, which is due to Coulomb interactions of electrons and energy spread of gun emission. The spot size contribution of chromatic aberrations d_c is given by

$$d_c = C_c \alpha \left(\frac{\Delta E}{E} \right),$$

where C_c is the coefficient of chromatic aberration. In addition to lens aberrations, diffraction limits the minimum beam diameter by

$$d_f = 0.61 \frac{\lambda}{\alpha},$$

where d_f is the spot size contribution from diffraction. The de Broglie wavelength of electrons is given by

$$\lambda = \left(\frac{h^2}{2mE} \right)^{\frac{1}{2}},$$

which is 0.008 nm for electron energy 20 KeV. With a typical value 2.5 mrad of α, d_f is about 3.2 nm for electron energy 20 keV. The total beam diameter can be estimated by adding each of these contributions in quadrature

$$d_{tot}^2 = d_0^2 + d_s^2 + d_c^2 + d_f^2 .$$

By analyzing the equation of d_{tot}, the minimum electron beam diameter is obtained by using the highest stable accelerating voltage, lowest reasonable beam current, and the smallest practical working distance[5] (for smaller beam spot size). However, for typical conditions using field emission gun, the pattern resolution is not limited by beam spot size that can easily achieve sub-5 nm, rather electron beam scattering and proximity effect.

2.1.3. Electron scattering and proximity effect

When an electron beam is incident into resist, the electrons scatter both elastically and inelastically, causing the exposure region larger than the beam size[6]. Due to high energy electrons used, the penetration depth of electron beam is usually much larger than the resist thickness. The in-elastically scattering of high energy electrons by electrons in resist can generate secondary electrons with energies ~10-50 eV. The energy and range of the secondary electrons is largely independent of the incident electron energy. The secondary electrons interact with resist polymer and cause chain scission of PMMA molecular chain[7]. The inelastic scattering with electrons in resist is mainly in a small solid angle in forward direction, which increases the beam size in resist. For the highest resolution, thin resists are necessary to reduce the beam widening from forward scattering. The electron beam, which goes through the resist and is incident into substrate, also elastically scatters with the nucleus of the substrate atoms. Depending on the atomic number of the substrate atoms, from 10% to 40% of the incident electrons are back scattered and go into resist again. The back-scattered electrons have a much larger range and expose the resist outside of the primary beam.

Due to back-scattering, the exposure dose at a given location is the superposition of both the incident dose and the additional dose from all other exposure locations within the scattering range. This phenomena is called the proximity effect. A model of a sum of two Gaussian distributions, which characterize the electron distribution of the primary beam and forward scattering and the electron distribution of back scattering, was proposed by Chang to calculate exposure dose of proximity effect[8]. The equation is given by

$$f(r) = \frac{1}{\pi(1+\eta)}\left[\frac{1}{\sigma_f^2}\exp\left(-\frac{r^2}{\sigma_f^2}\right) + \frac{\eta}{\sigma_b^2}\exp\left(-\frac{r^2}{\sigma_b^2}\right)\right]$$

where f(r) is the exposure at a distance r from the axis of incident beam. The first term of a Gaussian distribution is described by the term σ_f (order of 10 nm) representing the electron distribution of forward scattering. The second term of a Gaussian distribution is described by the term σ_b (order of 1 μm) representing the electron distribution of back-scattering. The ratio of the back scattering exposure to forward scattering exposure is given by the η.

The proximity effect may be reduced by using thin substrates or membranes to reduce back scattering effects[9,10]. Sparse patterns, which are separated by distances greater than the back scattering electron ranges, may be exposed with very little proximity effect. In addition, the proximity effect may be compensated for by adjusting the dose of each feature and changing the shapes of the features with the help of simulation tools or experimental tests.

A Monte Carlo simulation is given in figure 2.3 to illustrate the dose distributions and electron scattering[11]. To have feature size mainly determined by primary beam, thin resist should be used to reduce forward scattering distribution through resist thickness, and the exposure dose should be reduced to only develop the resist exposed around the primary beam. The dose control to obtain an isolated feature with very small feature size is much easier than that to obtain dense features with the same feature size, because the forward scattering distributions of adjacent exposure points overlap and proximity effect is more serious for dense pattern.

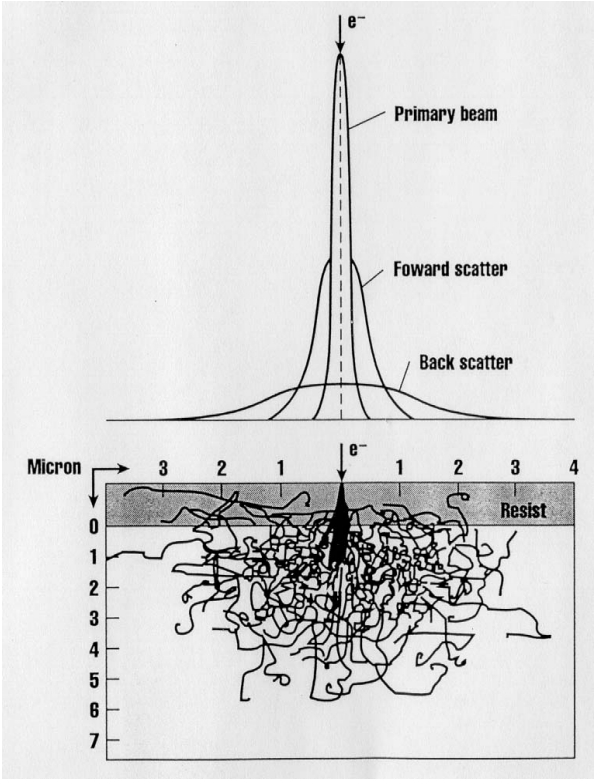

Figure 2.3. A Monte Carlo simulation showing electron trajectories[11]. Upper image shows the dose distributions of primary beam, forward scattering, and back scattering. Lower image shows the traces of electron scattering.

2.1.4. Resists and developers

The resists for electron beam lithography can be classified in two categories, positive resist and negative resist, which are different in how the resists react to exposure and development, as shown in figure 2.4. In a positive resist, the resist in the areas exposed by electron beam is removed after development, while the resist in unexposed areas remains. On the other hand, a negative resist leaves the exposed region after development and the unexposed areas are removed. The chemistry of positive resist is polymer chain scission by electron-polymer interaction that reduces the polymer chain length, thus making the resist in exposed areas dissolve much faster in developer than the unexposed resist. The chemistry of negative resist is to form cross-link of the polymer chains by electron exposure, making the cross-linked polymer hard to be dissolved in developer. Examples of common positive electron beam resist include polymethyl methacrylate (PMMA) and ZEP-520A. SU-8, HSQ and polystyrene are examples of negative EBL resist.

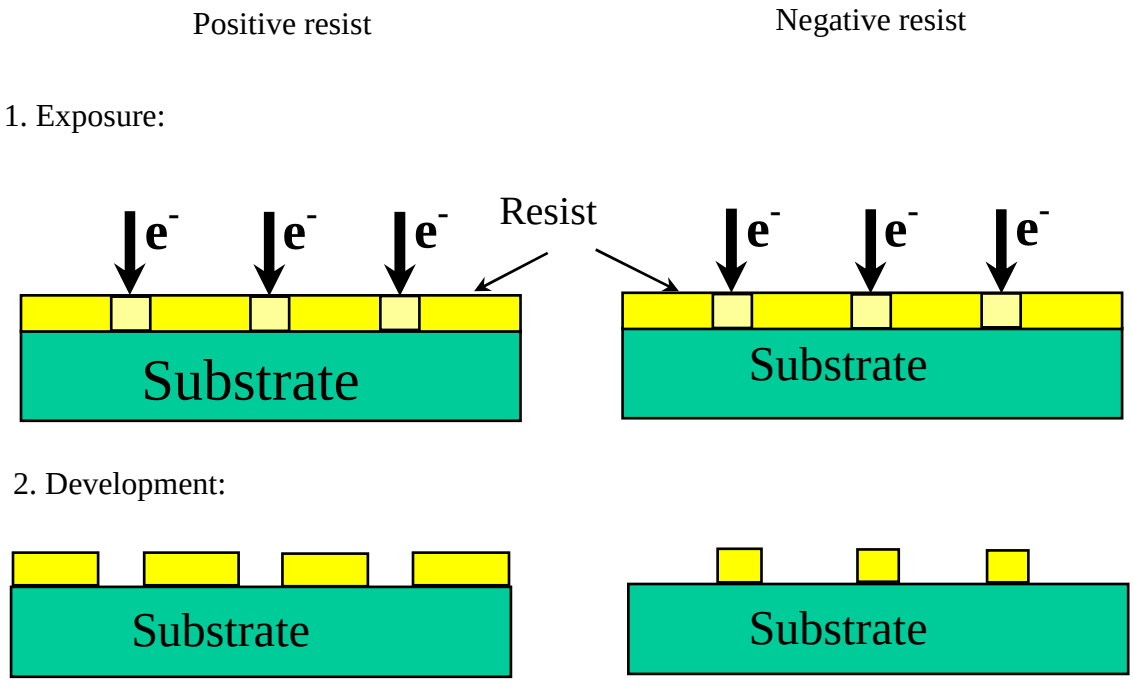

Figure 2.4. Schematic of positive resist and negative resist.

PMMA was first identified as a high-resolution EBL resist in 1968 and continues to be a most common resist used in high-resolution EBL today. One main reason for the continued use of PMMA is that it has very high resolution. In 1983, Craighead et al. obtained 10 nm linewidth on GaAs using PMMA with a lift-off technique[12]. This resolution was thought to be the limit of minimum feature size in PMMA due to the delocalization of secondary electron generation and subsequent straggling of the secondary electrons in the resist[13]. However, Chen et al. produced lines as narrow as 5-7 nm in 1100 K molecular weight PMMA using a 100 keV electron beam and an optimized development process in cellosolve and methanol with ultrasonic agitation[14]. The disadvantage of PMMA as an EBL resist is its relatively low sensitivity. A dose from 50 $\mu C/cm^2$ to 500 $\mu C/cm^2$ is required to expose PMMA.

Common developers for PMMA can be divided into two systems: solvent:non-solvent and co-solvent. Three examples of solvent:non-solvent developer system are cellosolve (2-ethoxyethanol): methanol, methyl isobutyl ketone:isopropyl alcohol (MIBK:IPA) and methyl ethyl ketone:methanol. In the co-solvent developer, two pure non-solvents are combined together to form a solvent. The developer isopropanol:water is an example of this system. In development, parameters such as developer temperature, developing time and developer strength are critical in obtaining repeatable results. For instance, the development sensitivity of PMMA changes by nearly 10% per ^0C[15].

Negative resist, HSQ (hydrogen silsesquioxane), was first studied by Frye and Collins[16]. It has high resolution capability similar to PMMA, and the exposed HSQ is effectively SiO_2. Van Delft[17] studied the effect of aging and storage of HSQ resist. He demonstrated that the aging of HSQ (has a shelf life of around six months) increased the sensitivity at a cost of decreasing the contrast and resolution. As HSQ is not stabilized at room temperature, it should be stored at low temperature. Recently, a non-polymer negative resist, calixarene, has been shown by Fujita et al. to have nanometer scale resolution[18]. The sensitivity of calixarene is 7000 $\mu C/cm^2$, which is significantly lower than that of PMMA. However, calixarene resists have significant resistance to plasma etching. Pepin et al[19] studied another very popular negative resist, SU-8, and demonstrated 75 nm wide lines in thin SU-8 with 50 keV electron beam energy. Polystyrene is also a very versatile negative resist which is discussed in details below.

The following elaborates my research on e-beam lithography using polystyrene and monolayer PMMA "brush" resist.

2.2. Effect of molecular weight on e-beam exposure properties of polystyrene

[This work is published in Microelectronic Engineering, 98, 254-257(2012)]

2.2.1. Introduction

Positive resist is typically used for EBL, largely because of the availability of the benchmark resist poly(methyl methacrylate) (PMMA) that offers high resolution with low cost and ease of process. With its higher sensitivity and etching resistance than PMMA, ZEP520 (positive-tone, Zeon Corp) is arguably the second most popular EBL resist. However, for some applications such as the fabrication of hole arrays in a metal film (the structure for extraordinary optical transmission[20]) by using liftoff, negative resist would offer substantially shorter exposure time, except when using a more complicated “resist tone reversal” process[21]. Unfortunately, there is no negative resist that gains similar popularity to PMMA and ZEP520. Bilenberg *et al*. has selected four negative EBL resists and compared their performance: calixarene (Tokuyama Corp), ma-N 2401 (Microresist Technology), SU-8 (Microchem Corp) and mr-L 6000 (Microresist Technology)[22]. As chemically amplified resists, SU-8 and mr-L 6000 offer superior sensitivity, but with low contrast and resolution (more strictly speaking, half-pitch for dense periodic line array patterns) that is limited by the diffusion of the photo-acid generator during post exposure baking. Ma-N 2401 has sensitivity comparable to that of ZEP520 resist, but with far inferior resolution. Among those four resists, calixarene offers the highest resolution. Calixarene has been studied as a candidate resist for fabricating using EBL bit-patterned recording media that have achieved areal density of 1.4 and 1.6 Tbits/in^2 (corresponding to a dot array of 20 nm period)[23,24] using very thin (sub-20 nm) film. However, it has low sensitivity despite being a chemically amplified resist, and the acid generated in the exposed area may diffuse into the unexposed area, blurring the latent image.

In recent years, hydrogen silsesqioaxene (HSQ) probably attracted more attention than any other negative tone resist[25, 26, 27]. HSQ is an excellent inorganic EBL resist that has demonstrated the highest resolution of 9 nm period line array patterns[28], thanks to its small molecular size and lack of swelling during development[29]. However, in addition to its low sensitivity, HSQ is not suitable for liftoff unless using a double layer resist stack such as HSQ coated on PMMA. The development process is also self-limiting due to cross-linking of resist by the developer, leading to incomplete removal of unexposed resist, though a salty developer can minimize this effect[30]. More importantly, HSQ is unstable, so spin coating, baking, exposure and development must be done quickly (yet this is not possible if the exposure time is long)[31].

In addition, all the above resists are commercially formulated with typically high cost and short shelf life. Therefore, it is desirable to have a negative resist like PMMA, which is a simple polymer with low cost and practically unlimited shelf life, and can be dissolved easily using various solvents to give desired film thickness. Polystyrene is such a resist, as it undergoes cross-linking when exposed to deep UV light or an electron beam. Previously, dense periodic patterns with 20 nm period lines and 15 nm period dots have been demonstrated using low molecular weight 2 kg/mol polystyrene resist[32]. However, the sensitivity of the 2 kg/mol polystyrene is very low, one order lower than the insensitive PMMA. Knowing that for negative cross-linking polymer resist the sensitivity is theoretically proportional to its molecular weight, here we investigate the exposure properties of high molecular weight (90 kg/mol, 170 kg/mol and 900 kg/mol) polystyrene, which demonstrated a very high sensitivity of 1 $\mu C/cm^2$ when exposed on 900 kg/mol polystyrene at 2 keV. Besides its high sensitivity, polystyrene is more (by ~3×) resistant to dry etching than PMMA. To compare, we also investigated the exposure properties of low molecular weight polystyrenes (2.5 kg/mol and 13 kg/mol).

2.2.2. Exposure properties of low molecular weight PS (2.5 kg/mol and 13 kg/mol)

As aforementioned, the principle to use polystyrene as EBL negative resist is that the electrons cause crosslink to form a network structure. Figure 2.5 illustrates a linear molecular chain of polystyrene and cross-linked PS exposed by e-beam. The network structure of polymer cannot be

dissolved by developer, which is typically a solvent capable of dissolving the uncross-linked polystyrene polymer. After development in the solvent, the heavily exposed region having the crosslinked polymer patterns left.

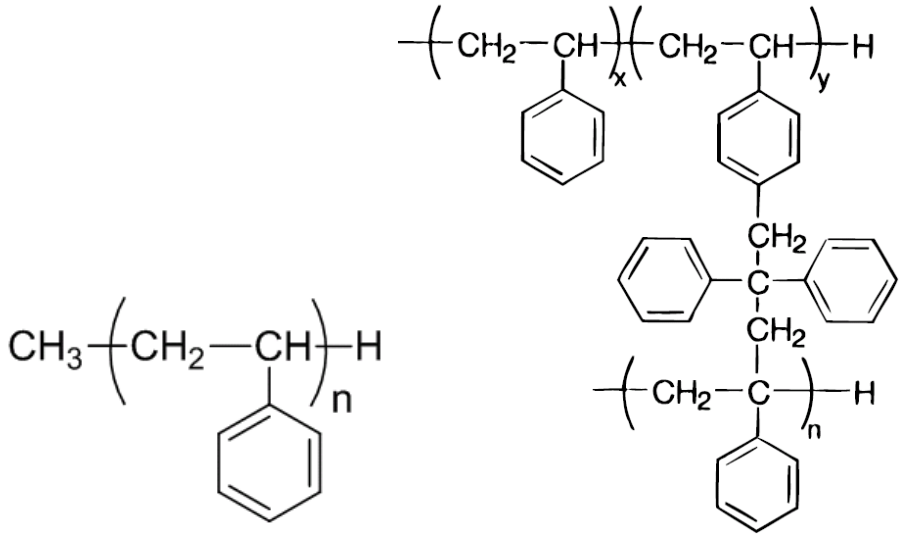

(a) (b)

Figure 2.5. Schematic of (a) a linear molecular chain of polystyrene, (b) cross-linked PS exposed by e-beam.

To carry out the experiment to obtain exposure properties of low molecular weight PS, polystyrene powder with a molecular weight of 2.5 kg/mol and 13 kg/mol was dissolved in chlorobenzene with a concentration of 1.3 w/v%, which was spun-coated onto a Si substrate to form a film thickness of 110 nm. Initially, the silicon wafer was cleaned using acetone and 2-proponol, followed by short exposure to oxygen plasma. After spin coating, the film was baked at 70 ^{o}C for 1 hour on a hotplate. The dependence of film thickness of polystyrene on spin-coater spin speed is shown in figure 2.6.

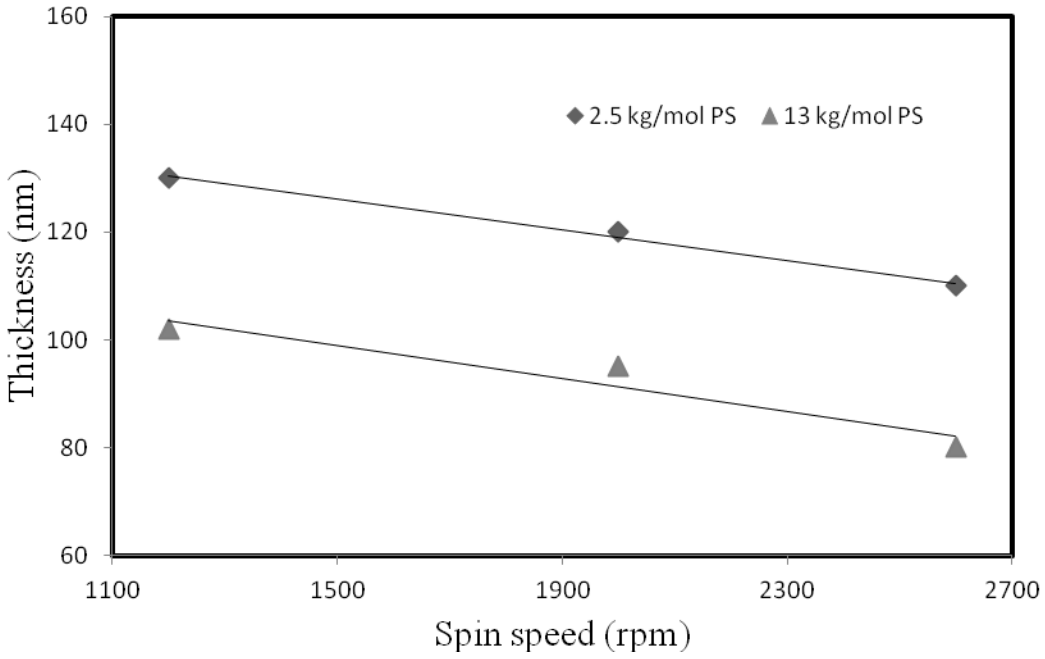

Figure 2.6. Thickness of polystyrene film as a function of spin speed.

The pattern was exposed using a LEO 1530 field emission SEM equipped with a Nabity nanometer pattern generation system (NPGS) at electron energies of 5 keV and 20 keV. The beam currents measured using Faraday cup were 45-100 pA that depends on the electron energy for an aperture of 20 µm. The periodic lines were exposed as single-pass lines with a beam step size of 12 nm for high resolution study. Following exposure, the samples were developed using tetrahydrofuran for 1 min, followed by a 2-propanol rinse and nitrogen dry. In principle, all solvents such as chlorobenzene, anisole and toluene that can dissolve un-exposed polystyrene can be used as developer since cross-linked polystyrene is insoluble to those corresponding solvents.

2.2.2.1. Dependence of dot size on exposure dose

The dose required to expose a dot is inversely proportional to the molecular weight of polystyrene. Figure 2.7 shows the dependency of dot diameter on exposure dose for polystyrene of molecular weights 2.5 and 13 kg/mol, exposed at 20 keV. It clearly shows 13 kg/mol PS is more sensitive than 2.5 kg/mol PS. The reason behind this is discussed in details in next section.

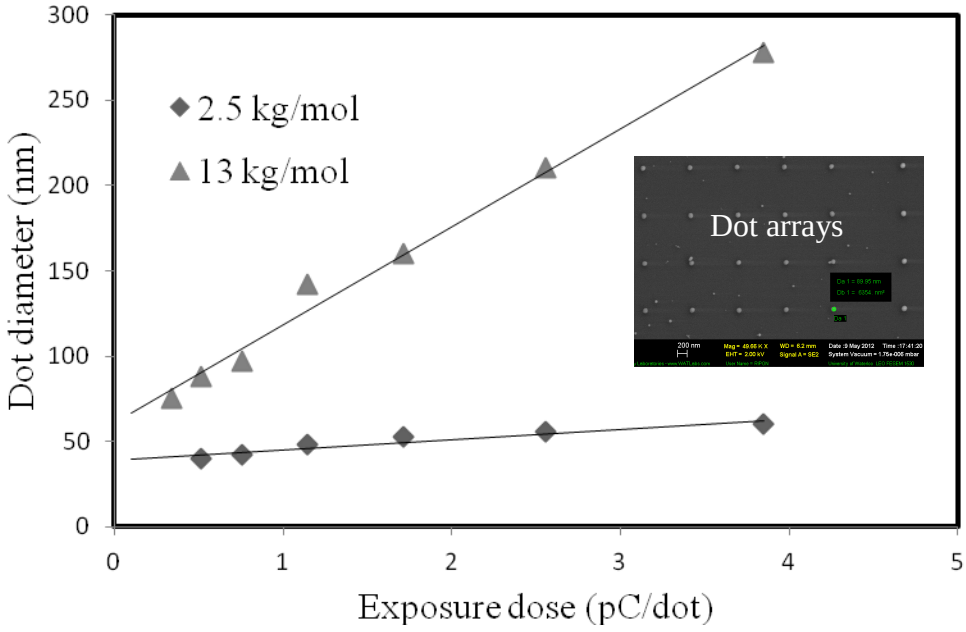

Figure 2.7. Dot diameter as a function of exposure dose for PS of molecular weight 2.5 kg/mol and 13 kg/mol, exposed at 20 keV. Inset shows SEM image of one dot array.

The dot size dependence on the electron energy relies on the forward electron scattering. The scattering angle of incident electron at lower electron energy is greater than that at higher electron energy. High energy electron beam penetrates much deeper into the substrate than low energy electron beam that reduces the secondary electron scattering volume in resist layer. Therefore, the area of effective energy deposition decreases with increasing acceleration voltage. Thus, low electron energy exposure gives higher sensitivity because more energy is deposited inside the resist layer. Figure 2.8 shows that lower energy gives higher sensitivity for both 2.5 kg/mol PS (a) and 13 kg/mol PS (b), where the polystyrene were exposed at 5 keV and 20 keV.

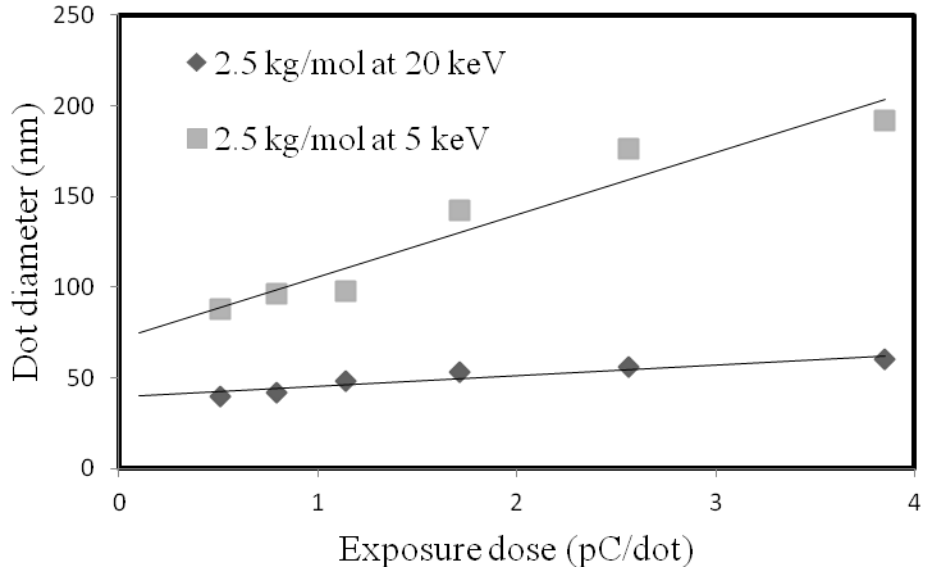

(a)

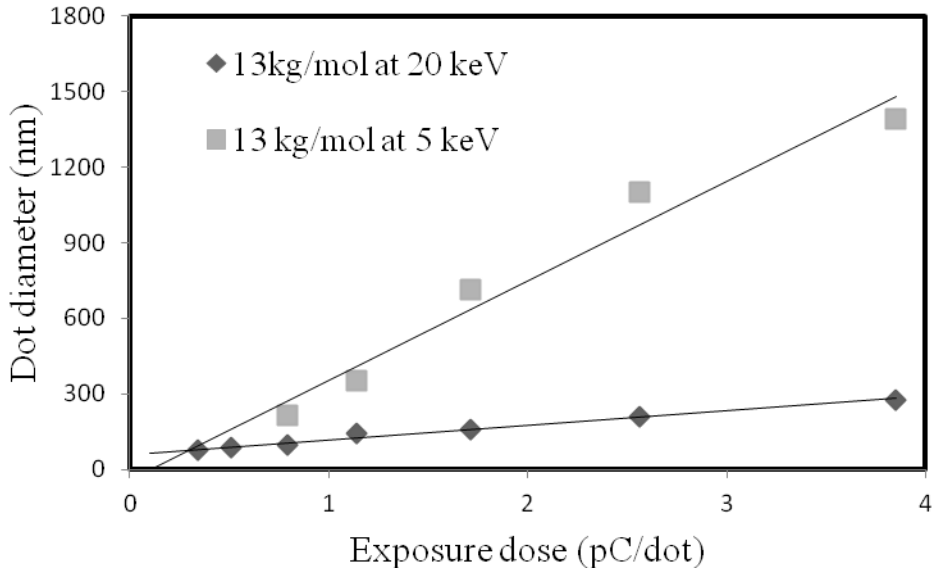

(b)

Figure 2.8. Dot diameter as a function of exposure dose for low and high electron energies of (a) 2.5 kg/mol PS, and (b) 13 kg/mol PS.

2.2.3. Exposure properties for high molecular weight PS (90-900 kg/mol)

Unlike the low molecular weight polystyrene, the high molecular weight polystyrene was found able to form a uniform film, though its adhesion could be further enhanced by coating the silicon wafer with a mono-layer surfactant trichloro(phenyl)silane. Thus, in experimental procedure, polystyrene with a molecular weight of 90 kg/mol, 170 kg/mol and 900 kg/mol (Mw/Mn=1.10) were baked at 120 ^{o}C for 5 min, after spin coating. The films were exposed at energies of 20 keV, 5 keV and 2 keV where measured currents are 35-100 pA for 20 μm aperture. After exposure, the samples were developed using tetrahydrofuran for 2 min. Such a relatively long development time is necessary since high molecular weight polystyrene is less soluble in the solvent than the low molecular weight one.

2.2.3.1. Sensitivity and resolution capabilities

Figure 2.9 shows the contrast curves for 90 kg/mol polystyrene resist exposed at 20 keV and 5 keV. The contrast for exposure at 20 keV, defined as $\gamma = [\log(D_{100}/D_0)]^{-1}$, is calculated to be 1.5, which is very close to the contrast at 5 keV exposure. The contrast is much lower than the popular chain-scission positive resist PMMA and ZEP-520A. For PMMA, a critical molecular weight around 10 kg/mol exists, below which the polymer becomes very soluble by the developer. For chain cross-linking resist polystyrene, apparently there is no such a critical transition point, and its solubility decreases gradually with the increasing degree of cross-linking. Nevertheless, the contrast is higher than the popular chemically amplified resist SU-8 (γ~1.0) [33]. The sensitivity (defined as D_{50}, the dose to result in 50% remaining thickness) is 120 μC/cm^2 and 26 μC/cm^2 for 20 keV and 5 keV exposure, respectively. This is in good agreement with the fact that sensitivity is roughly inversely proportional to the beam energy (E) as predicted by the Bethe equation for electron energy loss (E_{loss}) in the resist: $E_{loss} \propto 1/E \cdot \log(\alpha E)$ with α being a constant. The threshold dose where the contrast curve starts to rise (D_0) is the "gel point" that is roughly inversely proportional to the molecular weight for simple negative polymer resists[34]. This is because the number of cross-linking necessary to render the resist insoluble in the developer decreases with molecular weight. Contrary to the cross-linking negative resist, for positive resist based on chain scission such as PMMA, the sensitivity doesn't depend

significantly on molecular weight, because for longer chains, though more chain scission is needed to render it soluble in the developer, it also receives proportionally higher exposure dose. The sensitivity for 2 kg/mol polystyrene at 5 keV exposure is 1170 μC/cm^2 that is ~50× lower than 90 kg/mol polystyrene, which is in good agreement with the Charlesby theory[35].

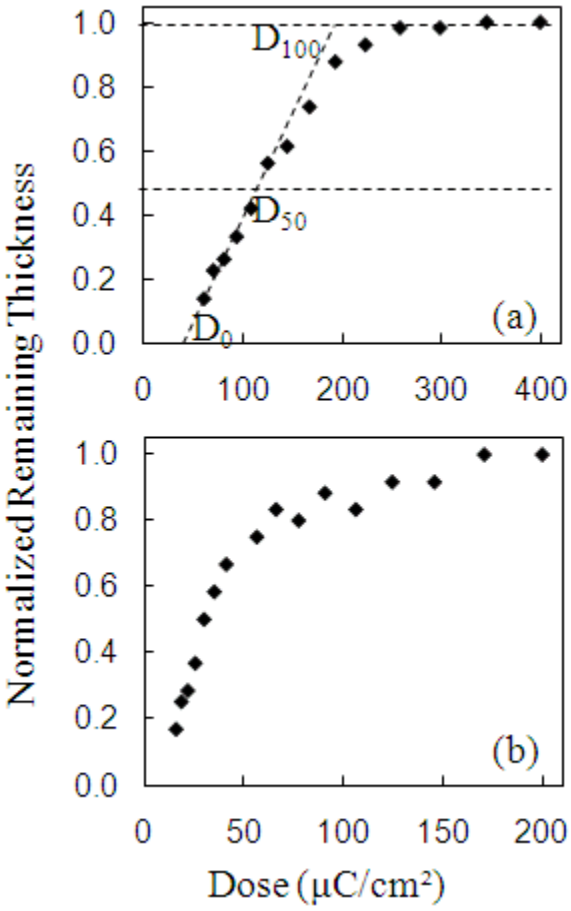

Figure 2.9. Contrast curves for 90 kg/mol polystyrene exposed at (a) 20 keV and (b) 5 keV, and developed by tetrahydrofuran for 2 min.

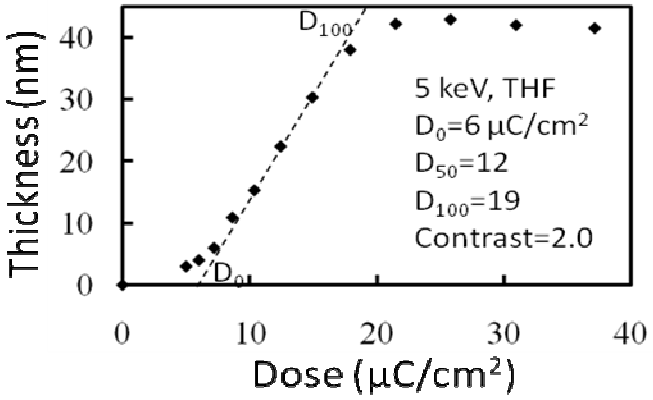

Figure 2.10. Contrast curves for 170 kg/mol polystyrene at 5 keV and developed by tetrahydrofuron for 2 min.

The contrast curve for 170 kg/mol polystyrene which was exposed at 5 keV and developed with tetrahydrofuron is shown in figure 2.10. As expected, 170 kg/mol is more sensitive (twice) than 90 kg/mol PS at 5 kV exposure. The contrast curves for 900 kg/mol exposed at different acceleration voltages are shown in figure 2.11. As expected, the sensitivity (14 $\mu C/cm^2$ and 2.1 $\mu C/cm^2$ for 20 keV and 5 keV exposure, respectively) is roughly one order higher than that for 90 kg/mol polystyrene exposed at 20 keV and 5 keV. It is also much higher than ZEP-520A resist when using the standard amyl acetate developer, and comparable to ZEP-520A resist when using a stronger developer of methyl ethyl ketone : methyl isobutyl ketone = 40 : 60 [36]. The sensitivity can be further enhanced by exposure at lower acceleration voltage, here 2 keV, which resulted in a sensitivity of 1.1 $\mu C/cm^2$. Further reduction of acceleration voltage would lead to more serious forward scattering and shallower resist penetration depth (e.g. 65 nm penetration for 1.3 keV exposure[37]), so was not experimented. Contrary to intuition and experience that high sensitivity generally comes with low contrast, the contrasts (γ=1.4, 1.6, 1.7 for 20 keV, 5 keV and 2 keV exposure, respectively) was found to be not noticeably worse than 90 kg/mol polystyrene. This might be explained by that the ratio of the exposure dose for full cross-linking (nearly insoluble in the developer) to the dose for partial cross-linking (e.g. 50% cross-linking, moderately soluble) should be independent of the molecular weight.

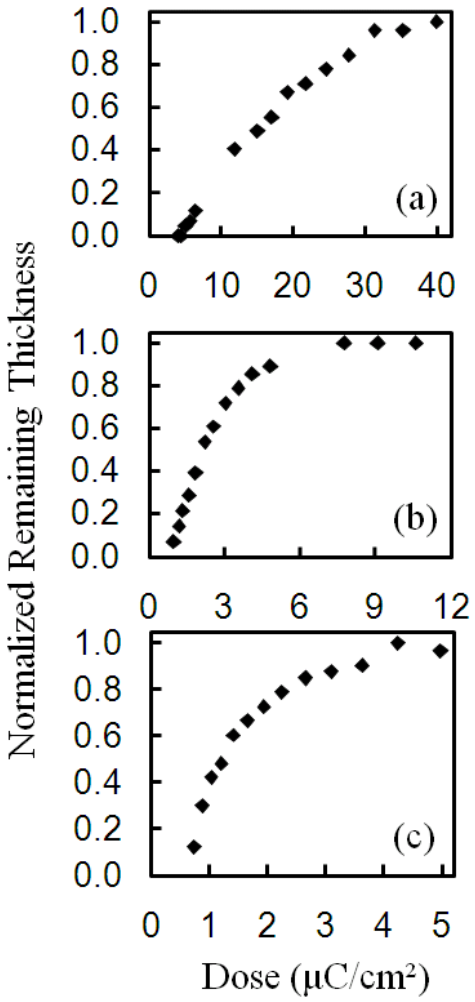

Figure 2.11. Contrast curves for 900 kg/mol polystyrene exposed at (a) 20 keV, (b) 5 keV and (c) 2 keV, all developed by tetrahydrofuran for 2 min.

To study the resolution capability of the polystyrene resist, we exposed periodic dense line arrays with periods 120 nm, 150 nm, 200 nm and 300 nm, all at 5 keV. Figure 2.12 shows the line array patterns of 150 nm and 200 nm period for 90 kg/mol polystyrene. Grating with 200 nm period was well defined, whereas the 150 nm one is fairly well defined. The next period (120 nm, not shown) was not resolved. For 900 kg/mol, as seen from figure 2.13, the lines for both 200 nm and 300 nm period were well defined. However, as the film thickness (140 nm) is about twice that of 90 kg/mol polystyrene, the capillary force is stronger, leading to line collapse during resist drying for the 200 nm period grating. We can conclude that the resolution capability for the two molecular weights are not significantly different, which agrees with the fact that the two

resists have similar contrast. It is well known that denser pattern can be obtained when proximity effect is insignificant owing to small pattern area compared to the range of backscattered electrons or exposure on a thin membrane. Here the pattern area is larger than the proximity effect range for 5 keV exposure, hence similar resolution is expected when writing over larger areas. The resolution or half pitch for the current polystyrene resist is lower than the very low contrast resist SU-8[38]. However, in that study the authors did not mention the pattern area as compared to the range of proximity effect for 100 keV exposure. In fact, when proximity effect is unimportant, very fine SU-8 line of only 24 nm wide has been obtained using 100 keV exposure[39].

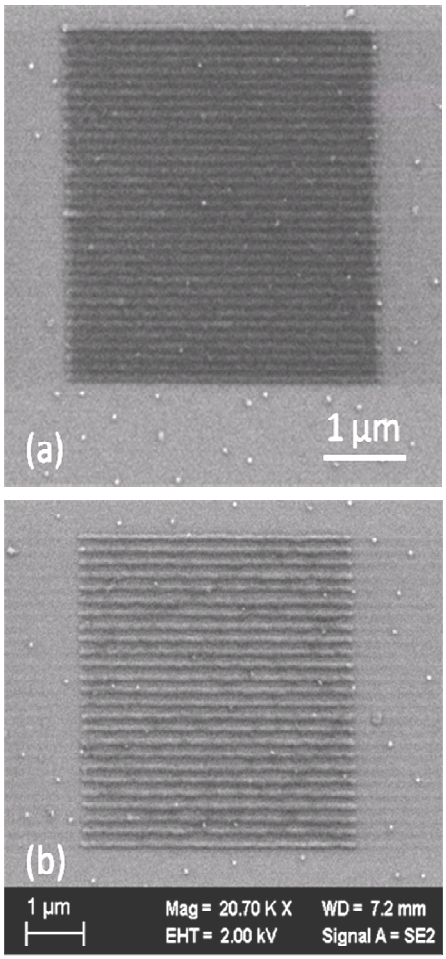

Figure 2.12. SEM images of 90 kg/mol polystyrene line array exposed at 5 keV with line dose of 0.54 nC/cm, and developed by tetrahydrofuran for 2 min. (a) 150 nm period, (b) 200 nm period.

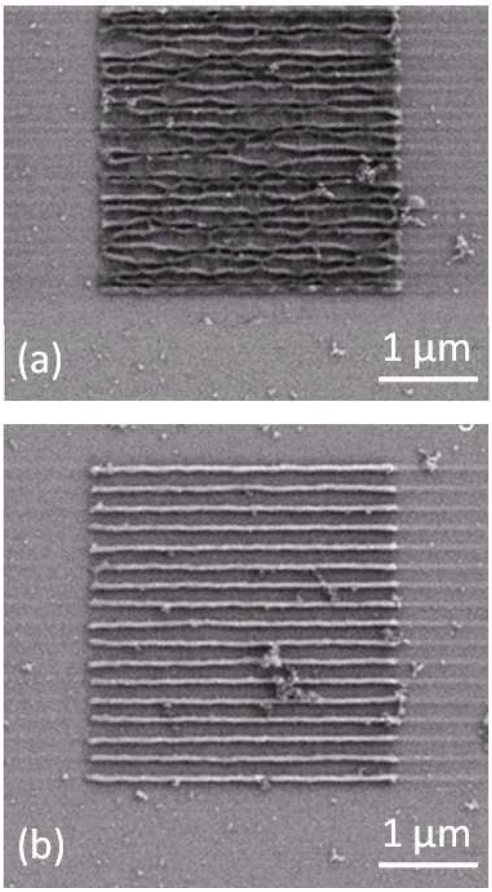

Figure 2.13. SEM images of 900 kg/mol polystyrene line array exposed at 5 keV with line dose of 0.043 nC/cm, and developed by tetrahydrofuran for 2 min. (a) 200 nm period and (b) 300 nm period.

Previously, Cord *et al.* has demonstrated robust undercut profile by using a bi-layer positive resist stack PMMA and PMGI[40] (more sensitive than PMMA when using aqueous basic developer, less sensitive than PMMA when using solvent developer[41]). Such a robust undercut profile could be realized readily by using a bi-layer polystyrene resist stack having higher molecular weight for the top layer. Similarly, by using a bi-layer stack with the top layer having lower molecular weight, two-level patterning could be achieved, which, after pattern transfer to a hard substrate, could be used to fabricate 3D mold for dual damascene process based on nanoimprint lithography[42].

2.2.4. Conclusions

We studied the exposure behavior of the negative EBL resist polystyrene with molecular weight of 90 kg/mol, 170 kg/mol and 900 kg/mol along with polystyrene with low molecular weights. Very high sensitivity of 1 $\mu C/cm^2$ was obtained for 900 kg/mol when exposed at 2 keV. The sensitivity for 90 kg/mol polystyrene is about one order lower. The resist has a contrast around 1.5 that is nearly independent of molecular weight for this range of molecular weight. The contrast is much lower than PMMA, but higher than the chemically amplified negative resist SU-8. The current resist can achieve fairly well-defined patterns of 150 – 200 nm period line arrays. In addition to its high sensitivity, polystyrene is a simple and low-cost resist with easy process control and practically unlimited shelf life. It is also considerably more resistant to drying etching than PMMA. We believe polystyrene is a very promising negative resist with tunable sensitivity and resolution capability over a broad range simply by choosing different molecular weights. For applications that need only moderate resolution, it is desirable to use high molecular weight such as 900 kg/mol in order to take advantage of its very high sensitivity; whereas if ultra-high resolution is the primary goal, very low molecular weight such as 2 kg/mol would be the choice.

2.3. Effect of molecular weight distribution on e-beam exposure properties of polystyrene

[This work is published in Nanotechnology, 24, 245302 (2013)]

2.3.1. Introduction

Previously we have demonstrated ultra-high sensitivity patterning using high Mw of 900 kg/mol[43]. In addition to molecular weight, another important parameter for a polymer is polydispersity index (PDI), which is defined as the ratio of weight averaged molecular weight $\overline{Mw}$ and number averaged molecular weight $\overline{Mn}$. For a strictly monodisperse polymer, $\overline{Mn}$ is equal to $\overline{Mw}$ and PDI is 1. For a polymer with broad molecular weight distribution, PDI is much

higher than 1. PDI is known to be an important parameter for micro-phase separation of a mixture of heterogeneous polymer[44], as well as for crystallization kinetics[45].

Polystyrene with very narrow molecular weight distribution with PDI ≤1.06 has been utilized by majority research groups[46, 47, 48, 49, 50, 51, 52] in order to avoid any uncertainties. Ku's paper published in 1969 also recommended polystyrene with narrow Mw distribution for EBL in order to avoid potential pinhole formation after development[53]. In this study we will show that there is no significant effect of very broad molecular weight distribution on resist contrast and achievable resolution. We didn't observe any pinhole formation after development, either. It is thus unnecessary to use monodisperse polystyrene whose cost is more than two orders higher than the general purpose polystyrene having high PDI.

Polystyrene powder with various molecular weights and polydispersity index (from Pressure Chemical Co. and Scientific Polymer Products Inc.) was dissolved in chlorobenzene with a concentration of 1-2 w/v%. Relatively thick film is desirable for contrast curve measured by AFM since the measurement is more accurate for thicker films, whereas relatively thin film is preferred for high resolution line array exposure because pattern collapse due to capillary force is less severe for thinner film. The films were baked at 120 ^{o}C for 5 min on a hotplate for the high Mw samples (170 kg/mol and above). For low Mw polystyrene resist (13 kg/mol and below), we decreased the baking temperature to 70 ^{o}C and increased the time to 1 hour in order to obtain a uniform and homogeneous film.

To investigate the effect of polydispersity index on exposure properties, since the PDI of commercially available general purpose polystyrene is unknown, we mixed two monodisperse polystyrene with very different molecular weights (thus bimodal distribution) to mimic a polystyrene with very broad molecular weight distribution and large PDI. For high Mw range, 170 kg/mol (PDI=1.06) and 900 kg/mol (PDI=1.10) polystyrene solution having the same concentration were mixed with 1:1 volume ratio, to give a film with 1:1 weight ratio after spin-coating. For low Mw range, 2.5 kg/mol and 13 kg/mol (both PDI=1.06) were mixed the same way.

2.3.2. Effect of molecular weight distribution on exposure properties

For positive resist based on chain scission such as PMMA, the dependence of resist sensitivity on molecular weight is rather weak because, for PMMA of longer chains, though more exposure is needed to cut it to below ~10 kg/mol (threshold Mw for fast dissolution in the developer), longer chains also receive more electron exposure proportionally. For instance, when Mw is decreased from 2200 kg/mol to 50 kg/mol, its sensitivity increases only by 26% for room temperature development, from approximately 500 $\mu C/cm^2$ to 370 $\mu C/cm^2$ [54]. Contrary to positive resist, Mw is fundamentally critical for chain cross-linking negative resist such as polystyrene whose sensitivity is roughly proportional to its Mw. This is because fewer cross-linking is needed for longer polystyrene chains to render it insoluble in a solvent developer. As for resist contrast and high resolution capability, though typically high Mw PMMA of 950 kg/mol is used for electron beam lithography, actually Mw as low as 15 kg/mol can achieve very high resolution of 15 nm line-width[55]. There is no obvious relationship between high resolution capability (resist contrast) and resist molecular weight for positive resist. But for chain cross-linking negative resist such as polystyrene, gel formation theory predicts that resist contrast increases as Mw decreases[56,57] which is in agreement with our previous studies. Given such an overwhelming significance of Mw on polystyrene's exposure properties, we studied the effect of polydispersity index over both high and low Mw ranges.

2.3.2.1. Polystyrene with high Mw

The contrast curves exposed at 20 keV for 170 kg/mol polystyrene (PDI=1.06), 900 kg/mol polystyrene (PDI=1.10) and the 1:1 mixture of the two are shown in figure 2.14. Here the polystyrene with high PDI was simulated by a 1:1 mixture of two polystyrene. As expected, the sensitivity for 900 kg/mol is much higher than that for 170 kg/mol. The sensitivity for 900 kg/mol is comparable to typical chemically amplified resists such as SU-8; and that for 170 kg/mol is close to ZEP-520A resist when using a strong developer[58], which is much higher than using regular high resolution developer. For the mixture with 1:1 weight ratio (i.e. $N_1M_1=N_2M_2$, M_1=170 kg/mol, M_2=900 kg/mol), if we assume the two components are strictly monodisperse (i.e. PDI=1.0), the weight averaged molecular weight can be calculated as $\overline{Mw}$ =

$(N_1M_1^2+N_2M_2^2)/(N_1M_1+N_2M_2)$ = (170+900)/2 = 535 kg/mol; for 1:1 weight ratio, the number ratio is $N_1:N_2$ = 900:170, thus the number averaged molecular weight can be calculated as $\overline{Mn}$ = (170×900+900×170)/(170+900) = 286 kg/mol. By definition, the polydispersity index of the mixture is PDI=535/286=1.87. The calculated contrast for the mixture (γ=1.3) lies between those of the two components (γ=0.9 and 1.9 for 900 and 170 kg/mol, respectively). As can be seen from the figure, the contrast curve for the 1:1 mixture resembles a hypothetical monodisperse polystyrene resist with Mw~300 kg/mol. Therefore polystyrene of certain molecular weight can be simulated by a mixture of two polystyrenes having very different Mw. It is thus unnecessary to acquire a large number of polystyrene resists with different Mw for different applications using EBL.

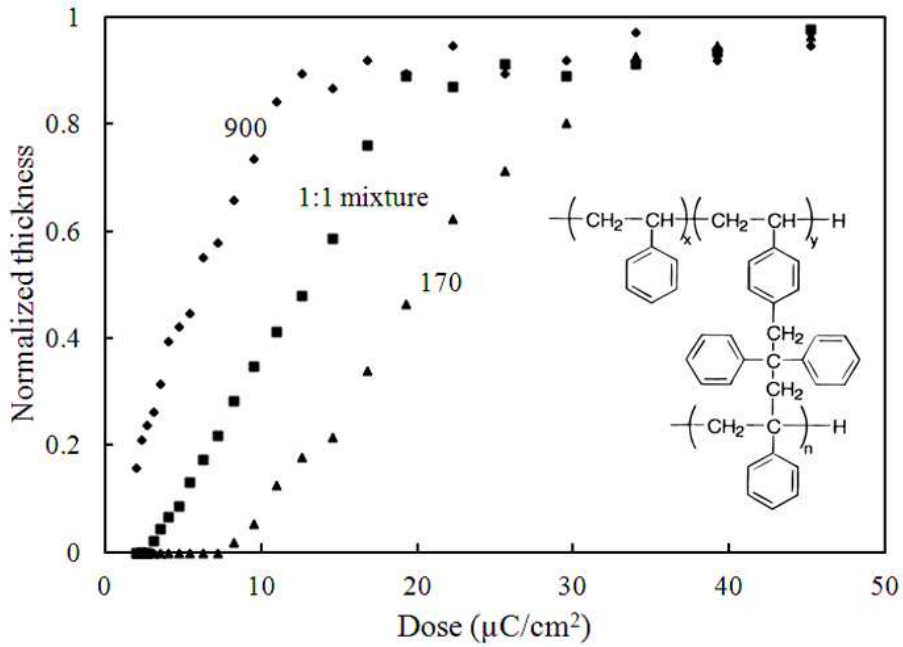

Figure 2.14. Contrast curves exposed at 20 keV for polystyrene resist of 170 kg/mol, 900 kg/mol and a mixture of the two with 1:1 weight ratio. The inset shows a possible configuration of a portion of cross-linked polystyrene (adapted from Ref.[59]).

To study the resolution capability of the polystyrene samples, we exposed dense line arrays each over an area of $(5\ \mu m)^2$ that is larger than the range of electron backscattering for 20 keV, so similar dense array is expected when patterning over larger area. The lines were exposed as single pass lines with step size of 5 nm. As seen in figure 2.15, the 150 nm period line array pattern was better defined using the 1:1 mixture than 900 kg/mol. The lower Mw of 170 kg/mol

can well define a line array of 80 nm period. For comparison, we also studied the resolution capability for a general purpose 260 kg/mol polystyrene with high polydispersity index (Figure 2.15 d), which showed improved pattern definition with smoother lines than the 170 kg/mol having narrow molecular weight distribution (see below for an explanation). This again manifests that the resist performance greatly depends on molecular weight, but not on its distribution.

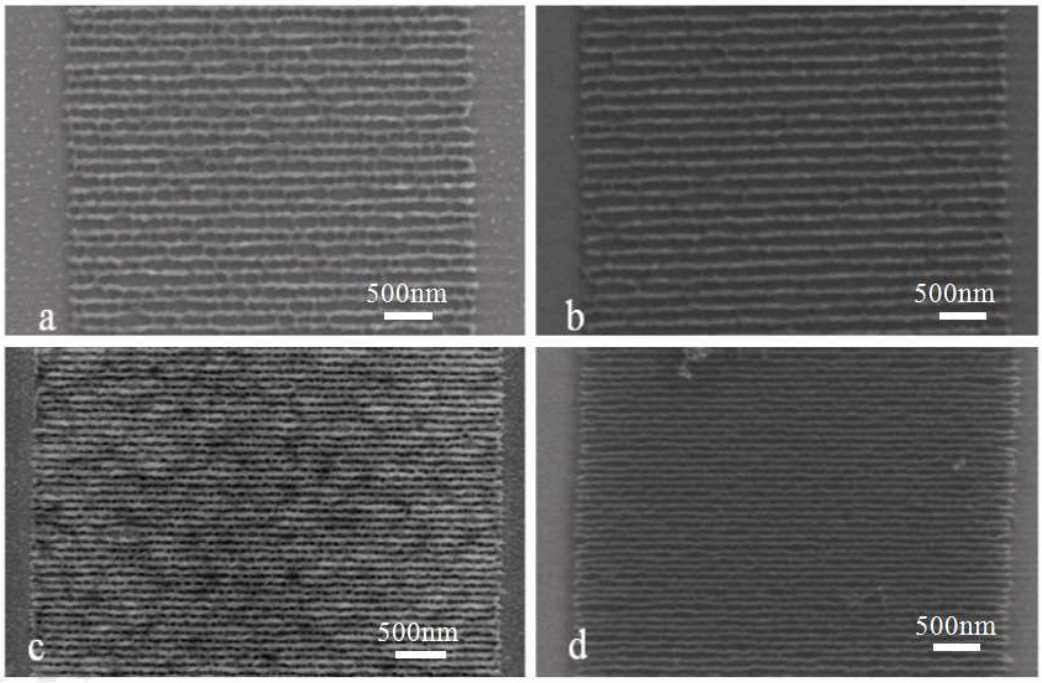

Figure 2.15. Dense line arrays exposed at 20 keV in polystyrene with different molecular weights. (a) Monodisperse 900 kg/mol, 150 nm period, 0.26 nC/cm line dose; (b) 1:1 mixture of 170 and 900 kg/mol, 150 nm period, 0.66 nC/cm; (c) Monodisperse 170 kg/mol, 80 nm period, 1.0 nC/cm; (d) General purpose polydisperse 260 kg/mol, 80 nm period, 0.91 nC/cm.

2.3.2.2. Polystyrene with low Mw

The contrast curves exposed at 20 keV for 2.5 kg/mol polystyrene (PDI=1.06), 13 kg/mol polystyrene (PDI=1.06) and the 1:1 mixture of the two are shown in figure 2.16. As expected, they all showed considerably higher contrast than the high Mw polystyrenes studied above, at the cost of greatly reduced sensitivity. For the 1:1 weight ratio mixture of 2.5 and 13 kg/mol, $\overline{Mw}$,

$\overline{Mn}$ and PDI is calculated as 7.75 kg/mol, 4.19 kg/mol and 1.85, respectively. The contrast curve for the 1:1 mixture resembles a hypothetical monodisperse polystyrene resist with Mw of 4-5 kg/mol. Since for low Mw polystyrene the resist surface after development is much smoother than high Mw polystyrene (this is related to its higher resolution capability), the contrast curve measured by AFM is more accurate than that for high Mw polystyrene resists that gave rough resist surfaces after development. It is thus more meaningful to carry out a quantitative study with the low Mw resists. Table 2.1 listed the three resists' gel point dose D_0, sensitivity D_{50} (dose for 50% normalized thickness), contrast, as well as the four products between $M_{w,n}$ and $D_{0,50}$. Theoretically the dose-molecular weight product should be independent of molecular weight. Apparently the products of dose and *number* averaged molecular weight are similar for the three resists, but those of dose and *weight* averaged molecular weight are very different. Moreover, $\overline{Mn}$ for the mixture is closer to that of 2.5 kg/mol than 13 kg/mol, so is the resist contrast. We can therefore conclude that the resist properties for polystyrene depend mainly on $\overline{Mn}$ if it differs from $\overline{Mw}$. It is known that for a polymer with broad molecular weight distribution, some properties such as tensile strength depend mainly on $\overline{Mn}$; whereas other properties such as viscosity depend mainly on $\overline{Mw}$ [60,61]. Longer chains are more important for the value of $\overline{Mw}$, whereas shorter ones with larger number are more important for the value of $\overline{Mn}$. Therefore, here the exposure property is mainly determined by the low Mw component due to its large number.

Table 2.1. Comparison of exposure properties of polystyrene resists with three different molecular weights, with the values derived from figure 2.16.

Mw (kg/mol)	Mn (kg/mol)	Con-trast	Sensit-ivity D_{50} ($\mu C/cm^2$)	Gel point D_0 ($\mu C/cm^2$)	$D_{50} \times$ Mw	$D_{50} \times$ Mn	$D_0 \times$ Mw	$D_0 \times$ Mn
2.5	2.4	3.6	3400	2310	8500	8160	5775	5544
7.8	4.2	3.5	1750	1220	13650	7350	9516	5124
13	12.3	3.1	600	370	7800	7380	4810	4551

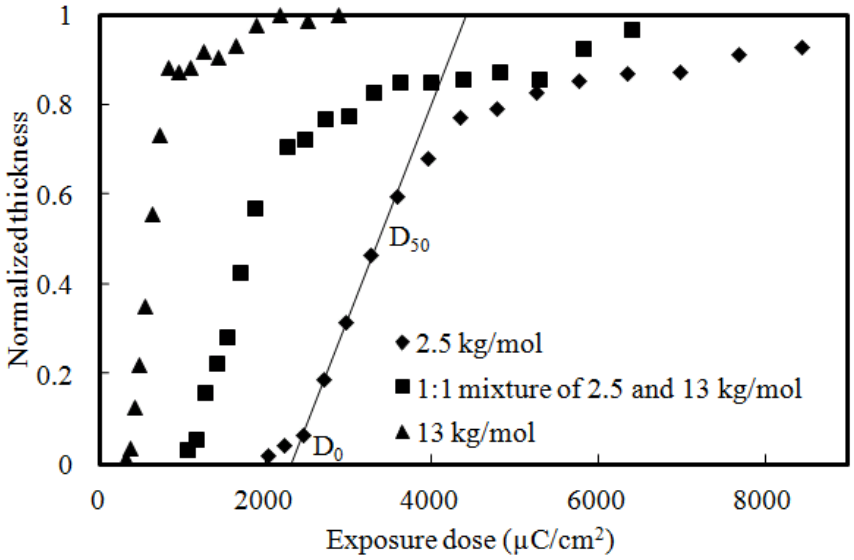

Figure 2.16. Contrast curves exposed at 20 keV for polystyrene resist of 2.5 kg/mol, 13 kg/mol and a mixture of the two with 1:1 weight ratio.

Polystyrene resists with different Mw and PDI have been studied previously. Feit et al. showed that for the same molecular weight of 233 kg/mol, D_{80} (dose for 80% normalized thickness) for polystyrene with higher PDI is considerably higher than near-monodisperse polystyrene, though the difference for D_{50} (dose for 50% normalized thickness) is less[62]. They thus concluded that PDI is a very important parameter for polystyrene resist. We disagree with their conclusion, and believe that higher dose was needed in their study for resist with larger PDI because its $\overline{Mn}$ is lower for the same $\overline{Mw}$. Lai et al. claimed that the contrast of polystyrene resist decreases with an increase in molecular weight distribution[63]. Yet this conclusion was drawn based on the contrast curves for several polystyrene resists that differed not only in PDI but also in molecular weight. Gel formation theory also implies higher contrast for uniform Mw distribution (PDI = 1) than random Mw distribution (PDI = 2)[64]. However, it was assumed that gel fraction is equal to normalized remaining film thickness after development, which is inaccurate since gel formation is a "bulk" process occurring throughout the film thickness whereas resist dissolution by developer is a layer by layer surface process. Our results indicate that PDI has insignificant effect on resist performance. One plausible explanation for this is that once two polymer chains are

cross-linked by electron beam exposure to form one larger chain, the chain length of the two original polymer molecules is no longer important, be it the two molecules of equal length or not.

Table 2.2. Comparison of exposure properties of polystyrene resists with two different molecular weights, with the values derived from figure 2.17.

Mw (kg/mol)	Mn (kg/mol)	PDI	Gel point D_0 ($\mu C/cm^2$)	Contrast	Sensitivity D_{50} ($\mu C/cm^2$)
62	58	1.06	78	1.9	115
286	64	4.5	45	1.4	90

Lastly, we performed Gel permeation chromatography (GPC) measurement on the above-mentioned general purpose polystyrene with molecular weight of 260 kg/mol, which showed $\overline{Mw}$=286 kg/mol, $\overline{Mn}$=64 kg/mol, and PDI=4.5. Due to its lower $\overline{Mn}$, this polymer achieved better pattern definition than the monodisperse (PDI=1.06) 170 kg/mol one as seen in figure 2.15. In table 2.2, we also compared it with a monodisperse polystyrene of 62 kg/mol (PDI=1.06, thus $\overline{Mn}$=58 kg/mol) that is commercially available. As expected and shown in figure 2.17, though their $\overline{Mw}$ differs by 4.6 times, the sensitivity of the two polymers is reasonably close (90 and 115 $\mu C/cm^2$, respectively). This again showed that number averaged molecular weight dominated the exposure properties of polystyrene resist.

Despite the fact that polystyrene's sensitivity is inversely proportional to its Mw, no significant effect of very broad molecular weight distribution on the sensitivity, contrast and achievable resolution is observed. It is thus unnecessary to use the costly monodisperse polystyrene for electron beam lithography.

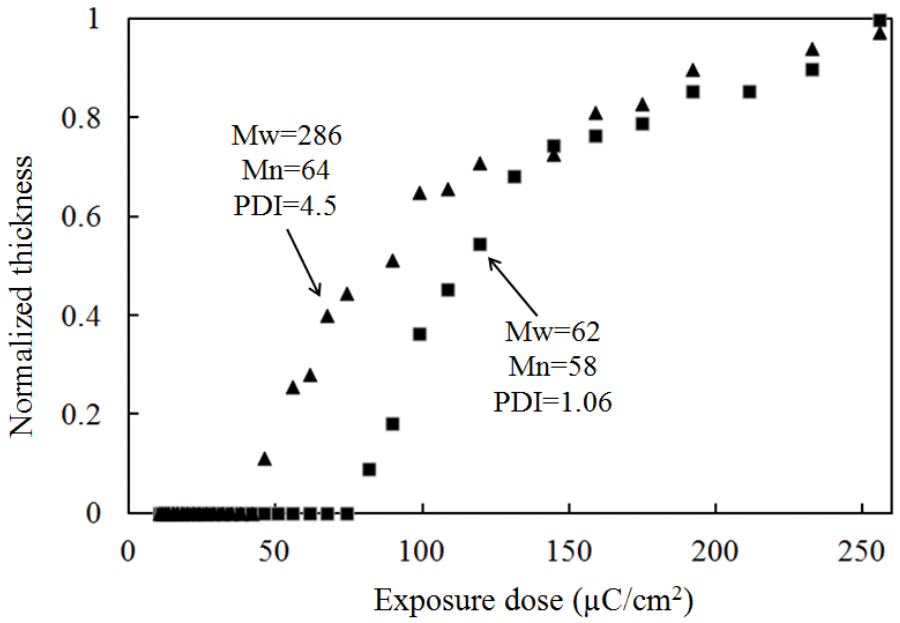

Figure 2.17. Contrast curves exposed at 20 keV for monodisperse (PDI=1.06) and general purpose polydisperse (PDI=4.5) polystyrene with similar number averaged molecular weight of ~60 kg/mol.

2.3.3. Conclusions

In our approach, we simulated a polystyrene with high polydispersity index by mixing at 1:1 weight ratio two polystyrenes with very different molecular weights. The exposure property of the mixture resembles that of a monodisperse polystyrene with a close number averaged molecular weight $\overline{Mn}$, which indicates that it is $\overline{Mn}$ rather than $\overline{Mw}$ that dominates the exposure properties of polystyrene resist. We also studied a general purpose polystyrene with a high polydispersity of 4.5, and found that its properties is comparable to those of monodisperse polystyrene having similar number averaged molecular weight. Therefore, one can use the low-cost general purpose polystyrene for electron beam lithography; and one doesn't need to have a large number of polystyrene resists with different molecular weights for different applications using EBL, as any given molecular weight can be simulated by a mixture of two polystyrene samples having different molecular weights.

2.4. Lift-off with solvent for negative resist using low energy electron beam exposure

[This work is published in J. Vac. Sci. Technol. B 32 (6), 06F507 (2014)]

2.4.1. Introduction

Direct etch and liftoff are the two most popular pattern transfer processes. In the direct etch process, the polymer resist is first patterned using a lithography technique such as electron beam lithography (EBL), then the pattern is transferred to the substrate or sub-layer with the resist as mask by a dry etching technique such as reactive ion etching. In the liftoff process, the film (commonly metal) is coated on the resist structure, and the film on top of resist structure is lifted off when the resist underneath is dissolved, leaving behind the film structure on the area previously uncovered by resist. Compared to direct etch, liftoff is more versatile since it can work for most metals, whereas many metals including most noble metals cannot be etched by dry etching. Positive resists are typically employed for liftoff; and if the metal to liftoff is too thick (e.g. > 100 nm), a double layer stack, such as PMMA/P(MMA-MAA)[65], PMMA/LOR[66], and high molecular weight PMMA/low molecular weight PMMA[67], can be used to give an undercut profile that facilitates a clean liftoff. However, for lifting off some structures such as nanoscale trenches or holes, a negative resist is preferred as it offers far less exposure time than positive resist (yet a complicated double liftoff process can be utilized with a positive resist for such structures[68]).

However, liftoff using (single layer) negative resist is very challenging for two reasons: 1) the resist profile is tapered with wider opening due to electron forward scattering, which leads to film coating on the sidewall and thus makes a clean liftoff difficult; 2) common negative resists such as polystyrene[69,70] and SU-8[71] become cross-linked and insoluble upon exposure, and thus a strong chemical such as a hot mixture of $NH_4OH : H_2O_2 : H_2O$ (RCA cleaning) must be used to dissolve it, which may attack the metal or sub-layer. Despite the challenge, liftoff using single layer negative resist has been reported. Lim et al. carried out liftoff of 20 nm Cr with ma-N 2401 resist using acetone[72]. Though acetone cannot dissolve the exposed ma-N 2401, the resist was

detached by prolonged ultrasonic agitation. However, as expected, the resulted Cr pattern had a rough edge. Similar rough edge was also resulted for the liftoff of Au using ma-N 1405 resist[73]. Passi et al. achieved liftoff of Ge and Pt (both resistant to HF) with hydrogen silsesquioxane (HSQ) resist using HF, for which the application is limited since HF attacks most metals[74].

A double layer stack may also be used for liftoff with negative resist, but it is more limited than positive resist. For example, the popular liftoff polymer LOR (based on polydimethylglutarimide, or PMGI) may not work well with negative resist for liftoff, because PMGI itself is a positive resist[75] and thus the LOR below the developed negative resist structure (i.e. the exposed area) will be dissolved far faster than the LOR at the opening (unexposed) area. As a result, one has to resort to a tri-layer structure[76] consisting of (negative) resist/hard material/polymer [e.g. resist/SiO_2/ARC (anti-reflection coating)] for liftoff after pattern transfer to the bottom polymer layer by dry etching. One exception is HSQ that is itself a hard mask material for polymer dry etching, and a bi-layer stack of HSQ/PMMA has been employed successfully for liftoff[77]. In principle, since the sensitivity ($\mu C/cm^2$) for negative resists like polystyrene is inversely proportional to its number averaged molecular weight[78], one can achieve an undercut profile using a bi-layer with the bottom layer having a lower molecular weight (thus less sensitive). However, despite our great effort and contrary to positive resist, we were not able to find a solvent that can dissolve polystyrene for spin-coating without dissolving significantly the bottom polystyrene layer during the spin-coating of the top layer.

In this section we will report a simple liftoff process with a single layer negative resist by low energy exposure, which resulted in an undercut profile, with an un-cross-linked or only partly cross-linked bottom layer soluble in common solvents. We chose polystyrene to demonstrate the process since it is a very versatile resist, for which the exposure property can be tuned simply by varying the molecular weight, and it can be thermally developed[79] as well as coated by thermal evaporation for nanolithography on non-planar surfaces[80,81]. The key advantage of our liftoff process is obviously its simplicity; however, we were not able to achieve sub-500 nm resolution with low energy exposure.

2.4.2. Experiment and numerical simulation

Polystyrene with weight averaged molecular weight of 283 kg/mol was dissolved in chlorobenzene to give two film thicknesses of 220 nm and 500 nm after spin-coating. The number averaged molecular weight, which determines the resist property, was 64 kg/mol, leading to a polydispersity of 4.5. As shown previously, this broad distribution would not affect substantially the resist exposure property. The film was baked at 120 ^{o}C for 10 min to drive off the solvent. Next, the resist was exposed at 1-5 keV using Leo 1530 SEM equipped with a NPGS pattern generation system, and developed with xylene for 45 and 90 s for 220 and 500 nm film, respectively. Subsequently 10 nm Cr was e-beam evaporated and lifted off by soaking the sample in xylene for 10 min.

In order to obtain the electron penetration depth into the resist at low energy exposure, we carried out numerical simulation with Casino v3 (University of Sherbrooke, freely available[82]). The software is based on Monte Carlo modeling to obtain the electron trajectory in solid, and it considers the interaction and generation of x-ray and backscattered and secondary electrons. In our simulation, the trajectories of 10000 primary electrons were simulated, from which we deduced the electron penetration depth into the resist at electron energy of 1-5 keV.

2.4.3. Results and discussion

An undercut profile (narrower opening) is essential for liftoff with a smooth pattern edge. However, as seen in figure 2.18 (a), for negative resist exposed at normal condition, a tapered profile (wider opening) is typically resulted due to electron forward scattering, and the longer dissolution time of the upper part of the resist than the lower part (this effect is insignificant if the resist has a high contrast for which lateral dissolution toward the less exposed region is negligible). In this study, we attempt to achieve an undercut profile using low energy exposure for which most electrons do not reach the resist bottom, as shown in figure 2.18 (b). Here the undercut at the resist bottom is owing to the very fast lateral development of the unexposed or under-exposed resist there. Figure 2.19 shows the developed polystyrene profile exposed at 2 and 5 keV for the 220 nm thick film, and 4 and 5 keV for the 500 nm thick film. As expected, when

exposed at relatively high energy, a positively tapered profile was obtained; whereas a clear undercut profile was resulted with low energy exposure.

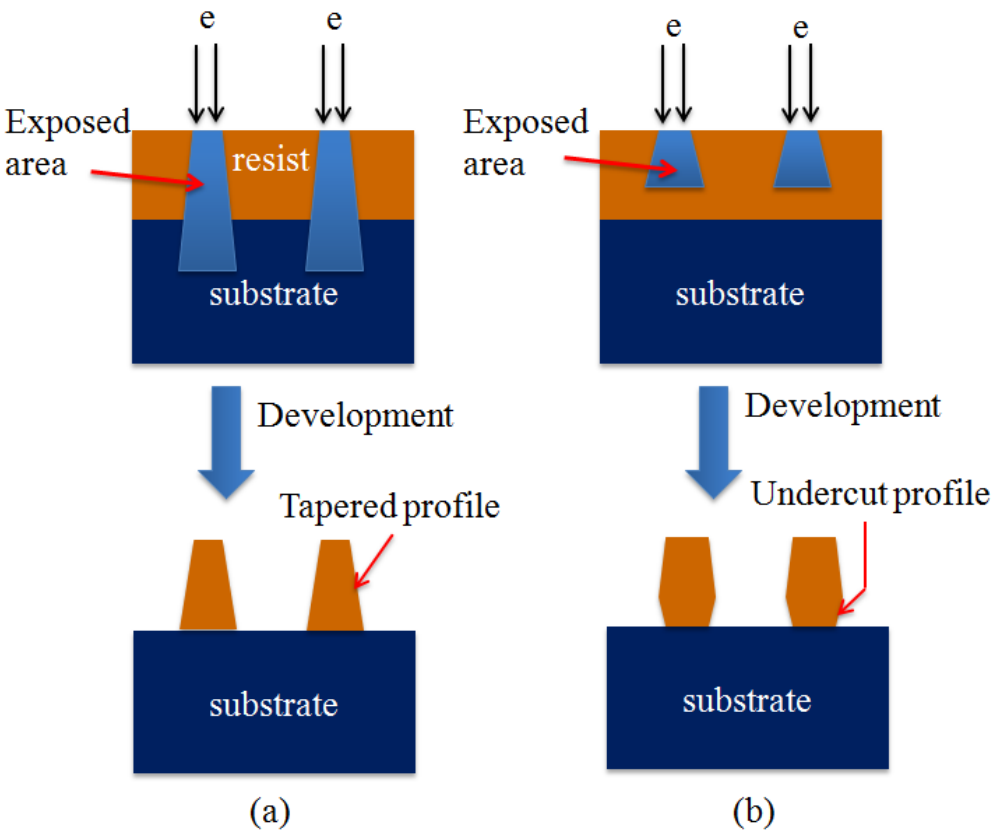

Figure 2.18. Schematic diagram showing the resulted resist profile for normal high energy exposure (a), and low energy exposure with electron penetration depth smaller than resist film thickness (b). The under-cut profile for low energy exposure is due to fast lateral development of the under-exposed/un-exposed resist at the bottom.

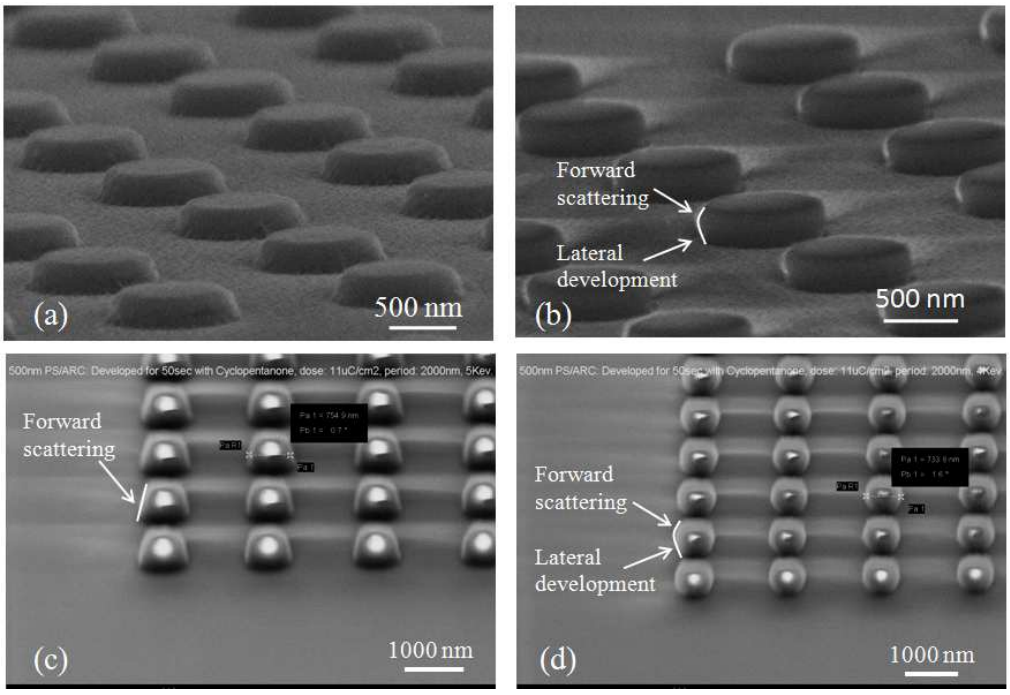

Figure 2.19. SEM images of polystyrene structure exposed at (a) 5 keV for 220 nm film; (b) 2 keV for 220 nm film; (c) 5 keV for 500 nm film; and (d) 4 keV for 500 nm film. Here the tapered profile is due to electron forward scattering, whereas under-cut at the resist bottom is due to fast lateral dissolution of the under-exposed resist there.

In order to estimate the electron penetration range and scattering volume, we utilized numerical simulation to obtain the distribution of electron trajectory. As is well known, secondary electrons (energy tens of eV), rather than primary ones (several keV), are mainly responsible for resist exposure due to its closer energy to the energy needed to induce a chemical reaction; and secondary electrons are generated along the path of the primary electrons. Figure 2.20 depicts the electron trajectories in 500 nm thick polystyrene coated on bulk silicon substrate at energy of 1-20 keV. At energy of up to 4 keV, forward scattering is significant and most electrons are stopped before reaching the substrate. At 5 keV, a significant percentage of electrons reached the film-substrate interface; and at 20 keV, most electrons penetrate deep into the substrate. The deduced electron penetration depth as a function of electron energy is shown in figure 2.21. This is in good agreement with the developed resist structure (Figure 2.19 (c) and (d)) that shows an undercut profile at 4 keV but a tapered profile at 5 keV for a film of 500 nm thick.

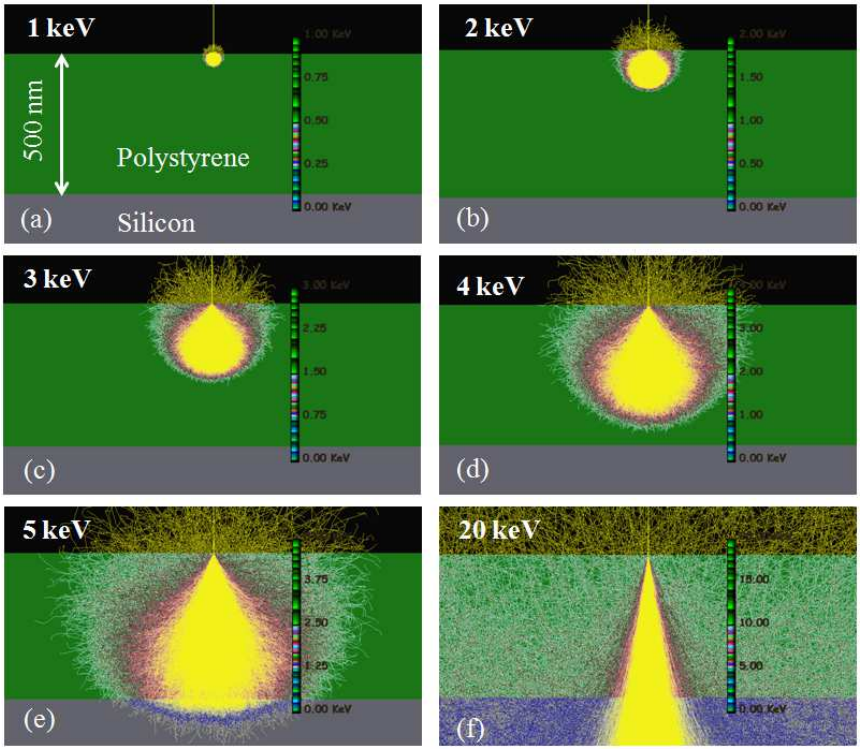

Figure 2.20. Monte Carlo simulation of 10000 electron trajectories in 500 nm thick polystyrene coated on silicon with electron energy of (a) 1 keV, (b) 2 keV, (c) 3 keV, (d) 4 keV, (e) 5 keV, and (f) 20 keV.

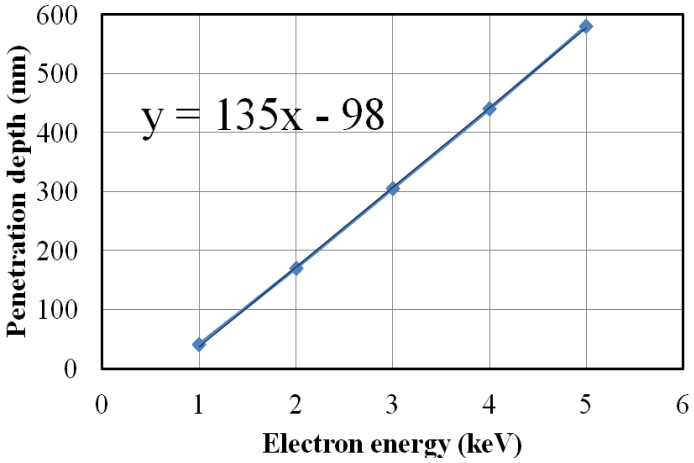

Figure 2.21. Simulated electron penetration depth in polystyrene resist as a function of electron energy.

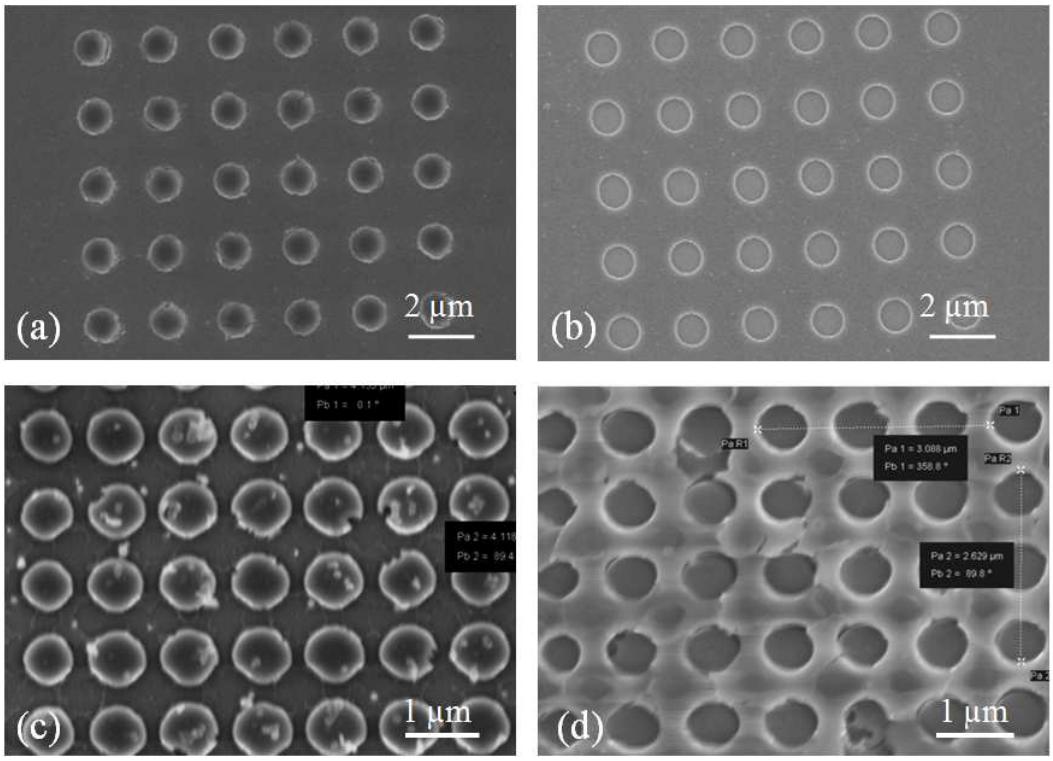

Figure 2.22. SEM images after liftoff of 10 nm Cr using polystyrene resist with different thicknesses and exposure energies. (a) 220 nm resist exposed at 5 keV; (b) 220 nm resist exposed at 2 keV; (c) 500 nm resist exposed at 5 keV; and (d) 500 nm resist exposed at 4 keV. The liftoff in (a) and (c) was not successful (resist pillars not dissolved) because cross-linked polystyrene became insoluble in xylene.

Since at low energy exposure the resist bottom part was not cross-linked or only partly cross-liked, lift-off using solvent is possible. Figure 2.22 shows liftoff of 10 nm Cr using xylene with 220 nm and 500 nm polystyrene resist. When the electron penetration depth is less than resist thickness, such as 220 nm film exposed at 2 keV and 500 nm film at 4 keV, the liftoff was successful. But at 5 keV exposure, the polystyrene pillars for both thicknesses were not dissolved since they would be cross-linked throughout the film thickness. Moreover, for low energy exposure, resist sensitivity is higher that leads to faster writing. Lastly, since most electrons are stopped in the resist layer at low energy exposure, electron beam radiation damage to the substrate/sub-layer is drastically reduced. Therefore, liftoff with the resist exposed at low energy may be utilized to fabricate metal nanostructures on top of an organic conducting layer; and our

group have demonstrated metallization of P3HT using a water soluble and developable resist poly(sodium 4-styrenesulfonate) exposed at low energy[83].

However, with low energy exposure we were not able to achieve regular array of polystyrene pillar structure having diameter much smaller than 500 nm, because the resist structures were found detached from or deformed and moved around on the substrate (Figure 2.23). Obviously, this is due to capillary force during drying of rinsing liquid. Adhesion of polystyrene structure to the substrate is also critical, and the adhesion must be weaker for exposure at low energy than high energy. To evaluate the effect of development process on adhesion, it is known that development is not a layer-by-layer linear dissolution process[84,85]. Instead, the solvent diffuses and penetrates below the top (recessing) surface and dissolve or swell the resist there. The situation is worse for low energy exposure because the under-exposed resist at the bottom is more susceptible to swelling/weakening by the solvent developer penetrated there. The smaller pillars suffer more from capillary force, since adhesion force is proportional to d^2 (d is pillar diameter) whereas capillary force is proportional to d.

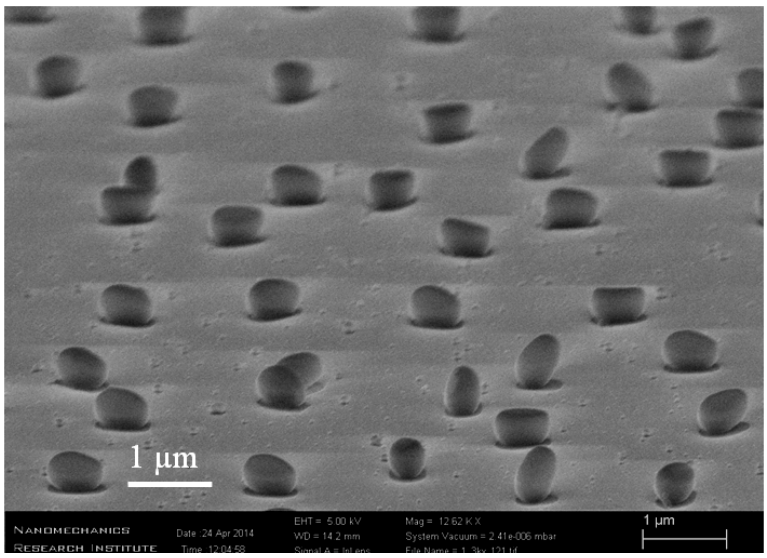

Figure 2.23. SEM image of polystyrene pillars exposed at 3 keV. The film thickness is 500 nm that is larger than the electron penetration depth of 300 nm for 3 keV exposure. The designed pattern consists of 2D periodic dot array, but most pillars were detached, deformed, and moved away from its original location.

In order to verify that the solvent can penetrate through the top cross-linked layer, we exposed large squares each with an area of 400 μm^2 in 500 nm thick polystyrene, at an area dose of 50 $\mu C/cm^2$ (very high dose to ensure fully cross-linking of the top layer) and electron energies of 1-5 keV. For such large squares, lateral development would be negligible, and the pattern would detach only if the polystyrene at the resist/substrate interface is attacked by the developer that may diffuse through the top layer to reach this interface. To magnify this effect, we developed the resist in xylene for up to 45.5 min. As shown in figure 2.24, the square exposed at 5 keV survived this long development, which is because the electrons at this energy can reach the interface to fully cross-link the resist there. For 1 keV exposure, the square was detached even after a short development time of 1.5 min. This is because the cross-linked top layer is very thin (around 40 nm, see figure 2.21) at 1 keV exposure, so the solvent developer penetrated through this layer easily. For exposure at 2, 3, and 4 keV, the squares were noticeably deformed, and they were found detached after 15.5, 26.5 and 45.5 min development, respectively. This clearly indicates that the solvent developer can diffuse to the interface and gradually dissolve the un-cross-linked or only partly cross-linked resist there.

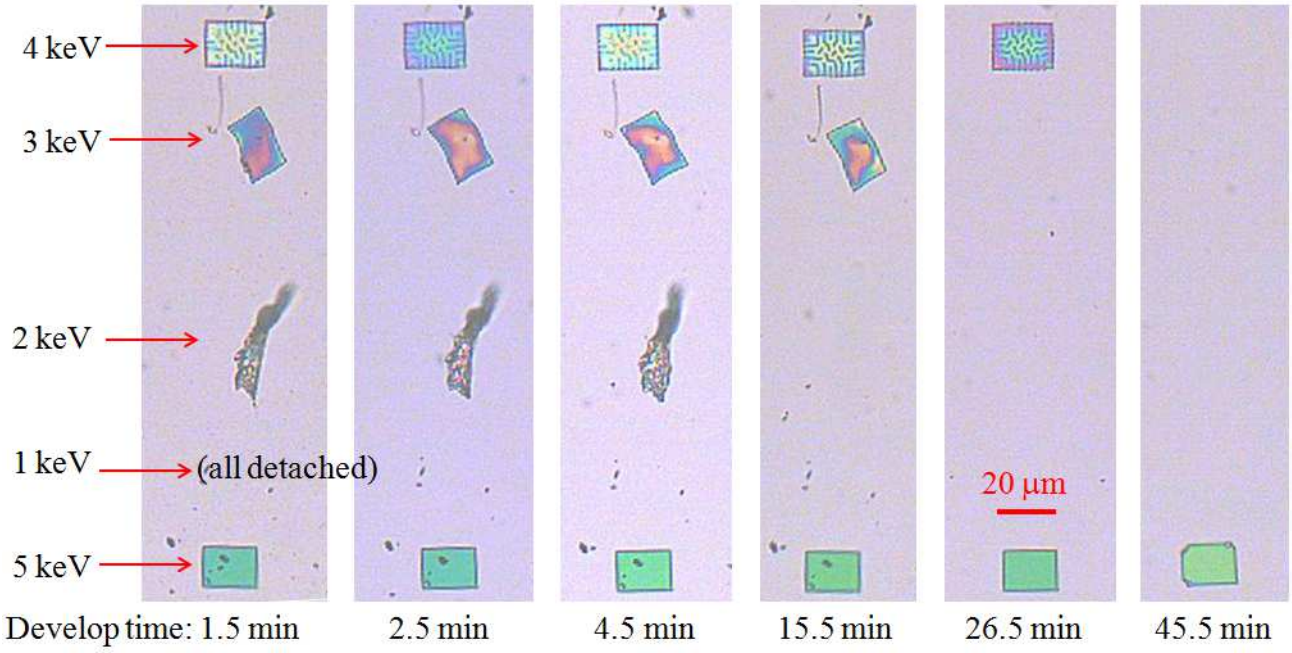

Figure 2.24. Optical microscope image of large polystyrene squares after exposure at 1-5 keV and development in xylene for 1.5 - 45.5 min.

2.4.4. Conclusions

We demonstrated metal lift-off using negative polystyrene resist by low energy exposure. It was shown that low energy exposure led to an undercut profile which is critical for a clean lift-off. Moreover, since the resist at the bottom is not cross-linked with low energy exposure, liftoff using common solvent was achieved. However, sub-500 nm resolution was challenging to attain using the current method due to capillary force that detached the fine polystyrene structure exposed at low energy. The effect of capillary force is more serious for low energy exposure because the developer can diffuse through the top cross-linked layer to dissolve the un-cross-linked resist at the film-substrate interface. Since low energy electrons are mostly stopped inside the resist layer, radiation damage to the sub-layer is greatly reduced. Thus the current method, when polystyrene is replaced with a negative water soluble resist, may be used to fabricate metal nanostructures on top of an organic conducting layer insensitive to water.

2.5. Electron beam lithography on irregular surface using grafted PMMA monolayer "brush" as resist

[This work is presented at EIPBN conference and will be submitted for journal publication]

2.5.1. Introduction

A common challenge in nanofabrication is to fabricate nanostructures on irregular surfaces, which has application in many areas including optical devices[86], MEMS[87], super-adhesive devices[88] and electronic devices[89]. More specifically, tip-enhanced raman spectroscopy (TERS)[90] which is used for chemical analysis[91] requires nanofabrication on AFM tip, and lab-on-fiber technology[92] requires nanolithography on cylindrical optical fiber. Moreover, Scanning near-field optical microscopy (SNOM)[93,94], fundamental quantum mechanical systems[95,96], and roll-to-roll nanoimprint lithography (NIL)[97,98] which uses cylindrical roller as the mold, also require nanofabrication on nonflat surfaces.

To pattern on nonplanar surfaces is more challenging than on flat surfaces. This is because conventional coating methods, such as spin-coating method which is very popular in nanofabrication technique, cannot be reliably applied to coat uniform electron beam resist on nonflat surfaces. Unlike spin coating, spray coating method[99] and Langmuir-Blodgett (LB) technique[100] may be employed to coat resist on nonplanar surfaces, but they have several limitations including sample should be free from sharp corners or edges for spray coating, and very few materials are usable as e-beam resist for LB technique. Self-assembled monolayer resist[101] can also be applied in patterning on nonflat surfaces. To do pattern transfer after self-assembly process, typically an intermediary wet etching technique is performed (dry etch is not suitable since self-assembled monolayer is too thin). However, wet etching has poor critical dimension (CD) control compared to dry etching[102]; and those resists suffer from low sensitivity. In addition, several nanolithography methods, such as focused ion beam lithography, can also be employed to pattern on irregular surface, but it is more expensive than other conventional nano-patterning methods and its throughput is even lower than electron beam lithography. Daniel et al.[103,104] introduced a new type of patterning process (ice lithography) where water vapor introduced into the SEM chamber, formed ice on sample and cooled to <120 K. The thin ice film was patterned by electron beam exposure at low energy. However, there are two major drawbacks for ice lithography: the resist should be kept at very low temperature until pattern transfer is completed, and the resist sensitivity is very low compared to conventional resists, including PMMA which is three orders more sensitive than ice. Like ice resist, frozen CO_2 can also be used as an electron-beam resist. But it has similar drawbacks that include low temperature requirement and low sensitivity[105]. A few resists including polystyrene[106,107] and silicon dioxide[108] can be deposited by thermal/e-beam evaporation technique on nonflat surface. However, they still suffer from very low sensitivity, and vacuum deposition techniques are expensive compared to spin-coating. In addition, there are only a few resists that can be evaporated. A self-developing resist such as AlF_3, which can be evaporated on irregular surfaces, is also an extremely insensitive resist.

Therefore, there is still a great demand for an easier process where a cheap and readily available resist can be coated on nonflat surface for patterning nanostructures with high resolution. Here we showed that a monolayer PMMA "brush"[109] can be grafted reliably on nonflat surface such as

on an AFM cantilever, and can be used for patterning nanostructure using electron beam lithography.

The PMMA brush monolayer is thicker than self-assembled monolayer resist, thus easier for pattern transfer. In addition, it is a low cost process, as it employs only spin or dip-coating method. Moreover, the monolayer can reduce pattern collapse due to the capillary force while using solvent development, since it's a thin film and chemically bonded to the sub-layer/substrate. Another advantage for a polymer brush coating method over spin-coating is the lack of edge-bead effect, which is a serious problem for spin-coating[110]. It is thus suitable for patterning on ultra-small substrate without having any edge-bead effect. Furthermore, adhesion between conventional electron beam resists with the substrate is enhanced by using grafted monolayer PMMA brush as an adhesion layer, which will be reported elsewhere[111].

In this process, the brush is grafted onto a surface terminated with hydroxyl group the same way as forming the Polystyrene-r-PMMA copolymer[112,113] brush that is widely used to provide a neutral surface for self assembly.

2.5.2. Polymer “brush” grafting and pattern transfer to substrate

We chose a low molecular weight (Mw: 34 kg/mol, Mn: 15 kg/mol) PMMA (contains 1.6% MAA, (meth)acrylic acid, to further promote the grafting process as MAA contains the desirable –COOH group) for deposition as an e-beam resist. AFM tip is typically used in tip-enhanced Raman spectroscopy. To this end, Nanoworld Arrow AFM probes (silicon) were chosen to demonstrate the capability of patterning on nonflat surfaces by grafting the 'brush' monolayer resist.

The sample surface was first cleaned by 2-proponol (IPA), followed by oxygen plasma cleaning for 1 min (20 sccm O_2, 20 mTorr and 20 W). For easier handling, the tip was attached to a piece of regular silicon wafer by using photoresist as a "glue". To transfer the pattern into the substrate by dry etching, a hard etch mask of thin (5-9 nm) aluminum film was deposited onto the AFM probe with a chamber background vacuum of 2 μTorr using an Intlvac vacuum deposition

system. During metal deposition, the heating power was increased slowly until a desired deposition rate of ~0.5 Å/s was achieved. As shown in figure 2.26, to form a monolayer brush, PMMA dissolved in anisole with a concentration of 1 v/v % was coated on the samples by dip or spin coating. Next, the resist was baked overnight at 160 ^{o}C on a hotplate to induce the chemical reaction between –COOH on resist and -OH on the surface-treated silicon substrate (or substrate with aluminum sub-layer). This reaction leads to the production of water and chemical bonding between the resist and substrate (–CO-O-Si- for silicon, –CO-O-Al- for aluminum). Figure 2.25 shows the schematic diagram of chemical reaction between PMMA-co-PMAA and a silicon surface treated with oxygen plasma. Finally, the bulk of PMMA was washed away by rinsing with acetic acid, leaving behind a monolayer "residual" that was chemically bonded to the substrate.

Electron beam lithography was conducted using a Leo 1530 FESEM system with 3 kV acceleration voltage and 89 pA beam current (30 μm aperture). The exposed resist was developed by MIBK:IPA (1:3) for 7 sec, except for the overexposed case where longer development times were needed to show any measurable dissolution. Such a very short development time is enough to develop the monolayer resist. After development, the pattern was first transferred into the aluminum film using PAN etching (PAN etch recipe: Phosphoric acid : Nitric Acid : Acetic Acid : DI Water = 16 : 1 : 1 : 2) at room temperature for 5 sec, followed by washing with DI water. Next, the pattern in Al film is transferred into bulk silicon by dry etching (ICP RIE, Trion PI system with the recipe of 40 sccm CF_4, 3 sccm O_2, 8 mTorr pressure and 50 W RF power) for 30 sec. Finally, the pattern was observed by using either LEO 1530 FESEM or Zeiss Ultra FESEM.

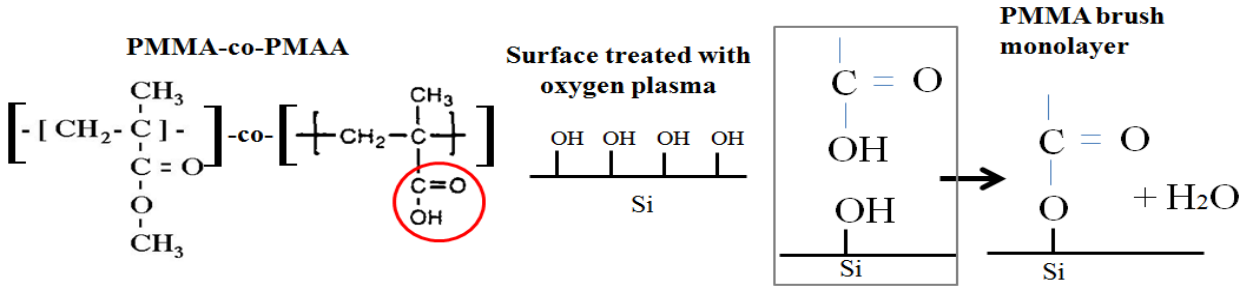

Figure 2.25. Schematic diagram of chemical reaction between PMMA-co-PMAA and a silicon surface treated with oxygen plasma, which leads to monolayer "brush" grafting.

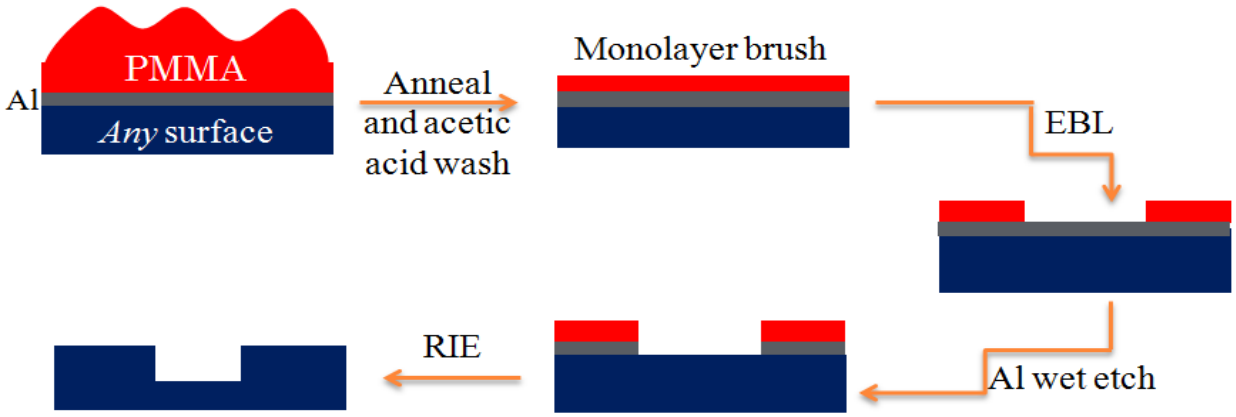

Figure 2.26. Schematic diagram of fabrication process using brush monolayer resist and Al intermediate hard mask for pattern transfer.

2.5.3. Results and discussion

To characterize the monolayer, PMMA monolayer brush was exposed and developed to dissolve the exposed area. Figure 2.27 shows the AFM image of the grafted monolayer brush with a height of 12 nm. Since this monolayer brush is too thin for lift-off or direct-etch pattern transfer, an intermediate hard-mask (here Al) is needed for etching deep into the substrate.

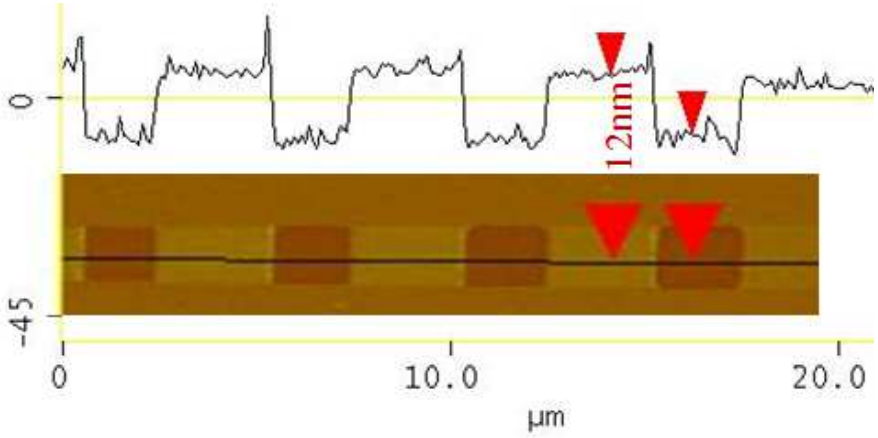

Figure 2.27. AFM image of the grafted monolayer brush with a thickness of 12 nm.

To study the resolution capability of the brush monolayer, we exposed periodic dense line arrays with periods from 300 nm down to 100 nm. The lines were written by e-beam exposure at a voltage of 3 kV with a step size of 5 nm. Figure 2.28 shows the SEM images of grating patterns

with a line dose of 31 pC/cm and periods of 200 nm (a) and 100 nm (b) fabricated on the flat part of the AFM cantilever. Grating patterns with periods of 200 and 100 nm are clearly well-defined with good contrast. The grating line-width resolution is down to 30 nm, as shown in inset of figure 2.28 (b). Resolution is higher for thin film because there is less proximity effect and less pattern collapse.

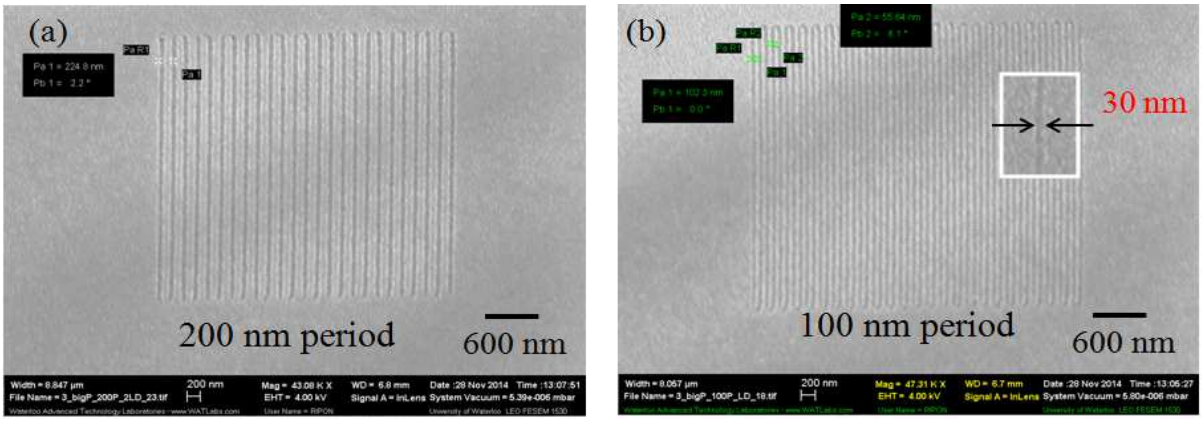

Figure 2.28. SEM images of grating patterns on flat region of an AFM cantilever (silicon) using PMMA monolayer "brush" s resist. (a) 200 nm and (b) 100 nm period gratings on the flat part of the AFM cantilever exposed at a line dose of 31 pC/cm, with high resolution line-width of 30 nm in inset of (b).

Figure 2.29 shows the SEM images of dense grating arrays fabricated on *noneflat* region of AFM cantilever with period of 100, 200 and 300 nm and exposed at line dose range of 10-100 pC/cm.

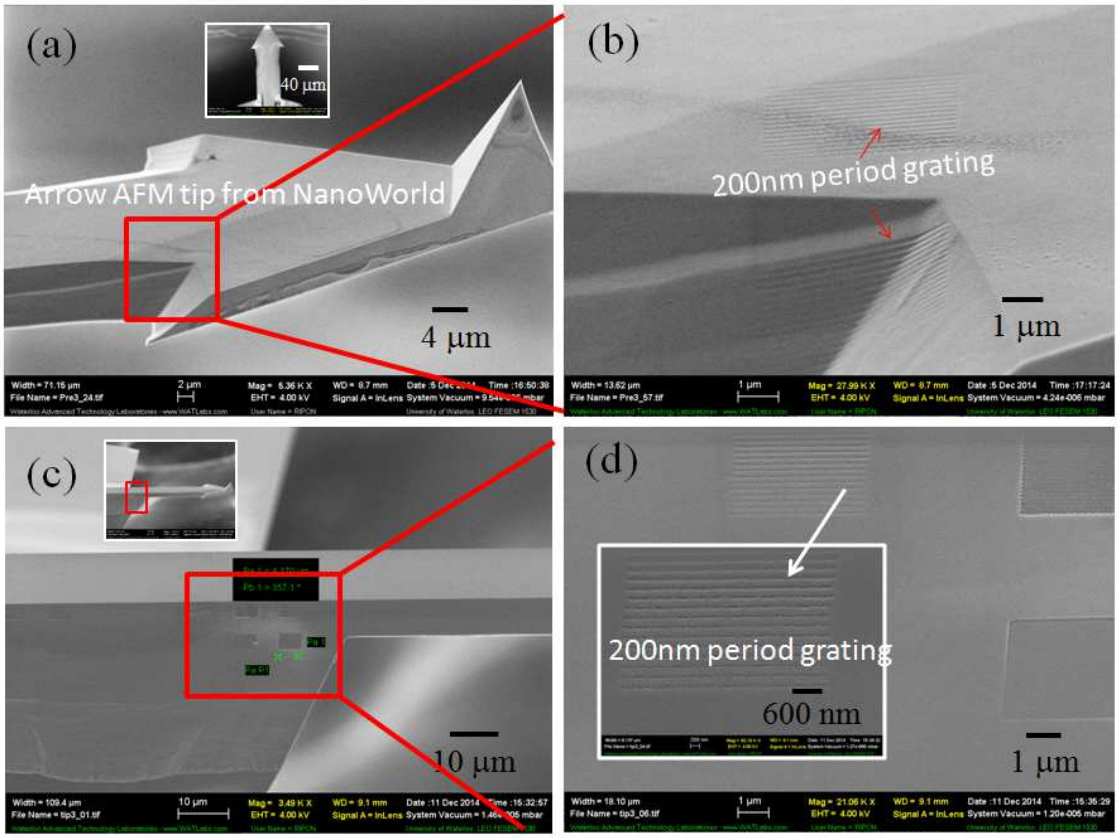

Figure 2.29. SEM images of 200 nm period gratings fabricated on *nonflat* region of an AFM cantilever. (a,b) Near the corner, exposed at 66 pC/cm; (c,d) At the side slope, 76 pC/cm. (a,c) low-magnification (top view in inset), (b,d) high magnification. Except for the top-view images, the sample was mounted on a 75° stub for SEM imaging.

For patterning on the sloped surface, the focal point of electron beam varies with vertical positions of surface. The sloped surface of AFM cantilever (Figure 2.29 (c)) has a ~60° incidence angle for electron beam. The patterns exposed with a slope are different from that exposed from the top in the same EBL system (Figure 2.28). Therefore, as shown in figure 2.29 (d) inset, the gratings exposed on top surface are better defined than the gratings at the sloped side surface. This occurred because of several reasons. Firstly, due to slope, dose on sidewall is lower by cosθ, where θ is the incident angle of e-beam exposure to the slope surface; and the grating period is larger by 1/cosθ. Secondly, on the surface with a slope, the electron beam may get '*out-of-focus*' during electron exposure. Therefore, the resolution of nanostructures on the cantilever side surface depends on the depth of focus of the electron beam in EBL system,

ignoring the wave nature and diffraction of the beam. Note that the depth of focus is inversely proportional to the aperture size and proportional to the working distance (WD) in EBL system. Thus, like typical camera, higher depth of focus is achievable using a smaller aperture size or a longer WD. One drawback for using smaller aperture is longer exposure time because it leads to low beam current, since current is roughly proportional to the square of the aperture size of the SEM system. Pattern resolution gets worse at slope sidewall at larger aperture (smaller depth of focus). For instance, in our previous work, we achieved 80 nm resolution on a flat surface with 37 μm out of focus and 30 μm aperture size[114]. However, here the cantilever thickness is only ~10 μm. As a consequence, the electron beam should be well focused on the entire cantilever sidewall.

In addition to the depth of focus, there are two other important factors to pattern on the surface with slope: metal film deposition and substrate dry etching uniformity. In vacuum deposition system, the metal film thickness is proportional to cosθ, where θ is the vapor incident angle with 0° for the top horizontal surface of the cantilever, and 90° for the vertical surface of the cantilever. In order to get better uniformity of metal film, the cantilever can be mounted on a different slope to make the film uniform on all the side surface of the tip. For etching, when the top of the cantilever is properly etched, the sloped sides would be slightly over etched since metal is thinner there.

2.5.4. Conclusions

We demonstrated the feasibility of our approach where the PMMA monolayer "brush" as an e-beam resist is successfully grafted on treated nonflat surface (Si and Al as substrate/sub-layer). As a proof of concept of patterning on nonflat surface, we fabricated grating structures on the AFM cantilever. High resolution of 30 nm line width, and dense pattern of 50 nm half pitch, were etched into AFM cantilever using this brush monolayer resist and Al as hard mask intermediate layer. Nanopatterning on nonflat substrates may find applications in fields such as atomic force microscope (AFM) tip-enhanced raman spectroscopy[115] (TERS) for chemical analysis and lab-on-fiber technology[116].

2.6. General conclusions

Here we described fundamentals of electron beam lithography. Effect of molecular weight and molecular weight distribution on e-beam exposure properties of polystyrene was studied in this chapter. Lift-off with solvent for negative resist using low energy electron beam exposure was demonstrated. Electron beam lithography on irregular surface using grafted PMMA mono-layer "brush" was also demonstrated. The application of this optimized nanofabrication technique with electron beam lithography is vast and very important in nanotechnology.

.

2.7. References

[1] A. E. Grigorescu, C. W. Hagen, "Resists for sub-20-nm electron beam lithography with a focus on HSQ: state of the art", Nanotechnol. **20**, 292001 (2009).

[2] A. A. Tseng, "Recent developments in micromilling using focused ion beam technology", J. Micromech. Microeng. **14(4),** R15 (2004).

[3] H. Schift, "Nanoimprint lithography: An old story in modern times? A review", J. Vac. Sci. Technol. B **26(2),** 458 (2008).

[4] P. B. Fischer, Ph.D. thesis, University of Minnesota, December 1993.

[5] P. R. Krauss, Ph. D. thesis, University of Minnesota, September 1997.

[6] S. Mackie and S. P. Beaumont, "Materials and Processes for Nanometer Lithography", Solid State Technology, 117 (1995).

[7] D. Kyser, "Spatial resolution limits in electron beam nanolithography", J. Vac. Sci. Technol. B **1 (4)**, 1391 (1983).

[8] T. H. P. Chang, "Proximity effect in electron-beam lithography", J. Vac. Sci. Technol. B **12 (6)**, 1271 (1975).

[9] T. R. Neill and C. J. Bull, "High voltage electron lithography", Electronics Letters **16 (16)**, 621 (1980).

[10] G. A. C. Jones, S. Blythe, and H. Ahmed, "Very high voltage (500 kV) electron beam lithography for thick resists and high resolution", J. Vac. Sci. Technol. B **5 (1)**, 120 (1987).

[11] S. A. Chambell, "The Science and Engineering of microelectronic Fabrication", Oxford University Press, 2001.

[12] H. G. Craighead, R. E. Howard, L. D. Jackel, and P. M. Mankiewich, "10-nm linewidth electron beam lithography on GaAs", Appl. Phys. Lett. **42 (1)**, 38 (1983).

[13] A. N. Broers, "Resolution limits for electron-beam lithography", IBM J. Res. Develop. **32 (4)**, 502 (1988).

[14] W. Chen and H. Ahmed, "Fabrication of 5–7 nm wide etched lines in silicon using 100 keV electron-beam lithography and polymethylmethacrylate resist", Appl. Phys. Lett. **62**, 1499 (1993).

[15] G. H. Bernstein and D. A. Hill, "On the attainment of optimum developer parameters for PMMA resist", Superlattices and microstructures, **11 (2)**, 237 (1992).

[16] C. L. Frye, and W. T. Collins, "Oligomeric Silsesquioxanes, $(HSiO_{3/2})_n$", J. Am. Chem. Soc. **92,** 5586 (1970).

[17] F. C. van Delft, "Delay-time and aging effects on contrast and sensitivity of hydrogen silsesquioxane", J. Vac. Sci. Technol. B **20**, 2932 (2002).

[18] Y. Fujita, Y. Ohnishi, Y. Ochiai, E. Nomura, and S. Matsui, "Nanometer-scale resolution of calixarene negative resist in electron beam lithography", J. Vac. Sci. Technol. B **14 (6)**, 4272 (1996).

[19] A. Pepin, V. Studer, D. Decanini and Y. Chen, "Exploring the high sensitivity of SU-8 resist for high resolution electron beam patterning", J. of Microelectronic engineering **73-74(1),** 233-237 (2004).

[20] T. W. Ebbesen, H. J. Lezec, H. F. Ghaemi, T. Thio, P. A. Wolff, "Extraordinary optical transmission through sub-wavelength hole arrays", Nature **391,** 667-669 (1998).

[21] A. Hajiaboli, B. Cui, M. Kahrizi, V. V. Truong, "Optical properties of thick metal nanohole arrays fabricated by electron beam and nanosphere lithography", Physica Status Solidi A, **206(5),** 976-979 (2009).

[22] B. Bilenberg, M. Schøler, P. Shi, M. S. Schmidt, P. Bøggild, M. Fink, C. Schuster, F. Reuther, C. Gruetzner, A. Kristensen, "Comparison of High Resolution Negative Electron Beam Resists", J. Vac. Sci. Technol. B **24(4)**, 1776 (2006).

[23] S. Hosaka, H. Sano, K. Itoh, H. Sone, "Possibility to form an ultrahigh packed fine pit and dot arrays for future storage using EB writing", Microelectron. Eng. **83,** 792-795 (2006).

[24] Z. B. Mohamad, M. Shirai, H. Sone, S. Hosaka, M. Kodera, "Formation of dot arrays with a pitch of 20 nm x 20 nm for patterned media using 30-keV EB drawing on thin calixarene resist", Nanotechnol. **19**, 025301 (2008).

[25] M. J. Word, I. Adesida, P. R. Berger, "Nanometer-period gratings in hydrogen silsesquioxane fabricated by electron beam lithography", J. Vac. Sci. Technol. B **21(6),** L12 (2003).

[26] S. Choi, M. J. Yan, L. Wang, I. Adesida, "Ultra-dense hydrogen silsesquioxane (HSQ) structures on thin silicon nitride membranes", Microelectron. Eng. **86**, 521 (2009).

[27] J. Vila-Comamala, S. Gorelick, V. A. Guzenko, E. Farm, M. Ritala, C. David, "Dense high aspect ratio hydrogen silsesquioxane nanostructures by 100 keV electron beam lithography", Nanotechnol. **21**, 285305 (2010).

[28] J. K. W. Yang, B. Cord, H. Duan, K. K. Berggren, J. Klingfus, S. W. Nam, K. B. Kim, M. J. Rooks, "Understanding of hydrogen silsesquioxane electron resist for sub-5-nm-half-pitch lithography", J. Vac. Sci. Technol. B **27(6),** 2622 (2009).

[29] V. Sidorkin, A. van Run, A. van Langen-Suurling, A. Grigorescu, E. van der Drift, "Towards 2-10 nm electron-beam lithography: a quantitative approach", Microelectron. Eng. **85,** 805 (2008).

[30] J. K. W. Yang, K. K. Berggren, "Using high-contrast salty development of hydrogen silsesquioxane for sub-10-nm half-pitch lithography", J. Vac. Sci. Technol. B **25(6)**, 2025 (2007).

[31] N. Clark, A. Vanderslice, R. Grove, R. R. Krchnavek, "Time-dependent exposure dose of hydrogen silsesquioxane when used as a negative electron-beam resist", J. Vac. Sci. Technol. B **24(6),** 3073 (2006).

[32] S. Ma, C. Con, M. Yavuz, B. Cui, "Polystyrene negative resist for high-resolution electron beam lithography", Nanoscale Res. Lett. **6,** 446 (2011).

[33] R. Bonam, P. Verhagen. A. Munder, J. Hartley, "Performance characterization of negative resists for sub-10nm-nm electron beam lithography", J. Vac. Sci. Technol. B, **28(6),** C6C34 (2010).

[34] H. Y. Ku, L. C. Scala, "Polymeric Electron Beam Resists", J. Electrochem. Soc. **116,** 980 (1969).

[35] A. Charlesby, "A Theory of Network Formation in Irradiated Polyesters", Proc. R. Soc. Lond. A 10. **241(1227)**, 495-507 (1957).

[36] B. Shokouhi, J. Zhang and B. Cui, "Very high sensitivity ZEP resist using MEK:MIBK developer", Micro & Nano Lett. **6(12),** 992–994 (2011).

[37] J. Joo, B. Y. Chow, J. M. Jacobson, "Nanoscale patterning on insulating substrates by critical energy electron beam lithography", Nano. Lett. **6(9),** 2021 (2006).

[38] R. Bonam, P. Verhagen, A. Munder, J. Hartley, "Performance characterization of negative resists for sub-10-nm electron beam lithography", J. Vac. Sci. Technol. B **28 (6),** C6C34 (2010).

[39] B. Bilenberg, S. Jacobsen, M. S. Schmidt, L. H. D. Skjolding, P. Shi, P. Boggild, J. O. Tegenfeldt, A. Kristensen, "High Resolution 100 kV Electron Beam Lithography in SU-8", Microelectron. Eng. **83,** 1609 (2006).

[40] B. Cord, C. Dames, J. Berggren, J. Aumentado, "Robust shadow-mask evaporation via lithographically controlled undercut", J. Vac. Sci. Technol. B **24 (6),** 3139 (2006).

[41] B. Cui, T. Veres, "High resolution electron beam lithography of PMGI using solvent developer", Microelectron. Eng. **85,** 810 (2008).

[42] S. M. S. Rahman, B. Cui, "Mold Fabrication for 3D Dual Damascene Imprinting", Nanoscale Res. Lett. **5,** 545 (2010).

[43] C. Con, R. Dey, M. Ferguson, J. Zhang, R. Mansour, M. Yavuz and B. Cui, "High molecular weight polystyrene as very sensitive electron beam resist", Microelectron. Eng. **98**, 254 (2012).

[44] L. Liping, H. Yajiang, Y. Qi, "Effect of Polydispersity on the Phase Behavior of Polystyrene (PS)/Poly (Vinyl Methyl Ether) (PVME)", Journal of Macromolecular Science Part B: Physics. **50**, 2140 (2011).

[45] C. Chen, T. Hsieh, M. Ju, "Effects of polydispersity index and molecular weight on crystallization kinetics of syndiotactic polystyrene (sPS)", Journal of Alloys and Compounds. **480**, 658 (2009).

[46] K. Itaya, K. Shibayama and T. Fujimoto, "High Resolution Electron Beam Negative Resist with Very Narrow Molecular Weight Distributions", J. Electrochem. Soc. **129**, 663 (1982).

[47] S. Manako, J. Fujiga, Y. Ochiai, E. Nomura and S. Matsui, "Nanometer-Scale Patterning of Polystyrene Resists in Low-Voltage Electron Beam Lithography", Jpn. J. App. Phys. **36**, 7773 (1997).

[48] S. Manako, J. Fujiga, Y. Ochiai, E. Nomura and S. Matsui, "Resolution-Limit Study of Chain-Structure Negative Resist by Electron Beam Lithography", Jpn. J. App. Phys. **36**, L724 (1997).

[49] Y. Ochiai, S. Manako, J. Fujita and E. Nomura, "High resolution organic resists for charged particle lithography", J. Vac. Sci. Technol. B. **17**, 933 (1999).

[50] M. Austin, W. Zhang, H. Ge, D. Wasserman, S. Lyon, S. Y. Chou, "6 nm half-pitch lines and 0.04 μm^2 static random access memory patterns by nanoimprint lithography", Nanotechnology **16**, 1058 (2005).

[51] P. W. Whipps, "Negative resists based on polystyrene", Microcircuit Engineering 118 (1979).

[52] J. C. Jagt, P. W. Whipps, "Negative Electron Resists for VLSI", Philips Technical Rev. **39**, 346 (1980).

[53] H. Y. Ku and L. C. Scala, "Polymeric Electron Beam Resists", J. Electrochem. Soc.: Solid State Science. **116**, 980 (1969).

[54] M. Yan, S. Choi, K. R. V. Subramanian and I. Adesida, "The effects of molecular weight on the exposure characteristics of poly(methylmethacrylate) developed at low temperatures", J. Vac. Sci. Technol. B. **26**, 2306 (2008).

[55] M. Khoury and D. K. Ferry, "Effect of molecular weight on poly(methyl methacrylate) resolution", J. Vac. Sci. Technol. B. **14**, 75 (1996).

[56] N. Atoda and H. Kawakatsu, "Gel Formation in Negative Electron Resists", J. Electrochem. Soc.: Solid-State Science and Technology **123**, 1519 (1976).

[57] K. Sugita and N. Ueno, "Resists for microlithography: Present status and recent research trends", Prog. Polym. Sci. **17**, 319 (1992).

[58] B. Shokouhi, J. Zhang and B. Cui, "Very high sensitivity ZEP resist using MEK:MIBK developer", Micro & Nano Lett. **6**, 992 (2011).

[59] S. S. Sheiko, M. Gauthier, M. Möller, "Monomolecular Films of Arborescent Graft Polystyrenes", Macromolecules **30**, 2343 (1997).

[60] H. W. McCormick, F. M. Brower, L. J. Kin, "The effect of molecular weight distribution on the physical properties of polystyrene", Polym. Sci. **39**, 87 (1959).

[61] E. H. Merz, L. E. Nielson, R. Buchdahl, "Influence of Molecular Weight on the Properties of Polystyrene", Ind. Eng. Chem. **43**, 1396 (1951).

[62] E. Feit, L. Stillwagon, "Electron-beam lithography of chlorinated polystyrenes with narrow molecular weight distributions", Polym. Eng. Sci. **20**, 1058 (1980).

[63] J. H. Lai, L. T. Shepherd, "Experimental Observations of Nearly Monodisperse Polystyrene as Negative Electron Resists", J. Electrochem. Soc. **126**, 696 (1979).

[64] N. Atoda and H. Kawakatsu, "Gel Formation in Negative Electron Resists", J. Electrochem. Soc.: Solid State Sci. Technol. **123,** 1519 (1976).

[65] L. Ji, P. D. Dresselhaus, S. Han, K. Lin, W. Zheng, and J. E. Lukens, "Fabrication and characterization of single electron transistors and traps", J. Vac. Sci. Technol. B **12**, 3619 (1994).

[66] Y. Chen, K. Peng, and Z. Cui, "A lift-off process for high resolution patterns using PMMA/LOR resist stack", Microelectron. Eng. **73–74**, 278 (2004).

[67] M. J. Rooks, S. Wind, P. McEuen, and D. E. Prober, "Fabrication of 30-nm-scale structures for electron transport studies using a polymethylmethacrylate bilayer resist", J. Vac. Sci. Technol. B **5,** 318 (1987).

[68] A. R. Hajiaboli, B. Cui, M. Kahrizi, and V. V. Truong, "Optical properties of thick metal nanohole arrays fabricated by electron beam and nanosphere lithography", Phys. Status Solidi A. **206,** 976 (2009).

[69] C. Con, R. Dey, M. Ferguson, J. Zhang, R. Mansour, M. Yavuz and B. Cui, "High molecular weight polystyrene as very sensitive electron beam resist" Microelectronic Engineering. **98,** 254-257 (2012).

[70] S. Ma, C. Con, M. Yavuz and B. Cui, “Polystyrene Negative Resist for High Resolution Electron Beam Lithography”, Nanoscale Research Letters. **6,** 446 (2011).

[71] B. Bilenberg, M. Scholer, P. Shi, M. S. Schmidt, P. Bøggild, M. Fink, C. Schuster, F. Reuther, C. Gruetzner, and A. Kristensen, "Comparison of high resolution negative electron beam resists", J. Vac. Sci. Technol. B **24,** 1776 (2006).

[72] K. M. Lim, S. Gupta, C. Ropp, E. Wak, “Development of metal etch mask by single layer lift-off for silicon nitride photonic crystals”, Microelectronic Engineering. **88,** 994–998 (2011).

[73] A. Aassime and V. Mathet, “Lift-off and hybrid applications with ma-n 1405 negative-tone resist”, J. Vac. Sci. Technol. B. **27,** 28 (2009).

[74] V. Passi, A. Lecestre, C. Krzeminski, G. Larrieu, E. Dubois, J. Raskin, "A single layer hydrogen silsesquioxane (HSQ) based lift-off process for germanium and platinum ", Microelectronics Engineering, **87(10),** 1872 (2009).

[75] B. Cui and T. Veres, “High resolution electron beam lithography of PMGI using solvent developer”, Microelectron. Eng. **85,** 810-813 (2008).

[76] B. Cui and T. Veres, “Pattern replication of 100 nm to millimeter-scale features by thermal nanoimprint lithography”, Microelectronic Engineering. **83,** 902–905 (2006).

[77] H. Yang, J. Aizi, L. Qiang, L. Junjie, G. Changzhi and C. Zheng, "Electron beam lithography of HSQ/PMMA bilayer resists for negative tone lift-off process", Microelectronic Engineering. **85 (5-6),** 814-817 (2007).

[78] R. Dey and B. Cui, "Effect of molecular weight distribution on e-beam exposure properties of polystyrene", Nanotechnol. **24**, 245302 (2013).

[79] C. Con, A. S. Abbas, M. Yavuz and B. Cui, “Dry thermal development of negative electron beam resist polystyrene”, Advances in Nano Research. **1,** 105-109 (2013).

[80]J. Zhang, C. Con and B. Cui, “Electron beam lithography on irregular surfaces with evaporated resist”, ACS Nano. **8,** 3483–3489 (2014).

[81] C. Con, J. Zhang and B. Cui, “Nanofabrication of high aspect ratio structures using evaporated resist containing metal”, Nanotechnology. **25,** 175301 (2014).

[82] R. Gauvin and D. Drouin, "Casino Model", University of Sherbrooke (2000), (http://www.gel.usherbrooke.ca/casino/What.html).

[83] A. S. Abbas, S. Alqarni, B. B. Shokouhi, M. Yavuz and B. Cui, “Water soluble and metal-containing electron beam resist poly(sodium 4-styrenesulfonate)”, Mater. Res. Express **1,** 045102 (2014).

[84] M. A. Mohammad, K. Koshelev, T. Fito, D. A. Zheng, M. Stepanova and S. Dew, "Study of Development Processes for ZEP-520 as a High-Resolution Positive and Negative Tone Electron Beam Lithography Resist", Jpn. J. Appl. Phys. **51,** 06FC05 (2012).

[85] M. A. Mohammad, K. P. Santo, S. K. Dew and M. Stepanova, “Study of the interaction of polymethylmethacrylate fragments with methyl isobutyl ketone and isopropyl alcohol”, J. Vac. Sci. Technol. B. **30**, 06FF11 (2012).

[86] C. R. Zamarreno, I. R. Matias, F. J. Arregui, "Nanofabrication Techniques Applied to the Development of Novel Optical Fiber Sensors Based on Nanostructured Coatings", IEEE Sens. J. **12,** 2699–2710 (2012).

[87] Y. N. Xia, G. M. Whitesides, "Soft Lithography", Annu. Rev. Mater. Sci. **28,** 153–184 (1998).

[88] M. P. Murphy, S. Kim, M. Sitti, "Enhanced Adhesion by Gecko-Inspired Hierarchical Fibrillar Adhesives", ACS Appl. Mater. Interface **1,** 849–855 (2009).

[89] H. C. Ko, M. P. Stoykovich, J. Z. Song, V. Malyarchuk, W. M. Choi, C. J. Yu, J. B. Geddes, J. L. Xiao, S. D. Wang, Y. G. Huang, "A Hemispherical Electronic Eye Camera Based on Compressible Silicon Optoelectronics", Nature **454,** 748–753 (2008).

[90] A. Han, A. Kuan, J. Golovchenko, D. Branton, "Nanopatterning on Nonplanar and Fragile Substrates with Ice Resists", Nano Lett. **12,** 1018–1021 (2012).

[91] B. S. Yeo, J. Stadler, T. Schmid, R. Zenobi and W. H. Zhang, "Tip-enhanced Raman Spectroscopy – Its status, challenges and future directions", Chem. Phys. Lett. **472,** 1–13 (2009).

[92] M. Consales, A. Ricciardi, A. Crescitelli, E. Esposito, A. Cutolo and A. Cusano, "Lab-on-Fiber Technology: Toward Multifunctional Optical Nanoprobes", ACS Nano **6,** 3163–70 (2012).

[93] T. W. Johnson, Z. J. Lapin, R. Beams, N. C. Lindquist, S. G. Rodrigo, L. Novotny, S. H. Oh, "Highly Reproducible Near-Field Optical Imaging with Sub-20-nm Resolution Based on Template-Stripped Gold Pyramids", ACS Nano **6,** 9168–9174 (2012).

[94] N. C. Lindquist, P. Nagpal, A. Lesuffleur, D. J. Norris, S. H. Oh, "Three-Dimensional Plasmonic Nanofocusing", Nano Lett. **10,** 1369–1373 (2010).

[95] P. Treutlein, D. Hunger, S. Camerer, T. W. Hänsch, J. B. Reichel, "Einstein Condensate Coupled to a Nanomechanical Resonator on an Atom Chip", Phys. Rev. Lett. **99,** 140403–140406 (2007).

[96] A. C. Bleszynski-Jayich, W. E. Shanks, B. Peaudecerf, E. Ginossar, F. von Oppen, L. Glazman, J. G. E. Harris, "Persistent Currents in Normal Metal Rings", Science **326,** 272–275 (2009).

[97] S. C. Tseng, W. Y. Peng, Y. F. Hsieh, P. J. Lee, W. L. Lai, "Electron Beam Lithography on Cylindrical Roller", Microelectron. Eng. **87,** 943–946 (2010).

[98] S. H. Ahn, L. J. Guo, "High-Speed Roll-to-Roll Nanoimprint Lithography on Flexible Plastic Substrates." Adv. Mater. **20,** 2044–2049 (2008).

[99] J. Linden, C. Thanner, B. Schaaf, S. Wolff, B. Lägel, E. Oesterschulze, "Spray coating of PMMA for pattern transfer via electron beam lithography on surfaces with high topography", Microelectron. Eng. **88,** 2030–2032 (2011).

[100] I. R. Peterson, "Langmuir-Blodgett electron-beam resists", IEE Proc.-I: Solid-State Electron Devices I. 130, 252–255 (1983).

[101] A. Gölzhäuser, W. Geyer, V. Stadler, W. Eck, M. Grunze, K. Edinger, T. Weimann, P. Hinze, "Nanoscale Patterning of Self-Assembled Monolayers with Electrons.", J. Vac. Sci. Technol. B. **18,** 3414 (2000).

[102] D. W. Carr, M. J. Lercel, C. S. Whelan, H. G. Craighead, K. Seshadri, D. L. Allara, "High-Selectivity Pattern Transfer Processes for Self-Assembled Monolayer Electron Beam Resists", J. Vac. Sci. Technol. A. **15,** 1446–1450 (1997).

[103] G. M. King, G. Schürmann, D. Branton, J. A. Golovchenko, "Nanometer Patterning with Ice", Nano Lett. **5,** 1157– 1160 (2005).

[104] J. A. Gardener, J. A. Golovchenko, "Ice-Assisted Electron Beam Lithography of Graphene." Nanotechnology **23,** 185302–185307 (2012).

[105] M. E. Bahlke, H. A. Mendoza, D. T. Ashall, A. S. Yin, M. A. Baldo, "Dry Lithography of Large-Area, Thin-Film Organic Semiconductors Using Frozen CO_2 Resists", Adv. Mater. **24,** 6136–6140 (2012).

[106] J. Zhang, C. Con and B. Cui, "Electron Beam Lithography on Irregular Surfaces Using an Evaporated Resist", ACS Nano **8,** 3483–3489 (2014).

[107] C. Con, J. Zhang and B. Cui, "Nanofabrication of high aspect ratio structures using evaporated resist containing metal", Nanotechnology **25,** 175301 (2014).

[108] G. Pennelli, M. Totaro, M. Piotto, "Selective Doping of Silicon Nanowires by Means of Electron Beam Stimulated Oxide Etching", Nano Lett. **12,** 1096–1101 (2012).

[109] L. Oria, A. Ruiz de Luzuriaga, J.A. Alduncin, F. Perez-Murano, "Polystyrene as a brush layer for directed self-assembly of block co-polymers", Microelectronic Engineering **110,** 234–240 235 (2013).

[110] J.-C. Gerbedoen, A. Aliane, A. Giguère, D. Drouin, R. Ares, V. Aimez, "All Evaporation Submicron Lift-off Lithography Process with Negative E-Beam QSR-5 Resist", Microelectron. Eng. **103,** 123–125 (2013).

[111] N. V. Francesco, R. K. Dey, R. Caputo and B. Cui, "Enhanced adhesion of electron beam resist by grafted monolayer PMMA brush" (submitted to J. Vac. Sci. Technol. B).

[112] R. A. Segalman, "Patterning with block copolymer thin films", material science and engineering R **48,** 191 (2005).

[113] B. H. Sohn and S. H. Yun, "Perpendicular lamellae induced at the interface of neutral self-assembled monolayers in thin diblock copolymer films", Polymer **43 (8),** 2507 (2002).

[114] R. K. Dey, B. Cui "Electron Beam Lithography with Feedback Using in-situ Self-Developed Resist," Nanoscale Res. Lett. **9 (1),** 1-6 (2014).

[115] A. Han, A. Kuan, J. Golovchenko, D. Branton, "Nanopatterning on nonplanar and fragile substrates with ice resists", Nano Lett. **12,** 1018–1021 (2012).

[116] M. Consales, A. Ricciardi, A. Crescitelli, E. Esposito, A. Cutolo, A. Cusano, "Lab-on-Fiber Technology: Toward Multifunctional Optical Nanoprobes", ACS Nano **6,** 3163–3170 (2012).

CHAPTER 3

Electron beam adjustment for electron beam lithography using self-developing resist

To a certain degree, conventional electron beam lithography is a "blind" process due to the lack of in-situ feedback. This chapter describes one method to see in-situ the exposed pattern on a test resist, before carrying out exposure on the real resist. Using such an in-situ feedback the electron beam adjustment can be optimized and thus one can be more certain that the time consuming and costly exposure on the real resist would generate the expected pattern. The key of the current approach is self-developing resist, for which the exposed test patterns can be examined by high magnification SEM right after exposure. This is in contrast to conventional resist that requires ex-situ development. We will demonstrate not only more accurate write field alignment, but also finer electron beam tuning within one large write field.

3.1. Introduction

Electron beam lithography (EBL) is undoubtedly the most popular nanolithography tool for nanofabrication. Typically the writing field (similar to viewing field in SEM) is on the order of one hundred micrometers, depending on the magnification. To expose larger patterns it requires electro-mechanical stage movement which should be very precise to obtain accurate alignment between writing fields. There are roughly three categories EBL systems: I) SEM (scanning electron microscope) added with beam blanker and hardware controller that is of low cost; II)

dedicated EBL (still based on SEM) with laser interferometer stage and height sensing that costs $1M; and III) fully automated EBL system with high energy column (100 keV) and dynamic compensation that costs much higher. It is generally considered that only the category III system is capable of large scale exposure. For the category II systems, in principle it can also be used for large scale writing. However, compared to the category III systems, there are three major limitations: 1) the stage movement and focus adjustment is slower; 2) the beam is not optimized except near the central region of each write field because there is no dynamic compensation, leading to distorted and large beam away from the center of each write field and 3) large stitching error between write-fields due to misalignment of those. The exposure speed is limited by the scanning speed of a system, or the response speed of beam deflectors. Here, our goal is to overcome these limitations so that researchers would be able to use the category II tools for large scale writing. For category I tools, this method will also be useful for fine adjustment of electron beam within a large write field, though obviously the stitching error will still be large due to the lack of laser interferometer stage.

For a fixed pattern area, apparently the time spent for stage movement and focus adjustment is inversely proportional to the square of the write field size. Here we propose to use in-situ feedback to enable large write fields (in-situ is important as otherwise the electron column condition would be different if one has to turn off the tool to take out the exposed sample for development).

The in-situ feedback will be realized by using a *self-developing* resist, so one can see in-situ by SEM the pattern right after exposure (since no need of development) using magnification much higher than that used during exposure. Here, self-developing resist is defined as a material which volatilizes during exposure to radiation, eliminating the necessity for a following ex-situ wet or dry development. Geis et al.[1] first reported nitrocellulose as a self-developing resist with submicrometer resolution and processing stability.

In the following, we will present two types of e-beam adjustment ((2) and (3) above) using self-developing resist.

3.2. Electron beam lithography with feedback using in-situ self-developed resist

[This work is published in Nanoscale Research Letters 9 (1), 184 (2014)]

For a large writing field, more patterns can be exposed within the field, which can reduce field stitching errors and leads to higher scanning speed and shorter writing time, thus increasing the throughput. Typically the beam is optimized (stigmation compensated and well focused) at high magnification (e.g. 100,000×), so only the central spot of the write field is optimized to attain a beam spot size of <5 nm. Therefore, the farther away from the central region, the larger beam-spot distortion (due to stigmation) and size (due to stigmation and out of focus). On the other hand, for vast majority applications, the minimum feature size is, say 20 nm, so it is not necessary to have the beam spot size of <5 nm in the central region. To optimize the beam globally, our idea is thus to write dot/line arrays at different locations, examine them using SEM at high magnification, modify the stigmation and working distance (focus) parameters, repeat the task until we achieve a relatively uniform shape/size distribution of the dots/lines across the entire write field. That is, when the beam is optimized this way, the beam spot is considerably smaller than normal beam adjustment near the corner regions at the cost of larger spot than normal beam adjustment at the central region.

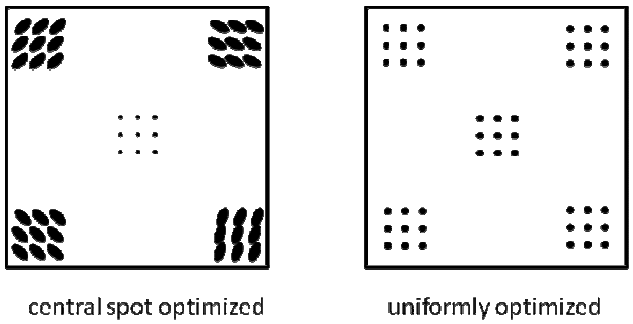

Figure 3.1. Beam spot optimization: (a) Central spot optimized, (b) Globally optimized.

Figure 3.1 shows the schematic showing two schemes of beam spot optimization. In normal adjustment, the beam at center is optimized at high magnification, leading to a typically sub-5 nm

beam spot size but much larger with distortion farther away from the center. In our method, the beam is optimized globally using in-situ feedback, leading to relatively uniform beam size/shape distribution (e.g. ~20 nm everywhere).

3.2.1. Introduction

Electron beam lithography (EBL) is the most popular nanolithography method for research and device prototyping. Due to its much lower cost, most EBL systems for academic research are based on scanning electron microscope (SEM) without dynamic compensation. For such systems, the beam is typically optimized (stigmation compensated and well focused) at high magnification (e.g. 100,000×), so only the central spot of the writing field is optimized to attain a beam spot size of a few nanometers. At a distance farther away from the center, the beam spot is larger due to beam distortion and deterioration of focus. Due to the lack of in-situ feedback, conventional EBL is a "blind" open-loop process where the exposed pattern is examined only after ex-situ resist development, which is too late for any improvement. Therefore, it is highly desirable to examine in-situ the electron beam and optimize it before the time-consuming exposure of large area pattern. This is particularly important for exposing large area patterns that, in order to keep a reasonable exposure time, necessitates a large writing field and high beam current, which both magnify the issue of beam enlargement and distortion near the writing field corners. For instance, to expose a $(1\ \text{cm})^2$ area with a writing field of $(100\ \mu\text{m})^2$ using the Raith 150^{TWO} system, the total time for stage movement (10^4 movements to expose the 10^4 writing fields) would be 40000 s (11 hours) for a stage movement time between adjacent writing fields of 4 s. Obviously the larger the pattern area is, the more significant the use of a large writing field is, though at the cost of reduced resolution. Furthermore, if all the structures for a device can be put inside one large writing field, the stitching error between the structures would be eliminated. Previously in-situ feedback on electron beam drift based on imaging a mark or a grid pre-patterned on the substrate was reported[2,3,4], but no in-situ feedback on electron beam spot size has been demonstrated.

Here we propose to use self-developing resist, for which the exposed pattern shows up right upon exposure without an extra development step, as in-situ feedback for the first time. With this

closed-loop process, the beam spot can be optimized globally across an entire writing field, such that the beam spot size is evenly distributed. That is, the optimized beam spot size will be larger at the writing field center than obtained using conventional beam adjustment procedure, but much smaller near the writing field corners, thus allowing reasonably high resolution patterning across the entire large writing field. Our procedure involves first writing test patterns in the self-developing resist at the center and corners within the writing field, analyzing them using SEM at high magnification, adjusting the electron beam (notably working distance and stigmation), and repeating the task till achieving a relatively uniform shape/size distribution across the entire writing field. Afterwards, under the same optimized beam condition, the exposure will be carried out to pattern the device using normal high performance resist like PMMA. It is noted that here in-situ optimization is important as otherwise the electron column condition would be different if one has to turn off the system to take out the exposed sample for ex-situ development to examine the beam spot size at different locations.

The in-situ feedback is provided by self-developing resist, for which the exposed test pattern shows up and can be examined right after exposure by SEM at high magnification. This is in contrast to conventional resist that requires ex-situ development using solvent or aqueous developer. Self-developing electron or ion-beam resists had been extensively studied in the 1980s. For instance, metal halides such as AlF_3 is decomposed to form volatile fluorine gas upon electron beam exposure, thus it behaves as a positive self-developing resist[5,6,7,8,9]. Similarly, nitrocellulose is decomposed upon exposure to electron or ion beam, thus it is also a positive self-developing resist[10,11,12,13]. However, those self-developing resists are nearly forgotten by the EBL community after their discovery. We believe this is because the metal halide resists suffer from extremely low sensitivity and inability to expose arbitrary structure other than very thin line and dot patterns since the decomposition product of metallic halide cannot migrate far away from the directly exposed area; whereas nitrocellulose resist always leave behind a thick non-volatile residual layer. In fact, nitrocellulose was mostly used as an ion beam resist for which the residual layer is thinner because physical bombardment by ion beam can help remove the non-volatile species[14]. Though metal halides offer extremely high resolution, the film is found to be degraded by humidity after long (several weeks) exposure to air. More recently, ice and frozen carbon

dioxide were shown to behave as an electron beam resist without the need of a development step[15,16,17,18]. However they both require significant modification of the EBL system to maintain a low temperature, which greatly limits their application. Lastly, PMMA and ZEP resists have also demonstrated self-developing behavior; yet the resist thickness reduction due to over-exposure at ~15× normal clearance dose was less than 30% of the original film thickness if without ex-situ post-exposure thermal annealing[19]. Therefore, here we have chosen nitrocellulose for the purpose of in-situ feedback. As expected, it behaves like a positive resist since e-beam exposure can also generate secondary electrons to decompose the resist, as ion-beam does; and the amount of residual layer is significant. However, a thick residual layer, though undesirable since it lowers SEM imaging contrast, is acceptable for the purpose of in-situ feedback. Interestingly, nitrocellulose was also found to be developable using a solvent developer to give a mixed positive and negative tone behavior.

3.2.2. Exposure properties of nitrocellulose with and without ex-situ development

As purchased nitrocellulose (Sigma-Aldrich) was further diluted with pentyl acetate at 1:1 volume ratio, which gave a film thickness of 300 nm by spin-coating. The film was then baked at 80 ^{o}C for 5 min to drive away the solvent. To obtain the contrast curve of the nitrocellulose resist, we exposed an array of large squares each with 5 μm by 5 μm at 20 keV with exponentially increasing doses using a Raith 150^{TWO} electron-beam lithography system. As a self-developing resist, nitrocellulose displays a positive tone right after exposure. It is also interesting to investigate whether the exposed resist can be developed using a solvent, for which we tried to develop the resist using pentyl acetate and observed a mixture of positive and negative tone behavior. The contrast curves with and without solvent development were measured using atomic force microscope (AFM), with the film thickness measured by Dektak profilometer. For the case with solvent development, the development time was long enough to remove all the resist in the unexposed area. In the contrast curves, the remaining resist thickness was normalized to the film thickness after spin-coating and baking. In order to investigate the high resolution

capability of nitrocellulose resist, periodic line array with period of 600 nm was exposed at 20 keV over a broad line dose range, and subsequently coated with 30 nm Cr for SEM imaging.

Figure 3.2 shows the contrast curves for nitrocellulose exposed at 20 keV without ex-situ development (Figure 3.2a) and with pentyl acetate development for 60 sec (Figure 3.2b). As expected, for both cases a thick residual layer of nearly ~20% of original film thickness was left behind even at very high exposure doses. Consequently, nitrocellulose is not a useful electron beam resist for pattern transfer purpose; but it is acceptable for the purpose of providing in-situ feedback for electron beam lithography. As a self-developing resist, the sensitivity is about 2000 $\mu C/cm^2$. The sensitivity is about 10 times lower than PMMA (clearing dose ~200 $\mu C/cm^2$ at 20 keV), but again this is not a serious drawback for our purpose since the time to expose the test pattern is short enough. As for the contrast, one cannot derive a meaningful value from the contrast curve, yet clearly the nitrocellulose resist has a low contrast, which makes it unsuitable for exposing high resolution dense pattern. Nonetheless, it is capable of delineating high resolution sparse pattern for which proximity effect is insignificant, as seen in figure 3.3a that shows a resolution down to 15 nm. Actually another very low contrast resist SU-8 has also achieved a high resolution of 24 nm[20].

After additional solvent development, the contrast curve (Figure 3.2b) shows a mixed behavior, rather than a simple positive or negative tone behavior. At very low exposure doses, since the unexposed resist is soluble in pentyl acetate developer whereas electron beam exposure decomposed the resist to generate less soluble decomposition product, the resist exhibited a negative tone. At higher doses, on one hand, the resist was increasingly decomposed and vaporized with increasing doses, which led to the tendency of positive tone; on the other hand, as the degree of decomposition increased, the decomposition product became less soluble in the solvent developer, resulting in the tendency of negative tone after solvent development. As a consequence of those two competing trends, there exists a turning point exposure dose (~1200 $\mu C/cm^2$) that gave a maximum remaining thickness. Such an exposure behavior can lead to complex structure as shown in figure 3.3b, which is due to proximity exposure at the surrounding area beyond the directly exposed area. In fact, such kind of mixed exposure property is well

known for long time for PMMA that displays a positive tone at low doses, and becomes negative tone at ~10× higher doses[21], which was also employed to generate complex structures[22]. Though less known, another popular resist ZEP-520A actually also exhibits a mixed tone behavior just like PMMA[23]. However, unlike PMMA and ZEP for which negative tone behavior appears only after roughly 10× higher doses, for nitrocellulose the negative tone behavior proceeds the positive tone, and the dose ranges for the two tones have a large overlap and thus they are not clearly separated.

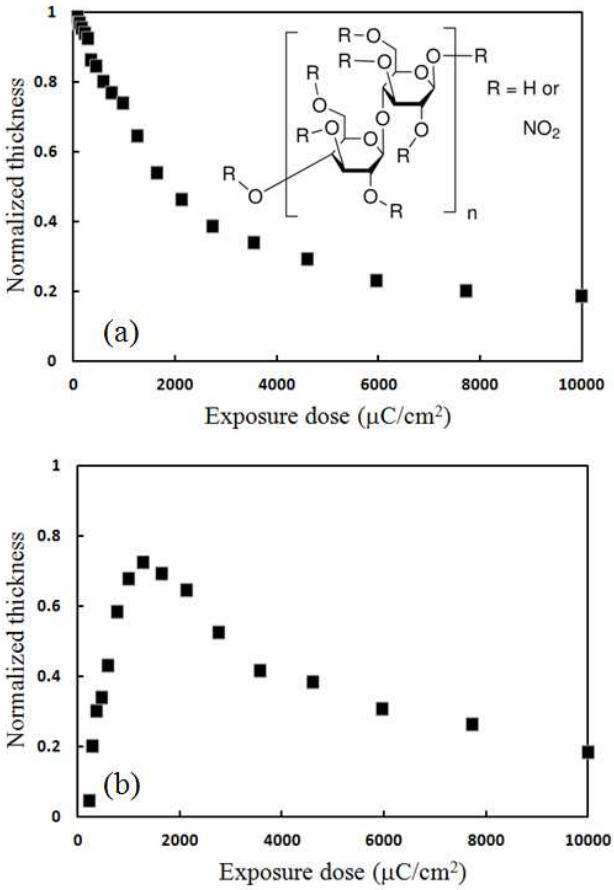

Figure 3.2. Contrast curves for nitrocellulose. Exposure at 20 keV without ex-situ development (a), and with 60 sec development in pentyl acetate (b). The inset in (a) shows the chemical structure of nitrocellulose.

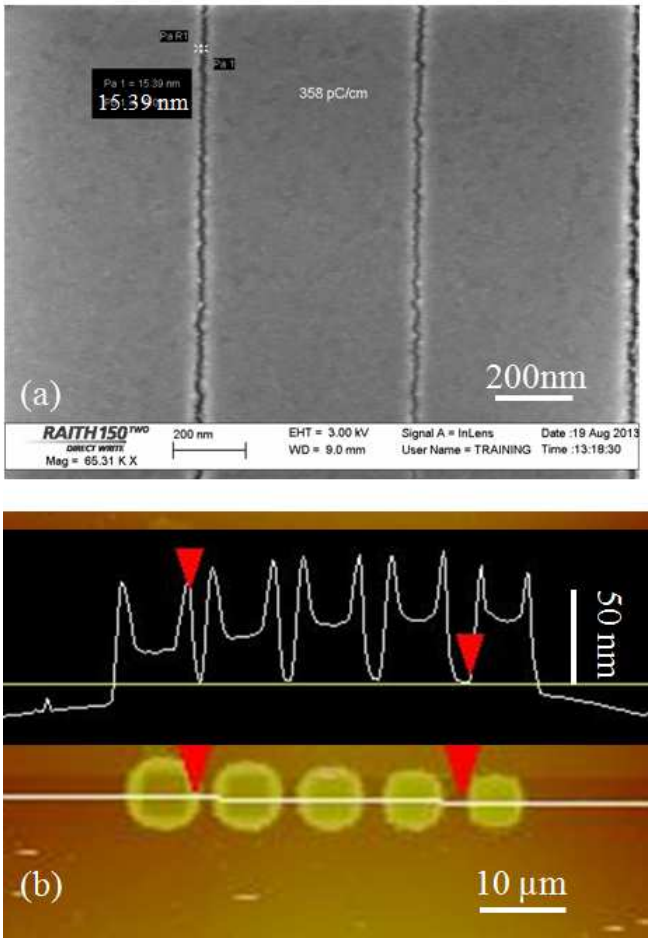

Figure 3.3. SEM and AFM images of structures in nitrocellulose. (a) SEM image of line array exposed in nitrocellulose without ex-situ development, showing a line-width of 15 nm. (b) AFM image and cross-section of complex microstructure exposed in nitrocellulose after ex-situ solvent development.

3.2.3. E-beam working distance optimization using nitrocellulose resist

For electron beam optimization across a large writing field, we first followed the standard process to adjust the beam at high magnification of 50000×. Then we exposed, with exponentially increasing line doses of 30-500 nC/cm for nitrocellulose, the test pattern containing five identical designs at the writing field center and four corners, respectively. Here a large writing field of 1 mm × 1 mm obtained at a low magnification of 100× was chosen. Afterwards we examined the exposed pattern at high magnification, which naturally revealed a well defined

structure at the writing field center, but poorly defined ones at the corners. This is because, when the center is well focused, the corners are actually greatly defocused because the distance from the electron objective lens to the corner is longer than to the center. Next, the same procedure was repeated at a new location, but with an increased working distance value (the working distance value was entered manually, without physically raising or lowering the stage). At this increased working distance value, the writing field center will be defocused, but the corners will become less defocused. In principle the stigmation values can also be finely tuned, but here we focus our effort on optimizing the working distance. After several iterations, similar exposed line widths were observed at the writing field center and corners, which suggests that an optimal working distance was achieved to give a relatively uniform exposed pattern across the entire writing field. To verify the effectiveness of our method, under the optimal exposure parameters, we exposed the high resolution resist PMMA (100 nm thickness, coated on silicon that was mounted besides the wafer coated with nitrocellulose) at line dose of 400 - 3300 pC/cm. Note that the optimal exposure parameters remain valid as long as the aperture size (that determines the depth of focus, as well as beam current) and working distance remain the same (if the sample is at a height level different from the nitrocellulose film, the stage can be raised/lowered to obtain roughly the same working distance). After development using the standard developer MIBK:IPA (1:3) for 40 sec, the pattern was coated with 10 nm Cr and examined by SEM.

Figure 3.4a illustrates the pattern design within the 1 mm $\times$ 1 mm writing field that consists of five identical wheel-structure array at the center and four corners, respectively, with the inset showing the wheel-structure array having exponentially increasing line doses from the upper left to the lower right wheel. A broad range of exposure dose is critical because, a relatively low dose is needed to reveal the high resolution capability when the beam is well focused, yet a high dose is essential to self-develop the resist to a certain visible depth when the beam is seriously enlarged. The wheel design is advantageous as it contains lines along various directions, which ensures that some lines (those roughly along the beam spot elongation direction when there is severe astigmatism) would be adequately self-developed to become visible under SEM.

Figure 3.4b-c show two wheel structures at the center and corner, respectively, when the electron beam was well focused at the writing field center with a working distance of 8 mm. As expected, the center wheel (50 nm wide line at dose 34 nC/cm) was well defined, whereas the corner one (315 nm wide line at dose 34 nC/cm, developed to a small depth) was seriously blurred. Here the SEM image has a low contrast, which is because of the low yield of secondary electrons for the polymer resist at 20 kV (the imaging acceleration voltage has to be the same as the exposure voltage in order to maintain a consistent electron column condition). The contrast could be improved by coating the resist with a thin metal island film that allows vaporization of the decomposed resist through the island film. After several iterations with increasing working distance values, we achieved relatively uniform pattern definition at a defocus value of 37 μm (i.e. working distance 8.037 mm), as shown in figure 3.4d-e for the two wheel structures at the center and corner, respectively. As a simple estimation, the distance from the electron object lens to the writing field center is 8 mm, whereas that from the lens to the writing field corner is $(8^2+0.5^2+0.5^2)^{1/2}$ = 8.031 mm, or 31 μm farther than to the writing field center, which is in the same order as our optimal defocus value. Clearly the optimal defocus value and the degree of improvement using our method depend on the depth of focus, which is inversely proportional to the aperture size and proportional to the working distance. Our approach would be less effective when the depth of focus is high that leads to less beam broadening and distortion at writing field corners. However, high depth of focus means either the aperture size is small that results in long exposure time because beam current is roughly proportional to the square of aperture size, and/or the working distance is large that makes the exposure more susceptible to electromagnetic and vibrational noise.

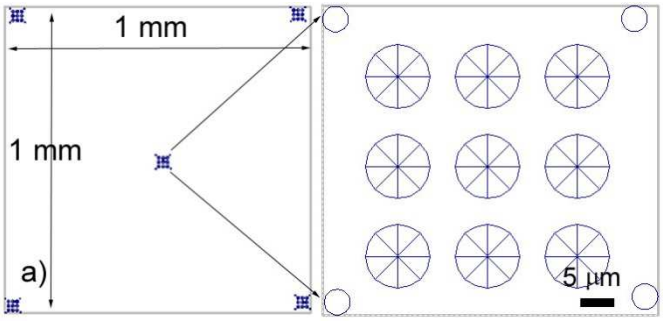

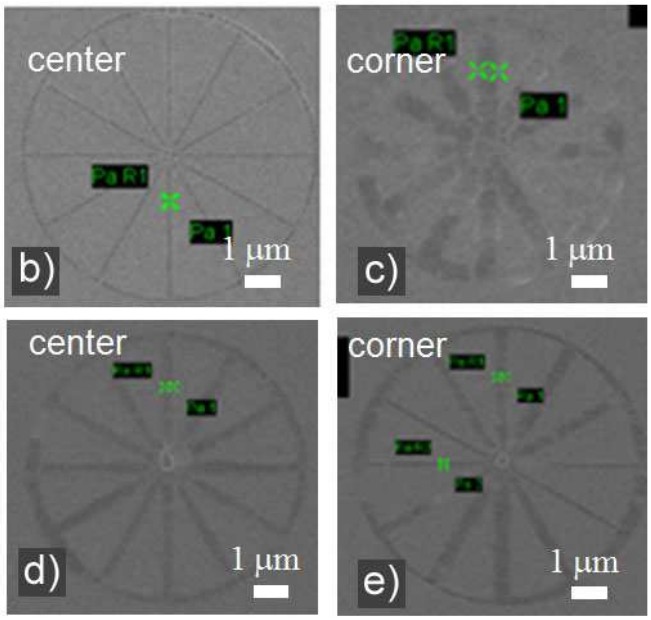

Figure 1.4. CAD pattern design and structures exposed in nitrocellulose. (a) The CAD pattern design consisting of five identical wheel array structures (see right side for zoom-in view) at the 1 mm × 1 mm writing field center and four corners. (b-c) One particular wheel structure exposed in nitrocellulose at the center (b) and corner (c) without beam optimization by defocusing. (d-e) One wheel structure at the center (d) and corner (e) with beam optimization by defocusing of 37 μm.

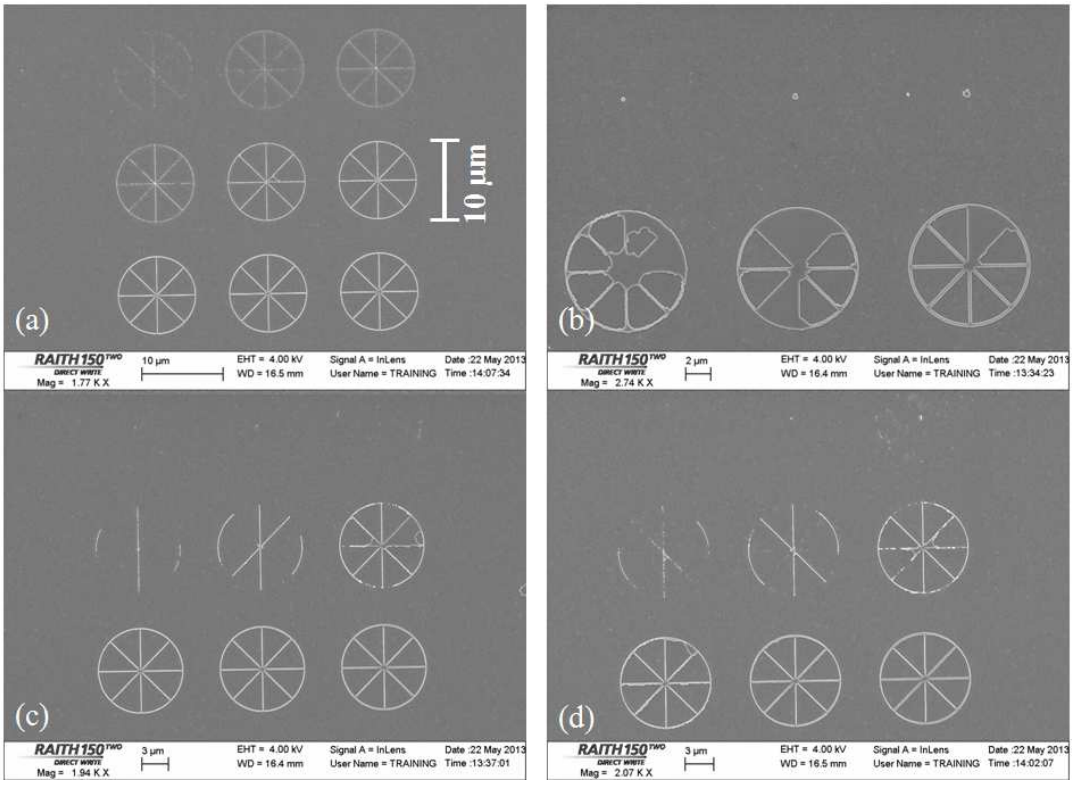

Figure 3.5. Cr pattern created by electron beam lithography with PMMA resist followed by a liftoff process. (a-b) Wheel array at writing field center (a) and corner (b) exposed without beam optimization by defocus. (c-d) Wheel array at writing field center (c) and corner (d) exposed with beam optimization using self-developing nitrocellulose resist. The exposure dose increases from top left to the lower right wheel structure.

To verify the optimal beam adjustment, under same exposure condition with and without a defocus of 37 µm, we exposed PMMA at a dose range appropriate for PMMA and carried out a standard liftoff process of 10 nm Cr. Figure 3.5 shows the resulted wheel array pattern in Cr. Table 3.1 listed the Cr line width at different doses and positions within the writing field, with and without beam optimization by defocusing. When the dose is low and/or the beam is greatly broadened, the resist was not developed to bottom, leading to no pattern after Cr liftoff. As expected, without defocus, the minimum line width at the writing field corner is 210 nm; with optimal defocus, fairly high resolution of about 80 nm was obtained across the entire writing field size of 1 mm × 1 mm.

Table 3.1. The resulting Cr line-width as a function of exposure dose with or without beam optimization by defocusing at writing field center and corner.

Line dose (nC/cm)	Well-focused at center (nm)	Well-focused at corner (nm)	De-focused at center (nm)	De-focused at corner (nm)
0.4	42	Resist not developed to bottom due to beam broadening at the writing field corner, thus no Cr pattern after liftoff.	Resist not developed to bottom.	Resist not developed to bottom.
0.56	43			
0.79	47			
1.10	51		78	84
1.15	62		89	91
2.15	70		120	128
3.01	91	210	127	138
4.21	108	251	146	152
5.90	117	272	167	172

3.2.4. Conclusions

Here we studied the exposure properties of nitrocellulose resist and its application as in-situ feedback for electron beam optimization in electron beam lithography. It was found that, as a self-developing resist, nitrocellulose showed low sensitivity and low contrast, making it unsuitable for patterning high resolution dense features. Nevertheless, it achieved 15 nm resolution for sparse pattern where proximity effect is insignificant. In addition to self-developing, nitrocellulose resist can also be developed using a solvent that displayed a mixed tone behavior - negative tone for low doses and positive for high doses. Using nitrocellulose as in-situ feedback to optimize the electron beam (notably working distance) across a large writing field of 1 mm × 1 mm, we achieved ~80 nm resolution across the entire wring field, as compared to 210 nm (occurred at the writing field corners) without the beam optimization process. This approach is most efficient in reducing the writing time for large writing field size such as 1 mm × 1 mm as needed for large area exposure of moderate resolution pattern.

3.3. Stitching error reduction in electron beam lithography with in-situ feedback using self-developing resist

[This work is published in J. Vac. Sci. Technol. B, 31, 06F409 (2013)]

In electron beam lithography (EBL), a large area pattern is divided into smaller writing fields, which are then stitched together by stage movement to generate the large area pattern. Precise stage movement is essential to minimize the stitching error, and this can be achieved by using laser interferometer-controlled stage. In addition, electron beam deflection must be adjusted to match the stage movement, which is referred to as "writing field alignment". To expose large area nanostructures, a large writing field must be used, otherwise the stage movement time would be impractically long. However, writing field alignment accuracy decreases with a larger writing field owing to its low magnification. To examine the write field alignment, here we will write the dots/lines near the boundaries of each write field on the self-developing resist, as shown in figure. 3.6. Using SEM at high magnification, if we see, for instance, that the two central dots/lines are more separated than the rest, then we know that there is a gap between the two write fields and the zoom factor should be increased. Similarly, by writing an array of 3 by 3 fields (each with dot/line array pattern) near the four boundaries of each write field, one can adjust other write field alignment parameters such as rotation. After several iterations, it is expected that the write field alignment gets better and thus stitching error is to be minimized.

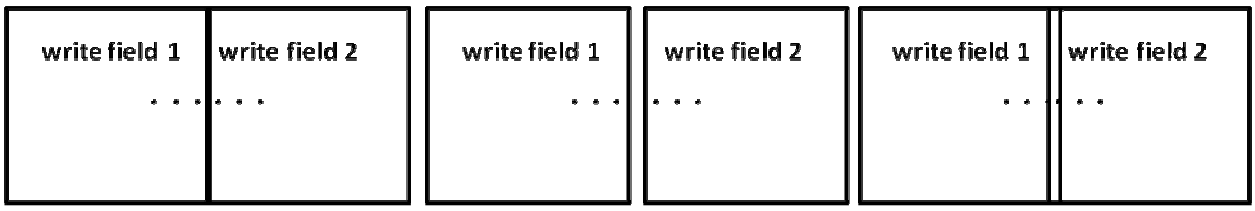

(Well aligned) (Gap) (Overlap)

Figure 3.6. Write field alignment with in-situ feedback. The small dots are exposed in a self-developing resist, whose relative location reveals the alignment accuracy.

3.3.1. Introduction

Electron beam lithography (EBL) is the most popular nanolithography method for research, prototyping and low volume production. The EBL system has a limited area of exposure (writing field), and the large pattern is divided into many writing fields exposed side by side with stage movement between each field exposure. The deviation from perfect alignment between consecutive writing fields is called stitching error. Due to the lack of in-situ feedback, conventional EBL is a "blind" open-loop process where the exposed pattern is examined only after ex-situ resist development, which is too late for any improvement. It is thus highly desirable to detect and correct the errors in-situ before the lengthy exposure of the designed pattern. This method can be used to detect misalignment between adjacent writing fields, as well as distorted or enlarged beam spot due to defocus and stigmation. With this closed-loop process, the beam spot can be optimized globally across an entire writing field[24], and the stitching error can be minimized. The former application has been detailed in the previous section. In this section we will demonstrate substantial reduction of stitching error when using a very large writing field as needed for fast writing.

There are roughly four types of stitching errors as summarized by Bogdanov et al.[25]: shift error, field distortion (negligible when the e-beam column is well adjusted), field rotation and deflector scale error, as shown in figure 3.7. These stitching errors can be categorized as stochastic and systematic errors. The shift error is caused by the stage movement and is stochastic, and its amplitude depends on the precision of the laser interferometer stage. The deflector scale (zoom) error and rotation error are caused by imperfect calibration of the writing field size and rotation relative to stage travel, respectively. They are equal at every writing field border and are thus systematic. Previously, various methods have been demonstrated to minimize the stitching error. Multiple (e.g. 4) exposures, each at reduced dose (e.g. 1/4×) with shifted boundaries or different writing field sizes, can be used to average the stage positioning and decrease the shift error [26, 27, 28]. Spatial-phase-locked EBL, in which all writing is done with reference to a grid having long-range spatial-phase coherence that provides feedback on beam location, gives the most accurate field stitching, but with the expense of extra process steps to fabricate the grid using interference

lithography[29]. Another method to eliminate stitching error is fixed-beam-moving-stage writing that is available for some EBL tools such as the Raith 150 [30]. However, it is effective only for thin or wide line patterns such as a long optical waveguide.

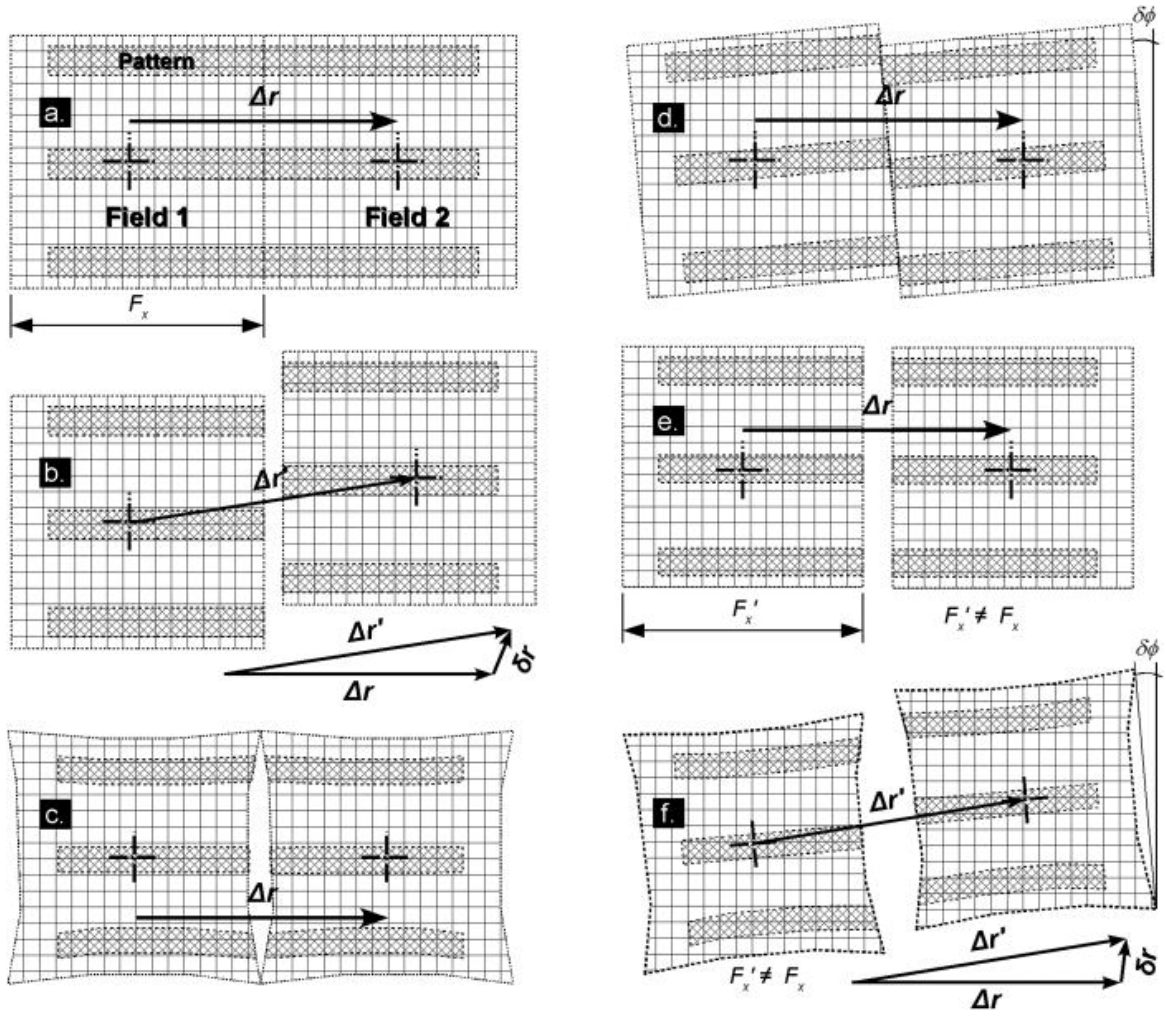

Figure 3.7. Types of field stitching errors[25]: (a) ideal case, (b) shift error, (c) field distortion, (d) field rotation, (e) deflector scale error, and (f) combined error (includes all types of errors).

Unlike the multiple exposure approach for minimizing the effect of *stochastic* stitching error, our method aims to reduce the *systematic* stitching error. It is relatively straightforward as it doesn't require the modification of exposure software or the pre-patterning of the wafer with alignment marks. In the process, the writing field is first aligned relative to stage travel, and then a test pattern is exposed in the self-developing resist near the boundary of each writing field with a minimum of two writing fields exposed next to each other. Next, the exposed pattern at the

border of two consecutive writing fields is examined at high magnification, which provides feedback to adjust the writing field alignment parameters (zoom and rotation values for the Raith 150^{TWO} tool). The same procedure is repeated until an acceptable stitching error is obtained.

Obviously, this method cannot be applied to the state-of-art dedicated EBL tool for which e-beam adjustment and writing field alignment are fully automatic. However, such tools are less accessible and more costly. Our method is also not effective for small writing fields such as 100 µm where the random stage movement error (40 nm for the Raith 150^{TWO} tool) would dominate the stitching error for experienced operators. Nevertheless, it may be used as a means to confirm the accurate writing field alignment. This method is most effective for large writing fields such as 500 µm and above, where accurate writing field alignment is challenging due to the low magnification needed for a large writing field. A large writing field is essential if the tool is used to expose large patterns since the time for stage movement is inversely proportional to the *square* of the writing field size. For instance, the total stage movement time would reach 40000 sec for a pattern of 1 cm^2 at 100 µm writing field size using the Raith EBL tool.

3.3.2. Experimental procedure

For the Raith EBL system, there is a standard procedure for the writing field alignment. The laser interference stage movement accuracy is 40 nm, which sets the upper limit of writing field alignment accuracy. Basically, the alignment procedure is to calibrate the beam deflection against the stage movement that is assumed to be absolutely accurate (i.e. ignore the 40 nm random error). In the process, a feature such as a sharp corner of a dust particle is first identified, then the stage is moved by a pre-defined distance along a certain direction, and the beam is deflected to that position to capture an image of the identified feature. This procedure is repeated for a total of four stage movements along four directions. The locations of the feature within the four images are used to generate the transformation matrix to match the beam deflection with stage movement across the entire writing field. The basic alignment principle for other typical EBL system should be similar. The achievable alignment accuracy obviously depends on the magnification that is determined by the writing field size, as well as on the skill of the operator. After completing this standard alignment procedure, a line array pattern with 500 nm pitch was

exposed in the self-developing resist near each writing field boundary at a dose of 22 nC/cm. Next, the exposed pattern was examined at high magnification (e.g. 4000×, versus 100× as determined for the writing field size of 1 mm), which revealed in a “fool-proof” manner, the magnitude of the stitching error. The measured magnitudes of the stitching error along the horizontal and vertical directions were then used to correct the zoom (deflector scale) and rotation value, according to the simple formula shown in figure 3.8 caption. The steps of resist exposure, SEM measurement and zoom/rotation value adjustment were repeated until a satisfactory stitching error was obtained.

Once acceptable stitching was achieved, using the same zoom and rotation value, we carried out exposure of a regular resist PMMA at line dose of 2.0 – 3.4 nC/cm, followed by development using MIBK:IPA (1:3) for 40 sec. Finally, 10 nm Cr was evaporated and lifted off, and the Cr pattern was examined by SEM in order to verify the effectiveness of our method.

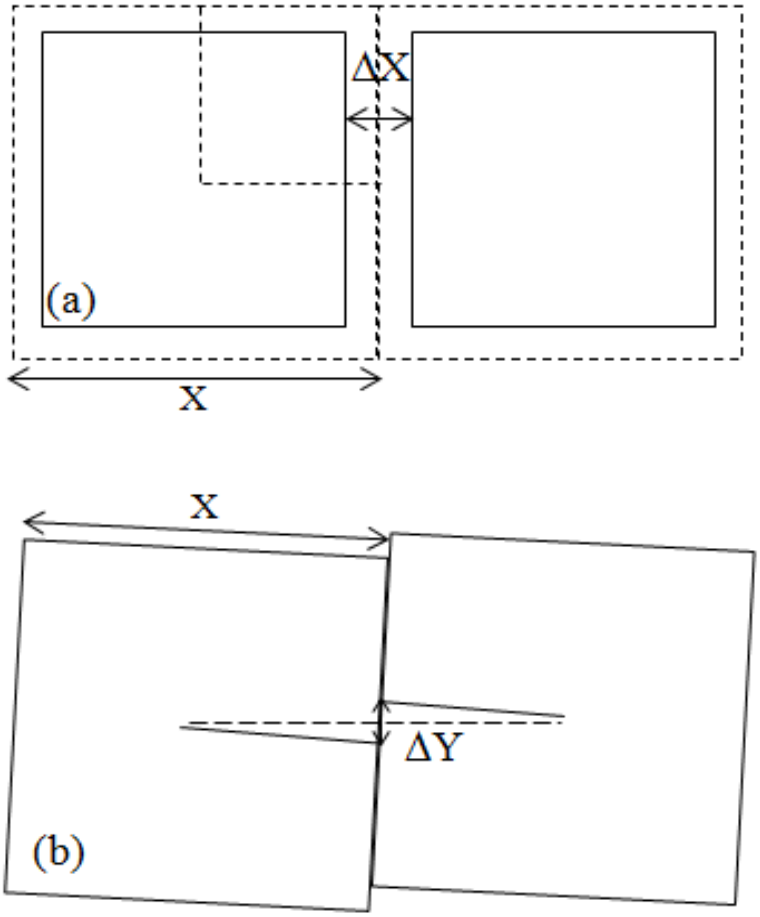

Figure 3.8. Schematic showing the adjustment of zoom and rotation value. (a) If the gap or overlap between two adjacent writing fields is ΔX, then the zoom value should be adjusted by a factor of ΔX/X. (b) If misalignment along the vertical direction is ΔY, then the rotation value should be adjusted by $\Delta\theta = \tan^{-1}[(\Delta Y/2)/(X/2)] = \tan^{-1}(\Delta Y/X)$ degree.

3.3.3. Stitching error minimization using nitrocellulose resist

As stated before, the sensitivity for nitrocellulose is approximately 2000 $\mu C/cm^2$ which is approximately 10 times lower than PMMA, but again this is not a serious drawback for our purpose since the time to expose the line arrays near the writing field boundary is very short (~10 sec at 0.1 nA beam current). On the other hand, the sensitivity is approximately few orders higher than metal halide self-developing resist, for which one must design fewer and shorter lines at the

writing field boundary if it were to be used for the same purpose. For the current application, the relative location of the lines exposed at the writing field boundary is more important than their width or array periodicity, so in principle, a low contrast resist can be used to provide accurate feedback on stitching error. However, a low-contrast resist results in a sloped profile for the exposed trenches, which, combined with the low yield of secondary electrons for polymers, leads to reduced SEM imaging contrast at high magnification.

Figure 3.9 shows the CAD pattern design (a) and SEM images of the exposed pattern in nitrocellulose with large stitching error (b), and negligible stitching error after several iterations using the aforementioned procedure (c). Here the writing field size is 1 mm, one order higher than the typical value for high resolution exposure. The pattern consists of 20 periodic lines near the writing field edges with a pitch of 500 nm and length of 10 μm. The distance between the outmost line and the writing field edge is 250 nm, so, when perfectly stitched, the gap between the two outmost lines on the two adjacent writing fields should be 500 nm that is equal to the array pitch. In addition, a horizontal line that is 1 μm above/below the lower/upper end of the vertical lines is designed to connect (group) the 20 vertical periodic lines, in order to tell whether a particular vertical line belongs to the writing field at the left side or the right. This pattern design is not optimized, but is enough to serve our purpose. The SEM images (Figure 3.9b-c) have a low contrast because nitrocellulose resist has a low contrast that leads to non-vertical profile; and, in order to keep the electron column condition unchanged, the images were taken at the same high acceleration voltage (20 kV) as for lithography, which gives low secondary electron yield. Imaging at higher magnification showed little improvement because the resist pattern was degraded rapidly during the scanning. One potential solution to this issue is by coating an island film (e.g. Ag or In island film that allows decomposed component to escape) that has much higher secondary electron yield than the polymer resist. It would then be possible to detect misalignment of substantially lower than 50 nm.

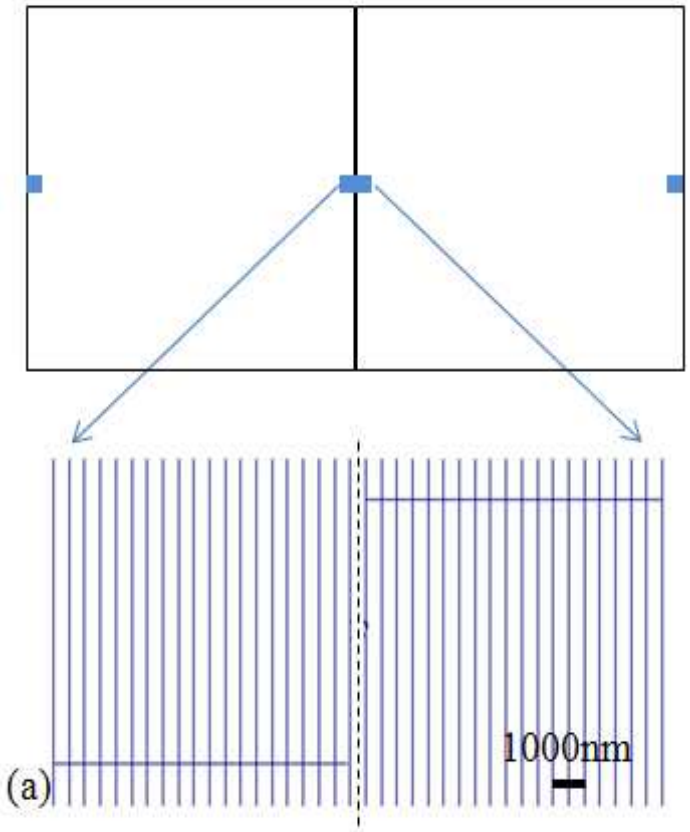
1000nm
(a)

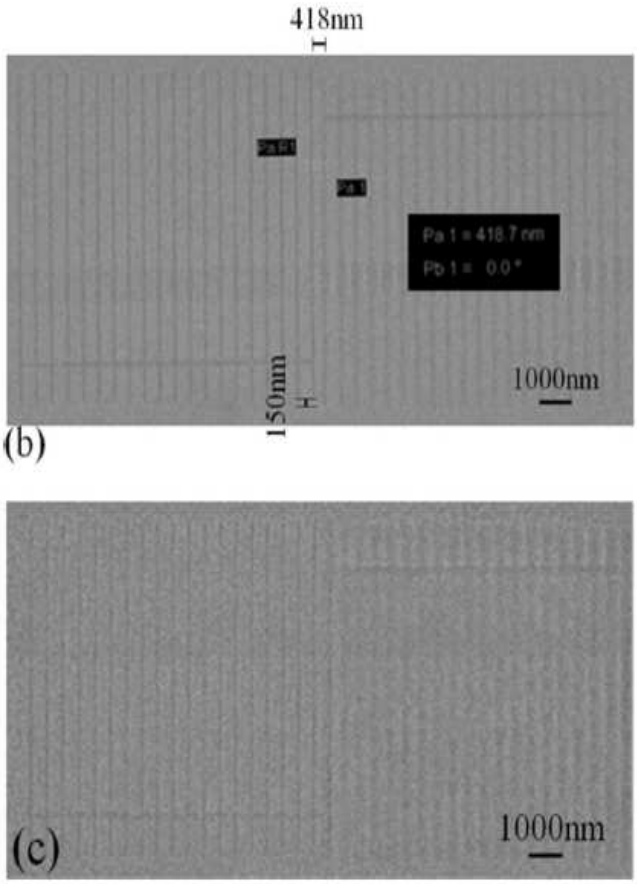

Figure 3.9. (a) The pattern design at the writing field boundary; (b) SEM image of a pattern exposed in nitrocellulose at the boundary of two adjacent writing fields, showing significant misalignment of 82 nm and 150 nm along X and Y directions, respectively; (c) SEM image of the exposed pattern showing negligible (<50 nm) misalignment.

Using only the standard writing field alignment procedure, the stitching is stochastic and the error can sometimes reach a high value, depending on the skill of the operator. We achieved an average stitching error (=sqrt[$(\Delta x)^2+(\Delta y)^2$]) of 543 nm with a standard deviation of 334 nm. This large stitching error is not due to the beam drift relative to the stage, since the drift for the Raith 150^{TWO} system was found to be only ~1 nm/min and the total beam drift would be negligible during the exposure of the test patterns. This large error is partly due to the greatly distorted and enlarged electron beam spot at locations far away from writing field center where small imaging "windows" were opened during writing field alignment procedure. This beam spot distortion can be reduced by defocusing (manually increasing working distance) under the feedback of self-

developing resist that described in the previous section. Figure 3.9b shows an error of 82 nm overlap along the horizontal direction that indicates too high a zoom value, and an error of ~150 nm shift along the vertical direction that indicates a counter clockwise rotation error. After writing field alignment optimization using the self-developing resist, we obtained nearly perfect alignment, as shown in Figure 3.9c, with an error of less than 50 nm in both directions. Under this condition, the same pattern was exposed in PMMA but at a different line dose matching PMMA resist's sensitivity, followed by ex-situ development and Cr liftoff. Figure 3.10 shows a SEM image of Cr line array pattern across two adjacent writing fields, which again confirmed the nearly perfect alignment.

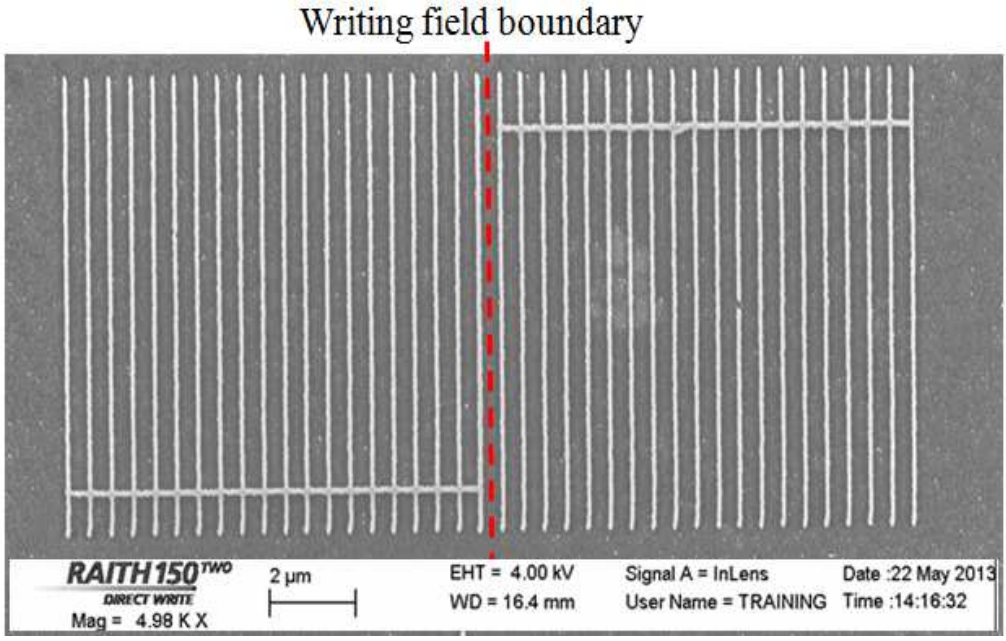

Figure 3.10. SEM image of Cr line array pattern across two adjacent writing fields using optimal zoom and rotation values for writing field alignment, showing negligible stitching error.

3.3.4. Conclusions

We here reported a self-developing resist (nitrocellulose) can be used very effectively to optimize writing field alignment. In the process, we first exposed a test pattern in nitrocellulose resist near the writing field boundary, and then examined the pattern at high magnification, which provided feedback on the writing field alignment accuracy. Based on such feedback, the parameters for

writing field alignment (notably zoom and rotation values for the Raith 150^{TWO} tool) were adjusted accordingly. After several iterations, we were able to reproducibly achieve nearly perfect (<50 nm stitching error) writing field alignment with a very large (1 mm^2) writing field size.

3.4. References

[1] M. W. Geis, J. N. Randall, T. F. Deutsch, N. N. Efremow, J. P. Donnelly, and J. D. Woodhouse, "Nitrocellulose as a self-developing resist with submicrometer resolution and processing stability", J. Vac. Sci. Technol. B **1**, 1178 (1983).

[2] Y. H. Kuo, C. J. Wu, F. T. Kuo, J. Y. Yen and Y. Y. Chen, "Image based in situ electron-beam drift detection by silicon photodiodes in scanning-electron microscopy and an electron-beam lithography system", Microelectron Eng. **103,** 137 (2013).

[3] J. Ferrera, V. V. Wong, S. Rishton, V. Boegli, E. H. Anderson, D. P. Kern and H. I. Smith, "Spatial-Phase-Locked Electron-Beam Lithography: Initial Test Results", J. Vac. Sci. Technol. B **11**, 2342 (1993).

[4] J. T. Hastings, F. Zhang and H. I. Smith, "Nanometer-level stitching in raster-scanning electron-beam lithography using spatial-phase locking", J. Vac. Sci. Technol. B **21,** 2650 (2003).

[5] A. Muray, M. Scheinfein, M. Isaacson and I. Adesida, "Radiolysis and resolution limits of inorganic halide resists", J. Vac. Sci. Technol. B **3,** 367 (1985).

[6] A. Murray, M. Isaacson and I. Adesida, "AlF3 - A new very high resolution electron beam resist", Appl. Phys. Lett. **45,** 589 (1984).

[7] E. Kratschmer and M. Isaacson, "Nanostructure fabrication in metals, insulators, and ... inorganic resist", J. Vac. Sci. Technol. B **4,** 361 (1986).

[8] E. Kratschmer and M. Isaacson, "Progress in self-developing metal fluoride resists", J. Vac. Sci. Technol. B **5,** 369 (1987).

[9] J. M. Macauley, R. M. Allen, L. M. Brown and S. D. Berger, "Nanofabrication using inorganic resists", Microelectron. Eng. **9,** 557 (1989).

[10] H. Kaneko, Y. Yasuoka, K. Gamo, "Nitrocellulose As A Self-Developing Resist For Focused Ion-Beam Lithography", J. Vac. Sci. Technol. B **6(3),** 982 (1988).

[11] M. W. Geis, J. N. Randall, T. F. Deutsch, P. D. Degraff, J. P. Drohn and L. A. Stern, "Self-developing resist with submicrometer resolution and processing stability", Appl. Phys. Lett. **43,** 74 (1983).

[12] M. W. Geis, J. N. Randall, T. F. Deutsch, N. N. Efremov, J. P. Donelly and J. D. Woodhouse, "Nitrocellulose as a self-developing resist with submicrometer resolution and processing stability", J. Vac. Sci. Technol. B **1,** 1178 (1983).

[13] M. W. Geis, J. N. Randall, R. W. Mountain, J. P. Woodhouse, E. I. Bromley, D. K. Astolfi and N. P. Economou, "Nitrocellulose as a positive or negative self-developing resist", J. Vac. Sci. Technol. B **3,** 343 (1985).

[14] T. Uchida, H. Kaneko, Y. Yasuoka, K. Gamo, S. Namba, "Self-Development Mechanism Of Nitrocellulose Resist - Electron-Beam Irradiation", Jpn. J. Appl. Phys. **34,** 2049 (1995).

[15] G. M. King, G. Schurmann, D. Branton and J. A. Golovchenko, "Nanometer patterning with ice", Nano Lett. **5,** 157 (2005).

[16] A. Han, A. Kuan, J. Golovchenko and D. Branton, "Nanopatterning on nonplanar and fragile substrates with ice resists", Nano Lett. **12,** 1018 (2012).

[17] J. A. Gardener and J. A. Golovchenko, "Ice-assisted electron beam lithography of graphene", Nanotechnol. **23,** 185302 (2012).

[18] M. E. Bahlke, H. A. Mendoza, D. T. Ashall, A. S. Yin and M. A. Baldo, "Dry Lithography of Large-Area, Thin-Film Organic Semiconductors Using Frozen CO2 Resists", Adv. Matter. **24,** 6136 (2012).

[19] D. A. Zheng, M. A. Mohammad, S. K. Dew and M. Stepanova, "Developer-free direct patterning of PMMA/ZEP 520A by low voltage electron beam lithography", J. Vac. Sci. Technol. B **29,** 06F303 (2011).

[20] B. Bilenberg, S. Jacobsen, M. S. Schmidt, L. H. D. Skjolding, P. Shi, P. Boggild, J. O. Tegenfeldt and A. Kristensen, "High resolution 100 kV electron beam lithography in SU-8", Microelectron. Eng. **83,** 1609 (2006).

[21] B. Cord, J. Lutkenhaus and K. K. Berggren, "Optimal temperature for development of polymethylmethacrylate", J. Vac. Sci. Technol. B **25,** 2013 (2007).

[22] S. Gautsch, M. Studer and N. F. de-Rooij, "Complex nanostructures in PMMA made by a single process step using e-beam lithography", Microelectron. Eng. **87,** 1139 (2010).

[23] M. A. Mohammad, K. Koshelev, T. Fito, D. A. Zheng, M. Stepanova and S. Dew, "Study of development processes for ZEP-520 as a high-resolution positive and negative tone electron beam lithography resist", Jpn. J. Appl. Phys. **51,** 06FC05 (2012).

[24] R. K. Dey, R. Mansour and B. Cui, "Effect of molecular weight distribution on e-beam exposure properties of polystyrene", Nanotechnology **24,** 245302 (2013).

[25] A. L. Bogdanov, J. Lapointe, and J. H. Schmid, "Electron-beam lithography for photonic waveguide fabrication: measurement of the effect of field stitching errors on optical performance and evaluation of a new compensation method", J. Vac. Sci. Technol. B. **30**, 031606 (2012).

[26] R. SteingrUber', H. Engela, and W. Lessle, "Essential reduction of stitching errors in electron-beam lithography using a multiple exposure technique", 'Emerging lithographic technologies V-Edited by E. A. Dobisz', Proceedings of SPIE. **4343**, 317 (2001).

[27] J. Albert, S. Theriault, F. Bilodeau, D. C. Johnson, K. O. Hill, P. Sixt, and M. J. Rooks, "Minimization of phase errors in long fiber Bragg grating phase masks made using electron beam lithography", Photonics Technol. Lett. **8**, 1334 (1996).

[28] D. J. Dougherty, R. E. Muller, P. D. Maker, and S. Forouhar, "Stitching-error reduction in gratings by shot-shifted electron-beam lithography", J. Lightwave Technol. **19**, 1527 (2001).

[29] J. Ferrera, V. V. Wong, S. Rishton, V. Boegli, E. H. Anderson, D. P. Kern, and H. I. Smith, "Spatial-phase-locked electron-beam lithography: Initial test results", J. Vac. Sci. Technol. B **11**, 2342 (1993).

[30] J. E. Sanabia, K. E. Burcham, J. Klingfus, G. Piaszenski, M. Kahl and R. Jede, "Fixed Beam Moving Stage Electron Beam Lithography of Waveguide Coupling Device Structures", Lasers and Electro-Optics (CLEO), Technical Digest, OSA (2012).

CHAPTER 4

Introduction to AFM probes fabrication

This chapter reviews atomic force microscopy (AFM) probes fabrication techniques. At the end, our technique to fabricate high aspect ratio AFM tips with low-cost will be introduced.

4.1. Background

4.1.1. Overview of AFM

Scanning probe microscopy (SPM), which includes mainly scanning tunneling microscopy (STM)[1], atomic force microscopy (AFM)[2], and scanning near-field optical microscopy (SNOM)[3], was developed to observe surface characteristics by detecting interactions between the probe and solid material. STM and AFM are the most widely used technologies in the SPM family. STM was developed by Binning et al[1] in 1982, and is used to measure the surface topography to an atomic resolution by detecting the tunneling current. After the development of STM, several micro-structuring and nano-structuring technology approaches[4] using STM were developed to enable researchers to manipulate even single atom. Thus SPM can be used as not only a measuring tool but also as a nano-structuring tool. However, as STM is controlled by detecting a tunneling current between the probe and sample, the measured sample is limited to conductive material. To overcome this problem, AFM was developed by Binning et al[2] in 1986. The advantage of AFM is that any type of materials can be measured and the operation can be conducted under normal atmospheric conditions. AFM works by adjusting short-range and long-

range forces between the probe and sample instead of the tunneling current. In principle, while the tip approaches the sample, attractive force between the sample and the tip causes the flexible cantilever to deflect towards the sample surface. However, while the cantilever is brought even closer to the sample, so as to the tip gets contact with surface, repulsive force dominates and deflects the cantilever away from the surface.

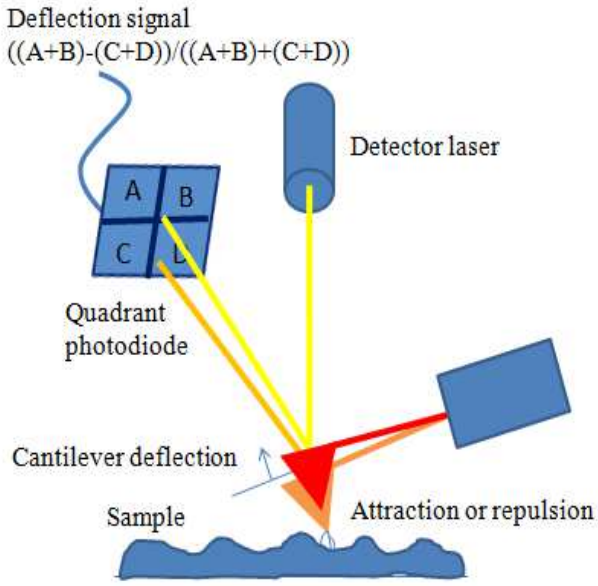

Figure 4.1. Schematic drawing of AFM operation[5].

An AFM probe consists of a nano-sized tip at the end of a flexible cantilever attached to a holder, which 'feels/senses' the surface to generate an image of the surface topography. As the tip scans across the sample, the force of interaction between the surface and the tip is measured via a feedback system. The force is directly related to the deflection of the cantilever. For the measurement, a laser is shone on the cantilever and reflected off the cantilever arm to strike a position-sensitive photodiode (PSPD), as shown in figure 4.1. In its simplest mode of operation, the piezo (on which the cantilever is mounted on) is fed a voltage to raise or lower the cantilever to maintain a constant height above the sample. This voltage is then converted into a distance using the known electromechanical properties of the piezo-device. An AFM thus gives the three dimensional topography map of a sample surface by scanning the cantilever over the surface. AFMs is capable of atomic resolution, and unlike electron microscopes, the sample can be imaged in air or under liquids. To obtain a high resolution topography image, it is essential to use a sharp and high aspect ratio AFM tip.

4.1.2. Applications of AFM

As a general purpose nano-metrology instrument, AFM is employed in many different areas. There are three major AFM markets: (1) Semiconductor and electronics sectors. AFM is routinely used in product inspection and failure analysis for detecting nanometer features. In production environments, such as microelectronics and solar cells, and precision manufacturing industries (such as automotive device manufacturing and aerospace), AFMs characterize the products throughout the manufacturing process; (2) Nanotechnology and nano-material research area; and (3) Biomedical and life sciences sector where AFMs can be used in, e.g., biophysics to measure the mechanical properties of living material (such as tissue or cell).

Beside imaging, AFM is also used to induce local modification of surfaces: oxidation, local heating or object manipulation. Tip-based nanofabrication (TBN) is an effective method compared to conventional fabrication processes due to its simplicity, high resolution, and low cost. Various AFM-based nano-scale fabrication methods have been proposed/implemented using lithography capable AFM tool, such as electrochemical oxidation, material transfer, mechanical lithography, thermally induced modifications etc. The following sections introduce the tip-based nanofabrication techniques.

4.1.2.1. Electrochemical oxidation technique

In this technique, voltage bias is imposed between a pyramidal or sharp conducting probe tip and the sample in presence of high humidity, which generates an intense electric field between the tip and the sample chuck that leads to localized oxidation of silicon or anodization of metallic surface. When sample bias was applied, oxide patterns of a few monolayers to a few nanometers are formed due to field emission etching of hydrogen in presence of water. Oxygen extracted from water molecules due to sample bias provides the reactant source to oxidize the sample. Since the oxidation process requires an electrical current, both the tip and substrate must have some conductivity.

The electrochemical oxidation on silicon has been performed using non-contact mode AFM technique based on the force gradient[6,7]. Using AFM anodic oxidation technique, Wilder et al.[8] patterned the minimum feature sizes below 30 nm. Then they performed reactive ion etching to transfer the pattern into Si (100) substrates, yielding a high aspect ratio, as shown in the figure 4.2. This figure shows the SEM images of line arrays pattern written by using the non-contact AFM technique and pattern transferred into the underlying silicon, (a) top-view image of 28 nm wide lines patterned with a DC sample bias of 84 V, (b) magnified image demonstrating line edge roughness (LER) and uniformity of lines, (c) tilted view that demonstrated the connecting ends of the line arrays, and (d) magnified image of cross-section view of standing line. Using a batch of tip arrays in AFM, oxidation process can be enhanced by increasing the throughput of patterning.

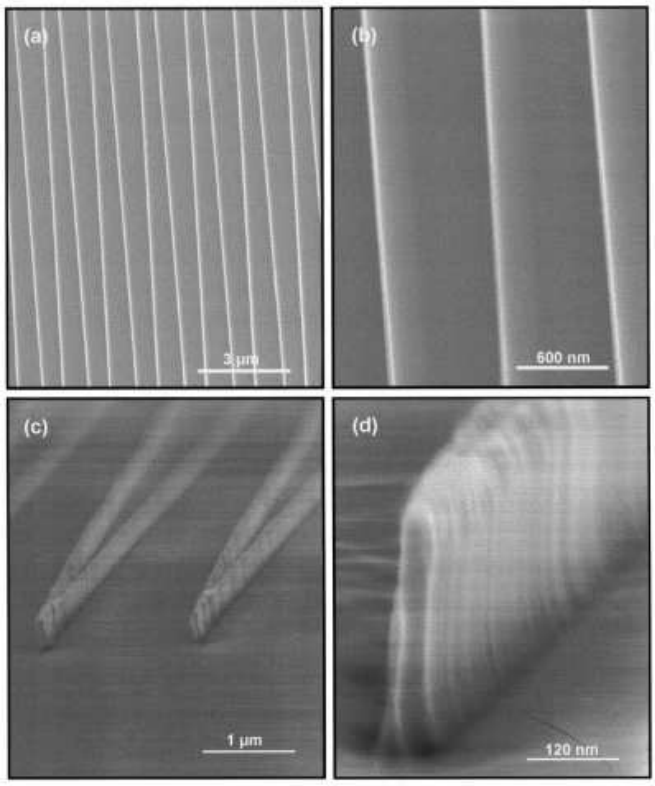

Figure 4.2. SEM images of line array pattern written using AFM electrochemical oxidation technique and etched into the substrate. (a) Top-down image of 28 nm wide lines written with an exposure dose of 20 nC/cm and a sample bias of 84 V, (b) higher magnification image showing pattern continuity and uniformity, (c) the sample was tilted to show the ends of the zig-zag

patterns, and (d) a higher magnification of the turn-around point. The feature is 32 nm wide and etched 320 nm deep into the silicon, yielding a 10:1 aspect ratio[8].

Recently, Davis et al.[9] demonstrated that the AFM oxidation on Al substrate could be applied to fabricate nano-mechanical CMOS device (Figure 4.3). They maintained a particular distance between tip and sample to obtain even 10 nm line width. Figure 4.3 shows the schematic illustration and AFM image of an oxidized line with a small tip-sample interaction distance and high voltage (a) and large tip-sample distance and low voltage (b).

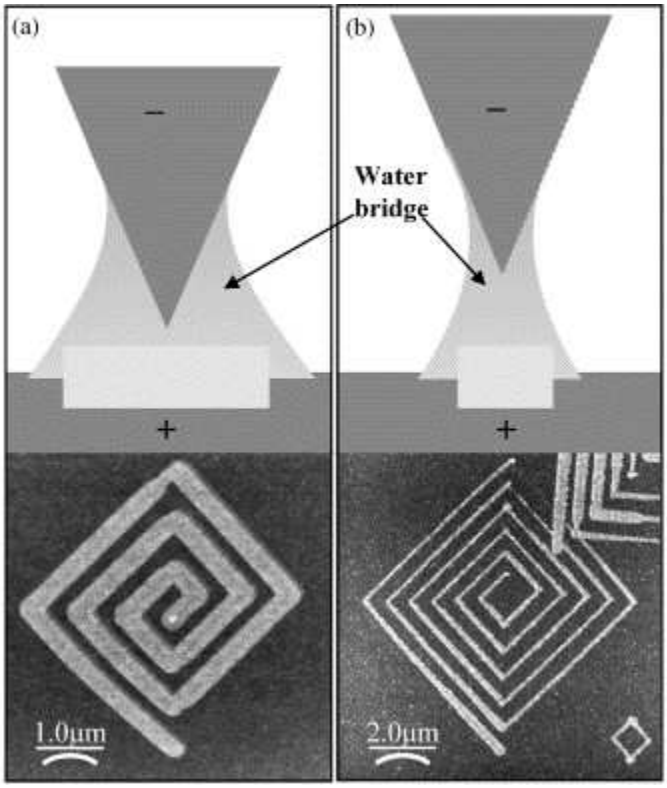

Figure 4.3. Schematic illustration and non-contact AFM image of an oxidized pattern with (a) a small tip/sample distance and high voltage, and (b) large tip/sample distance and low voltage[9].

4.1.2.2. Material transfer process

Unlike electrochemical oxidation method, material transfer process does not require any sample bias applied to the sharp probe of AFM tool since the target material is transferred from the

probe to the surface due to capillary force, van dar waals force or chemical attraction. Thus, material transfer process technique needs a target material storage part in the probe.

Piner et al.[10] demonstrated a new technique of AFM fabrication known as dip-pen nanolithography (DPN). They showed that the 1-Octadecanethiol (ODT) was transferred from the AFM tip to the sample by capillary force and made a pattern when the tip, coated with ODT, was in contact with a sample surface. Figure 4.4 shows a demonstration of material transfer process where dots, patterned with ODT-coated AFM probe by material transfer process, had been created on Au substrate.

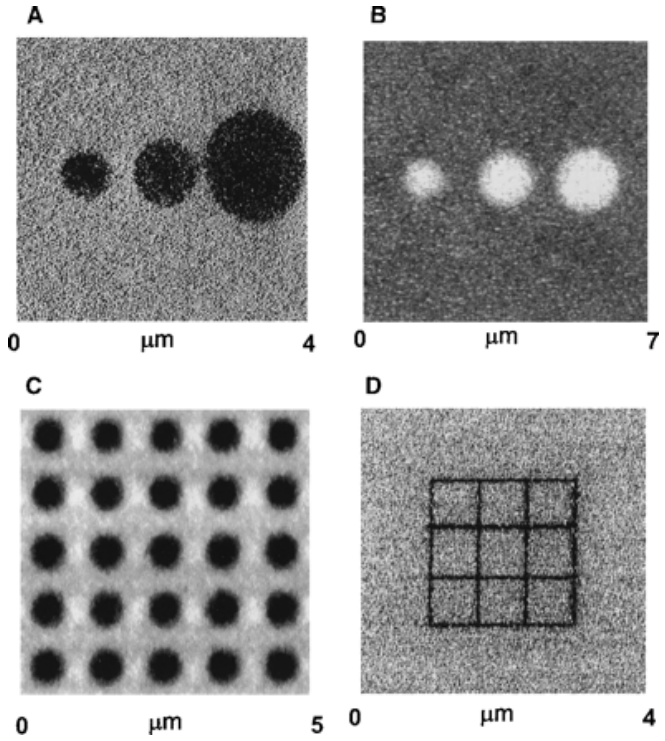

Figure 4.4. (A) Lateral force image of an Au substrate after an AFM tip, which was coated with ODT, had been in contact with the substrate for 2, 4, and 16 min (left to right); the relative humidity was held constant at 45%, and the image was recorded at a scan rate of 4 Hz. (B) Lateral force image of dots of 16-mercaptohexadecanoic acid on a Au substrate. To generate the dots, an AFM tip coated with 16-mercaptohexadecanoic acid was held on the Au substrate for 10, 20 and 40 s (left to right). The relative humidity was 35%. (C) Lateral force image of an array of dots generated by DPN. Each dot was generated by holding an ODT-coated tip in contact with the surface for ~20 s. Writing and recording conditions were the same as in (A). (D)

Lateral force image of a molecule-based grid. Each line is 100 nm in width and 2 μm in length and required 1.5 min to write[10].

4.1.2.3. Material removal process

AFM material removal process is a mechanical lithography method in which a solid material is scratched out from the sample. In general, AFM scratching is more popular in patterning soft materials, such as polymers, biomaterials, resists and mica than that of hard materials, including metals, ceramics and semiconductors. To scratch polymer materials, Si or Si_3N_4 AFM probes are typically used. Generally, after resist removal by using mechanical lithography method, wet etching or lift-off can be used to transfer the patterns into the substrate. Sohn and Willett reported[11] a resist removal process by AFM lithography and subsequently they performed a lift off to pattern 40 nm wide and 50 nm thick Cr wires on a GaAs surface, as shown in figure 4.5. They used Si_3N_4 AFM probe to scratch the PMMA resist at a normal force range of 1100-1130 nN. The patterned resist was then baked and Cr was deposited on the surface later on. Upon completing lift off, the Cr wires were obtained as a structure arrays on the substrate area. The resolution depends on a few fabrication parameters such as the tip force, development duration and resist dimension.

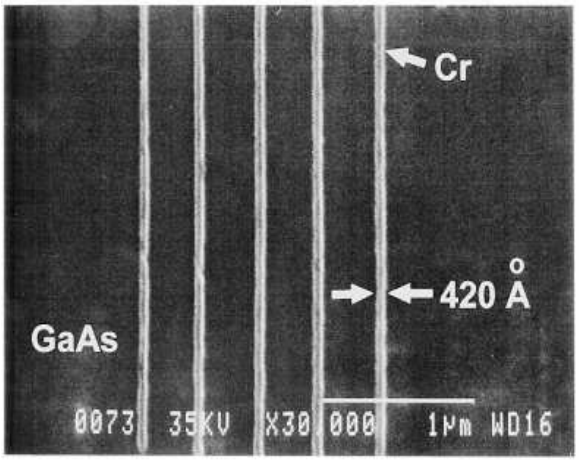

Figure 4.5. SEM image of 40 nm wide, 50 nm thick Cr wires fabricated on a GaAs substrate where force is 1100–1130 nN, development time is 5 s and top resist-layer thickness is about 24 nm[11].

Lee et al.[12] and Park et al.[13] patterned Si (100) surface by direct AFM scratching and subsequent wet etching. After the AFM patterning, the Si-H bonds were broken and reacted with oxygen atoms as sample surface was kept in the air, leading to a native oxide layer on the substrate, which was used as etching mask in the subsequent KOH etching of Si, as shown in figure 4.6.

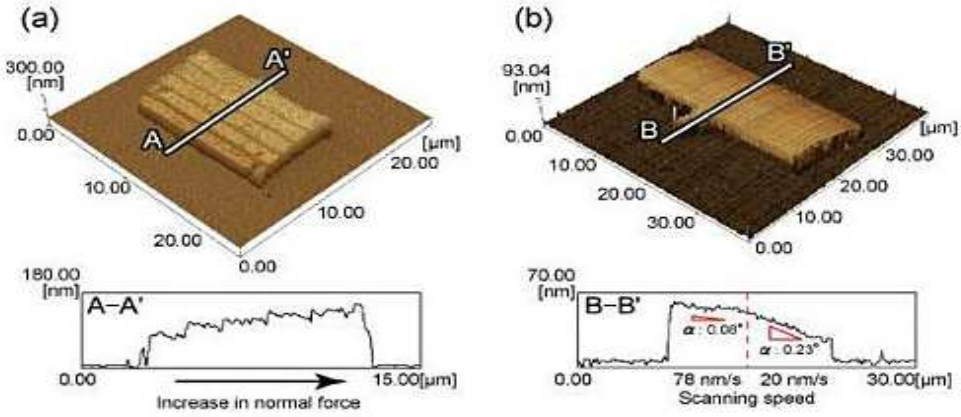

Figure 4.6. AFM images of (a) silicon surface was fabricated by five different amount of forces, 124-372 μN and subsequently etched in 10 wt.% KOH for 10 min, (b) Nano-structure prepared in 5 wt.% KOH solution[12,13]. Here, the tip force and tip scanning speed is not well enough to make the line patterns.

4.1.2.4. Thermal probe lithography

Thermal probe lithography technique is a form of scanning probe lithography where material is patterned in nanoscale by a hot AFM probe. While patterning, a hot tip heats the polymer surface up, so the tip deforms the softened polymer to create a nanostructure (a bit). Mamin et al.[14] (worked in IBM lab) is the pioneer in demonstrating the thermal probe lithography. In 1992, they first demonstrated the technique using laser beam heated probe. Later on, they developed/improved the technique and integrated resistive heaters and piezoresistive sensors for writing and reading of bit/data[15]. The thermo-mechanical high density data storage idea formed the basis of the Millipede project which was initialized by Peter Vettiger and Gerd Binnig[16] at the IBM. This was developed in order to write, read and erase bit data by a read-write capable multi-tip based AFM. Lutwyche et al[17] reported the writing and reading of 1024 bits using similar technique, by using a 32 x 32 probe array.

4.1.3. AFM probe

An essential part of an AFM tool is the AFM probe which consists of cantilever and tip. For easy handling, AFM probe is connected with holder/'support chip'. The typical dimension of each part of AFM probe including the holder is shown in the figure 4.7. AFM tip requires a small radius of curvature of tip apex for high lateral resolution imaging but at a cost of less flexibility/stability. The sizes, shapes and materials of AFM cantilever control the spring constant and resonant frequency of probe. To increase the spring constant, cantilever beam would be shorter or thicker. On the other hand, shorter cantilever provides higher resonant frequencies than regular sized cantilevers.

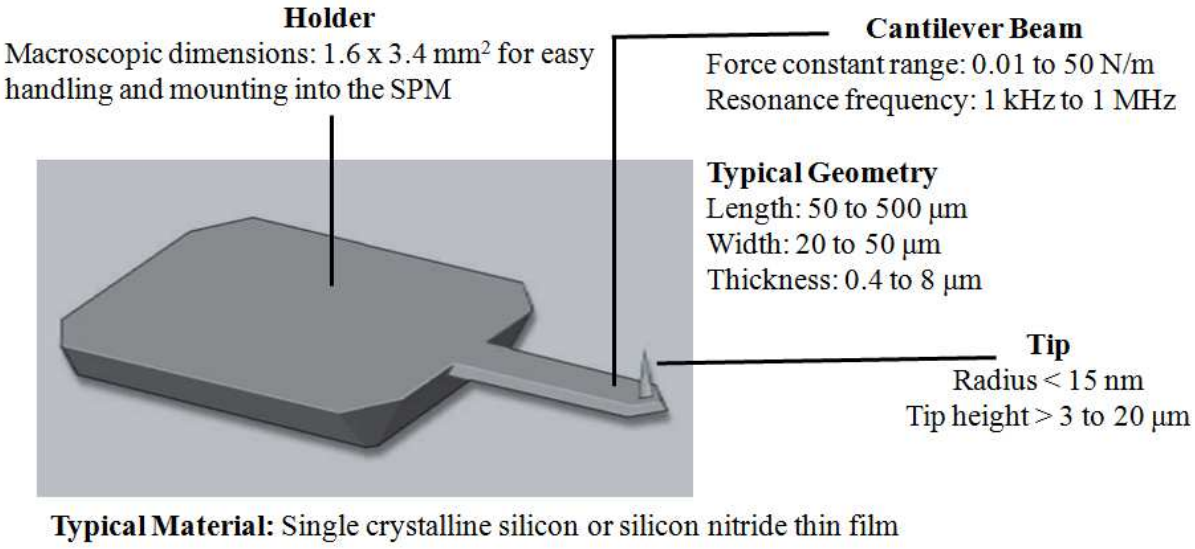

Figure 4.7. Basic of AFM probe[32].

The common material of AFM probe is silicon (doped to increase the electrical conductivity, or undoped. Single crystalline or polycrystalline) or silicon nitride (insulator). Frequently, gold or aluminium is coated on back-side of AFM probe to promote the laser reflection signal. Depending on samples to be characterized, AFM probe may be coated with electrically conductive, magnetic or wear resistant material such as aluminium, iron and diamond respectively. Undoped silicon and silicon-nitride tips that suffer from poor electrical conductivity are most widely used for topography characterization. One may coat metal films such as aluminium, gold etc onto the undoped silicon or silicon nitride cantilever by using evaporation or

sputtering method to increase the conductivity. Doped diamond tip is another type of AFM tips, which is popular due to their hardness and electrical conductivity. Kim et al.[18] reported the use of diamond in AFM tips. Doped diamond is potentially an ideal probe material not only for its unbeatable hardness and stiffness, but also for its low electrical and wear resistance, and its chemical inertness. In summary, for several applications, such as measurement of friction force and elastic properties of samples, as well as wear property, which requires hard contact between probe and sample, diamond tips are recommended.

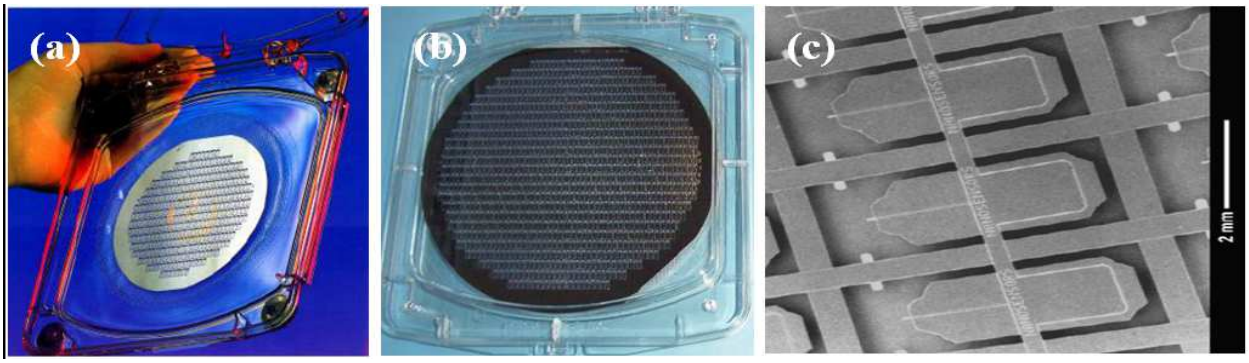

Figure 4.8. Image of commercial (a) 4-inch wafer with 380 probes, (b) 6-inch wafer with more than 1000 probes, (c) Close-up view of those tips enclosed in the box (Courtesy: NanoWorld Inc.[46]).

Lastly, AFM tips are fabricated out of a whole wafer using MEMS process. Figure 4.8 shows the optical images of commercial 4-inch wafer with 388 probes (a), 6-inch wafer with more than 1000 probes (b) and close-up view of those tips enclosed in the box (c).

4.2. Fabrication techniques of an entire AFM probe

AFM probes used in imaging can be fabricated by two major methods: the inverse-pyramid-shaped probes fabricated through a molding technique (Albrecht et al. 1990[19], Takahashi et al. 2009[20]) and probes machined either by wet or dry etching followed by oxidation sharpening (Rangelow 1994[21]; Folch et al. 1997). In inverse-pyramid cavity method (Figure 4.10), a cavity is formed at first by aqueous wet etching into a silicon substrate and a layer of thin film is then filled into the cavity. The silicon substrate is etched back to detach the cantilever-tip area after the thin film is selectively removed. Even though this technique is relatively simple, it is limited

by having the final tip apex curvature not as good as formed by other techniques. At present, most AFM probes are micro-machined directly by anisotropic wet etching (Figure 4.9) or dry reactive ion etching (Boisen et al. 1996[22]; Liu and Gamble 1998[23]; Rasmussen et al. 2001[24]; Alves et al. 2005[25]; Neuzil and Nagarajan 2006[26]; Li et al. 2008[27], Hantsche et al 1998[28]). Anisotropic wet etching is cheaper than plasma etching (RIE) and thus it can be easily employed without using expensive instruments. One barrier of anisotropic wet etching such as aqueous KOH dipping is that the silicon tip stops sharpening once the mask was fallen down from the pyramid apex; and therefore, additional oxidation sharpening was often necessary (as followed by Resnik et al. 2003[29]; Han et al. 2006, Duriau et al[30] 2007). To avoid oxidation sharpening, Burt et al.[31] demonstrated that a triangular mask parallel to <310> directions will produce a single self-sharpening tip during aqueous KOH etching, and a tip with minimum radius of curvature of less than 5 nm are defined.

As examples, in figure 4.9 and 4.10, we show standard fabrication methods to produce regular silicon probe in '*undercut concept*' and regular nitride probe in '*inverse-pyramid cavity concept*' (courtesy: NanoWorld[32]) respectively.

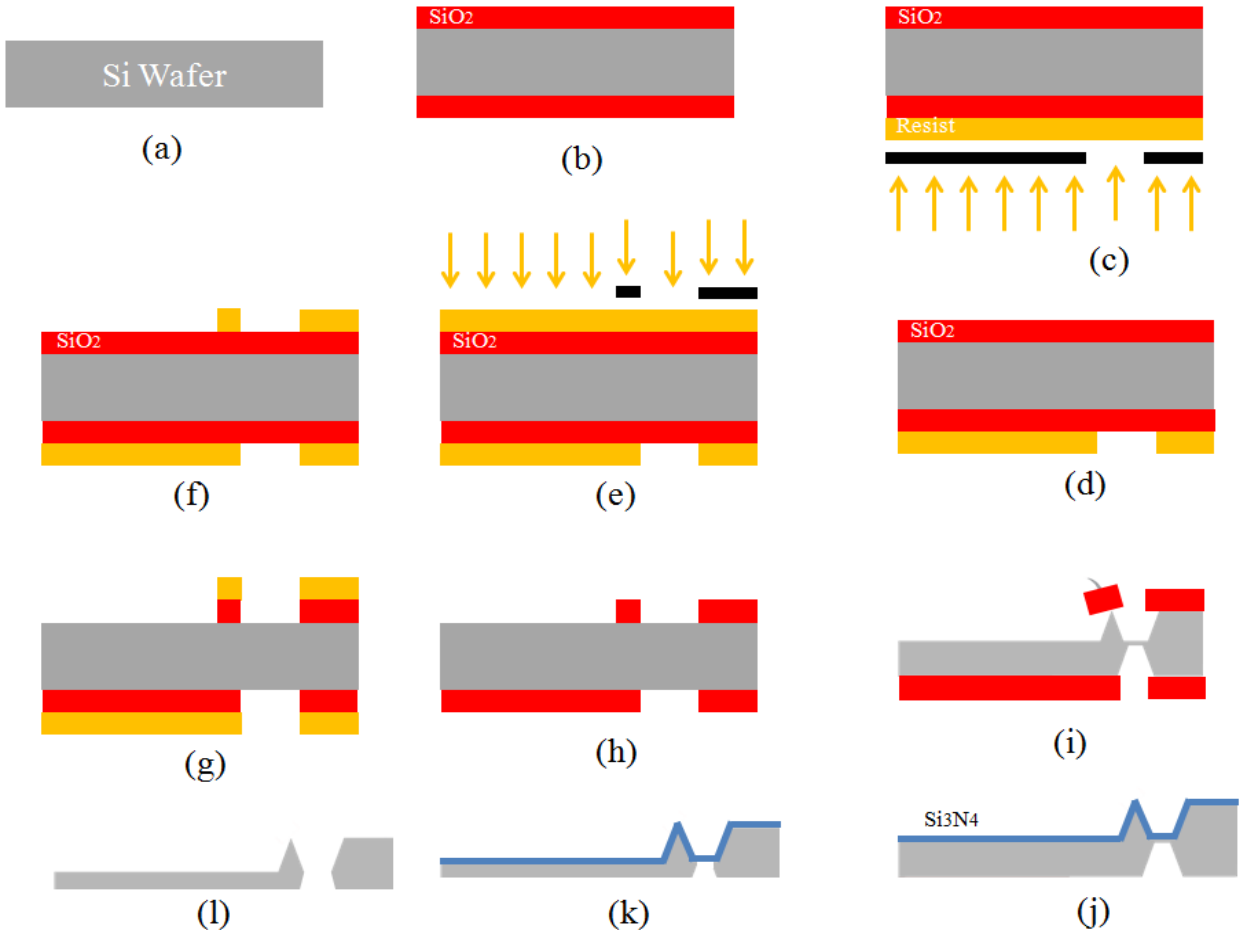

Figure 4.9. Fabrication steps of regular silicon probes (*Undercut concept).* (a) Start with Si wafer, (b) next, coat SiO_2 on both sides of silicon wafer (<100> orientation), (c) then, coat photoresist on back side of wafer and photolithography (exposure of the photoresist through a chromium/quartz mask) to define the cantilever back shape, (d) next, develop the exposed photoresist, (e) deposit photoresist in front side of the sample and photolithography to shape the cantilever top side, (f) development of the exposed photo resist, (g) isotropic wet etch to remove the silicon dioxide, (h) next, dissolve the photo resist, (i) anisotropic wet etch with KOH to remove silicon. The formation of the tip is finished when the "oxide shield" falls off, (j) isotropic wet etch to remove silicon dioxide and then deposit the silicon nitride layer to protect the tip side of the probe, (k) next, anisotropic KOH wet etch to remove silicon from back side. The thickness of the cantilever is determined during this step, (l) finally, isotropic wet etch to remove the silicon nitride[32].

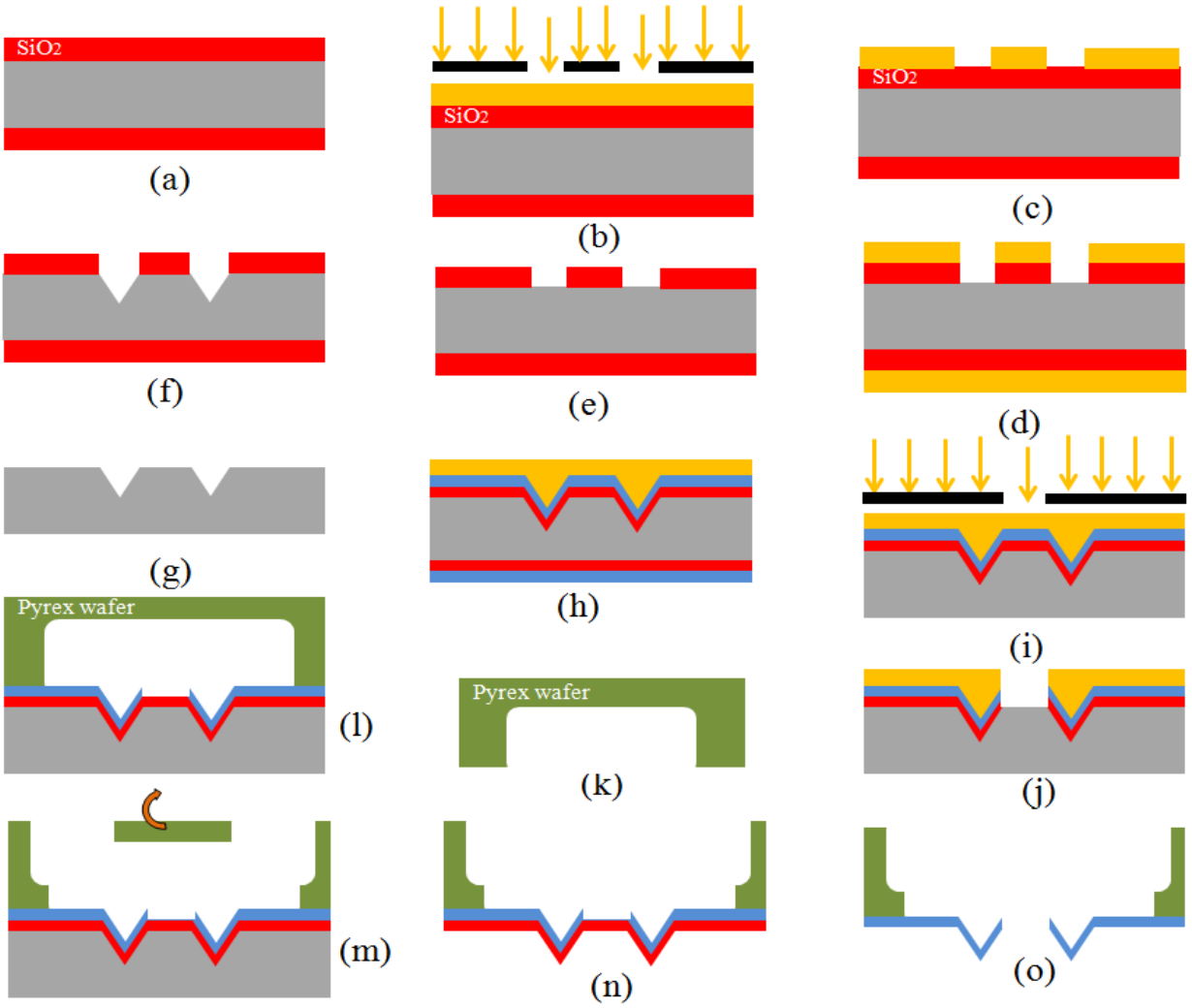

Figure 4.10. Fabrication steps of regular nitride probes. (a) thermal oxidation to coat oxide on both sides of silicon wafer (<100> orientation), (b) photolithography to expose resist, (c) resist development, (d) spin coating of protection resist on back side and etch oxide with BHF, (e) remove resist with acetone/isopropanol, (f) KOH wet etch to remove Si, (g) remove oxide with BHF, (h) grow oxide, deposit nitride, remove them on the backside, and spin-coat photoresist, (i) photolithography to expose the resist, (j) develop the resist and etch oxide then nitride, (k) dice pyrex wafer (to be used as a handle), (l) anodic bonding the nitride and the pyrex wafer, (m) dice and remove unnecessary portion of pyrex, (n) KOH wet etch to remove Si, and (o) BHF etch to remove the oxide layer[32].

4.2.1. Fabrication with combined masked–maskless etching and P+ doping

Han et al.[33] have demonstrated and developed high-yield manufacturing technique to fabricate the single-crystalline silicon AFM probes. In this process, tips and cantilevers were concurrently designed by a combined masked–maskless anisotropic etching method. In anisotropic etch, KOH solution was employed. This process is shown in figure 4.11.

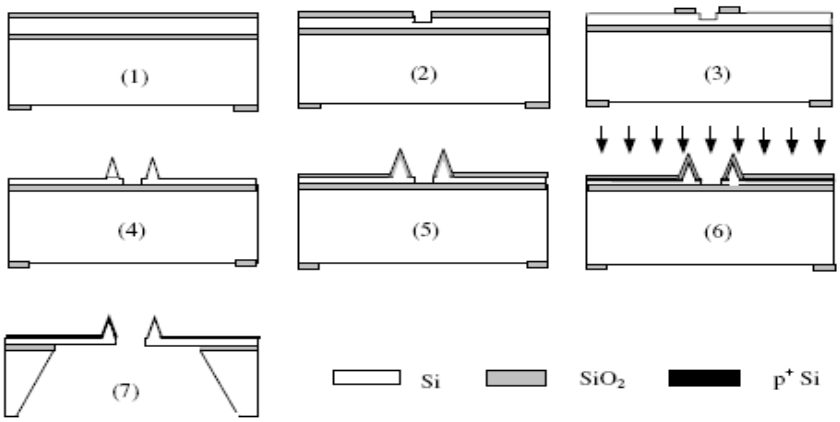

Figure 4.11. Masked-maskless fabrication steps for the AFM probe. (1) First, start the fabrication process with SOI wafers that have a 12 μm thick silicon layer. Then, grow a silicon dioxide layer at 1100 °C, which is 0.5 μm thick on both sides of the wafer. Next, remove the silicon dioxide from the front side by buffered HF. Afterwards, deposit a new 100 nm thick of silicon dioxide. On the backside of wafer, openings are patterned for next cantilever release etching. (2) For the cantilever precursory, pattern the silicon dioxide layer at the front side. It shaped the (110) plane by masked wet etching with 40% KOH. (3) Next, pattern the circular silicon dioxide mask for the tip contour at the end of the cantilever. (4) On the top of the cantilever precursor, etch silicon dioxide as maskless. Next, form the tip contour by convex-corner undercutting which involved the masked etching. Then, define cantilever contour by the maskless etching. (5) Next, low temperature oxidization at 950 °C to sharpen the tip contour with a nano-metric radius. (6) Implant boron. and next, activate the implanted boron by annealing at 950 °C in order to reduce the residual stress. Later, etch with buffered HF to remove the backside silicon dioxide film. (7) Anisotropic etch to remove the silicon from the back of the cantilevers. Finally, etch silicon dioxide from the front side to expose the electrically conductive and single crystalline silicon probe[33].

4.2.2. Inverse pyramid shaped molding: Graphene probes

The inverse-pyramid-shaped probes were fabricated through a molding technique (Albrecht et al. 1990, Takahashi et al. 2009) where a cavity is formed first by aqueous wet etching into a silicon substrate and a layer of thin film is then filled into the cavity. The silicon substrate is etched back to detach the cantilever-tip area after the thin film is selectively removed. The most thin film filling the cavity is Si_3N_4, and nitride tips are the most widely used for contact mode AFM because nitride is more wear-resistant than silicon.

Recently, graphene has become one of the most powerful discoveries of this century. Martin-Olmos and his group[34] showed that graphene can be grown uniformly over different copper terraces where the underlying substrate did not affect the atomic arrangement of the grown material. In addition, they were able to grow graphene on AFM probes. Figure 4.12 illustrates the fabrication of probe by inverse-pyramid molding method. First, they prepared the substrates for molding by using standard micro-fabrication methods. They grew 100 nm silicon dioxide thermally and copper by deposition method and finally graphene by Chemical vapor deposition (CVD) on top of silicon wafer, which was then patterned using lithography and dry etching to define the structure. Inverted pyramids were shaped after immersion into KOH solution, which were eventually used as mold for the AFM probes. The detail of the process is shown in figure 4.12.

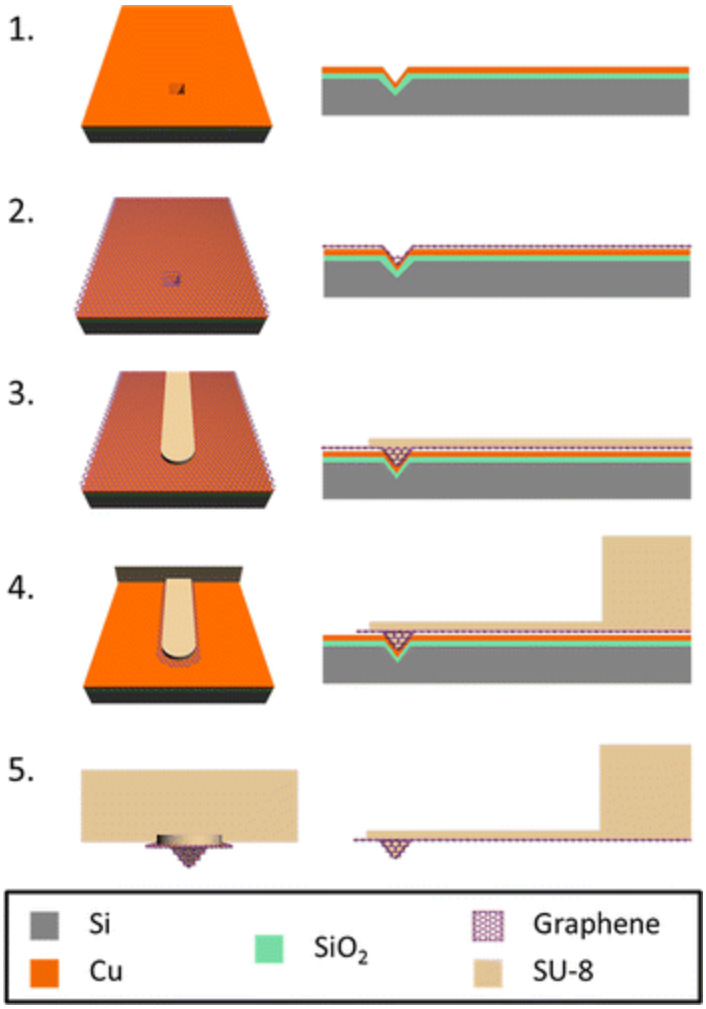

Figure 4.12. Fabrication process to make probe by molding scheme. (1) Prepare tip area by selectively etching of silicon with KOH solution. The pit and flat surfaces were grown with thermal silicon dioxide and finally coated with copper. (2) Grow a continuous layer of graphene on copper film by CVD method. (3) Coat a thin SU-8 resist to fill the tip mold and; expose and develop to define the cantilever. (4) Argon dry etch to remove the graphene elsewhere where there was no SU-8 film. Later, process a second and thick SU-8 to pattern the probe body. (5) After removal of silicon dioxide with HF solution, silicon with KOH and Cu with wet etchant, probe was released with graphene layer[34].

4.3. Fabrication techniques of AFM tip

4.3.1. Fabrication of tips by aligned-mask method

Li et al.[35] and later, Tang et al.[36] have demonstrated a method to fabricate nanosilicon tip where the tips with precise dimensions are sharpened by anisotropic wet etching technologies using a special pentagon etch mask design. Li et al. mainly followed the procedure of Burt et al.[37] who fabricated a triangular mask parallel to <310> directions for single self-sharpening tip during aqueous KOH etching. The orientation of the undercut generated during wet etching is most closely aligned to the square masks rotated by 63.4^0 (clockwise and anti-clockwise) from the <110> direction in the (100) surface plane as shown in figure 4.13.

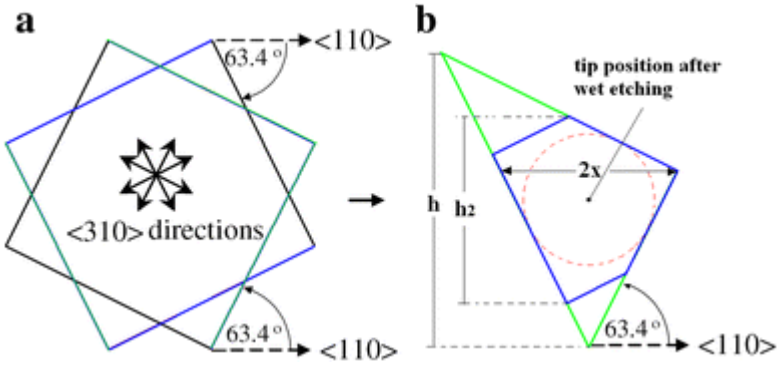

Figure 4.13. (a) Orientation of the <310> directions and the corresponding planes that are perpendicular to the 8 directions. (b) Pentagon shaped mask design comprising sides aligned to <310> directions shown in (a). The eight equivalent <310> directions are 310, $\bar{3}10$, $3\bar{1}0$, $\overline{31}0$; 130, $\bar{1}30$, $1\bar{3}0$ and $\overline{13}0$ [35].

The gradual geometrical modification of the tip contour using pentagon etching mask after several wet etch times, as shown in figure 4.14.

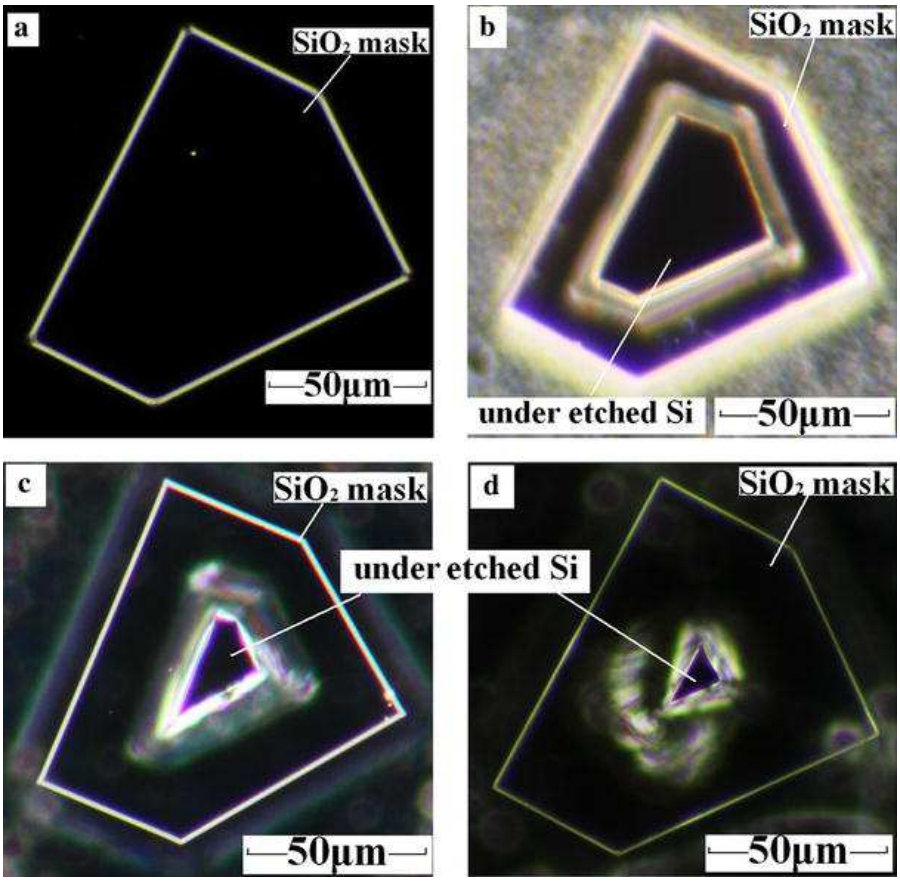

Figure 4.14. Geometrical modification of the tip contour (viewed from the top) using pentagon etching mask after several etch times, such as (a) at 0 min, (b) after 32 min, (c) after 52 min and (d) after 63 min. The final tip will have a triangular (rather than square) base [35].

4.3.2. Fabrication of tips using dry etching

As dry etching processes offer better uniformity and reproducibility than wet etching processes, several groups have reported AFM tips fabrication using reactive ion etching (RIE), such as monocrystalline silicon tips defined by a RIE with SF_6 gas[38], and Rocket tips defined by RIE (for apex) and deep reactive ion etching (DRIE) (for shaft)[39]. Villanueva et. al.[40,41] also used deep reactive ion etching (DRIE) to fabricate the sharp tip. Their process is shown in detail in figure 4.15.

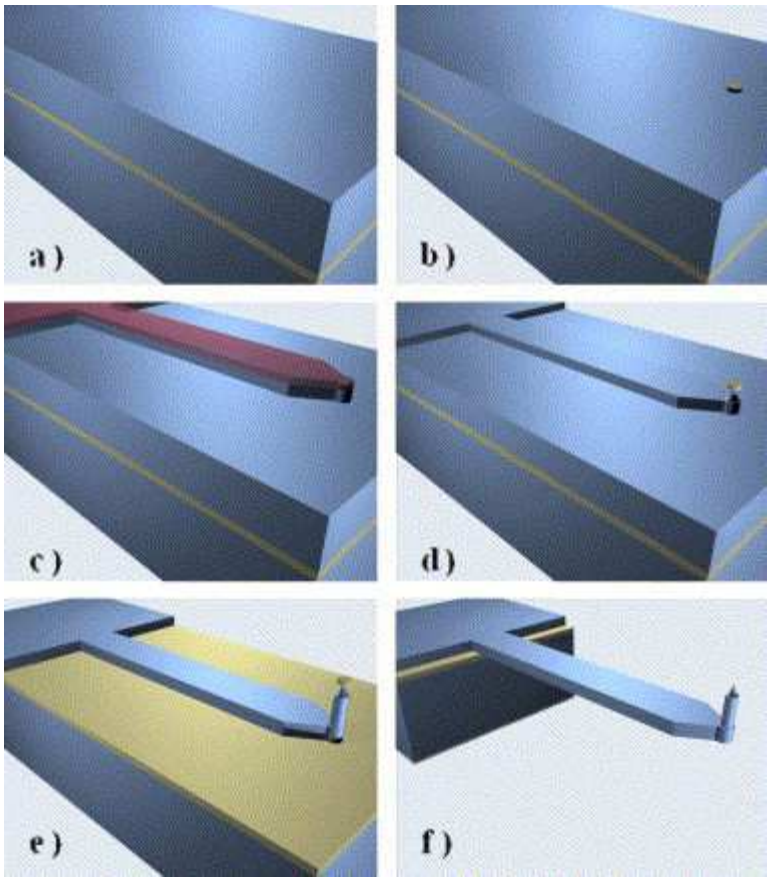

Figure 4.15. Fabrication process of entire probe using dry etch. (a) Start with SOI (silicon on insulator) as initial material (top silicon layer is 15 μm in thickness), (b) thermal oxidation to coat oxide on top side of SOI and photolithography to pattern a circular etch mask (finally this portion transforms to tip), (c) coat photoresist again to do second photolithography to define the cantilever, (silicon dioxide circular mask still on top of the cantilever which acts as etching mask for the following two DRIEs, (d) fabricate the shaft by using optimized DRIE recipe (described in table 4.1), (e) next, oxidation sharpening (wet oxidation at 1100 °C) to sharpen the tip, (f) deep dry etch (DRIE) to make high aspect ratio pillar and finally, release of the cantilevers by etching the buried silicon dioxide [40].

In this process, the shape of the cylinder of tip can be modified/controlled by changing dry etch gas flows. Figure 4.16 (a) shows the schematic of scalloping and undercutting shapes in a cylindrical wall where ripple was minimized by changing RIE recipes described in table 4.1 The final rocket tip fabricated by this DRIE method is shown in figure 4.16 (b).

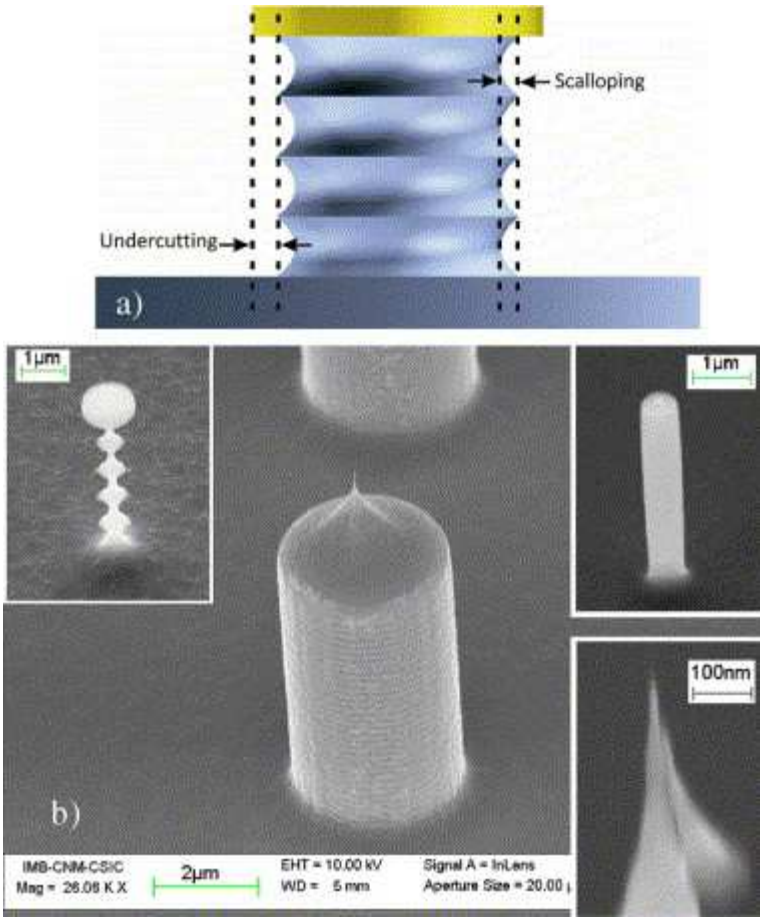

Figure 4.16. (a) Schematic of scalloping and undercutting shapes in a cylindrical wall. (b) SEM image of optimized DRIE result using standard process (top-left), ripple was minimized by changing RIE recipes described in table 4.1 (top-right) and, at center, rocket tip fabricated by combination of optimized DRIE. Inset at bottom right shows a high magnification SEM image of the vertex of a tip after oxidation sharpening with 5 nm diameter [40].

Table 4.1. Optimized DRIE etching recipes with A601 equipment at 20 °C [40].

Process	SF_6 flux	c-C_4F8 flux	Pressure (Pa)	Source power (W)	Bias power (W)	DC bias (V)
Shaft process	150 sccm/2.5s	100 sccm/1s	1.4–2.8	1500	15	80-120
Apex process	150 sccm/1s	100 sccm/0.33s	1.6–2.1	1500	15	75-100

4.4. Method for tip sharpening

4.4.1. Oxidation sharpening

Marcus et al.[42,43] reported the sharpening method by oxide formation at very high temperatures (900–950 °C) and then oxide etching with HF. They observed the high stress can be an effective obstacle to reduce the oxidation rate in the tip apex during the thermal oxidation process, and by repeatedly growing oxide film on the silicon tips and etching the oxide with HF, they demonstrated <1 nm radii of curvature at the silicon tip apex. Figure 4.17 shows the concept of oxidation sharpening. This sharpening works because the oxidation rate decrease with stress, which is higher for smaller curvature of radius. As a result, the oxidation is slower at places closer to the very top of the apex. Thus, oxidation sharpening is a self-limiting process.

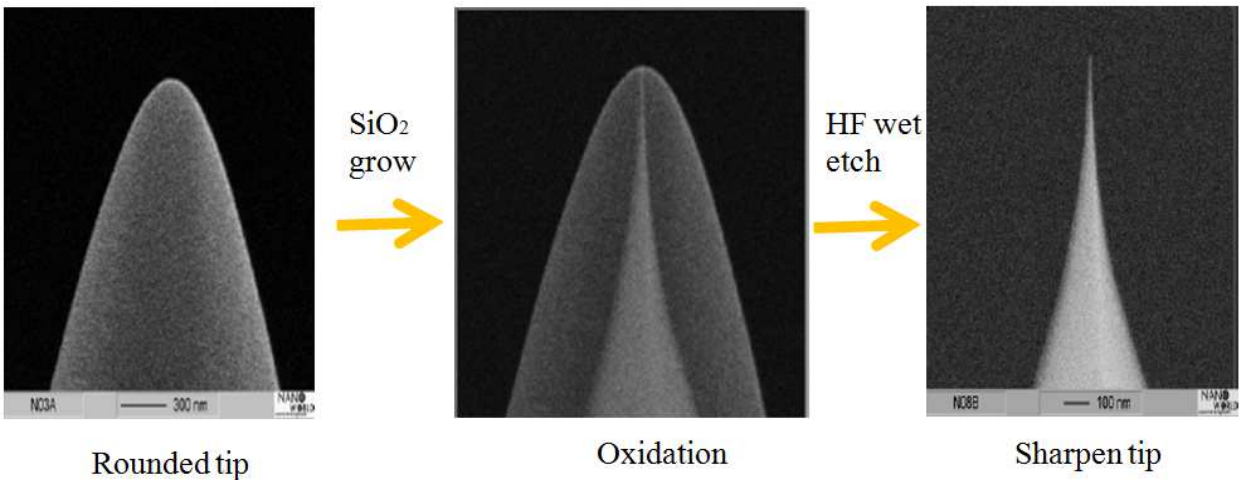

Figure 4.17. Oxidation sharpening steps (Courtesy: NANOSENSOR[44]).

Folch et al.[45] demonstrated a simple process that allows them to microfabricate silicon nitride cantilevers with integrated Si tips, which can be repeatedly sharpened without affecting the nitride cantilever. They first performed wet isotropic etch to fabricate the regular tip, and subsequently, the regular pyramid-shaped silicon tip was oxidized at 1000 ^{o}C and then the oxide removed by hydrofluoric acid to make the tip sharp.

However, the improvement of this oxidation sharpening technique in term of aspect ratio is very limited, and thus the pillar dimensions, such as height and width, cannot be controlled with interest in this oxidation sharpening method.

4.5. Fabrication techniques of high aspect ratio (HAR) tip

The basic principle of AFM is whereby a fine tip is scanned across the surface of the sample to measure surface morphology and properties to construct a 3D image of the surface. Compared to scanning electron microscope (SEM), AFM has lower cost, much more accurate (by one order of magnitude in the z-direction, as well as in the x-y direction if the sample is flat), easier sample preparation, less intrusive, and can work equally well with insulating sample or even inside a liquid environment. Nevertheless, SEM is still far more popular than AFM for topographical structure characterization, mostly because of the intrinsic limit in the AFM image when mapping a non-flat surface (e.g. a deep and narrow hole/trench) where the tip cannot fully follow the sample surface. The natural solution to overcome this issue is by using thin and high aspect ratio tips that can follow the sample surface more precisely. This section reviews the fabrication method for high aspect ratio tips. Probe aspect ratio is defined as the probe apex height divided by the probe apex base diameter, and high aspect ratio means that the probe apex height is at least three times that of apex base diameter. Figure 4.18 shows the schematic diagram of the problem that arises using the low aspect ratio AFM tip. The low aspect ratio tips prevent precise observation of tall or deep structures.

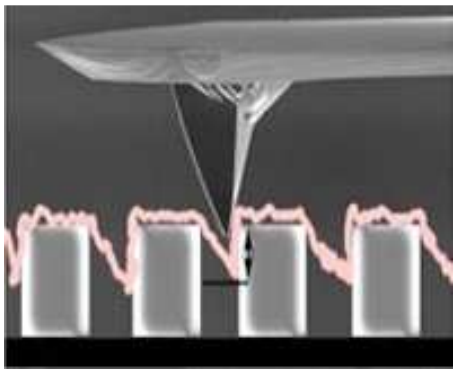

Figure 4.18. Schematic diagram of a measurement having severe artifact achieved using regular low aspect ratio AFM tip.

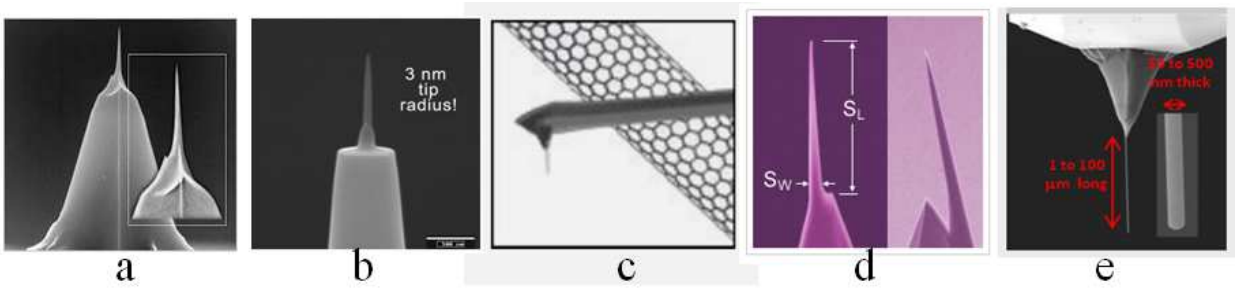

Figure 4.19. SEM images of various high aspect ratio AFM tips that are commercially available. Image taken from corresponding distributor's websites[46].

Figure 4.19 shows several high aspect ratio tips which are currently available in market where tips are fabricated with (a) focused-ion-beam milling, (b) electron-beam-induced-deposition, (c)-(d) carbon nanotube attachment, and (d) "Nauga-needle formation" technique. The manufacturing method of corresponding tips are described in details as below.

4.5.1. Focused-ion-beam milling method

An obvious method to pattern the high aspect ratio tips is using focused ion beam (FIB) to "machine" the tips one by one (see figure 4.19 (a), Courtesy to Nanoworld website[47]). In this method, the material near the tip is milled away except the material along the tip axis, leading to a slender HAR pillar along the axis. This method is the most versatile one, because in principle FIB can create any arbitrary shape with resolution down to sub-5 nm and aspect ratio well beyond 10:1. Cockins et al.[48] demonstrated a method to fabricate a high-aspect ratio metal tip attached to machined cantilevers with controlled angle, length, and radius by focused ion beam. According to their method, the original tip of probe is completely milled away from the cantilever using FIB, and then the cantilever is glued with a wire attached onto the corner. Afterwards, the wire is sharpened to obtain the required tip shape using the technique reported in Refs.[49,50]. This fabrication technique usually takes less than 1 h. Figure 4.20 shows an example of final cantilever along with tip.

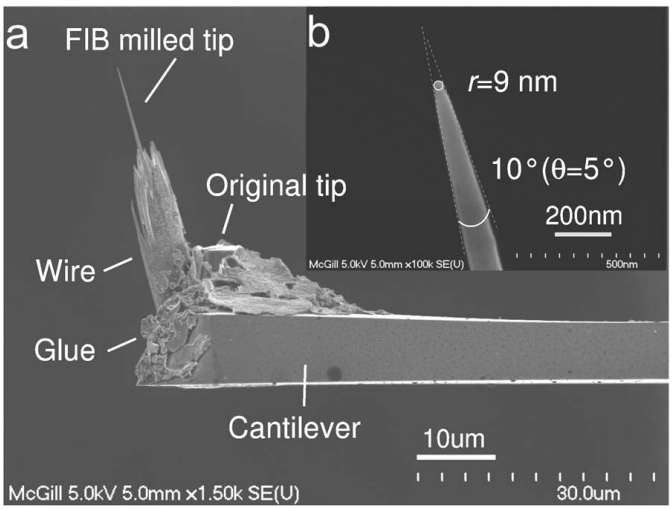

Figure 4.20. SEM images of (a) a fabricated HAR tip, (b) achieved radius of the tip[48].

Nitride tip also can be milled with FIB. Fu et al.[51] demonstrated the fabrication process to make the high aspect ratio 'nitride' tip by FIB milling, as shown in figure 4.21.

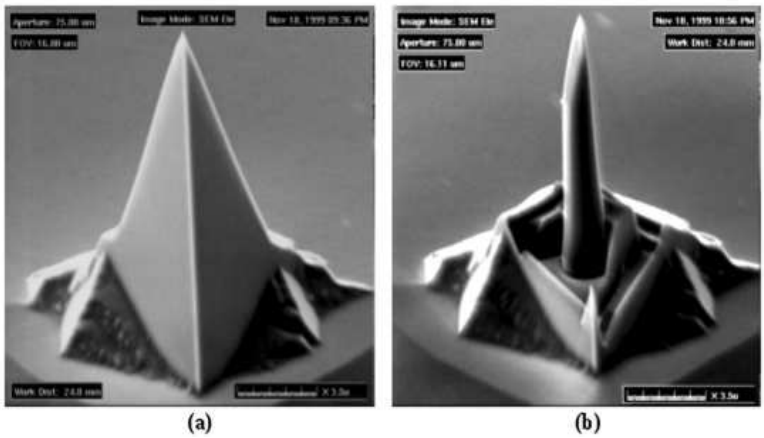

Figure 4.21. SEM images of a nitride AFM tip before and after FIB milling to fabricate high aspect ratio AFM tip[51].

4.5.2. Electron/ion-beam-induced-deposition (EBID/IBID) method

By adding precursor gas, extremely high aspect ratio pillars (the idea is discussed in Ref.[52]) can be grown onto AFM tip apex by ion or electron beam induced deposition (Figure 4.19 (b)). David et al.[53] first fabricated the high aspect ratio tip using the electron beam of a scanning electron microscope (SEM) by depositing thin carbon pillar on the end of commercially available

silicon nitride AFM cantilevers. They started their process by aligning the electron beam (in SEM tool, Hitachi S-800, equipped with organometallic gas flow such as $W(CO)_6$) directly down the axis of the commercial regular pyramid shaped nitride tip (30 nm Palladium-gold coated) mounted on standard aluminum stub. The SEM is then switched into spot (thus the beam is not in scanning mode) mode for a particular exposure time to grow the carbon pillar at the end of the cantilever. The tip apex is approximately 30 nm in diameter and about 15° of cone angles, and become cylindrical down the shank (Figure 4.22).

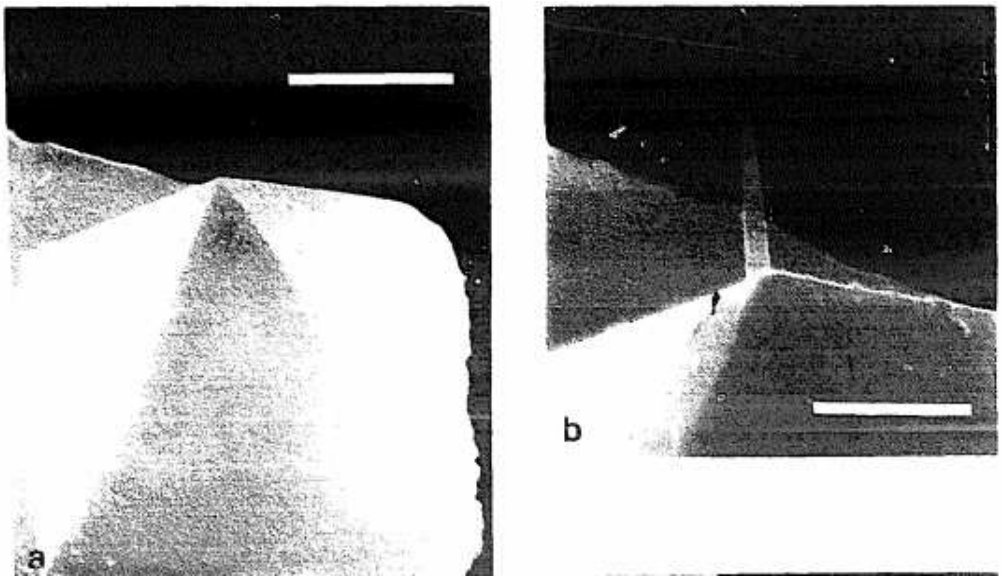

Figure 4.22. SEM images of (a) pyramidal nitride tip, and (b) the same tip after depositing a carbon pillar on its apex[53].

Comstock et al.[54] demonstrated the manufacturing method of a nanoneedle using electron beam induced deposition (EBID) process at the end of the probe to make it high aspect ratio tip. This process is shown in figure 4.23 where they initiated the process flow by FIB milling to flatten a particular area of the tip where EBID is used to deposit a long metal wire. Couple of atomic layer deposition (ALD) processes are employed to coat a conductive gold (Au) film with an alumina which is an insulating film, and FIB milling is followed in order to expose the gold electrode at the apex of the tip.

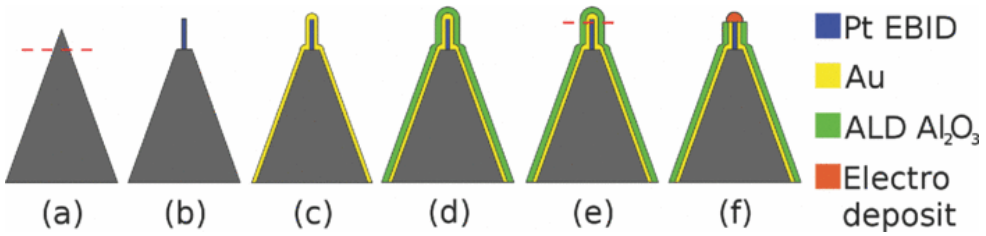

Figure 4.23. Schematic diagram of fabrication process of nanoneedle tip apex. (a) FIB milling to make a flat platform in tip. (b) Pt needle coated by EBID process. (c) Gold film deposited by evaporation technique. (d) Insulating layer of Al_2O_3 coated by ALD method. (e) FIB milled the insulated nanoneedle to expose an electrode layer. (f) Functional metal selectively electro-coated at the exposed tip apex[54].

As shown in figure 4.24, they also demonstrated nanoneedle (fabricated by EBID method) height is tunable by using different growth time.

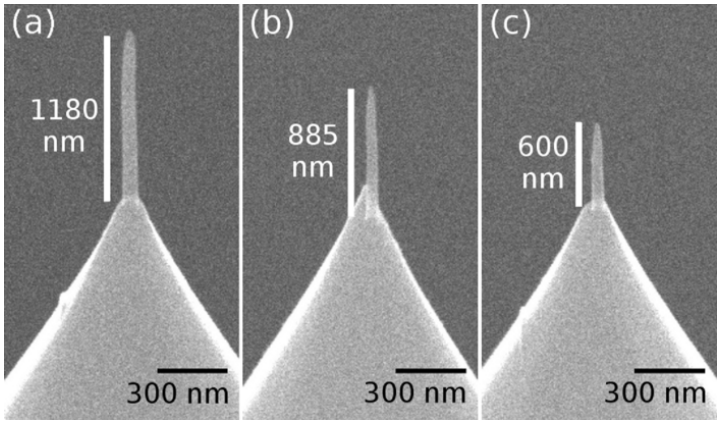

Figure 4.24. SEM images of electron beam deposited nanoneedle height as a function of deposition time, (a) 20 s. (b) 10 s. (c) 5 s [54].

This method was also followed by Brown et al[55] where they fabricated electrically conducting, ultra-sharp, high-aspect ratio probes by electron-beam-induced deposition of platinum. However, this process is too expensive and time consuming (as the tips are made one by one) for large area production.

4.5.3. Caron nanotube (CNT) attachment method

Carbon nanotube (Figure 4.19 (c)), or semiconductor nano-wire/spike (Figure 4.19 (d)) has also been used by attaching them or growing them at the apex of regular tips[56, 57, 58, 59]. It offers extremely high aspect ratio. Moreover, carbon nanotube has remarkable mechanical property, with much longer (by 20×) lifetime than regular silicon AFM tip[60]. However, it is very challenging to attach or grow a carbon nanotube at a precisely desired position with a fixed direction and length. Furthermore, though it offers a long scanning lifetime, in reality, tips are often damaged with the entire cantilever broken off the base during the handling process rather than get worn out after long continuous scanning. Woolley et al.[61] demonstrated the surface growth CVD nanotube tip preparation (in figure 4.25 (a)) where at top the schematic of the growth process is shown and at bottom image the TEM image of an individual SWNT tip produced using this technique was shown. Here, nanotubes were grown on the surface of the pyramidal structure and then guided by the edges towards the tip apex. Ye et al.[62] demonstrated directional-growth using plasma-enhanced CVD method to grow CNT on probe (Figure 4.25 (b)). In their method, each fabrication step was aligned to the global alignment mark which was fabricated with electron beam lithography. This assured the exact location of catalyst sites and thus the final CNT was located at the particular position on the cantilever. Figure 4.25 (b) shows the TEM image of a CNT fabricated on a cantilever produced by directional-growth plasma-enhanced CVD. In bottom image, CNT-deposited tip end was shown. The nickel catalyst on tip apex is clearly seen in this image. Additionally, Hafner et al.[63] demonstrated CNT pick up attachment method where a microfabricated pyramidal tip (Figure 4.25 (c)), which is coated with a thin layer of a UV-cure adhesive material, picks up a vertically aligned carbon nanotube. Figure 4.25 (c) shows schematic diagram of nanotube attachment through 'pick-up' method. In bottom of that image, it shows the TEM image of a picked SWNT tip.

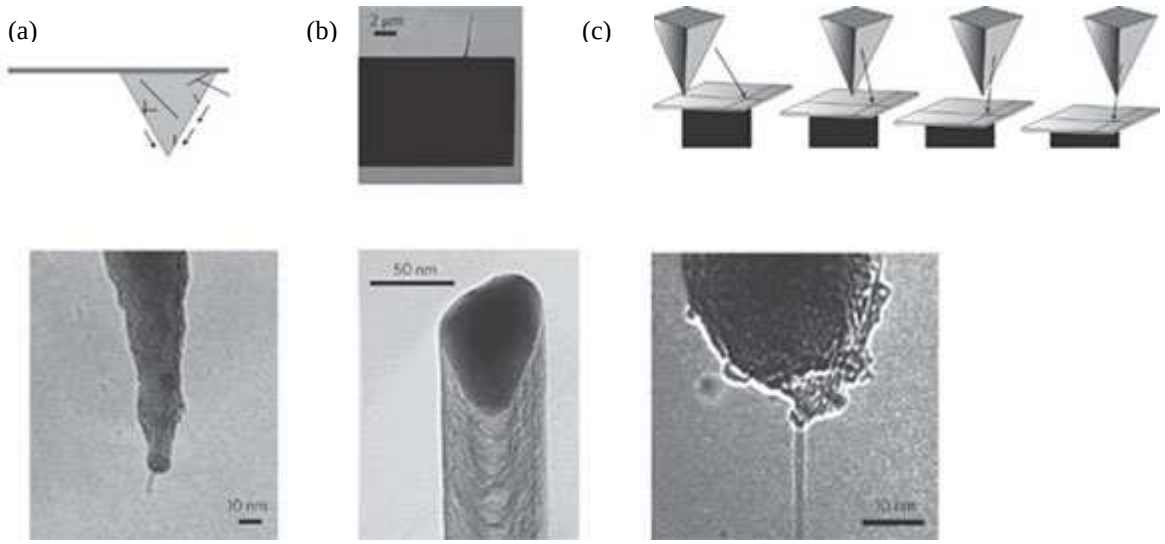

Figure 4.25. (a) Surface growth CVD nanotube tip fabrication method. Bottom: TEM image of single SWNT tip fabricated by this method[61]. (b) TEM image of single CNT attached on a cantilever produced by directional-growth plasma-enhanced CVD. Bottom: Nanotube tip apex[62]. (c) Nanotube attachment method through 'pick-up'. Bottom shows the TEM image of a SWNT tip[63].

4.5.4. "Nauga-needle formation" method

In this process, the regular AFM tip is first coated with metal (Ag), then it is dipped into a melted alloy of Gallium (Ga) The Ag-Ga alloy is gradually solidified/crystallized onto the tip while the tip is pulled out slowly, forming a solid alloy nanowire onto the tip. Recently this novel needle-shaped AFM tip was demonstrated and subsequently commercialized by NaugaNeedles Inc. (Figure 4.19 e)[64,65]. In this method, the localization of the needle to the tip is connected with both the longitudinal concentration gradient of Ag material that is dissolved from the tip apex[66] (Figure 4.26 (b)) and the transverse localization of the narrow-meniscus (Figure 4.26 (c)). Figure 4.26 (c) and (d) shows the possibility of several needles forming with one tip but eventually a single needle extends beyond the others. Another important issue is that (Figure 4.26 (d)) during joining Ga continues to reactively spread and make alloy with Ag attached to the tip and then it converts to a grainy pattern structure of Ag_2Ga crystallites over the probe. The ongoing spreading of Ga is finally detached from the excess un-reacted Ga, which in the end, reveals all the nanowire structures fabricated at the tip apex. They also demonstrated they could fabricate

freestanding needles at the end of tip-less probe and manufactured single needles of both horizontal and vertical orientations relative to the probe. However, the tip apex fabricated by this method is blunt as nanowire (formed with solid Ag-Ga alloy) diameter is quite big, as shown in figure 4.19 (e).

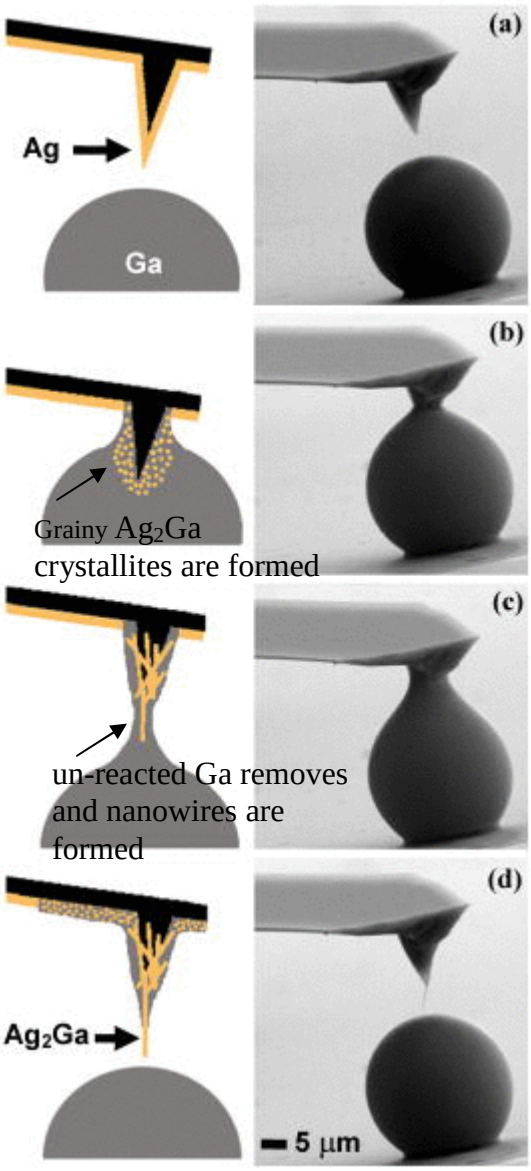

Figure 4.26. Fabrication steps for freestanding Nauga-needle fabrication: Schematic shown in left column and demonstration as recorded in time-sequential SEM images shown in right column[66].

4.5.5. Angle-dependant dry etching method (Our method)

All the above processes are serial process, where the high aspect ratio tips are formed one by one sequentially. Obviously, to drastically increase the throughput and reduce the cost, batch fabrication process is greatly desired. Therefore, manufacturing process where the patterns are formed spontaneously without using any lithography/alignment method is in great demand. One way to realize this lithography-free patterning is by using the spin-coating property of a polymer on non-planar AFM tips over a wafer[67]. Due to the protrusion nature of the tip out of the wafer, the polymer coating on it is less than that on the base of the AFM tip which, after a brief etch of the polymer, results polymer coating everywhere except near the tip apex. Alternatively, a metal can be coated onto the AFM tip, followed by electrochemical etching back of the metal[68]. The main issue for the above two lithography-free self-aligned patterning method is how to achieve sub-100 nm uniform feature size. For instance, the electrochemical etching method achieved aperture near the tip apex only down to 500 nm.

We, here, report a self-defined process to form metal dots right on top of the tip apex, without using any lithography. The process is based on the angle-dependent sputtering yield, which leads to slower sputtering of the metal film on top of the apex (normal incidence) than the film on the side of the apex (inclined incidence). Tips are then etched by ICP-RIE (Inductively Coupled Plasma – Reactive Ion Etching, a plasma etching process) using the metal as mask. Curvature radii and aspect ratio of fabricated high-aspect-ratio AFM tips prepared from commercial silicon tips are controllable and commercially viable. The details of this process are presented in Chapter 5.

4.6. Conclusions

In this chapter, we described an overview of AFM tool and its applications and later, recent fabrication techniques to make regular as well as high aspect ratio AFM probes. Currently, many AFM probes are fabricated directly by wet anisotropic etching or dry reactive ion etching. Compared with dry etching technique, wet etching is a cheaper procedure and is easily applied without involving expensive equipment. A simple, high yield method for the fabrication of

cantilever with nano-silicon tip by wet etching without oxidation sharpening steps for AFM applications is reviewed. The advantage of their method is that not only the tips but also the cantilevers are fabricated concurrently by the combined masked-maskless etching process, which makes the process cheaper. The benefit of novel DRIE based method is that dry etching processes offer better uniformity and reproducibility than wet etching processes. The feasibility of growing a continuous layer of graphene in probes is also discussed. Lastly, the methods to fabricate high aspect ratio AFM tips, such as FIB, EIBD, CNT attachment and "Nauga-needle formation" are reviewed in details. We, in addition, introduced our method (angle-dependent dry etching method) to batch fabricate high aspect ratio tips in a cheaper way compared with other commercial AFM probes fabrication methods.

4.7. References

[1] G. Binning, H. Rohrer, C. Gerber and E. Weibel, "Surface studies by scanning tunneling microscopy", Phys. Rev. lett. **49**, 57-61 (1982).

[2] G. Binning, C. F. Quate and C. Gerber, "Atomic force microscopy", Phys. Rev. Lett. **56**, 930-933 (1986).

[3] D. W. Pohl, W. Denk and M. Lanz, "Optical stethoscopy: Image recording with resolution lemda/20", Appl Phys. Lett. **44**, 651-653 (1984).

[4] A. A. Tseng, A. Notargiacomo and T. P. Chen, "Nanofabrication by scanning probe microscope lithography: A review", J. Vac. Sci. Technol. B. **23**, 877 (2005).

[5] JPK Instruments AFM Handbook, 2005.

[6] D. Wang, L. Tsau and K. L. Wang, "Nanometer-structure writing on Si (100) surfaces using a non contact mode atomic force microscope", Appl. Phys. Lett. **65**, 1415-1417 (1994).

[7] A. J. Bard, F. R. F. Fan, J. Kwak and O. Lav, "Scanning Electrochemical Microscopy. Introduction and Principles", Anal. Chem. **61**(2), 132-138 (1989).

[8] K. Wilder, C. F. Quate, D. Adderton, R. Bernstein and V. Elings, "Noncontact nanolithography using the atomic force microscope", Appl. Phys. Lett. **73**, 2527-2529 (1998).

[9] Z. J. Davis, G. Abadal, O. Hansen, X. Borise, N. Barniol, F. Perez-Murano and A. Boisen, "AFM lithography of aluminium for fabrication of nanomechanical systems", Ultramicroscopy **97**, 467-472 (2003).

[10] R. D. Piner, J. Zhu, F. Xu, S. Hong and C. A. Mirkin, "Dip-pen lithography", Science **283**, 661-663 (1999).

[11] L. L. Sohn and R. L. Willett, "Fabrication of nanostructures using atomic force microscope based lithography", Appl. Phys. Lett. **67**, 1552-1554 (1995).

[12] H. T. Lee, J. S. Oh, S. J. Park, K. H. Park, J. S. Ha, H. J. Yoo and J. Y. Koo, "Nanometer scale lithography on H-passivated Si (100) by atomic force microscope in air", J. Vac. Sci. Technol. **A 15**, 1451-1454 (1997).

[13] J. W. Park, N. Kawasegi, N. Morita and D. W. Lee, "Tribonanolithography of silicon in aqueous solution based on atomic force microscopy", Appl Phys.Lett. **85**, 1766-1768 (2004).

[14] H. J. Mamin and D. Rugar, "Thermomechanical writing with an atomic force microscope tip", Appl. Phys. Lett. **61,** 1003 (1992).

[15] H. J. Mamin, R. P. Ried, B. D. Terris, D. Rugar, "High-density data storage based on the atomic force microscope". Proceedings of the IEEE **87 (6),** 1014 (1999).

[16] P. Vettiger, G. Cross, M. Despont, U. Drechsler, U. Durig, B. Gotsmann, W. Haberle, M. A. Lantz, H. E. Rothuizen, R. Stutz, G. K. Binnig, "The millipede - nanotechnology entering data storage", Nanotechnology, IEEE Transactions **1.1,** 39-55 (2002).

[17] M. I. lutwyche, M. Despont, U. Drechsler, U. Durig, W. haberle, H. Rothuizen, R. Stutz, R. Widmer, G. K. Binning and P. Vettiger, "Highly parallel data storage system based on scanning probe arrays", Appl. Phys. Lett. **77**, 3299-3301 (2000).

[18] H.J. Kim, N. Moldovan, J.R. Felts, S. Somnath, Z. Dai, T.D. B. Jacobs, R.W. Carpick, J.A. Carlisle, and W.P. King, "Ultrananocrystalline diamond tip integrated onto a heated atomic force microscope cantilever", Nanotechnology **23,** 495302/1-9 (2012).

[19] T. R. Albrecht, S. Akamine, T. E. Carver, C. F. Quate, "Microfabrication of cantilever styli for the atomic force microscope", J Vac Sci Technol A. **8,** 3386–3396 (1990).

[20] H. Takahashi, Y. Mimura, S. Mori, M. Ishimori, A. Onoe, T. Ono, M. Esashi, "The fabrication of metallic tips with a silicon cantilever for probe-based ferroelectric data storage and their durability experiments", Nanotechnology **20,** 365201 (2009).

[21] I. W. Rangelow, "Sharp silicon tips for AFM and field emission", Microelectron Eng. **23,** 369–372 (1994).

[22] A. Boisen, O. Hansen, S. Bouwstra, "AFM probes with directly fabricated tips", J Micromech Microeng. **6,** 58–62 (1996).

[23] C. Liu, R. Gamble, "Mass-producible monolithic silicon probes for scanning probe microscopes", Sensor Actuat. A. **71,** 233–237 (1998).

[24] P. A. Rasmussen, J. Thaysen, S. Bouwstra, A. Boisen "Modular design of AFM probe with sputtered silicon tip", Sensor Actuat. A. **92,** 96–101 (2001).

[25] M. A. R. Alves, D. F. Takeuti, E. S. Braga, "Fabrication of sharp silicon tips employing anisotropic wet etching and reactive ion etching", Microelectron. J **36,** 51–54 (2005).

[26] P. Neuzil, R. J. Nagarajan, "The formation of sharp AFM tips by single step etching", Micromech Microeng. **16,** 1298–1300 (2006).

[27] L. Li, X. Han, W. G. Wu, F. Ding, Q. H. Chen, "Fabrication of novel cantilever with nanotip for AFM applications", Solid State Integr. Circuit Technol. ICSICT **20–23,** 2383–2386 (2008).

[28] T. Hantsche, P. D. Wolf, T. Trenk1er, R. Stephensona, W. Vandervorst, "Fabrication and use of metal tip and tip-on-tip probes for AFM.-based device analysis", SPIE Conference on Materials and Device Characterization in Micromachinina; Santa Clara, California. September 1998.

[29] D. Resnik, D. Vrtacnik, U. Aljancic, M. Mozek, S. Amon, "Different aspect ratio pyramidal tips obtained by wet etching of (100) and (111) silicon", Microelectron. J **34,** 591–593 (2003).

[30] E. Duriau, T. Clarysse, T. Hantschel, W. Vandervorst, "Fabrication of cantilevers and double AFM tips for the NanoProfiler", Microelectronic Engineering **84,** 1162–1167 (2007).

[31] D. P. Burt, P. S. Dobson, L. Donaldson, J. M. R. Weaver, "A simple method for high yield fabrication of sharp silicon tips", Microelectron Eng. **85,** 625–630 (2008).

[32] "AFM TIP NanoWorld Webinar", P. Russell Appalachian State Univ., 10 November 2008.

[33] J. Han, X. Li, H. Bao, G. Zuo, Y. Wang, F. Feng, Z. Yu, and X. Ge, "AFM probes fabricated with masked–maskless combined anisotropic etching and p+ surface doping", Journal of Micromechanics and Microengineering, **16(2),** 198– 204 (2006).

[34] C. Martin-Olmos, H. I. Rasool, B. H. Weiller, and J. K. Gimzewski,"Graphene MEMS: AFM probe performance improvement", ACS nano **7(5),** 4164–70 (2013).

[35] J. Li, J. Xie, W. Xue, and D. Wu, "Fabrication of cantilever with self-sharpening nanosilicon-tip for AFM applications", Microsystem Technologies **19(2),** 285– 290 (2012).

[36] B. Tang, K. Sato, H. Tanaka and M. A. Gosalvez, "Fabrication of sharp tips with high aspect ratio by surfactant-modified wet etching for the AFM probe", micro electro mechanical systems (mems) - ieee 24th international conference, 328 - 331 (2011).

[37] D. P. Burt, P. S. Dobson, L. Donaldson, J. M. R. Weaver, "A simple method for high yield fabrication of sharp silicon tips", Microelectron Eng. **85,** 625–630 (2008).

[38] J. Brugger, R. Buser, N. De Rooij, "Silicon cantilevers and tips for scanning force microscopy", Sensors and Actuators A – Physical **34(3),** 193–200 (1992).

[39] R. J. Fasching, Y. Tao, F.B. Prinz, "Cantilever tip probe arrays for simultaneous SECM and AFM analysis", Sensors and Actuators B – Chemical **108 (1–2),** 964–972 (2005).

[40] G. Villanueva, J. A. Plaza, A. Sánchez, K. Zinoviev, F. Pérez-Murano, and J. Bausells, "DRIE based novel technique for AFM probes fabrication",Microelectronic Engineering **84(5–8),** 1132–1135 (2007).

[41] G. Villanueva, J. A. Plaza, A. Sánchez-Amores, J. Bausells, E. Martínez, J. Samitier, A. Errachid, "Deep reactive ion etching and focused ion beam combination for nanotip fabrication", Materials Science and Engineering C **26,** 164–168 (2006).

[42] R. B. Marcus, T. S. Ravi, T. Gmitter, K. Chin, D. Liu, W. J. Orvis, D. R. Ciarlo, C. E. Hunt and J. Trujillo, "Formation of silicon tips with <1 nm radius" Appl. Phys. Lett. **56 (3),** 236 (1990).

[43] T. S. Ravi, R. B. Marcus, and D. Liu, "Oxidation sharpening of silicon tips", J. Vac. Sci. Technol. B **9(6),** 2733 (1991).

[44] http://www.nanosensors.com/

[45] A. Folch, M. S. Wrighton, and M. A. Schmidt, "Microfabrication of Oxidation- Sharpened Silicon Tips on Silicon Nitride Cantilevers for Atomic Force Microscopy",Journal of microelectromechanical systems **6(4),** 303–306 (1997).

[46] http://www.nanoworld.com/, http://nanosensors.com, http://www.nauganeedles.com.

[47] NanoWorld AG, Neuchatel, Switzerland.

[48] L. Cockins, Y. Miyahara, R. Stomp, and P. Grutter, "High-aspect ratio metal tips attached to atomic force microscopy cantilevers with controlled angle, length, and radius for electrostatic force microscopy", Review Of Scientific Instruments **78,** 113706 (2007).

[49] K. Akiyama, T. Eguchi, T. An, Y. Fujikawa, Y. Yamada-Takamura, T. Sakurai, and Y. Hagegawa, "Development of a metal tip cantilever for non-contact atomic force microscopy", Rev. Sci. Instrum. **76**, 033705 (2005).

[50] M. J. Vasile, D. Grigg, J. E. Griffith, E. Fitzgerald, and P. E. Russell, "Scanning Probe Tip Geometry Optimized for Metrology by FIB Ion Milling", J. Vac. Sci. Technol. B **9**, 3569 (1991).

[51] Y. Fu, W. Zhou and L. Lim, "Geometrical characterization issues of plasmonic nanostructures with depth-tuned grooves for beam shaping", Optical Engineering **45(10),** 108001 (2006).

[52] W. Li and P. A. Warburton, "Low-current focused-ion-beam induced deposition of three-dimensional tungsten nanoscale conductors", Nanotechnology **18,** 485305 (2007).

[53] J. K. David., and C. Chou, "Imaging steep, high structures by scanning force microscopy with electron beam deposited tips", Surface Science **268**, 333-339 (1992).

[54] D. J. Comstock, J. W. Elam, M. J. Pellin and M. C. Hersam, "High aspect ratio nanoneedle probes with an integrated electrode at the tip apex", Review of scientific instruments **83,** 113704 (2012).

[55] J. Brown, P. Kocher, C. S. Ramanujan, D. N. Sharp, K. Torimitsu, J. F. Ryan, "Electrically conducting, ultra-sharp, high aspect-ratio probes for AFM fabricated by electron-beam-induced deposition of platinum", Ultramicroscopy **133,** 62–66 (2013).

[56] H. J. Dai, J. H. Hafner, A. G. Rinzler, D. T. Colbert, R. E. Smalley, "Nanotubes as nanoprobes in scanning probe microscopy", Nature **384,** 147 (1996).

[57] N. R. Wilson and J. V. Macpherson, "Carbon nanotube tips for atomic force microscopy", Nature Nanotechnology **4,** 483 (2009).

[58] C. V. Nguyen, Q. Ye and M Meyyappan, "Carbon naotube tips for scanning probe microscopy: fabrication and high aspect ratio nanometraology", Measurement Science and Technology **16,** 2138 (2005).

[59] S. Kuwahara, S. Akita, M. Shirakihara, T. Sugai, Y. Nakayama, H. Shinohara, "Fabrication and characterization of high-resolution AFM tips with high-quality double-wall carbon nanotubes", Chemical Physics Letters **429,** 581–585 (2006).

[60] T. Larsen, K. Moloni, F. Flack, M. A. Eriksson, M. G. Lagally, C. T. Black, "Comparison of wear characteristics of etched-silicon and carbon nanotube atomic force microscopy probes", Appl. Phys. Lett. **50,** 1996 (2002).

[61] A. T. Woolley, C. L. Cheung, J. H. Hafner, and C. M. Lieber, "Structural biology with carbon nanotube AFM probes", Chem. Biol. **7,** R193–R204 (2000).

[62] Q. Ye et al., "Large-scale fabrication of carbon nanotube probe tips for atomic force microscopy critical dimension imaging applications", Nano Lett. **4**, 1301–1308 (2004).

[63] J. H. Hafner, C. L. Cheung, T. H. Oosterkamp, and C. M. Lieber, "High-yield assembly of individual single-walled carbon nanotube tips for scanning probe microscopies", J. Phys. Chem. B **105**, 743–746 (2001).

[64] R. Jalilian, J. Rivera, D. Askari, S. Arva, J. M. Rathfon, R. W. Cohn and M. M. Yazdanpanah, "Toward wafer-scale patterning of freestanding intermetallic nanowires", Nanotechnology **22,** 295601 (2011).

[65] http://nauganeedles.com/.

[66] M. M. Yazdanpanah, S. A. Harfenist, A. Safir and R. W. Cohn, "Selective self-assembly at room temperature of individual freestanding Ag_2Ga alloy nanoneedles", J. Appl. Phys. **98,** 073510 (2005).

[67] E. Yenilmez, Q. Wang, R. J. Chen, D. Wang and H. Dai,"Wafer scale production of carbon nanotube scanning probe tips for atomic force microscopy",Appl. Phys. Lett. **80,** 2225 (2002).

[68] H. Hu, H. Yeom, G. Mensing, Y. Chen, M. A. Shannon and W. King, "Nano-fabrication with a flexible array of nano-apertures", Nanotechnology **23,** 175303 (2012).

CHAPTER 5

Batch fabrication of high aspect ratio AFM tips

This chapter describes our method to batch fabricate high-aspect ratio AFM tips by dry etching. The key point that differentiates our technology from the competing ones is that the tips are fabricated in high throughput batch manner, whereas the current commercially available high aspect ratio tips are all fabricated one by one.

5.1. Introduction

A widely used tool in nanotechnology is the Atomic Force Microscope (AFM) for which the most important part is the tip (also popularly called as “probe”) which can "feels" the sample surface and creates an image. In order to get high quality images, very high aspect ratio tips are required, i.e. have to be long and thin. But these high aspect ratio tips are extremely difficult to make and consequently very expensive ($70-$500 per tip) and therefore only bought sparingly. We developed a disruptive technique that enables the fabrication of these tips much cheaper than the cheapest alternative in the current market. The key feature of the technology is that it is a batch fabrication process with potentially high yield. The process starts from a wafer of AFM tips containing 380 regular pyramid-shaped (low aspect ratio) tips, and process them simultaneously to produce fine and high aspect ratio pillars at the tip apex. Currently all the commercially available high aspect ratio AFM tips are made one by one, in a slow, costly (~5-20× that of regular AFM tips) and serial manner, which was elaborated in details in previous chapter. On the contrary, our process is a batch process, and thus with much higher throughput and much lower manufacturing cost per tip. The benefit of using such tips, as compared to

regular pyramid-shaped low aspect ratio ones, is most pronounced when measuring a sample having deep recessed features like nanoscale trenches or holes, for which significant artifact would result if using regular AFM tips.

In below, we will first describe how to fabricate pyramid structure on flat silicon wafer to mimic costly AFM tip. Then we will detail the process to make high aspect ratio tips out of those pyramid structure in large scale. Next, we will transfer this process to real commercial regular AFM tips. Finally, we will characterize/verify the tips manufactured by our technique on high aspect ratio patterns to show its high quality for imaging.

5.2. Fabrication of pyramidal structures on flat silicon wafer

We fabricated pyramid-shaped "tips" on flat silicon wafer, to mimic the costly real AFM tips. A wafer of real tips (some 380 tips on a 4" wafer, the individual tips can be lifted out using tweezers) is commercially available but at relatively high price. Therefore, it would be cost-efficient to work on large scale pyramid "tips" fabricated by us. We fabricated pyramid structures[1] (without a cantilever) on a flat silicon wafer to develop our fabrication process. Once the process is developed, it could be transferred to the large-scale whole wafer of commercial AFM tips.

5.2.1. Fabrication of random pyramid arrays without using lithography

Pyramid structure can be fabricated on single crystalline Si wafer using aqueous KOH wet etch without any lithography. Orientation selective etch of [100]-oriented silicon wafers occur in basic (base) solutions partly because of the closer packing of some orientations relative to other orientations. Since density of planes <111> > <110>, <100>, the etch rate R(111) << R(110) and R(100). The reason behind lower etching rate is that {100} and {110} have 2 bonds below surface and 2 dangling bonds that can react; on the other hand, {111} plane has three of its bonds below surface and only one dangling bond to react, hence {111} has much slower etch rate. This bulk wet anisotropic wet etching process is widely used in MEMS (micro electro mechanical systems) since it is inexpensive, fast and easy to process.

To describe the process, the wafer was first cleaned by HF dipping in order to remove the native oxide (1:50 diluted HF, dip for 30 sec), then we performed aqueous KOH etching right away. The KOH wet etching was carried out using 20% (w/v%) KOH at 50 °C for 11 min and then washed with DI water.

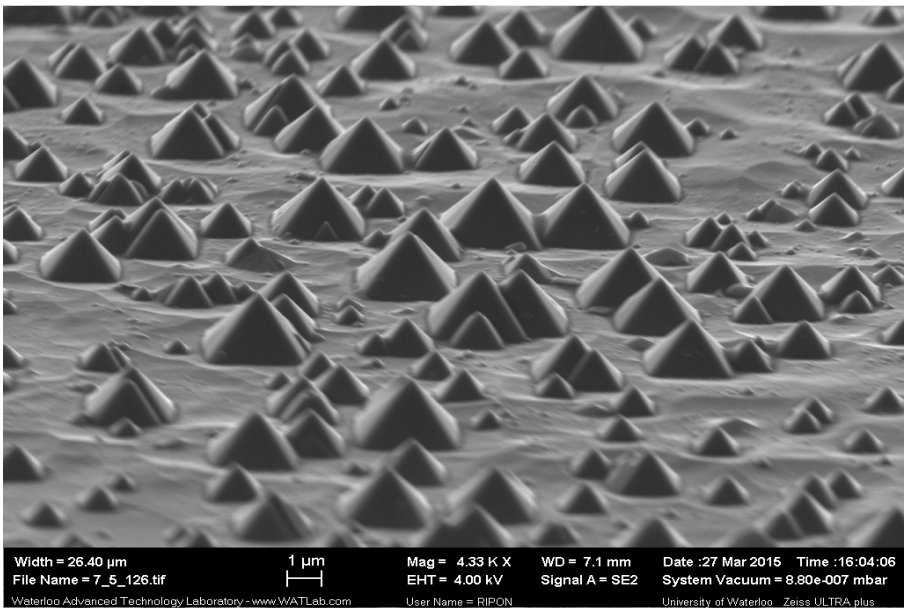

Figure 5.1. Random pyramid arrays of different dimensions.

Fabricated pyramids of different sizes, patterned at random locations, is demonstrated in figure 5.1. The largest dimension of pyramid sidewall edge is about 3 µm. Some pyramids are connected with other pyramids. These random pyramids of different dimensions are very useful for process development purpose since it is fabricated without using any costly lithography and the pyramids covers everywhere of a whole wafer (large-area).

5.2.2. Fabrication of pyramid arrays using lithography

In previous section, we described a process to fabricate uncontrolled pyramid with different dimension which are randomly patterned. However, for ultimate AFM tip fabrication, we need to manufacture pyramid tips with specific dimension and at controlled location. Here, we show how to fabricate the pyramid arrays of controlled dimension and at controlled placement using electron beam lithography as described below. We started with a silicon wafer (100) with oxide

of ~180 nm, as shown in figure 5.2. After solvent cleaning, we spun-coat 300 nm polystyrene (PS) on silicon dioxide. We demonstrated the polydispersity does not make any significant influence on material exposure properties[2]. Thus, we mixed two different molecular weights polystyrene to make an equivalent 550 kg/mol (broad distribution) polystyrene on Si. Different sizes of square arrays were exposed on PS/SiO_2 at 20 KeV with 0.306 nA beam current at dose 30 μC/cm^2 which would be used as mask later. After developing with tetrahydrofuron for 1 min, the pattern was transferred to SiO_2 and Si by dry etching with CHF_3 gas using PS as an etching mask (RIE recipe: CHF_3: 20 sccm, RF: 100 W, ICP: 0 W, P: 20 mT, T: 480 sec, SiO_2 etching rate: 38 nm/min). After oxygen plasma cleaning of possible fluorocarbon polymer, KOH (20 w/v%) wet anisotropic etching was performed at ~50 ^{0}C for 11 min in order to fabricate pyramid structure on flat silicon wafer.

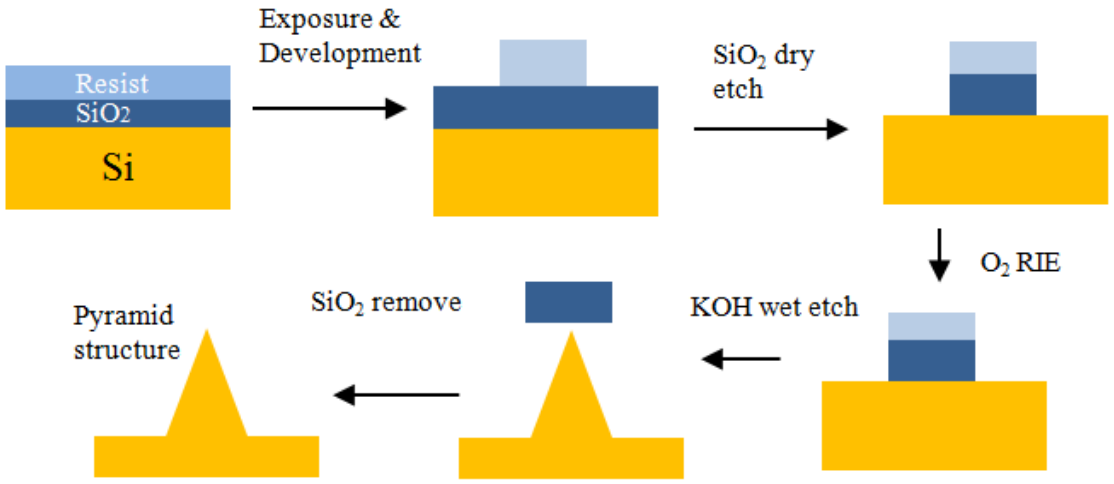

Figure 5.2. Process steps to fabricate the pyramid structure on single crystalline silicon.

Figure 5.3 shows the tilted view of pyramidal structure below the SiO_2 mask layer. KOH etching duration controls the pyramid apex dimension such as the area of top and shape of the pyramid. KOH etching is exponentially temperature-sensitive, thus it is crucial to maintain a constant etching temperature for reproducibility.

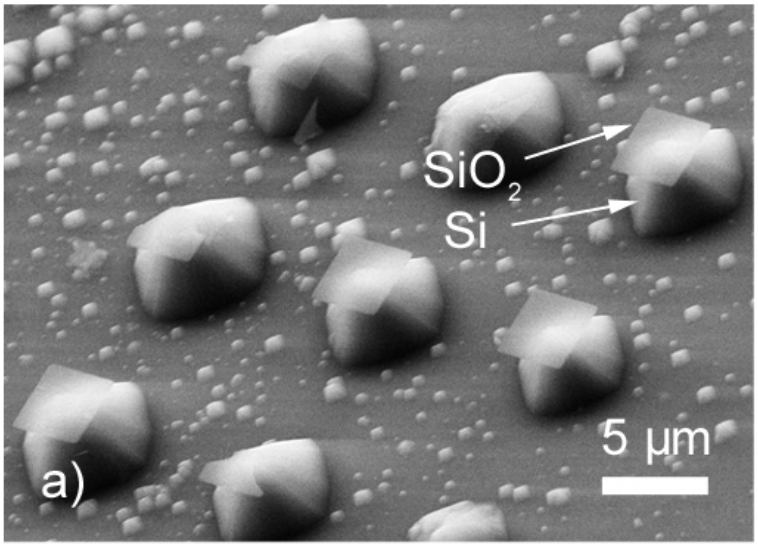

Figure 5.3. SEM micrographs of fabricated pyramidal structure with SiO_2 mask layer still remains on the top.

The wet etching time and mask size define the pyramid tip apex dimension. Less wet etching time than required makes the structure blunt. As shown in figure 5.4 (a-b), sharp apex was achieved by optimal KOH etching time, here 11 min at 50 ^{0}C, whereas blunt pyramid resulted for inadequate KOH etching time of 10 min (figure 5.4 c) and 7 min (figure 5.4 d).

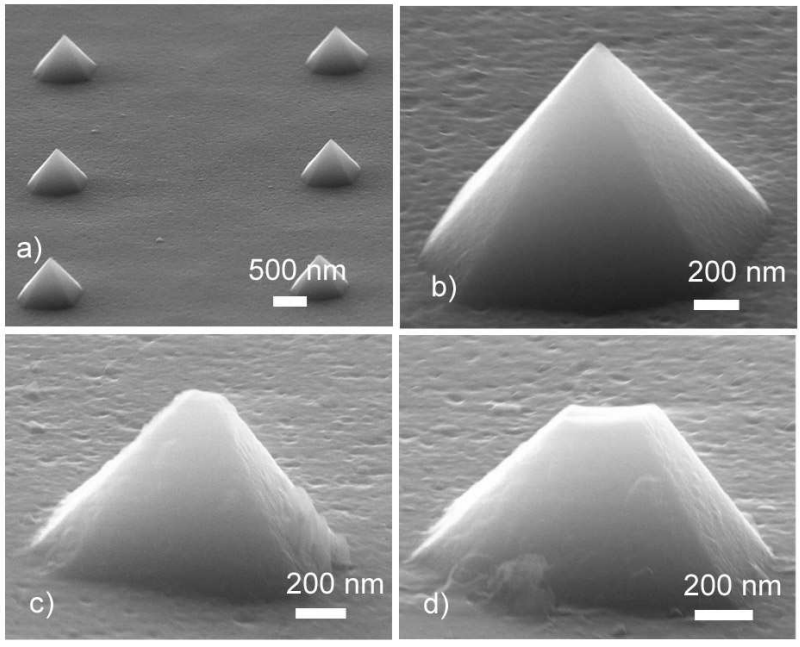

Figure 5.4. SEM images of fabricated silicon pyramid structures with sharp apex (a-b), and blunt apex (c-d). Here, (a-b) is etched for 11 min, (c) for 10 min and (d) for 7 min etched at 50 ^{0}C.

In below, we will apply our proposed process on random pyramid arrays fabricated without lithography where pyramids cover randomly in the entire wafer surface, as it is easy to handle and cost-effective to fabricate.

5.3. Fabrication of high aspect ratio (HAR) tips

Our process is a lithography-free self-aligned fabrication process, where the whole wafer of regular tip can be batch-processed simultaneously to convert the pyramid-shaped or point-shaped tips into high aspect ratio pillar-shaped tips. We propose two ways to make high aspect ratio tips with dry etching technique, (1) To fabricate HAR tips by forming etch mask using angle-dependant dry etching; and (2) To fabricate those tips by forming etch mask using two-angle evaporation method. We achieved expected result using the first process, but not with second process.

5.3.1. Fabrication of HAR tip by forming etch mask using angle-dependant etching

The idea of this process is based on the intrinsic properties of physical etching of a film. The efficiency of physical etching by ion bombardment/sputtering of the substrate material is characterized by sputtering yield defined as number of recoiling atoms out of the target surface per incident ion. Yamamura et al[3,4] have demonstrated an empirical formula to calculate the mean value of the sputtering yield for many incident ion-target combinations over a wide range of ion energy as well as a range of incidence angles from the normal of the target surface. In principle, the incident projectile ion loses energy by two separate mechanisms: collisions with the target nuclei, known as nuclear losses; and collisions with electrons in the target material, known as electronic losses. Incident ion energy and the target to projectile mass ratio control the contributions of both of these energy loss factors in terms of the net energy loss. The sputtering yield depends on the angle at which the energetic ion collides the target material, incident energy and atomic mass of projectile ion and cohesive energy of target material. Incidence ion angles

are frequently defined from the normal of target surface, where 0° corresponds to normal incidence (horizontal flat surface) and 90° corresponds to vertical surface. As the incidence angle of projectile ion increases at a certain level, the sputtering yield (target atoms/ion) is observed to increase. However, at large angles (when the projectile ion passes almost parallel to the target interface), such as close to 90°, "surface channeling" makes the sputtering yield almost zero.

Figure 5.5 shows the dependency of the sputtering yield (Y) on the angle of incidence and target material at different ion energies of 300 eV and 90 keV (In RIE, the typical ion energy range is 10-300 eV). In figure 5.5 (a), since Ti has higher cohesive energy (as shown in inset table) than Al, Ti has the lower sputtering yield by Ar ion. We employed three different materials (Al, Cr and Ti) for metal coating, and here we showed the result with Fe (iron) to mimic Cr, since their cohesive energies are very close to each other. In addition, we employed BCl_3 or Cl_2 gases for metal etching, however, we simulated the data with Ar (18) gas since its atomic number is close to Cl (17). The maximum sputtering yield occurs at a relatively large incident angle of 72° which is 2.5 times higher than the sputtering yield at normal incident angle (namely 0°) for each ion/target material at low energy as shown in figure 5.5 (a). However, in figure 5.5 (b), sputtering yield is much higher for higher energy (90 keV) for each ion-target material than that for low energy. The maximum yield of Ar/Al (ion/target) at 90 keV is 58 atoms/ion, where that at 300 eV is 1.7 atoms/ion. The incident angle for maximum yield is shifted to 85° at such high energy.

We employed fluorine (F) gas for silicon etching, however, here we simulated the etching with Boron (5) gas since its atomic number is close to F (9), as shown in figure 5.5 (b). It is shown that the sputtering yield of Si by B ion is very low, in comparison with other ion/target materials simulated here.

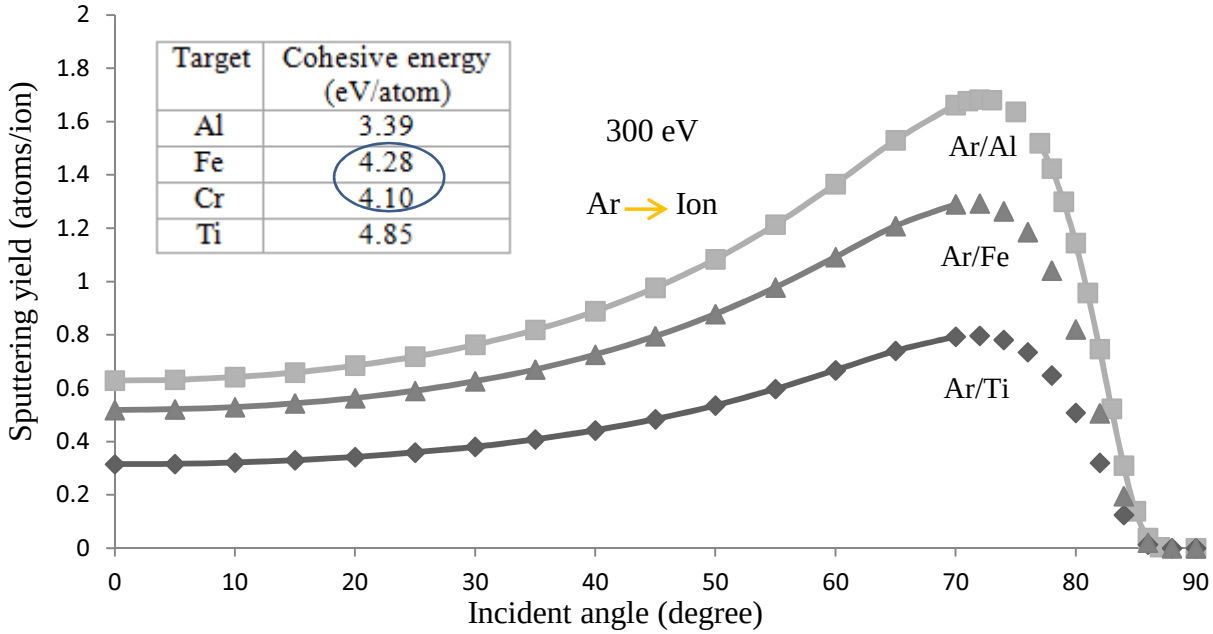

(a)

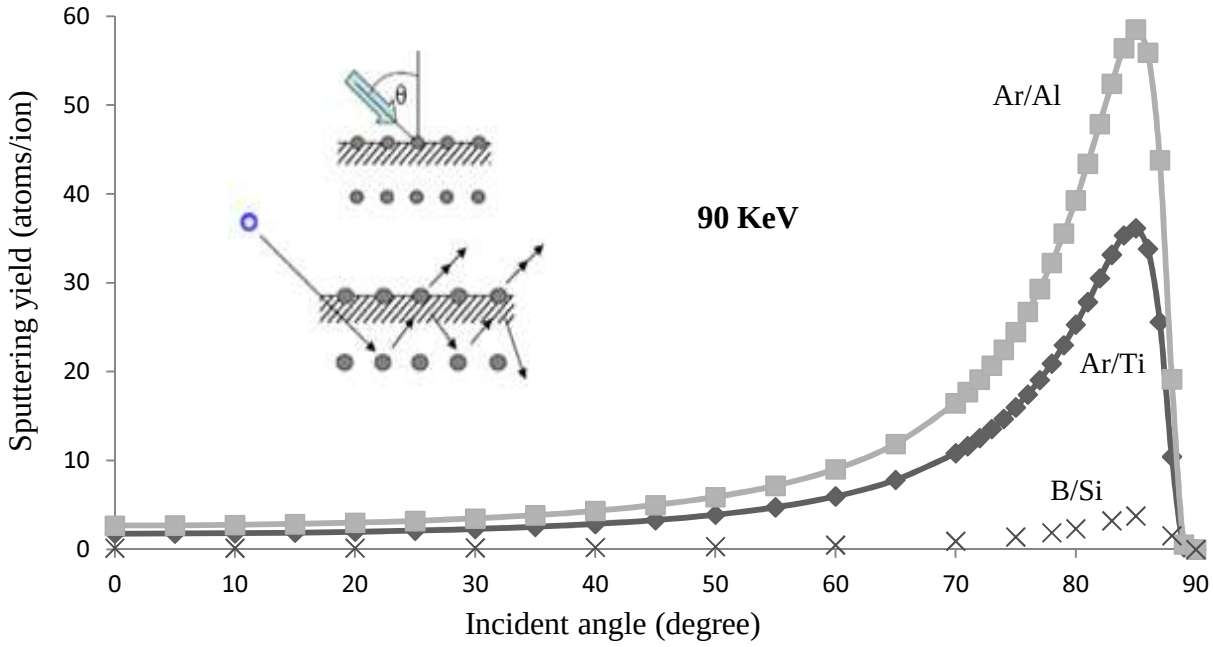

(b)

Figure 5.5. TRIM simulation results. (TRIM[5,6] is a commercial software: "Transport of Ions in Matter", a Monte Carlo computer program that calculates the interactions of energetic ions with target material). Sputtering yield as a function of incident angle with ion at (a) low energy, (b) high energy. Inset table in (a) shows the cohesive energies (amount of energy that takes to break

the material into isolated atoms) of particular target atoms. Inset in (b) shows the schematic of sputter yield as a function of ion incidence angle (θ) in a single crystalline surface.

In simulation, we neglected re-deposition of small amount of ejected atoms on an already sputtered surface.

5.3.1.1. Fabrication process of HAR tip

Based on the property of angle dependent sputtering yield, our batch fabrication process is shown in figure 5.6. We first coat a metal layer, such as Al, Cr or Ti, on top of the regular pyramid-shaped tips. Then we etch the metal using Ar, BCl_3 or Cl_2 gas depending on the metal deposited on the pyramid-shaped tips. The etching by Ar is physical, without any chemical reaction whereas the etching by BCl_3 and Cl_2 is both physical and chemical (physical enhanced chemical etching). As aforementioned, the etching rate on the side of the pyramid is faster than that on the very top apex, because: 1) the local ion incident angle on the side of the pyramid is closer to the maximum etching rate angle of ~72° at low ion energy than that on the very top of the tip apex where near normal incident is expected; and 2) the film thickness on the sidewall is less than that on top of the tip apex by a factor of cosθ. As a result, with well controlled etching time, it is possible to remove all the metal from the pyramid sidewalls, with some metal film would still remained on the horizontal surface at the tip apex. Next, the tip is etched in a reactive ion etching (RIE) system using fluorine-based gas, which etches the silicon anisotropically with vertical sidewall and very high selectivity to that of metal mask material self-formed on the tip apex. This will result in a silicon pillar right below the metal mask. The height of the pillar, thus the aspect ratio, can be controlled simply by the silicon etching time as long as metal etch mask left. As the process contains only three major steps (metal deposition, metal etch, Si etch), the time to process one wafer of tips (380 of them) is ~2-3 hours in a typical cleanroom (much faster in a production environment where wafers are processed cassette by cassette, each cassette containing 25 wafers).

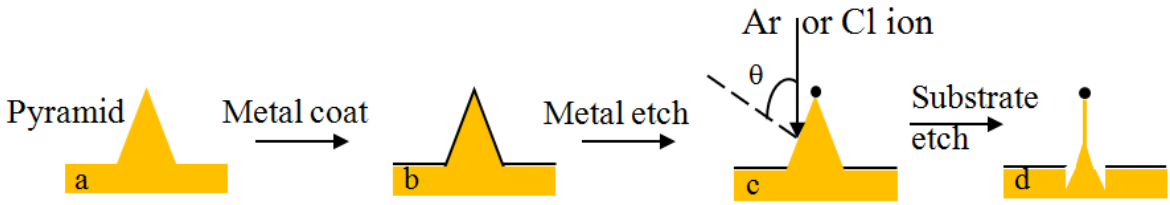

Figure 5.6. Process flow of fabricating high aspect ratio AFM tip. a) Start from a regular AFM tip with pyramid shape; b) Coat a thin layer of metal film; c) Etch the film using Ar, BCl_3 or Cl_2 gas plasma depending on the metal deposited; d) Etch the silicon using SF_6/C_4F_8 plasma, and finally the remaining metal can be removed easily by wet etching.

The key advantages of the current method are summarized here: (1) It is a batch process, where a wafer of regular tips (380 tips over 4" wafer) are processed simultaneously to create high aspect ratio tips. (2) It contains only three major steps, thus the yield is expected to be reasonably high. (For comparison, to make regular AFM tips starting from a wafer takes more than 10 major steps, thus it is much more challenging to achieve a high yield. For instance, if assuming each step has a yield of 98%, then after 10 steps the yield is $(0.98)^{10}$=82%. (3) The cost of fabrication is expected to be well below (estimated 10-25% that of) the other competing methods used to make commercial high aspect ratio AFM tip in batch. (4) Tip dimensions can be controllable, notably sidewall height are tunable according to the different applications. (5) The sharp apex of the original tips is unaltered, as it is protected by the metal mask atop during silicon RIE process.

In table 5.1 and 5.2, the metal dry etching recipes with Ar, BCl_3, Cl_2 gases and substrate dry etching recipe (developed by Prof. Saini's group[7], University of Waterloo) with SF_6/C_4F_8 plasma gases, and etching rate for different materials using these recipes are summarized. The metal dry etch recipes were adjusted to enhance energetic particle bombardment similar to ion milling (physical etching), by using higher RF power and lower pressure as long as we can still turn the plasma on. The etching rates shown in the tables are calculated based on horizontal surface only, not tilted surface. As we see in the table 5.2, the selectivity of etching rates of Al and Cr with Si is very high for Si etch, which are 108:1 and 96:1 respectively. As a result, only a very thin film of Al or Cr is required as etching mask to etch either silicon or silicon nitride vertically.

Table 5.1. Metal RIE recipes for etching different materials at low pressure.

Gases flow (sccm)	Pressure (mT)	RF power (W)	ICP power (W)	Temp. (°C)	Materials to etch	Etch rates (nm/min)
BCl_3: 50	1	300	800	22	Al	115
					Cr	10
					Ti	98
					Si	190
Cl_2: 50, O_2: 5	2	300	600	50	Cr	39
					Al	30
Ar: 20	7	300	100	RT	Cr	4.8

Table 5.2. Silicon RIE recipe for etching different materials.

Gases flow (sccm)	Pressure (mT)	RF power (W)	ICP power (W)	Temp. (°C)	Materials to etch	Etch rates (nm/min)
C_4F_8: 38, SF_6: 22	10	20	1200	15	Si	432
					Si_3N_4 (LPCVD)	117
					Cr	4
					Al	4.5

5.3.1.2. Results on large-area pyramidal structure on a silicon wafer

Our ultimate target is batch processing of pre-made regular tips to obtain the high aspect ratio tips. Due to the very high cost for a wafer of tips ($4000 for a wafer of 380 tips), we had been working on simultaneous processing of small batches of ~2 AFM tips (instead of a wafer of 380 tips) for each round. However, alternatively, we employed whole wafer containing pyramid arrays (cost-effective to fabricate and easy to handle) to see the result of uniformity, reproducibility, yield and so on, in a large scale (across a 4" wafer).

Here we present the results applying our technique on large-area pyramidal tips fabricated on a Si wafer. We coated Cr metal layer on top of the regular pyramid-shaped tip arrays. Then, we etched the metal using Cl_2 and O_2 gases (according to table 5.1). As a result, with well controlled etching time, it removed all the metal on the pyramid sidewall, leaving some metal mask on the horizontal surface of pyramidal tip apex. Next, the tip was etched in a reactive ion etching system using fluorine-based gas, which etched the silicon anisotropically with vertical sidewall. This resulted in a silicon pillar right below the metal mask. In figure 5.7, one side of whole silicon wafer was covered during metal evaporation, thus metal was coated only on the other side of the wafer. The covered area is marked as no-metal area. As seen in figure 5.7 the interface of metal and no-metal area is clear. In inset, a high aspect ratio AFM tip with diameter of 15 nm fabricated using this process is demonstrated (this tip is not the same tip as shown at the interface). As expected, on no-metal area, the pyramids were not terminated with high aspect ratio pillars on pyramid apex.

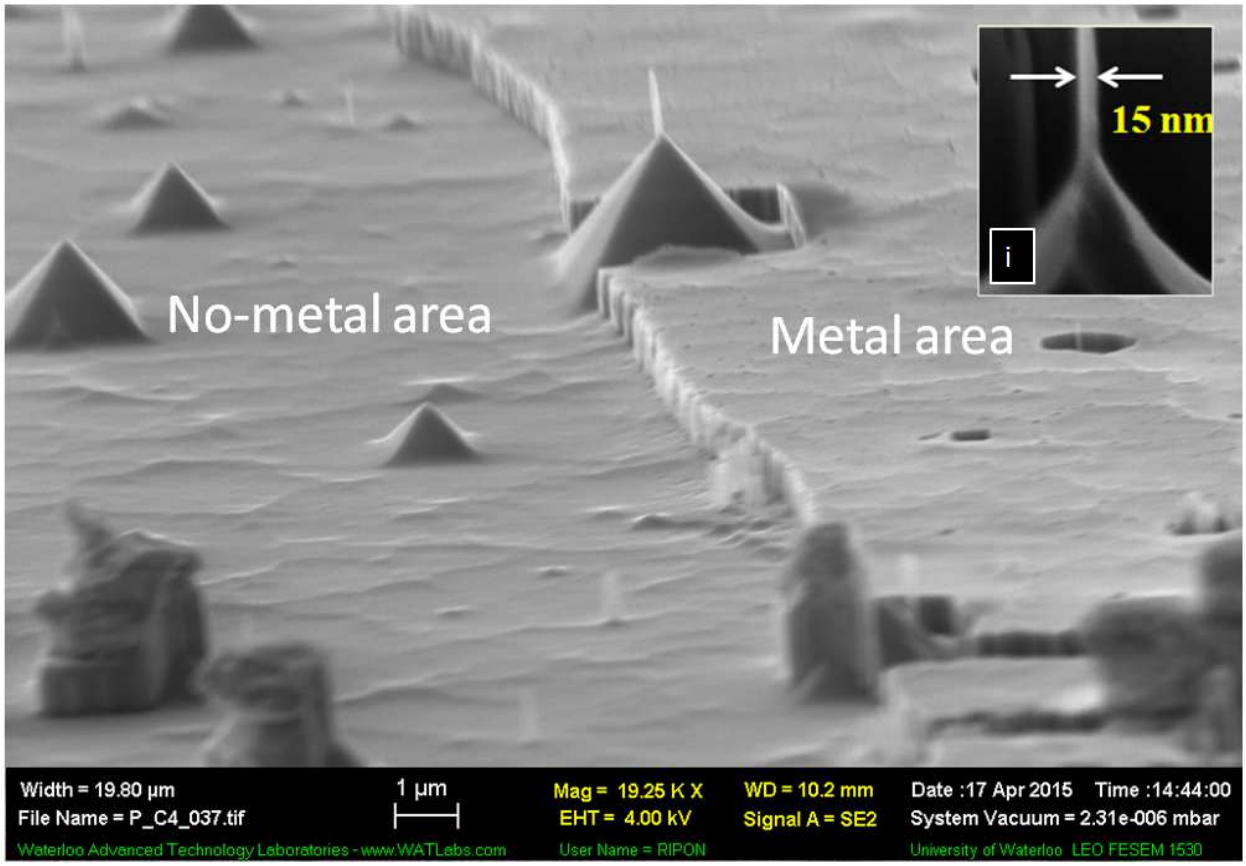

Figure 5.7. SEM image of interface of metal and no-metal area, In inset, a high aspect ratio AFM tip (not shown in big image) with diameter of 15 nm fabricated using this angle-dependent etching method is shown.

Prior to achieving the high throughput fabrication for production, there are a few essential steps that need to be streamlined. The following is the list of the technical challenges that need to be addressed in order to reach high throughput manufacturing:

1. *Reproducibility and uniformity, with a yield of ≥ 75%*. We developed the process using the selected metals such as aluminum, chromium and titanium for scaling up production. We here optimized the process steps to achieve reproducibly of the high aspect ratio AFM tips with desired tip dimensions using selected metals. The goal is to achieve high reproducibility (>70%) needed for production. We coated the whole 4" wafer pyramid arrays with metal (Cr 23 nm) and etched metal for 30 sec, and then etched silicon for 1:30 min. The results at five different locations of a whole wafer are shown in figure 5.8. In figure 5.8 (f), it shows the five different

placements where SEM images were captured. According to table 5.3, which was derived from the results in figure 5.8, the yield in the wafer center is highest which is 83% and that of other locations are lower than center of the wafer. This is expected because the metal film thickness and etching rate at the edge of wafer is lower than those in the center; and in addition, the metal incident angle from small crucible in evaporation chamber at edge of the wafer is different than that in the center. For evaporation of metal which finally acts as a hard mask on top, the metal film thickness for vacuum evaporation is proportional to $\cos\theta$, with θ being the incident angle relative to wafer normal direction. In addition, the film coated on an angled surface (relative to beam incidence) may not be as smooth as a film coated on a flat surface, thus complicating the process and slightly narrowing the process window. A common consequence of a rough film is the rough tip sidewall that amplifies the roughness of the etching mask after silicon etch due to the very high etching rate selectivity between Si and metal.

Regarding reproducibility, we fabricated several batches of pyramid tips and obtained satisfactory reproducible results. Once reproducible results were obtained, we focused on processing a wafer of tips (again, pyramids on wafer, not real AFM tips) in order to study the dimension/shape uniformity of the fabricated tips across the entire wafer of tips. We evaluated the uniformity of the process across an entire wafer of tips. According to table 5.3, the uniformity of tip dimension is best at wafer center. The variation in other positions of the wafer is also small. However, the results might be different for a real wafer of tips with uniform size of pyramid tips from the random size pyramids on a flat wafer as studied here.

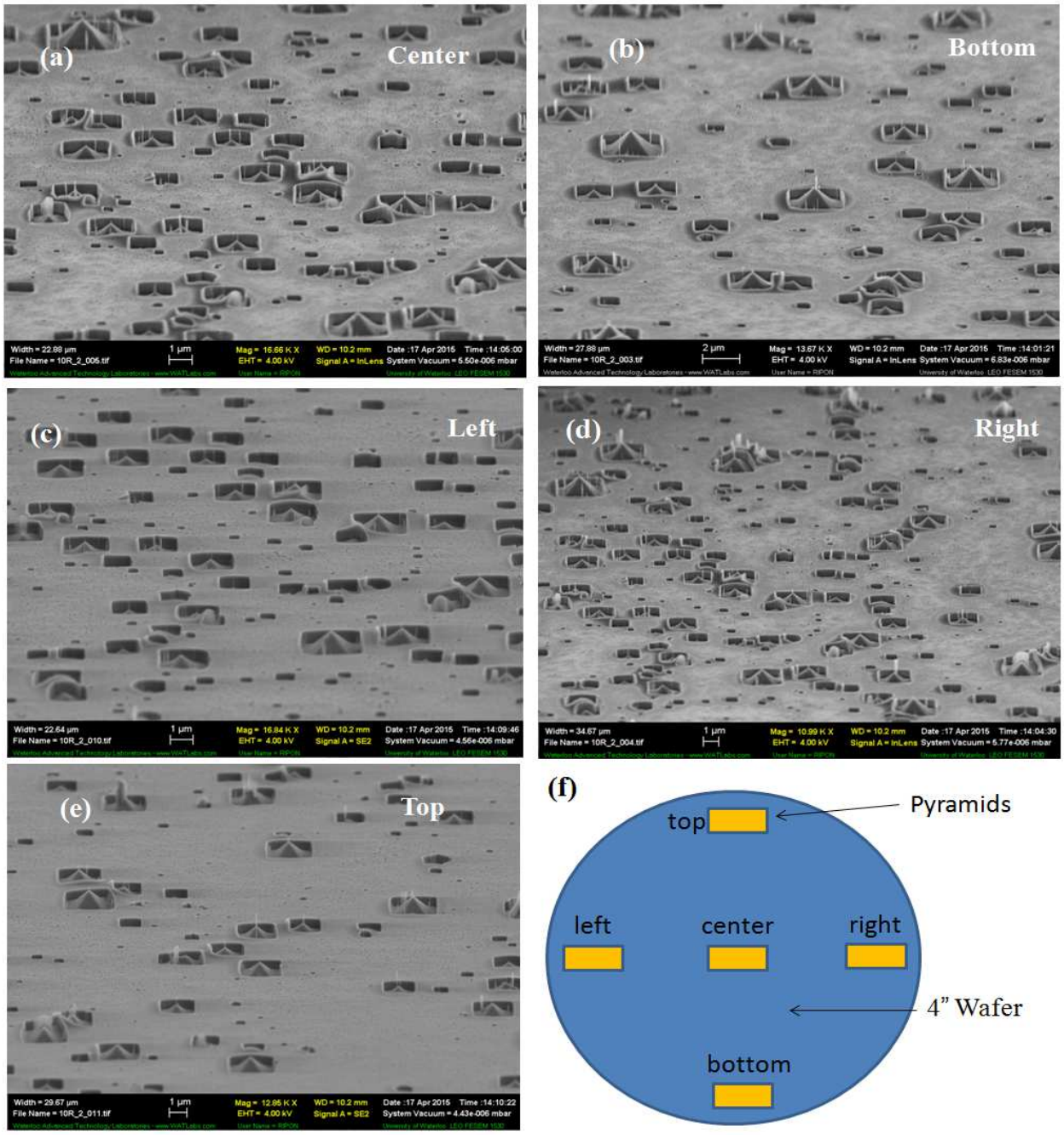

Figure 5.8. SEM images of arrays of high aspect ratio tips fabricated using angle-dependent etch method. The images were captured at five different places of whole 4" wafer, at the (a) center, (b) bottom, (c) left, (d) right and (e) top. (f) The schematic shows the positions where SEM images were captured.

Table 5.3. The yield and uniformity of HAR tips fabricated on pyramidal arrays at five different locations of a whole wafer.

Position	Total no of visible pyramids	No of HAR pyramids	Yield (%)	No of HAR pyramids of D: 35 ± 10 nm	Uniformity of apex of D: 35 ± 10 nm (%)	Average diameter of tip apex (nm)	Average height of tip pillar (nm)
Center	53	44	83	31	58	35	610
Bottom	34	26	77	17	50	37	635
Left	31	22	71	17	55	32	590
Right	59	42	71	30	51	36	560
Top	28	19	68	12	43	34	662
Total	**205**	**153**	**75**	**107**	**52**	**35**	**611**

2. Controlled tip diameter and height. It is very important to control the diameter of tip apex and height of the tip pillar for commercial production. We here demonstrate the fabrication of tips with a range of pillar apex diameters and heights. We tuned the metal deposition thickness and its etching time in order to obtain different silicon pillar apex radius for different applications. Though a smaller radius offers higher AFM imaging resolution, it also makes the tip less mechanically robust. Thus there exists an optimal tip radius for different applications, and this step is to achieve such optimal radius. Whereas the adjustment of the tip pillar height is straightforward, the tuning of tip diameter is less so. Nevertheless, we successfully obtained different pillar diameters by varying the metal film thickness and its etching time.

Before adjusting the pillar diameter, we studied the metal etching time for a particular thickness of metal film. In table 5.4, the optimum metal dry etch time is shown for particular mean thickness of a few metal films that we used so far. This time was adjusted to etch completely away the metal on sidewalls of pyramidal tips, leaving behind some metal on apex of the tips. A common consequence of an inadequate metal etch is the rough sidewall after silicon dry etch that amplifies the roughness of the metal etching mask due to the very high etching rate selectivity. Figure 5.9 illustrates the optimum metal dry etch time for particular mean thickness of the metal film (here, Cr).

Table 5.4. Optimum metal etch time for corresponding metal film thickness.

Materials (Recipes)	Mean thickness of metal film (nm)	Optimum metal etch time (s)
Al (BCl_3 gas)*	22	10
Cr (Cl_2+O_2 gas)**	10	10
	23	30
	30	40
	42	59
	60	86
Ti (BCl_3 gas)*	62	35

***** BCl_3 recipe: described in table 5.1 (1st row), ****** Cl_2+O_2 recipe: described in table 5.1 (2nd row).

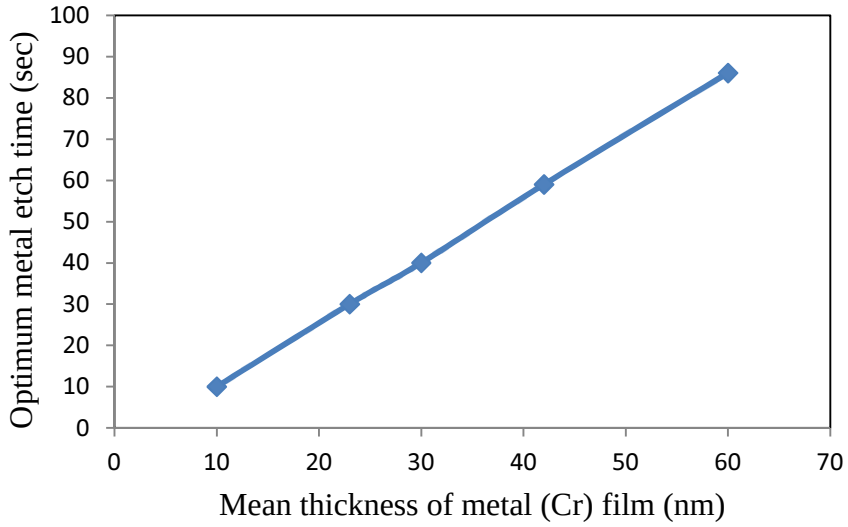

Figure 5.9. Optimum metal dry etch time for different thickness of Cr film.

We found that after metal etch on thinner metal film, smaller metal mask remains, and on the other hand, after metal etch on thicker metal film, larger metal mask remains. Figure 5.10 illustrates a plausible reason of variation of resulted apex diameter due to different thickness of metal film. Figure 5.11 shows that the mean diameter of apex is 25 nm for thinner film (10 nm Cr) and 70 nm for thicker film (60 nm Cr). Here, we coated different thickness of Cr film on large-area pyramidal arrays and performed appropriate metal etch and then silicon etch, according to table 5.2. We obtained the average of tip apex diameter as summarized in table 5.3.

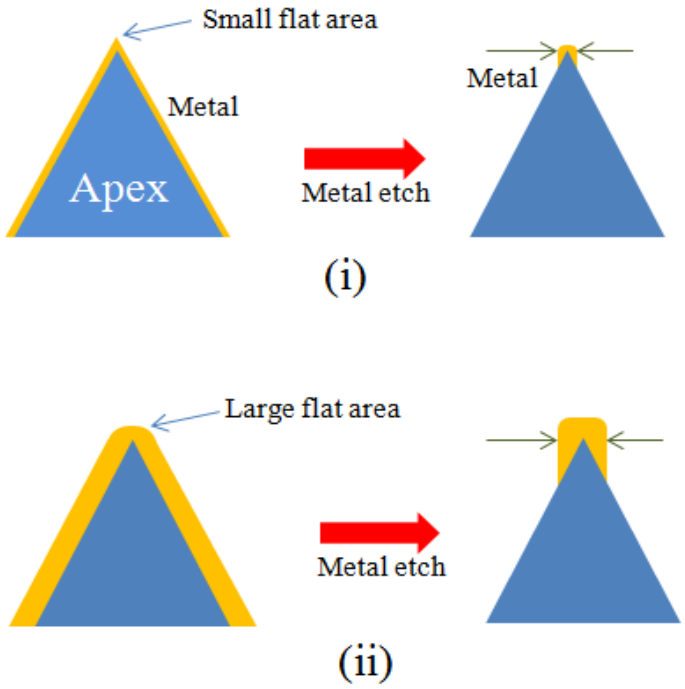

Figure 5.10. Schematic illustrating the dependence of the final pillar diameter (close to the diameter of the resulted metal island mask at apex) on the metal film thickness. (i) thin metal film that leads to small metal island mask, and (ii) thick metal film that leads to large metal island mask.

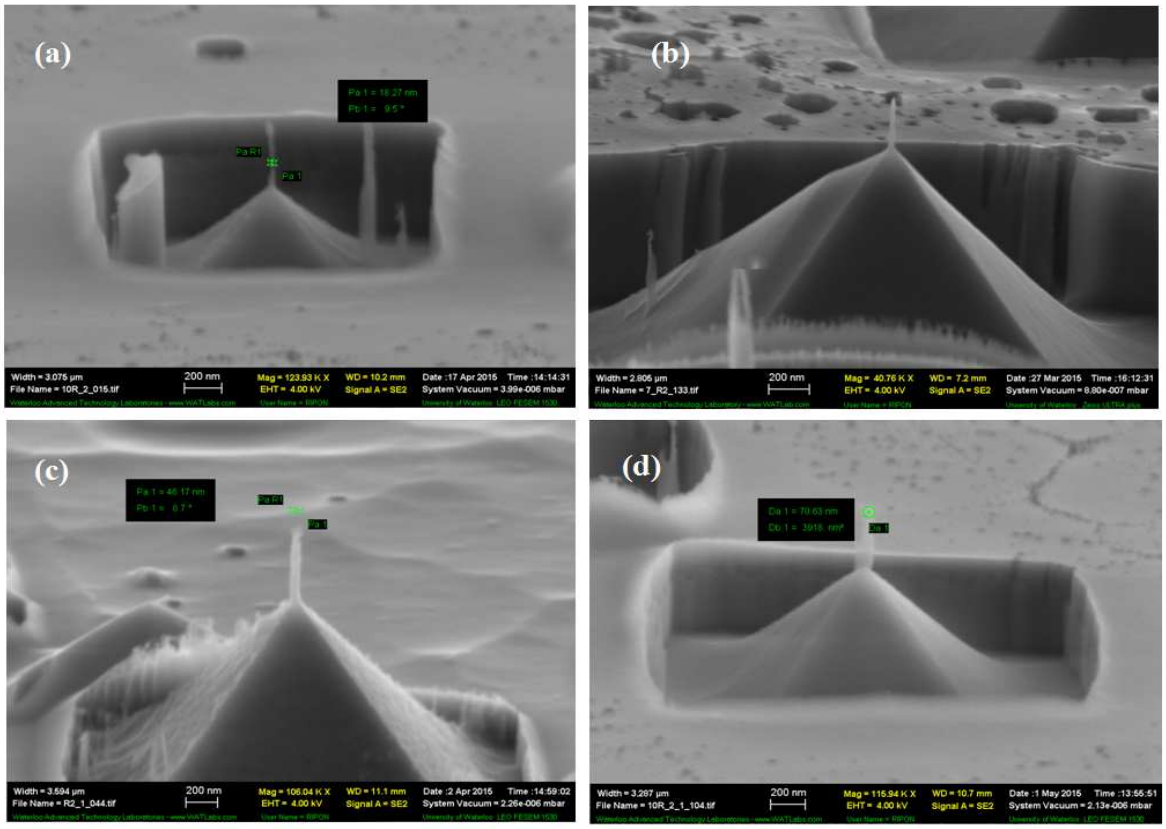

Figure 5.11. SEM images of mean diameter of tip apex for different metal thickness. (a) 25 nm for 10 nm Cr, (b) 35 nm for 23 nm Cr, (c) 50 nm for 42 nm Cr, and (d) 70 nm for 60 nm Cr. Metal etch time was performed according to table 5.4.

Figure 5.12 shows the average diameter of tip apex as a function of average metal thickness. Here we demonstrated the result only for Cr metal film.

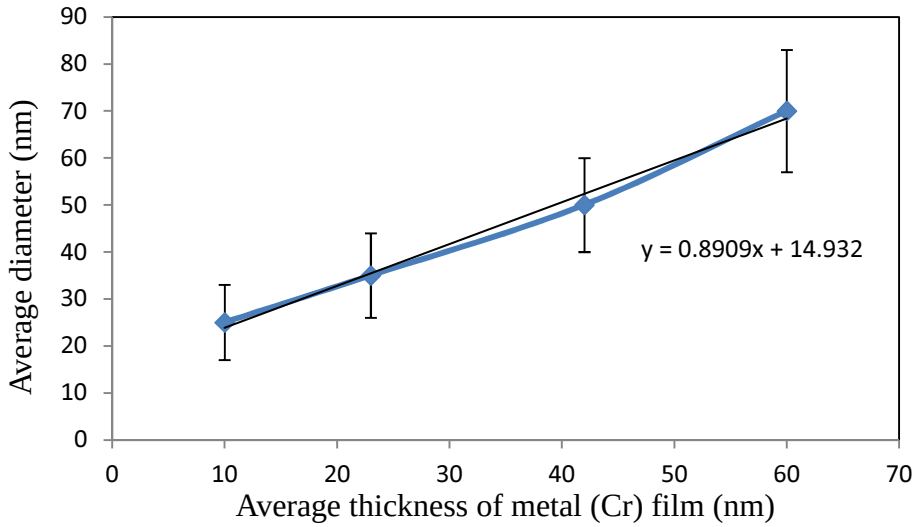

Figure 5.12. Average diameter of tip apex as a function of average metal (Cr) thickness.

The height of the pillars gets apparently longer with increasing silicon etch (as the selectivity of silicon to metal etch with Si recipe is very high) as long as there is metal mask left. Figure 5.13 shows that the pillar heights are in good agreement with silicon etching depth, according to table 5.2.

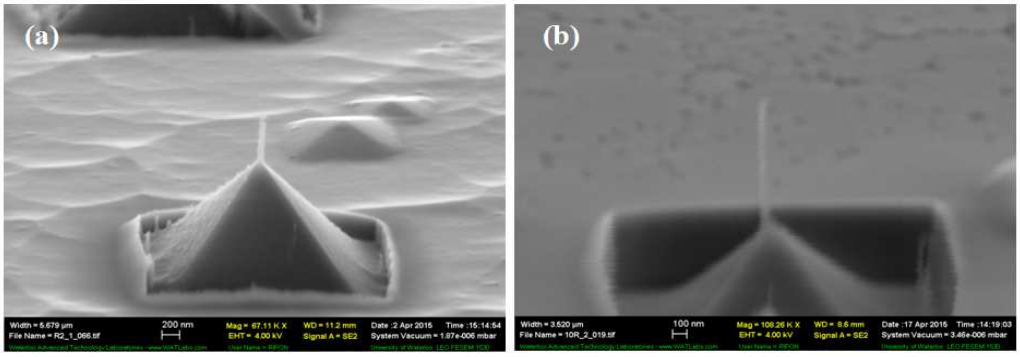

Figure 5.13. SEM images showing the height of the pillar of pyramid as a function of Si etch time, such as (a) 410 nm height for 1 min silicon etch; and (b) 780 nm height for 2 min silicon etch.

3. Controlled tip shape: As aforementioned, to make the tip more mechanically robust, a slight taper (e.g. 3-5 deg sidewall angle) may be desirable for some applications. The Si etching tool has a silicon etching recipe for etching pillar with vertical sidewall, and if desirable, we can

modify the recipe for Si etching to achieve tapered pillars for different slopes of HAR AFM tips. The sidewall angle depends on the balance of chemical etching by SF_6 gas and passivation by C_4F_8 gas. Thus a fine tuning of the ratio of the two gases could achieve this goal.

Saffih et al.[8] in our group demonstrated a one-step etching step with Cr as hard mask using a dry etching recipe with C_4F_8/SF_6 gases. The recipe was significantly modified from a standard pseudo-Bosch process that gives a vertical profile. They achieved a taper angle of 22° by changing the gas flow ratio of C_4F_8/SF_6 from 38/22 to 59/1, as shown in figure 5.14 (a-d). In addition, by further reducing RF bias power, they attained very large taper angle of 39°, but with much lower etching rate. The dependence of taper angle of silicon structure on the ratio of SF_6 flow and total gas flow is shown in figure 5.14 (e). However, here the etching results are for etching silicon on a flat wafer, and we haven't applied this technique to etch real AFM tips, since the sidewall is already slightly tapered for the Rocket tips we fabricated (shown later) even using the recipe that normally gives vertical sidewall for etching silicon on a flat wafer. Nevertheless, if desirable, those modified etching recipes can be utilized to further tune the sidewall angle of the high aspect ratio AFM tip. As can be seen, a flow ratio of 10/50 will give an angle of 4°, may desirable for some AFM applications.

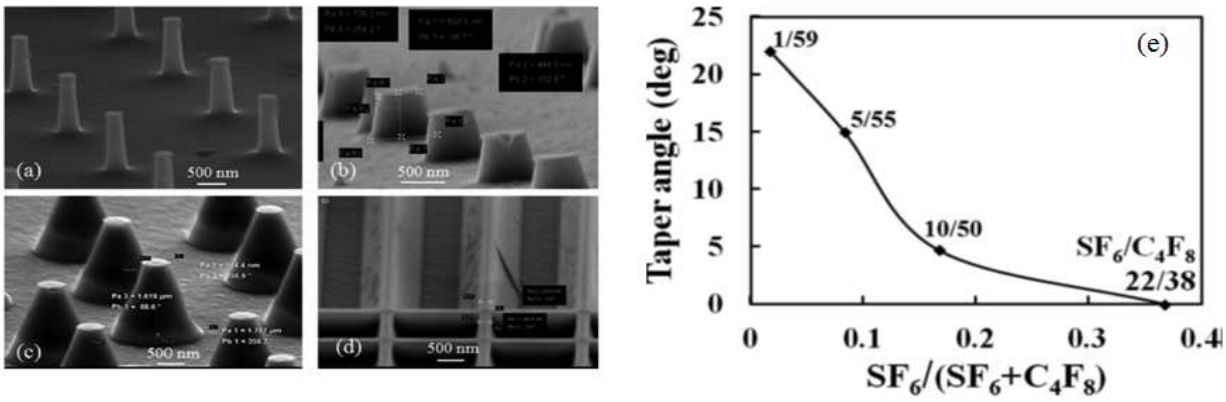

Figure 5.14. (a-d) SEM images[8] of silicon structures etched with different C_4F_8/SF_6 ratios. The ratios and taper angles are: (a) 50/10, 4.7°; (b) 55/5, 15 °; (c) and (d) 59/1, 22 °. (e) Dependence of taper angle of nanostructure on the ratio of SF_6 flow and total gas (SF_6 + C_4F_8) flow which is fixed at 60 sccm[8].

5.3.1.3. Results on regular commercial AFM tips

In previous section, we showed the result of HAR tips fabricated on pyramidal arrays on silicon wafer. Here we show the fabrication results on regular commercial AFM tips. We purchased four different types of AFM tips: PointProbe (Nanoworld[9]), Arrow (Nanoworld), Nitride-pyrex (Nanoworld) and Rocket tips (NT-MDT[10]) in order to verify our technology.

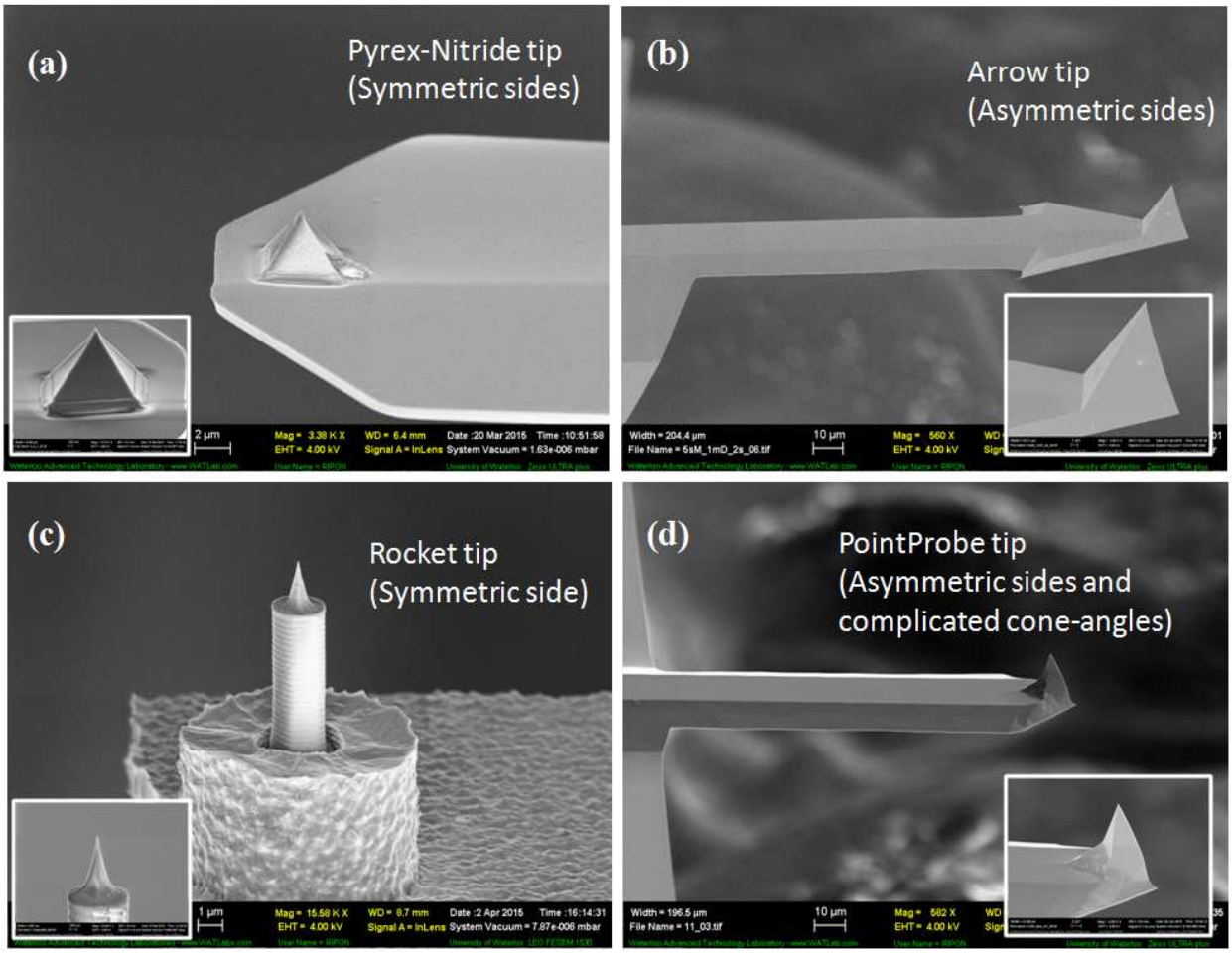

Figure 5.15. SEM images of regular commercial tips that we purchased. (a) Nanoworld Pyrex-Nitride tip, (b) Nanoworld Arrow tip, (c) NT-MDT Rocket tip, and (d) Nanoworld PointProbe tip.

5.3.1.3.1. Silicon nitride probe

Nanoworld low-stress silicon nitride probes are used in contact mode AFM; and nitride's excellent hardness leads to good wear resistance and extended lifetime. Since the cantilevers are supported by a handle made of pyrex-glass, it is termed as 'Pyrex-Nitride' tip by Nanoworld. It has multi-lever design with four rectangular cantilevers, two at each side of the handle. The company claims the height of tip is 3.5 µm, the diameter of tip apex is typically < 20 nm and the sidewall slope angle of the tip is 60°. These nitride tips are sharper than regular Arrow tips. In fabrication process, as gold contaminates the RIE chamber, gold coating was removed at the very beginning using gold etchant [HNO_3:HCl (1:3)] for 3 min before coating with metal. Oxygen plasma cleaning was carried out before coating 23 nm Cr onto the tip and then the nitride film was etched for 2 min using Cr as hard mask by using C_4F_8 and SF_6 gases recipe, according to table 5.2. Figure 5.16 shows a regular nitride tip (a), and high-aspect-ratio nitride tip processed with Cr film as etching mask.

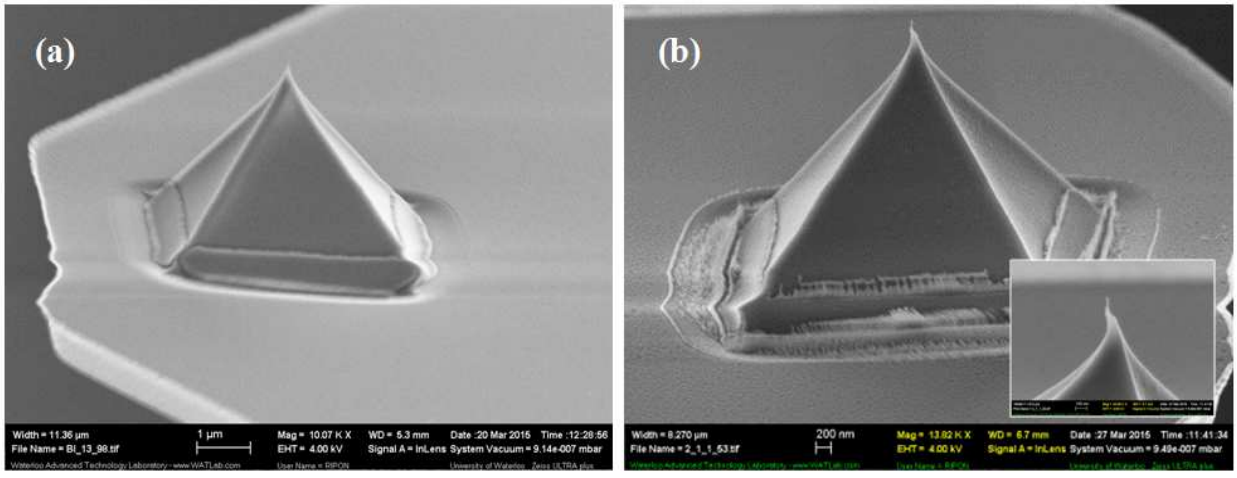

Figure 5.16. SEM image of a regular nitride tip (a), and high-aspect-ratio nitride tip with height of 110 nm and radius of apex of 18 nm fabricated using our process (b). Inset shows the high magnification image of the tip apex. Here the tip apex appeared not straight due to charging effect since nitride is insulator.

As etching rate of nitride with SF_6/C_4F_8 plasma is much lower than silicon (117 nm/min for Si_3N_4 and 420 nm/min for silicon), and one metal layer mask limits the achievable pillar height,

we modified the fabrication process (Figure 5.17) with two metal layers while keeping all other steps the same as before.

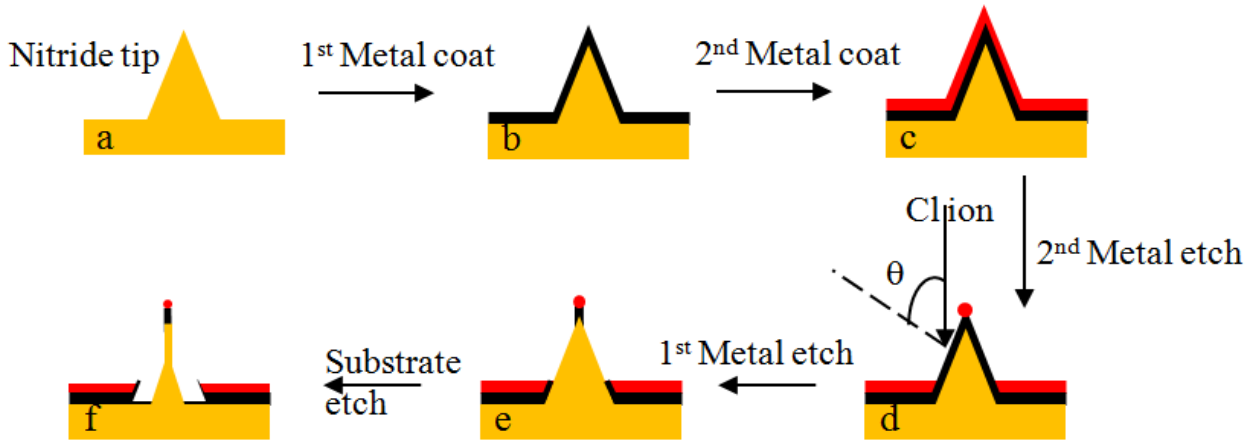

Figure 5.17. Process flow of fabricating high aspect ratio AFM tip using two metal layers as mask. a) Start from a regular nitride tip with; b) Coat first metal film (Al); c) Coat second metal film (Cr); d) Etch second metal film; e) Etch first metal film, and f) Etch the substrate (nitride) using SF_6/C_4F_8 plasma, and finally the remaining metals can be removed easily by wet etching. Since Cr etches 10 × slower than Al in BCl_3 plasma, a relatively thick Al metal mask can be obtained in order to etch deep into nitride.

In the modified fabrication process, after removing gold from backside of original tip by wet etch, O_2 plasma cleaning was performed. Next, Al (20 nm) and then Cr (23 nm) were coated on the top side of the tips. Subsequently Cr dry etch with Cl_2/O_2 gas and then Al dry etch with BCl_3 gas were performed for optimum times respectively. Finally, tips were etched for 4 min with silicon etching recipe using SF_6/C_4F_8. This results nitride pillar right below the metal masks. Here since Al etches 10 × faster than Cr, we can obtain a thick Al island mask at the tip apex as needed for longer silicon etch. That is, we effectively “amplified” the metal mask thickness by a factor of 10, knowing that Al is as good as Cr for masking silicon etch. The height of the pillar, thus the aspect ratio, can be controlled simply by tuning metal thicknesses. Figure 5.18 shows the SEM images of two high-aspect-ratio nitride tips fabricated on single nitride probe with two cantilevers, with pillar height of 410 nm (a), and 420 nm (b) respectively. 15 nm Cr was coated before SEM to reduce the charging effect.

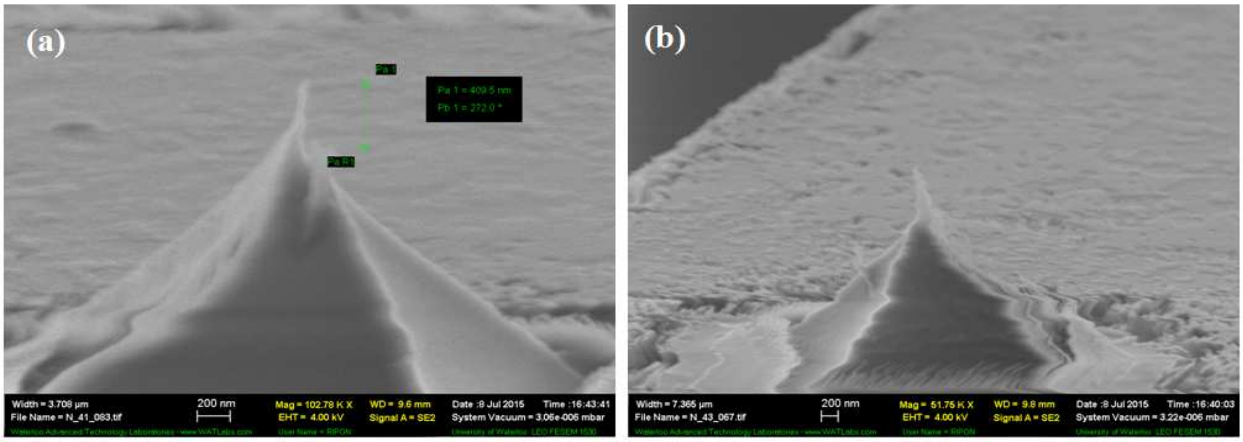

Figure 5.18. SEM images of two high-aspect-ratio nitride tips fabricated on single nitride probe with two cantilevers, with pillar height of 410 nm (a), and 420 nm (b) respectively. The tip pillars appeared not straight due to charging effect during SEM imaging.

5.3.1.3.2. Arrow silicon probe

For silicon tips, Nanoworld Arrow tips have the height of 10-15 µm and a diameter of curvature of typically < 30 nm, as claimed by manufacturer. The macroscopic half cone angles are 30° to 35° when seen along the cantilever axis, and 20° to 25° when seen from the side. The main challenge for those Arrow probes is how to etch uniformly because it has different half cone-angles in the three sidewalls. Figure 5.19 shows a regular Nanoworld Arrow tip (a), and a high-aspect-ratio Arrow tip processed with 22 nm Al film and 30 sec Si etch. Since it has very small half cone-angles in two back sidewalls, we frequently achieved high aspect ratio tips, but with a 'tail' along the back sidewalls. Note that, this 'tail' can be removed by performing SF_6 lateral etch (SF_6: 20 sccm, DC: 10 V, P: 50 mT, etch rate: 43 nm/min) after O_2 plasma cleaning. However, the steep back side is hard to etch, as shown in figure 5.19 (c-d), even though here it was etched for longer time (40 sec). To sum up, after extensive effort, we have not achieved satisfactory results using these tips, because its sidewall slope angle is quite different from the etched pyramidal structures on silicon, and the backside slope angle is so steep that the metal on it cannot be etched away completely before the metal on tip apex is already all etched away.

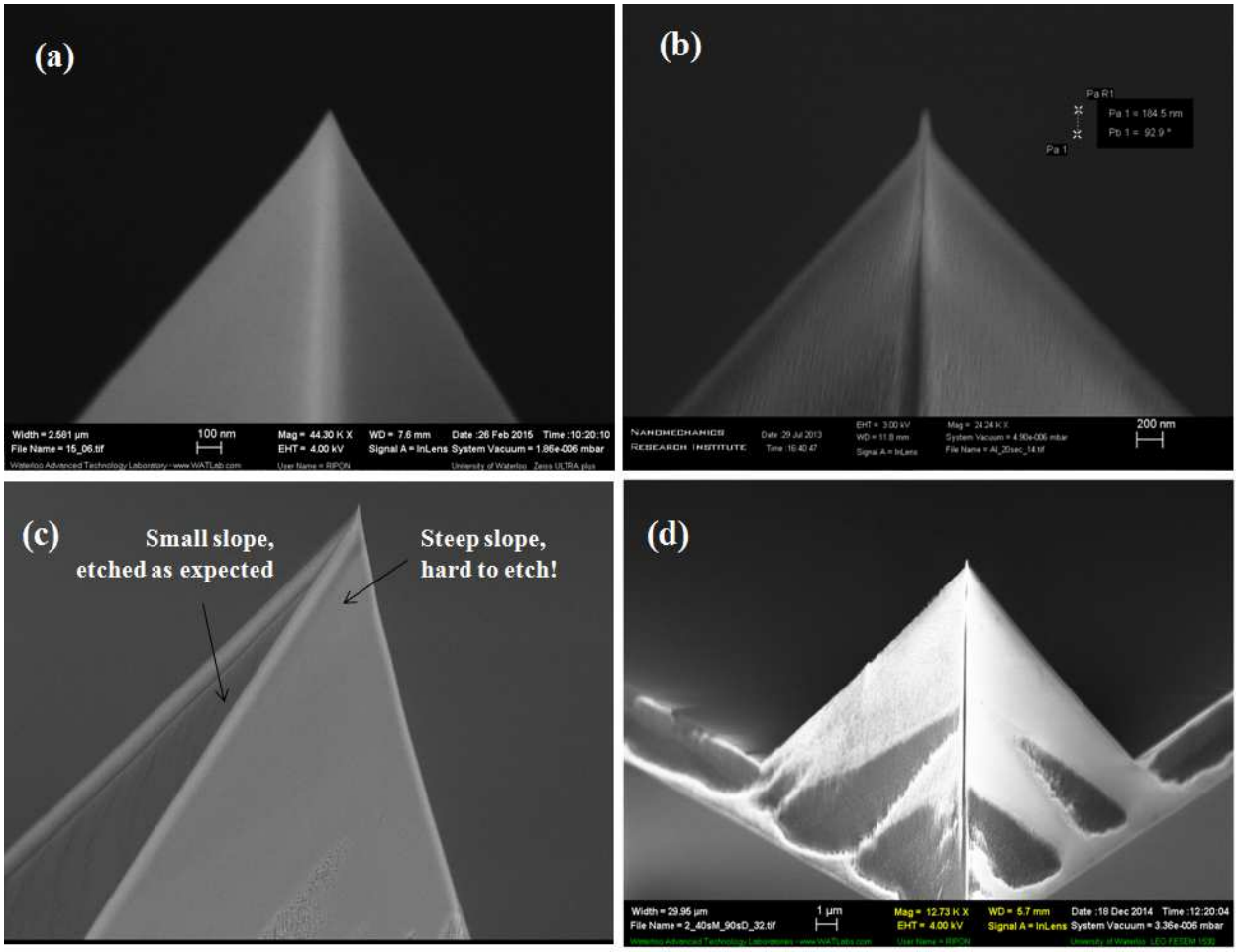

Figure 5.19. SEM image of a regular Arrow tip apex (a), a high aspect ratio Arrow tip (back view) with height of 185 nm, fabricated using our process (b), (c) side view of fabricated Arrow tip showing unsuccessful backsides etching, and (d) zoom-out back view of Arrow tip.

To overcome this barrier with Nanoworld Arrow tip, we evaporated metal onto the tip mounted on a slope, such that the back side will receive even less metal coating. As mentioned before, the metal film thickness for vacuum evaporation is proportional to cosθ, with θ being the local incident angle, which is 0° for normal incidence. Table 5.5 showed the evaporation metal film thickness as a function of incident angle, which shows that the theoretical mean thickness goes to zero for vertical surface and maximum for horizontal surface. The experimental mean thickness is in good agreement with theoretical thickness. When the tip is mounted on a horizontal support, incident angle of evaporation is 50° for the front sidewall and 80° for the joining of two back sides, as shown in figure 5.20 (ii), whereas top view has been illustrated in (i) and real Arrow tip

view was shown in (iii). By mounting the tip on a slope, the incident angle for the three sides is adjusted.

Table 5.5. Evaporated metal film thickness as a function of incident angle (proportional to cosθ, with θ being the incident angle) of the metal to the surface in evaporation chamber.

Incident angle (°)	Theoretical thickness of metal (nm)	Experimental thickness of metal (nm)
0 (flat, horizontal surface)	69	69
11	68	-
15	67	-
25	63	61
35	57	55
50	44	-
60	35	-
70	24	-
90 (vertical surface)	0	-

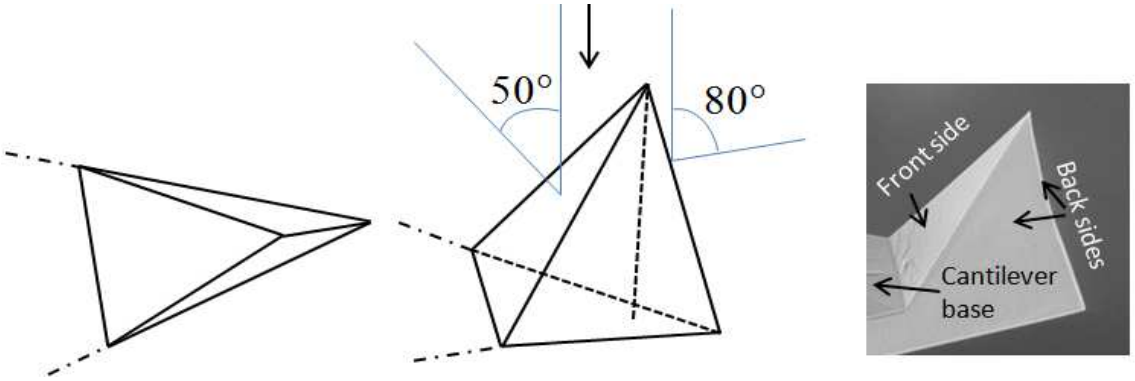

(i) Top view (ii) Side view (iii) Real tip view

Figure 5.20. Schematic shape of Nanoworld Arrow tip: top view (i), side view showing incident angle of evaporation direction to the normal of side surfaces (ii); and SEM image of real tip view (iii).

Figure 5.21 shows the result of Arrow tips coated with aluminum ((a-c) thickness 69 nm, (d) 28 nm) mounted at different slope angle, with or without etch. When mounted on a horizontal

surface (Figure 5.21 (a)), incident angle of evaporation relative to the normal of front side, joining of back sides and cantilever base are 50°, 80° and 0° respectively. When mounted on a slope of 25° (metal thickness for this angle is 69cos25°=63 nm), the incident angle of front side and joining of back sides are 25° and 105° respectively (Figure 5.21 (b)). The Al on the front side was all etched away, but not that on the back side and cantilever base. When mounted on a slope of 35°, the incident angle of front side and joining of back sides are 15° and 115° respectively (Figure 5.21 (c)); and the Al on the front side still remained, but the bottom half of the metal on the back sides was etched away, so was the metal on cantilever base. Metal in top part of back sides remained because the sputtering yield may very low at such incident angle (80°). Lastly, the tip was mounted on opposite side on a slope of -11° and the incident angle of front side and joining of back sides are 61° and 69° respectively (Figure 5.21 (d)). Note that, the sample in figure 5.21 (d) is over-etch to ensure metal from cantilever base (flat-area) is also removed. The Al on the front side and cantilever base were all etched away, but not that on the back sides. The substrate etch was for 1 min for all these cases.

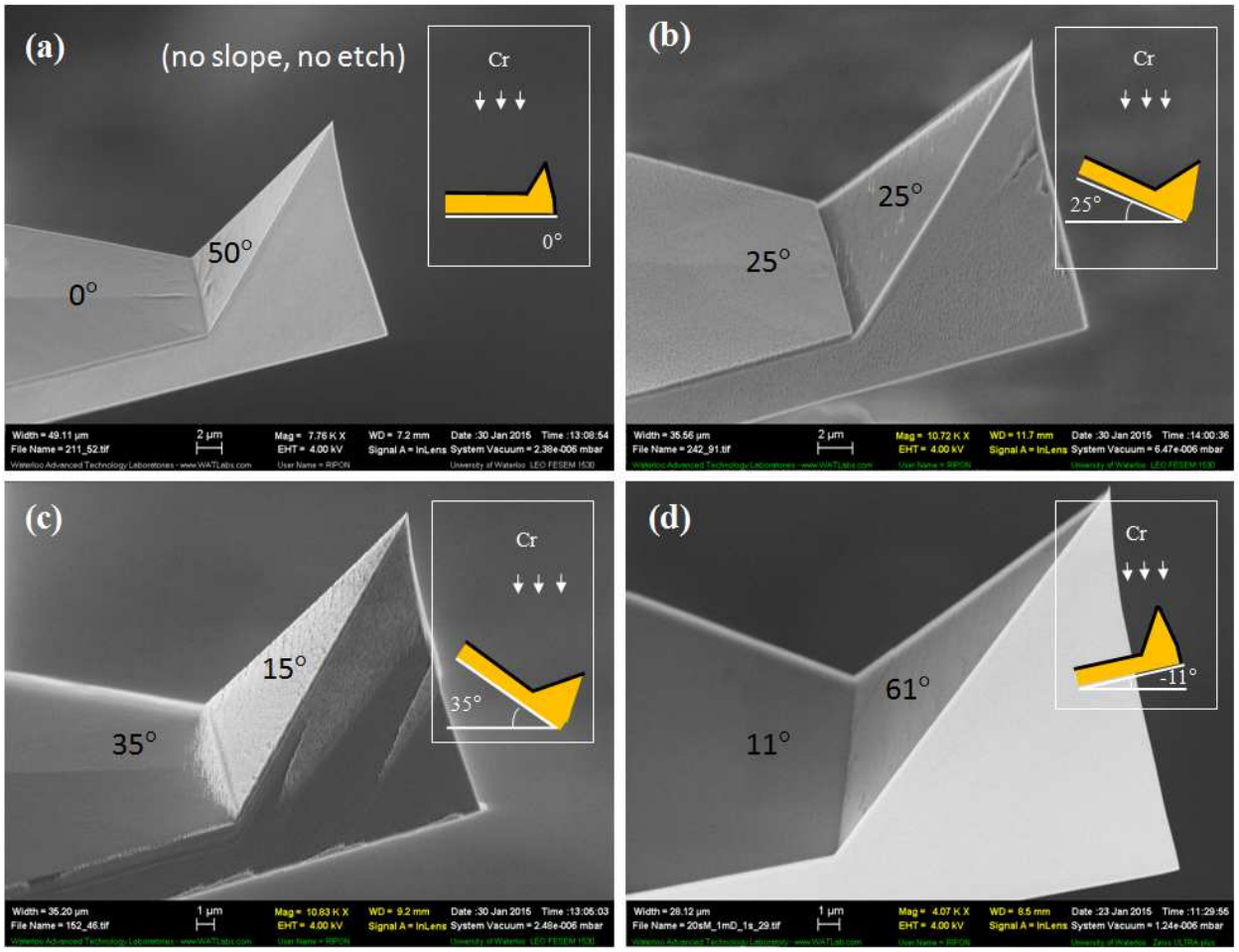

Figure 5.21. SEM images of (a) aluminium coated Arrow tip mounted horizontally (not on a slope) during Al evaporation, (b) completed Arrow tip with Al evaporation at 25° incident angle, (c) same as (b) but at 35° incident angle during Al evaporation, (d) same as (b) but at -11°. All failed to result a HAR structure after completing the process steps.

Even with balanced coating on the front and back sides by mounting the tip on a slope, the metal on the backsides was found still hard to etch due to the large steep slope angles of these sidewalls. Therefore, we designed a modified process for Arrow tips, as shown in figure 5.22. In the figure, we first coated aluminium with thickness of 40 nm in front sidewall of Arrow tips mounted on 60° stub in electron beam evaporator (ii). Then silicon was etched for 2:30 min to etch the back sidewalls (iii). This was followed by metal removal with hydrofluoric acid (HF, 1:50 diluted with water) for 25 sec (iv). Here, just before HF etch, the tips were cleaned with oxygen plasma to remove the fluro-carbon formed due to C_4F_8 plasma exposure. Next, Cr metal

was deposited on tips mounted horizontally in evaporator (v), and, finally metal (vi) as well as silicon (vii) etch were performed.

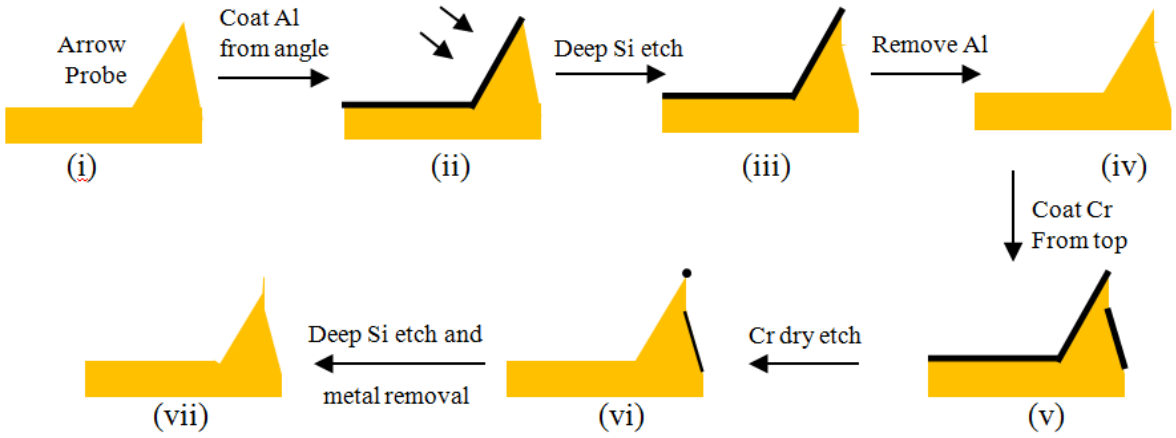

Figure 5.22. Schematic of modified process steps fabricating HAR pillar structure onto Arrow tip by two-angle evaporation technique.

Figure 5.23 shows the tip apex (a) followed by first silicon etch (b). In (c), high aspect ratio tip structure is presented where the height of the pillar is 950 nm and the radius of curvature is 25 nm. Though this process worked better for Arrow tips, it is two times more complicated, thus unsuitable for volume production.

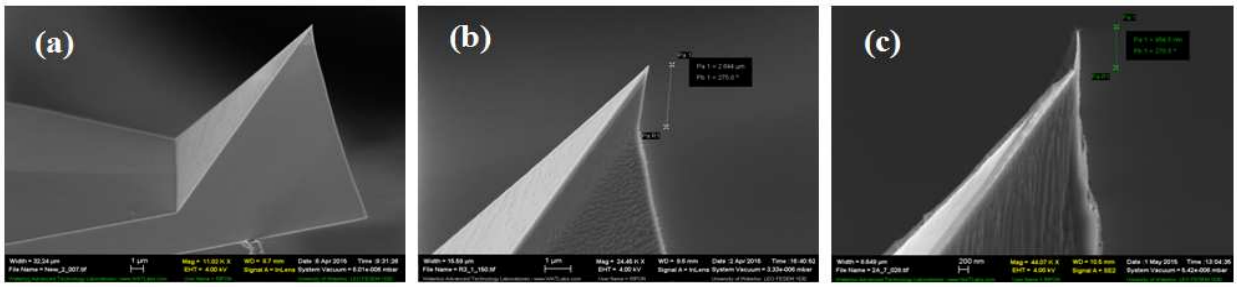

Figure 5.23. (a) Al coated (40 nm) Arrow tip, (b) tip apex followed by first silicon etch; and (c) HAR tip structure followed by final silicon dry etch (950 nm pillar height).

We additionally applied our technique on Nanoworld 'Point Probe' tips, but we were unsuccessful with these tips.

5.3.1.3.3. Rocket silicon probe

As we looked for AFM tips with symmetric and none-steep half cone-angles of sidewalls, we chose "Etalon" Rocket probes having symmetric cone structures. The "Etalon" Series probe has two polysilicon cantilevers (Figure 5.24 (b)) with monocrystal silicon tip standing on high aspect ratio microscale pedestal pillars. The reason to use polysilicon cantilever is that the deposited polysilicon gives a precise control for cantilever thickness that is equal to polysilicon film thickness. The diameter of curvature of tip apex is less than 20 nm, according to the manufacturer. Gold coated back side of cantilever enhances the reflection of the laser beam.

To study the uniformity of our process over a 4" wafer, five Rocket tips were mounted in four corners and one in center of a 4" silicon wafer and the fabrication process was carried out as usual (here the tips were taken off from the original wafer of tips, and glued onto another support wafer), as shown in figure 5.24 (a). As gold contaminates the RIE chamber, gold coating was removed at the very beginning using gold etchant [HNO_3:HCl (1:3)] for 4 min before coating with metal. Oxygen plasma cleaning was carried out before coating 23 nm Cr onto the tip. After coating the metal, the whole wafer went through metal dry etch for 30 sec, followed by silicon dry etch for 1 min 45 sec. Part of the original Rocket tip is shown in figure 5.25 (a). Figure 5.25. (b) - (f) shows the high aspect ratio tips which were mounted at different places of 4" wafer. It demonstrated that all the five tips are successfully processed into high aspect ratio ones, with close size and shape. Thus the uniformity across an entire 4" wafer is satisfactory. However, the result might be different for a real wafer of tips from tips glued on a flat wafer as studied here. We have achieved average radius of apex curvature as small as 15 nm. Average apex-pillar height is 1.6 μm; and average base width is down to 250 nm. The uniformity and reproducibility are as expected. However, the roughness of original tip sidewall caused slight non-uniformity of fabricated tip apex.

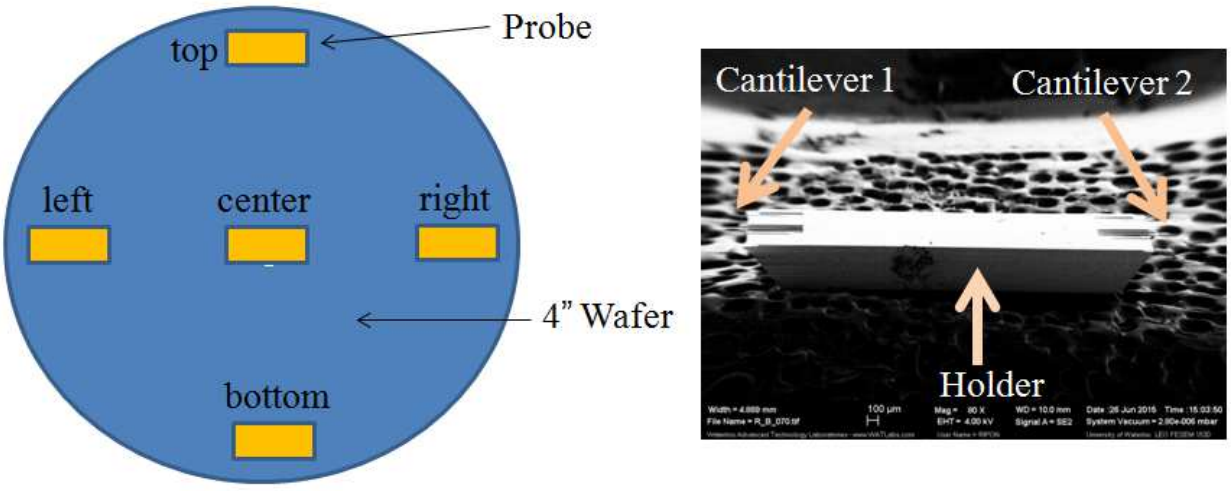

Figure 5.24. (a) Schematic of five Rocket probes placed at four corners and one at the center of a 4" silicon wafer. (b) SEM image of a Rocket probe having two cantilevers, one on each side of the holder.

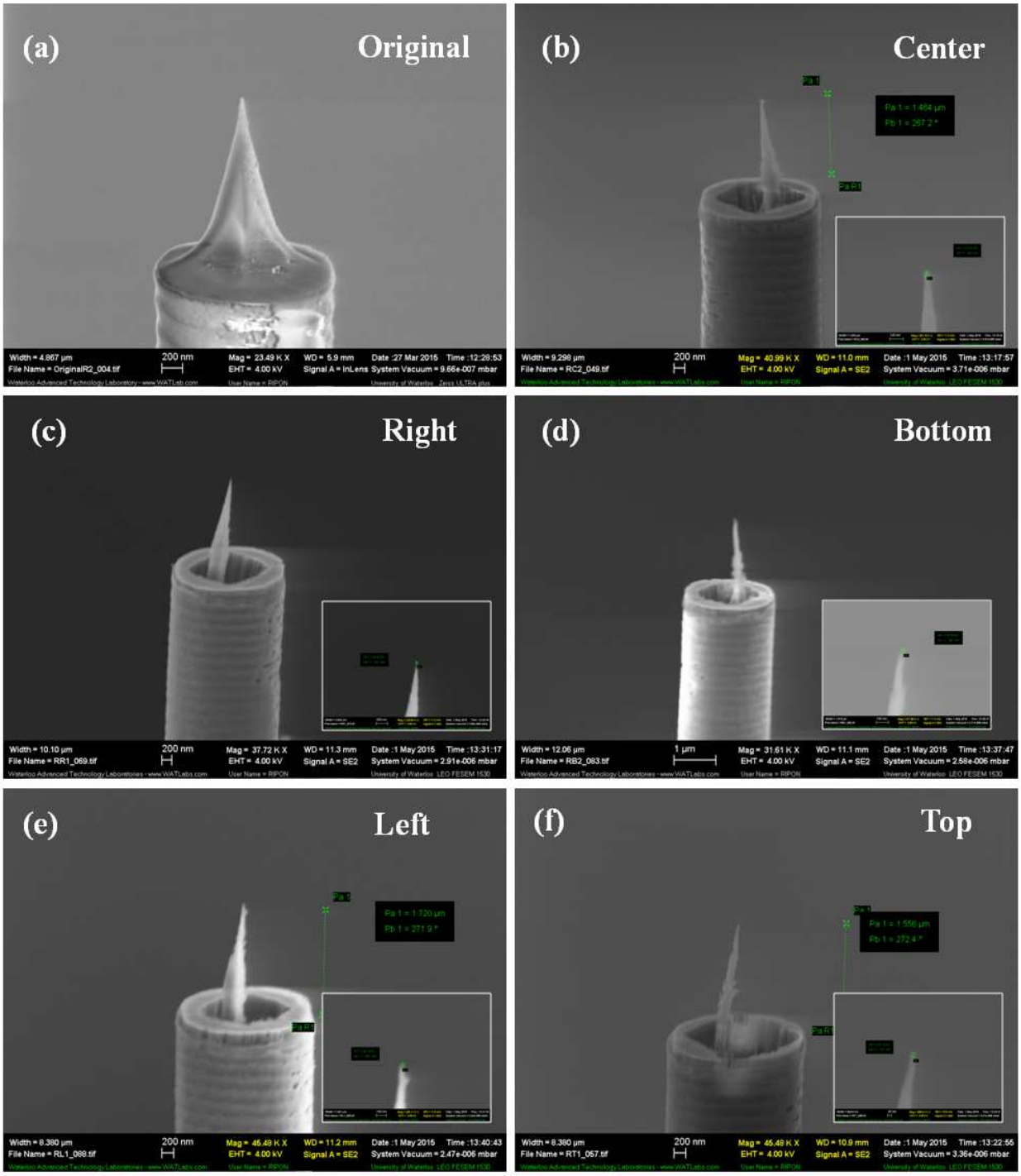

Figure 5.25. SEM images of (a) a structure of original Rocket tip apex; and fabricated high aspect ratio Rocket tip which were mounted in different positions of a 4" wafer while processing at (b) center, (c) right, (d) bottom, (e) left and (f) top of a 4" wafer to show the uniformity (across an entire wafer) of the process. Inset shows high magnification image of corresponding tip apex.

To study the yield, we glued 9 tips onto a flat wafer, and processed them in the same run. As seen in figure 5.26, 8 out of 9 tips turned out good, though having slightly different dimensions (notably probe 7 is not as sharp), with the 9th one broken (88% yield).

Figure 5.26. High aspect ratio tips processed from Rocket tip, processed in the same run to show the yield of the process.

Regarding reproducibility, we fabricated three batches of tips and obtained reproducible results (see figure 5.27).

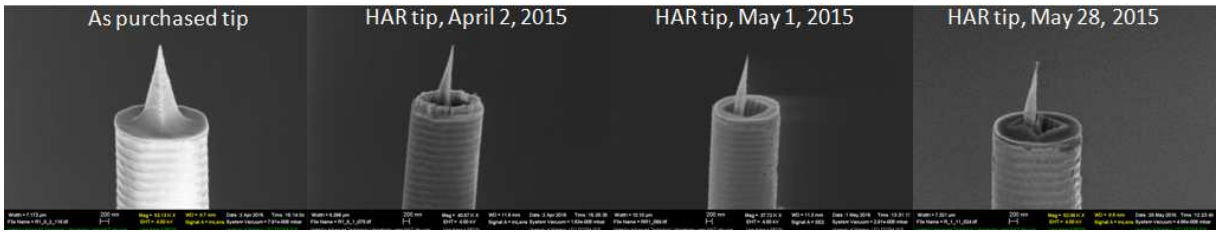

Figure 5.27. High aspect ratio tips processed out of Rocket tip at different times to show reproducibility.

Regarding tilt compensation, during real AFM scanning, the tip base is actually not parallel to the sample surface; instead it is tilted by ~10-13° as shown in figure 5.28 (a). It is thus desirable to fabricate an AFM tip with the pillar tilted at the same angle, so that the tip is perpendicular to the sample surface. Intuitively, one may consider it feasible to fabricate such tips using a regular RIE process with the wafer tilted by 10-13°, but this will not work because the self-bias field in a plasma is always perpendicular to sample surface no matter the sample is tilted or not. We didn't carry out experiment to intentionally fabricate high aspect ratio tips with tilt compensation, because, as it turned out for yet unknown mechanism (perhaps due to loading effect in reactive ion etching), the fabricated high aspect ratio tips out of Rocket tips are fortunately already tilt-compensated (see figure 5.28 (b)).

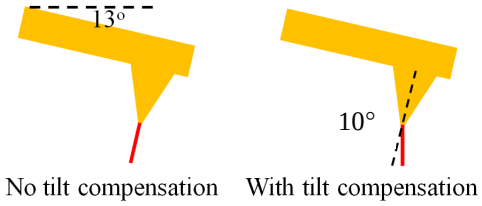

(a)

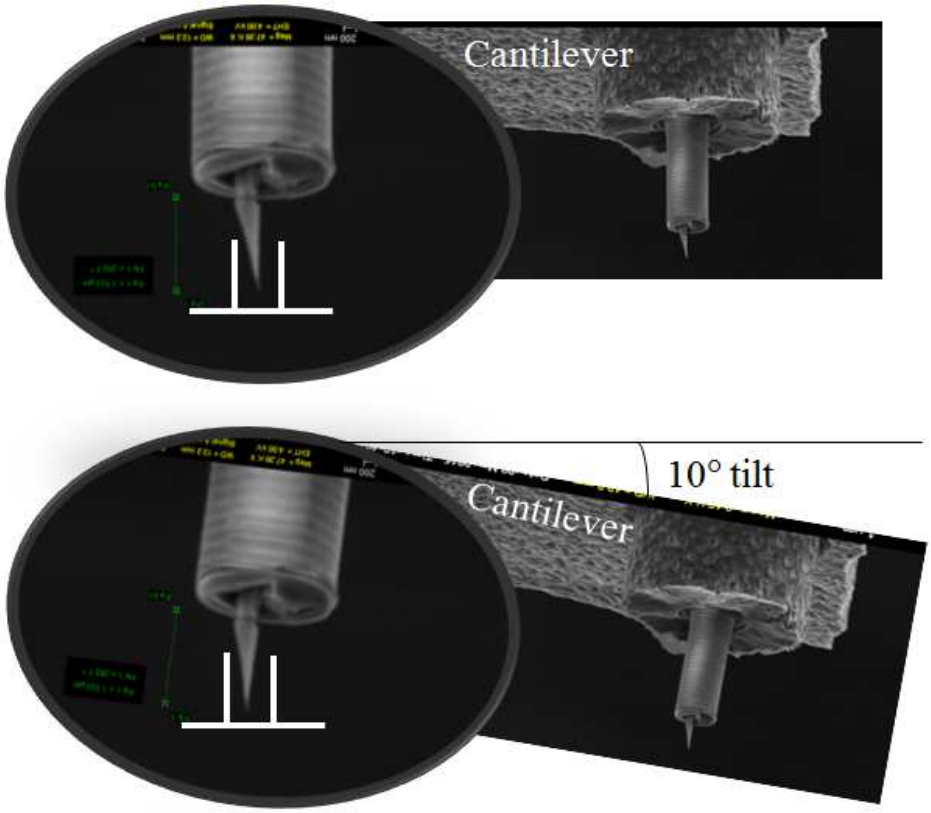

(b)

Figure 5.28. (a) Schematic showing the tilt compensation concept of AFM tips; (b) (top) SEM image of high aspect ratio tip; (bottom) same image rotated by 10° to mimic tip configuration when mounted on AFM instrument. The HAR tip is clearly tilt-compensated.

5.4. Characterization of regular and HAR tips

The commercial regular tips and the high aspect ratio tip that we processed were tested using an Vecco-AFM tool (Digital Instruments: Vecco metrology group). Figure 5.29 shows images that were obtained in tapping mode. The length, width and height of the cantilever used were similar for both test. The SEM images of both tips apex are shown in figure 5.29 (i). The HAR probe shows a much better scan-depth and higher resolution imaging quality than the regular probe, as shown in figure 5.29 (ii) and (iii).

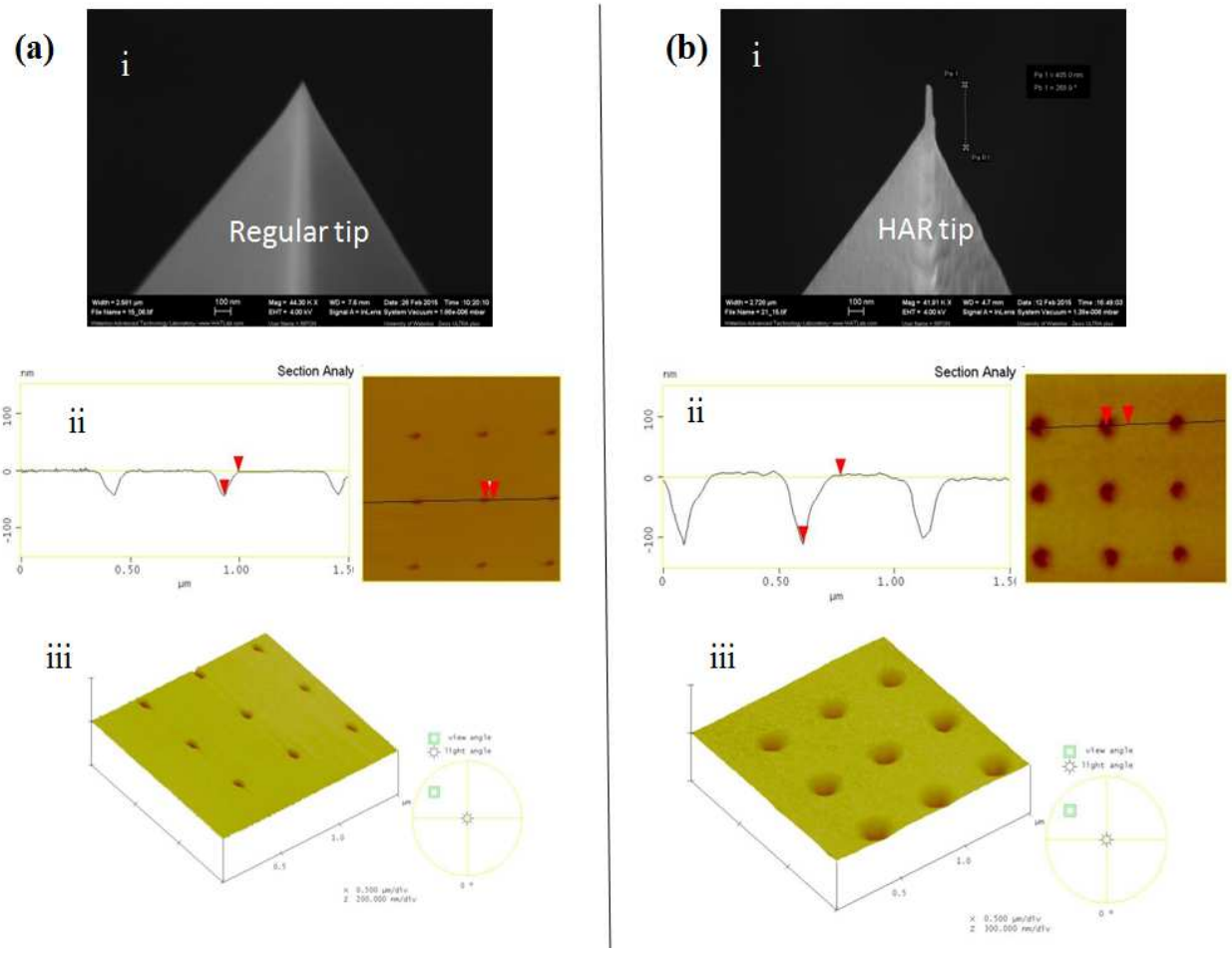

Figure 5.29. The AFM scanning results on hole arrays nanostructures (a) using the commercial regular Arrow probe and (b) using a HAR Arrow probe are shown; (i) SEM images of those corresponding tips, (ii) scanning depth and (iii) 3D view of scanned images also shown.

We also shows the tip scanning results with HAR Rocket tip on high aspect ratio pillar structures. Due to the tilt compensation and HAR tip geometry, the HAR tip reaches to the bottom of the pillars and generates better quality image with high resolution. Figure 5.30 shows the AFM images of the pillar structure produced by the regular Arrow tip (a), regular Rocket tip (b) and HAR Rocket tip (c). The height profile of pillar structures is maximum in the AFM image that generated by HAR Rocket tip (440 nm) than by commercial Arrow tip (390 nm) and Rocket tip (425 nm). In addition, the scanned image approaches to realistic by HAR Rocket tip.

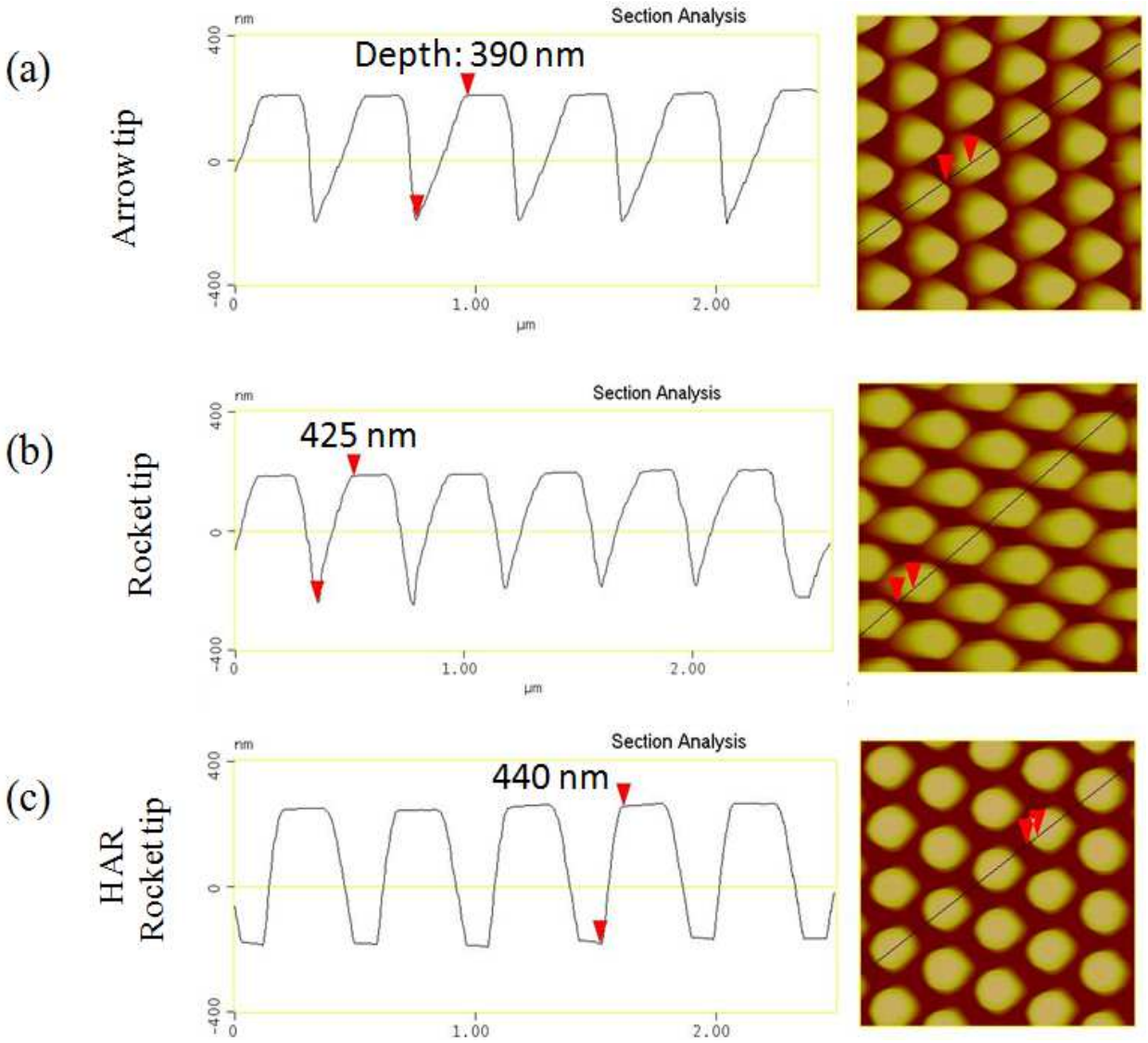

Figure 5.30. The AFM scanning results of a specimen consisting of 2D periodic pillar array structure, using (a) a regular Arrow tip; (b) a regular Rocket tip, and (c) a HAR Rocket tip.

5.5. Conclusions

We here developed a method to batch fabricate the HAR AFM tips by forming a hard metal etching mask just on the apex of the pyramid tip followed by silicon dry etching to achieve the HAR pillar right below the metal island mask. Since it is a batch and lithography-free process, it has much higher throughput and much lower manufacturing cost per tip. This technique was first successfully applied on large-area pyramid arrays and then transferred to the commercial regular

AFM tips, and has demonstrated the uniformity, reproducibility and yield of those HAR tips. Specifically, here we demonstrated the radius of curvature of tip apex down to 10 nm and aspect ratio up to 1:20. The tip apex diameter and tip pillar height are controllable by tuning metal thickness and silicon dry etching time respectively. In addition, the tip shape can be tunable by changing the etching gas ratio of silicon RIE. Finally, we demonstrated that the HAR tips fabricated using our technique gave a better imaging quality than the commercial regular low aspect ratio tips. The application of these low cost HAR tips is vast, since as a popular nano-metrology instrument, AFM is nowadays employed in many different areas of nanotechnology.

5.6. References

[1] O. Wolter, T. Bayer, J. Greschner, "Micromachined silicon sensors for scanning force microscopy", Journal of Vacuum Science and Technology B **9 (2)**, 1353–1357 (1991).

[2] R. Dey, R. Monsour, B. Cui, "Effect of molecular weight distribution on e-beam exposure properties of polystyrene", Nanotechnology **24,** 245-302 (2013).

[3] Y. Yamamura et al., Atomic Data and Nuclear Data Tables **62,** 149 (1996).

[4] Y. Yamamura, Y. Itikawa, and N. Itoh, "Angular dependence of sputtering yields of monatomic solids", Institute of Plasma Physics IPPJ-AM-26, Nagoya University, 1983.

[5] http://www.srim.org/

[6] http://www.asu.edu/clas/csss/NUE/FIBSputterCalcYamamura.html#Yamamura.

[7] https://ece.uwaterloo.ca/~sssaini.

[8] F. Saffih, C. Con, A. Alshammari, M. Yavuz, and B. Cui, "Fabrication of silicon nanostructures with large taper angle by reactive ion etching", J. Vac. Sci. Technol. B **32(6),** 06FI04 (2014).

[9] http://Nanoworld.com.

[10] http://www.nauganeedles.com.

CHAPTER 6

Conclusions

This thesis is focused on the nanofabrication and its application in high aspect ratio AFM tips. The contribution, thus, is the development of novel nanofabrication techniques and process to batch fabricate the high aspect ratio AFM tips.

For the first part, several projects based on nanofabrication have been performed:

(1) Effect of molecular weight on e-beam exposure properties of polystyrene. Polystyrene is a very promising negative resist with tunable sensitivity and resolution capability over a broad range simply by choosing different molecular weights. Thus high molecular weight polystyrene has low contrast but high sensitivity, up to 1 $\mu C/cm^2$, and low molecular weight polystyrene has high contrast but low sensitivity. For applications that need only moderate resolution, it is desirable to use high molecular weight such as 900 kg/mol in order to take advantage of its very high sensitivity; whereas if ultra-high resolution is the primary goal, very low molecular weight such as 2 kg/mol would be the choice.

(2) Effect of molecular weight distribution on e-beam exposure properties of polystyrene. Here we showed that, despite the fact that polystyrene's sensitivity is inversely proportional to its Mw, no noticeable effect of very broad molecular weight distribution on sensitivity, contrast and achievable resolution is observed. It is thus unnecessary to use the costly monodisperse polystyrene for electron beam lithography. This also implied that polystyrene of certain

molecular weight can be simulated by a mixture of two polystyrenes having different molecular weights.

(3) Lift-off with solvent for negative resist using low energy electron beam exposure. Here we showed metal lift-off using negative polystyrene resist by low energy exposure. It was shown that low energy exposure led to an undercut profile which positively cooperates for a clean lift-off. Moreover, since the resist at the bottom is not cross-linked with low energy exposure, liftoff using common solvent was achieved. However, sub-500 nm resolution was challenging to attain using the current method due to capillary force that detached the fine polystyrene structure exposed at low energy.

(4) Electron beam lithography on irregular surface using grafted PMMA brush. PMMA monolayer "brush" as EBL resist is successfully grafted on surface treated nonflat surface (Si and Al as substrate/sub-layer). As a proof of concept of patterning on nonflat surface, we fabricated line nanostructures on the AFM cantilever. High resolution of 30 nm line width, and dense pattern of 50 nm half pitch, were etched into AFM cantilever (non-planar surface) using this monolayer resist and Al hard mask intermediate layer. Nanopatterning on nonflat substrates may find applications in fields such as atomic force microscope (AFM) tip-enhanced Raman spectroscopy (TERS) for chemical analysis¸ mass-(bio)sensor using a cantilever and lab-on-fiber technology.

(5) Electron beam adjustment in EBL with feedback using in-situ self-developing resist. Here we studied nitrocellulose resist and its application as in-situ feedback for electron beam optimization in electron beam lithography. Using nitrocellulose as in-situ feedback to optimize the electron beam (notably working distance) across a large writing field of 1 mm $\times$ 1 mm, we achieved ~80 nm resolution across the entire wring field, as compared to 210 nm (occurred at the writing field corners) without the beam optimization process. This approach is most efficient in reducing the writing time for large writing field size such as 1 mm $\times$ 1 mm as needed for large area exposure of moderate resolution pattern.

(6) Stitching error reduction in electron beam lithography with in-situ feedback using self-developing resist. Nitrocellulose, which is a self-developing resist, can be used very effectively to optimize writing field alignment. In the process, we first exposed a test pattern in

nitrocellulose resist near the writing field boundary, and then examined the pattern at high magnification, which provided feedback on the writing field alignment accuracy. Based on such feedback, the parameters for writing field alignment (notably zoom and rotation values for the Raith 150^{TWO} tool) were adjusted accordingly. After several iterations, we were able to reproducibly achieve nearly perfect (<50 nm stitching error) writing field alignment with a very large 1 mm^2 writing field size.

For the second part, the project of batch fabricating the high aspect ratio AFM tips has been demonstrated.

(7) Batch fabrication of high aspect ratio AFM tips. We here developed a method to batch fabricate the HAR AFM tips by forming a hard metal etching mask just on the apex of the pyramid tip followed by silicon dry etching to achieve the HAR pillar right below the metal island mask. Since it is a batch and lithography-free process, it has much higher throughput and much lower manufacturing cost per tip. This technique was first successfully applied on large-area pyramid arrays and then transferred to the commercial regular AFM tips, and has demonstrated the uniformity, reproducibility and yield of those HAR tips. Specifically, here we demonstrated the radius of curvature of tip apex down to 10 nm and aspect ratio up to 1:20. The tip apex diameter and tip pillar height are controllable by tuning metal thickness and silicon dry etching time respectively. In addition, the tip shape can be tunable by changing the etching gas ratio of silicon RIE. Finally, we demonstrated that the HAR tips fabricated using our technique gave a better imaging quality than the commercial regular low aspect ratio tips. The application of these low cost HAR tips is vast, since as a popular nano-metrology instrument, AFM is nowadays employed in many different areas of nanotechnology.